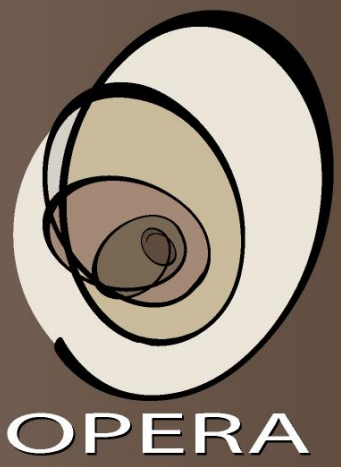

Scoping study examining the behaviour of Boom Clay at disposal depths investigated in OPERA

OPERA-PU-BGS523&616

Radioactive substances and ionizing radiation are used in medicine, industry, agriculture, research, education and electricity production. This generates radioactive waste. In the Netherlands, this waste is collected, treated and stored by COVRA (Centrale Organisatie Voor Radioactief Afval). After interim storage for a period of at least 100 years radioactive waste is intended for disposal. There is a world-wide scientific and technical consensus that geological disposal represents the safest long-term option for radioactive waste.
Geological disposal is emplacement of radioactive waste in deep underground formations. The goal of geological disposal is long-term isolation of radioactive waste from our living environment in order to avoid exposure of future generations to ionising radiation from the waste. OPERA (OnderzoeksProgramma Eindberging Radioactief Afval) is the Dutch research programme on geological disposal of radioactive waste.
Within OPERA, researchers of different organisations in different areas of expertise will cooperate on the initial, conditional Safety Cases for the host rocks Boom Clay and Zechstein rock salt. As the radioactive waste disposal process in the Netherlands is at an early, conceptual phase and the previous research programme has ended more than a decade ago, in OPERA a first preliminary or initial safety case will be developed to structure the research necessary for the eventual development of a repository in the Netherlands. The safety case is conditional since only the long-term safety of a generic repository will be assessed. OPERA is financed by the Dutch Ministry of Economic Affairs and the public limited liability company Electriciteits-Produktiemaatschappij Zuid-Nederland (EPZ) and coordinated by COVRA. Further details on OPERA and its outcomes can be accessed at www.covra.nl.

OPERA-PU-BGS523&616
Title: Scoping study examining the behaviour of Boom Clay at disposal depths investigated in OPERA
Authors: Harrington, J. F., Cuss, R. J., Wiseall, A. C., Daniels, K. A., Graham, C. C., and Tamayo-Mas, E.,
Date of publication: 2017
Keywords:

British Geological Survey
NATURAL ENVIRONMENT RESEARCH COUNCIL

Contents

List of Figures

Executive Summary

The Onderzoeks Programma Eindberging Radioactief Afval (OPERA) is the third national research programme for the geological disposal of radioactive waste in the Netherlands, operating during the period 2011 to 2017.

The rock types to host a geological disposal facility that are currently being considered in the Netherlands are salt and clay. Earlier Dutch work focussed mostly on salt, but the present programme OPERA is focused on a specific clay formation the Boom Clay. Previous studies have primarily focused on examining behaviour at the Belgium reference depth (~220m). The work presented in this study extends this knowledge-base to repository depths of potential interest in the Netherlands (~500m).

In this report, results from a scoping study examining the hydromechanical properties of Boom Clay are presented, including investigations on consolidation, swelling, hydraulic, gas and deformation behaviour. These were performed on preserved core material retrieved from the HADES underground research laboratory, Belgium. Sections of core were then consolidated to a depth representative of the Netherlands.

Permeability was sensitive to stress state and thermal load, though incremental changes in NaCl concentration had minimal impact. Hysteresis was observed in thermally induced changes in permeability. Gas entry was closely linked to the minimum principal stress component, with mass and volume changes of samples observed as a result of gas migration. Stress, porewater pressure and gas flow were integrally linked with pathways evolving temporally and spatially. A transition from brittle to ductile deformation was noted with increasing stress in both compression and shear. Boom Clay is both complex and anisotropic in its behaviour.

Acknowledgements

This study was undertaken by staff of the Minerals and Waste Programme of the British Geological Survey. The authors would like to thank the following: SCK-CEN, in particular Norbert Maes, for expertly coring Boom Clay at the HADES URL in Belgium; Richard Shaw (BGS) for project initiation and management; John Williams (BGS) for internal review of the report; Kay Green (BGS) for making the synthetic pore fluid used in all experiments; Tony Milodowski and Dan Parkes for SEM analysis of nano-particle injection; Neil Stacey (BGS) for sample preparation; Humphrey Wallis and Wayne Leman (BGS) for engineering design and build of bespoke apparatus

1 Introduction

In defining the long-term fate of radionuclides in a repository for radioactive waste, it is necessary to understand the hydrogeological context of the site and how this may evolve temporally and spatially. In the Netherlands, the rock types to host a geological disposal facility that are currently being considered are salt and clay. Earlier Dutch work focussed mostly on salt, but the present programme OPERA is focused on a specific clay formation the Boom Clay. As a plastic clay, this material is a suitable geological formation for long term disposal. A benefit in selecting the Boom Clay for investigation is the significant volume of research already conducted on this formation in Belgium, where the clay is currently the reference formation for the development of a safety case for a deep geological repository for radioactive waste. As such, a significant proportion of this research may be directly transferrable to the Netherlands national programme. However, important differences may occur as a result of the increased depth of burial of the formation in the Netherlands compared to that in Belgium.

1.1 *The disposal concept in Boom Clay investigated in OPERA*

In the Netherlands, current policy on the treatment of radioactive waste involves a period of interim storage (of at least 100 years), prior to its disposal. The disposal concept for the deep geological disposal of radioactive waste is based on the Belgium Supercontainer Concept (Verhoef, 2011) as well as other concepts for disposal in clay. In the Boom Clay concept it has been proposed that the waste would be disposed of in a formation with a thickness of around 100 metres. In contrast to the Belgian concept, the proposed dimensions of containers and disposal drifts are smaller, primarily a result of the amount and characteristics of the waste produced in the Netherlands, as well as the requirement for retrievability of the waste. Because of the probability of future glaciations in the Netherlands, a disposal depth of 500 m has been proposed in order to minimise the impacts of glacial processes, including erosion.

A number of favourable characteristics common to clay formations are particularly advantageous for a potential host, including:

- Low permeability;
- Chemical buffering capacity;
- Geochemical characteristics that favour low solubility of radionuclides;
- High capacity to retard the migration of radionuclides towards the accessible environment, e.g. through sorption capacity and diffusion-dominated transport.

Additional beneficial characteristics specific to the Boom Clay include the presence of low hydraulic gradients (Vis and Verweij, 2014) and a propensity for plastic deformation, resulting in rapid self-sealing of fractures and void spaces. The vast majority of studies on the Boom Clay to date relate to research conducted at (and material removed from) the Underground Research Laboratory (URL), HADES, at a depth of approximately 220 m beneath Mol, Belgium.

1.2 *Geological setting*

The geological and hydrogeological setting of the Boom Clay in the Netherlands has been summarised in (Vis and Verweij, 2014) and that in northern Belgium by Beerten and Leterme (2012). The Boom Clay (usually referred to as the Rupel Clay in the Netherlands) is of lower Oligocene (ca 28 to 34 Ma) age and forms part of the Rupel Formation. In the Netherlands the Rupel Formation has been subdivided into the Vessem, Rupel Clay and Steensel members (Wong et al., 2007). These members are diachronous, with both the

basal Vessem and the overlying Steensel members being sandy marine deposits (Vis and Verweij; 2014) laid down close to the palaeo-shorelines. The Boom Clay is a pyritic, grey to dark brown marine clay with septarian (carbonate-rich) concretions. Towards the basin margins the clays grade into sands. The formation reaches a maximum thickness of up to 250 m, with a mean thickness of around 65 m, and dips gently towards the north-east at between 1 and 2°. The formation is present beneath most of the Netherlands, both on- and off-shore, up to a depth of approximately 1500 m. Only in the Maastricht area, where older rocks crop out, is it completely absent. It is not a suitable host rock for radioactive waste disposal in all areas, because of its insufficient thickness (<100 m) or sand-rich composition.

Burial history can play an important role on the hydromechanical properties of clay-rich rocks and therefore requires careful consideration. Nickel (2003) used correlation of borehole profiles to estimate the Boom Clay depth and thickness for most of the Netherlands. The Boom Clay is shallowest in the west (Hellevoetsluis-1) and south-east (Broekhuizenvorst 52E/114) with a depth of 350 m and 416 m, respectively. The deepest the Boom Clay is found in the Asten-1 and Veldhoven-1 boreholes, with depths of 1317 m and 1122 m, respectively. This indicates that the deepest deposits of the clay have been buried close to 1.4 km beneath sea level. The Boom Clay was mainly buried as a result of continuous sedimentation within the North Sea Basin during the Oligocene and into the Chattian. Deposition episodes for the overlying strata were disrupted by a small tectonic uplifting/tilting event at about 27 Ma, which led to some erosion of sand layers deposited onto the Boom Clay. Based on the observations of Wildenborg et al., (2003) on core from Blija (in the North of the Netherlands), an approximate averaged value for preconsolidation stress in the Netherlands is 7.45 MPa (Wiseall et al., 2015). This maximum previous burial pressure would result in an over consolidation ratio at 500m of 1.5-1.7, indicating a lightly overconsolidated clay.

1.3 *Stress conditions and porewater chemistry*

Wiseall et al., (2015) discuss the available data for the Netherlands and HADES, which have been used as a guide to define the boundary conditions for the current experimental programme, as summarised in **Table 1-1**. Note that tests were conducted representative of 223 m (HADES) and 500 m (Netherlands).

Parameter	Symbol	Units	223 m	400 m	500 m	600 m
Total vertical stress	σ_v	MPa	**4.4**	8.0	**10.0**	11.9
Horizontal stress*	$\sigma_{H,h}$	MPa	**3.9**	7.1	**8.8**	10.6
Effective mean stress*	σ_{eff}	MPa	**1.9**	3.4	**4.3**	5.2
Pore water pressure	P_w	MPa	**2.2**	3.9	**4.9**	5.9

Table 1-1: Reference stress conditions used in this report. *Values are calculated based on a linear extrapolation with depth, from differential stress measured at Mol.

In low permeability formations, pore fluid may exhibit significant chemical gradients resulting from the low transport capacity of the material and it is, therefore, necessary to understand the degree of variation within the Boom Clay. A detailed analysis of pore fluid data for the formation was conducted by De Craen et al., (2004) and a reference pore water composition defined for HADES (**Table 1-2**). Given the importance of fluid chemistry on the behaviour of clay-rich materials, it is crucial that transport and mechanical testing is conducted using water in equilibrium with the test material. To do this a reference pore fluid has been used for all experiments in this study.

Ion	mg/l	mmol/l	Ion	mg/l	mmol/l	Property	Unit	Value
Ca	2.0	0.05	**Total S**	0.77	0.02	**pH**		8.5
Fe	0.2	0.003	**Cl -**	26	0.7	**pCO_2**	Atm	$10^{-2.62}$
Mg	1.6	0.06	**SO_4^{2-}**	2.2	0.02	**Eh**	mV	-274
K	7.2	0.2	**HCO_3 -**	878.9	14.4	**Ionic strength**		0.016
Si	3.4	0.1						
Na	359	15.6						
Al	0.6×10^{-3}	2.4×10^{-5}						

Table 1-2: Reference Boom Clay pore water after De Craen et al., (2004b).

1.4 *Experimental study*

This report presents the results of the experimental scoping study undertaken as part of the OPERA research initiative. The aim of the study was to obtain preliminary data on the hydromechanical properties of Boom Clay at a depth representative of the Netherlands. Material was cored at the HADES URL and a proportion of this was conditioned to represent 500 m (Chapter 2). Consolidation and hydraulic behaviour was investigated in Chapter 3, where a sample of Boom Clay was subject to a stress history to examine the evolution in parameters as a function of depth. A fundamental response of the Boom Clay is its capacity to swell and self-seal. This was investigated in Chapter 4 with tests conducted under free-swell and constant volume conditions. In a repository containing heat emitting waste, it is important to understand the impact of thermal load on the hydraulic behaviour of the Boom Clay, as reported in Chapter 5. In low permeability materials coupled flow phenomena (e.g. osmosis) have been cited by a number of researchers as a potential mechanism for non-Darcian fluid movement. In Chapter 6, an attempt was made to define the osmotic membrane potential, which because of the high permeability of the clay, was not possible within the scope of this study. However, the sensitivity of flow to changes in salinity (NaCl) were examined. Chapter 7 explores the mechanisms governing the advective movement of gas. Experiments were conducted in three test geometries and a detailed picture defining new processes controlling gas flow identified. Discontinuities (fractures, faults, joints etc.) may play a significant role in the hydrogeology and present zones of enhanced flow, which is explored in Chapter 8. The mechanical behaviour of Boom Clay controls the short- and long-term behaviour of a repository. The strength and elastic properties have been defined, as described in Chapter 9. Finally, a summary bringing all observations together and into context of disposal in the Netherlands is made in Chapter 10. At the end of each section, major outcomes from this scoping study and recommendations for research priorities are highlighted.

2 Conditioning of the Boom Clay

Cores of Boom Clay were acquired from SCK-CEN (Belgium) from the HADES URL for use in this scoping study. The Boom Clay from the HADES facility sits at a depth of 220m and therefore has not been consolidated to the same degree as the Boom Clay intended as the host rock material for the Netherlands Boom Clay disposal concept depths. As no material from the COVRA depths was available, the Boom Clay needed to be artificially consolidated to ensure that the stress-state matched the expected conditions and the behaviour was representative of that anticipated at the COVRA repository depths. Cores of the Boom Clay were drilled from the floor of the HADES URL in 2014 and were preserved in aluminium foil with a vacuum seal (**Figure 2-1**).

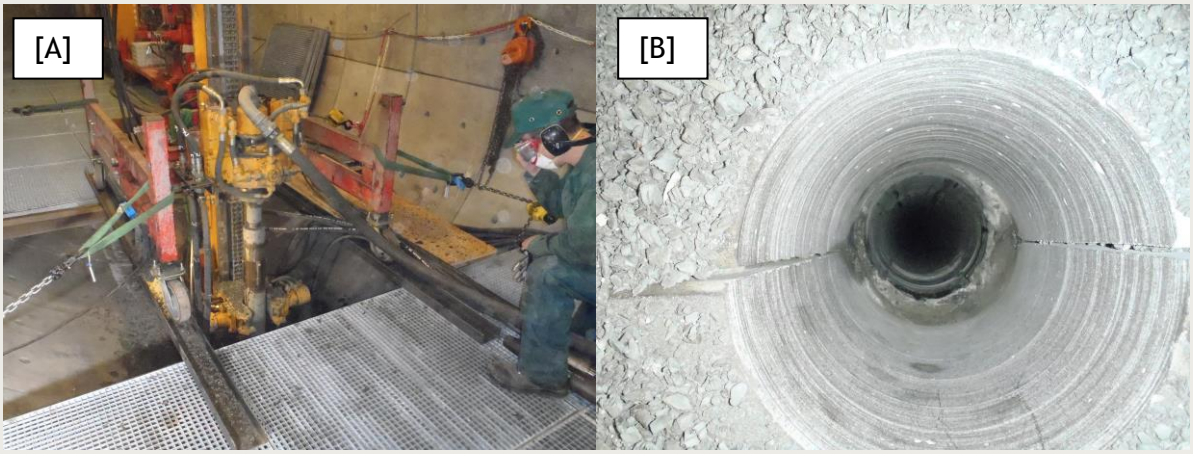

Figure 2-1: Acquisition of the Boom Clay cores from the HADES URL at Mol (courtesy of SCK-CEN) [A] Drilling into the floor of the HADES URL. [B] A down whole image of the borehole.

To condition the cores from the HADES URL to match the degree of consolidation at COVRA depths, sections of the core were placed in a custom built consolidation rig fitted with an EnerPac that allowed the pressure to be raised to the COVRA depth equivalent, before the material was removed and cut up to provide Boom Clay samples for the testing program. There are spatial variations in the Boom Clay in Belgium and whilst there may also be variations in mineralogy between the Belgian and Netherlands boom clay, any variability cannot be addressed in this study.

2.1 *Conditioning Apparatus Set-up*

Two large cores of the Boom Clay from the Hades URL were conditioned in the consolidation rig (**Figure 2-2**). Each piece of the cylindrical core was selected and the ends were sawn off perpendicular to the cylinder length. The core was imaged using conventional X-ray before and after conditioning (**Figure 2-3**). The core was slotted into the steel consolidation vessel and a filter and a sliding piston sealed with o-rings were fitted into the steel vessel on top of the clay. At the base of the vessel, a filter and a bottom closure with fixed closure ring retained the sample. An Enerpac collar securely attached the Enerpac ram unit and Enerpac plunger onto the top of the vessel to allow the consolidation to take place parallel to the core axis and perpendicular to bedding. Pipework was then connected to the base of the vessel on the fixed closure ring, and to the top of the piston which allowed the porewater pressure to be controlled from a Teledyne ISCO high precision syringe pump whilst the axial pressure was set by the Enerpac ram. The axial pressure was set at 15.5MPa at the start of each run and the porewater

pressure was set to 1MPa. The porewater used for the consolidation was a synthetic porewater with a composition representative of the conditions at the correct depth for the Netherlands repository concept (De Craen et al., 2004b, Wiseall et al., 2015). Each run was continued until the flowrate recorded by the syringe pump controlling the porewater pressure had reached an asymptote. Reaching the asymptote indicated that for the specific confining pressure the outflow from the sample had reached zero, no more volume change was occurring and the sample had reached equilibrium. To decommission the run, the Enerpac ram unit, the Enerpac plunger and Enerpac collar were removed from the top of the steel vessel, whilst the fixed bottom closure was removed from the vessel's base. The clay core and the piston were jacked out of the vessel from the base upwards (**Figure 2-4**).

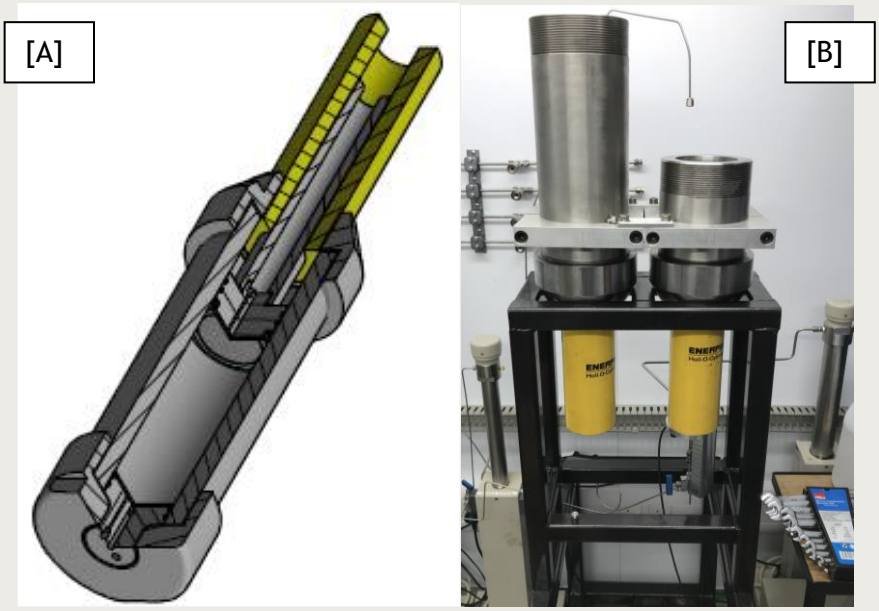

Figure 2-2: The clay conditioning apparatus. [A] Schematic diagram of the steel vessel with Enerpac piston (yellow) attached to the top. [B] Two consolidation vessels (partially dismantled) with yellow Enerpacs attached.

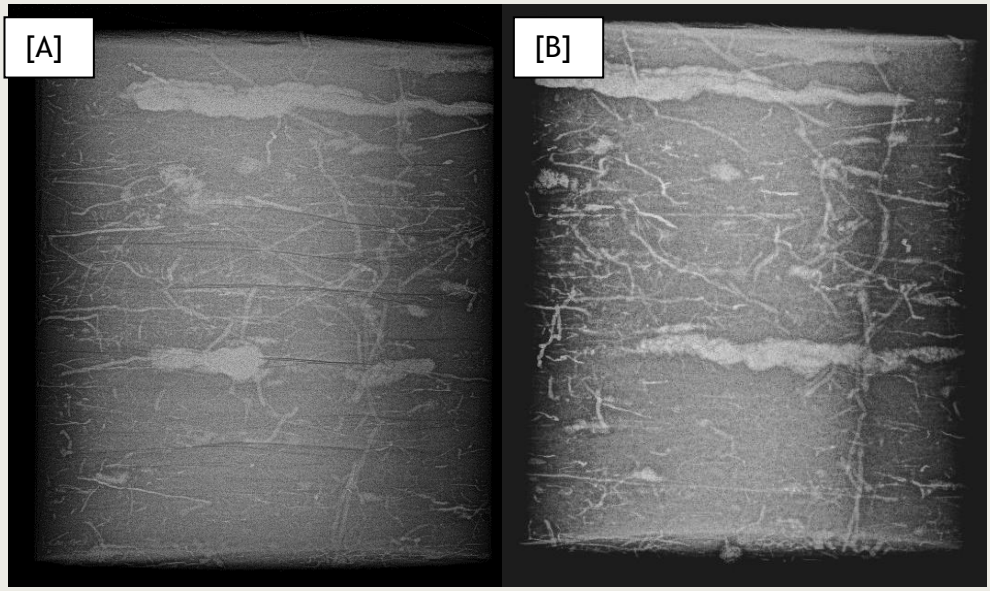

Figure 2-3: X-ray images showing core CGR107 Ref 10.27-10.4 (Consolidation Run 1). A) Image of the core prior to consolidation. B) Image of the core after consolidation. The linear striations visible in A) may represent micro-cracks which have opened after initial sampling and storage.

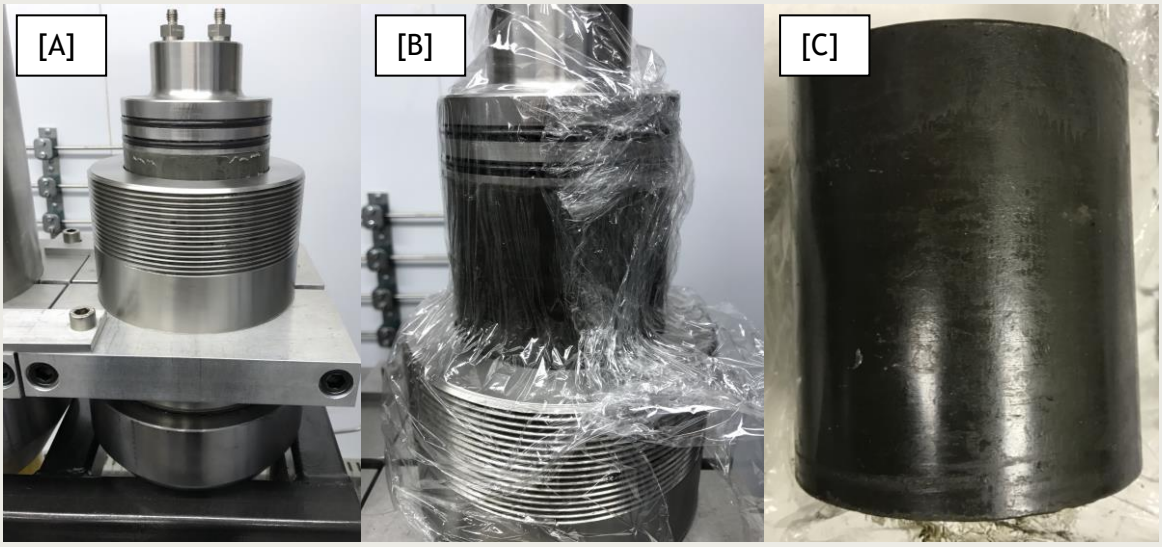

Figure 2-4: Removal of the Boom Clay from the apparatus after conditioning run 1. [A] The Enerpac is removed from the top of the steel vessel containing the core. [B] The core is pushed out of the vessel. Care was taken to minimise the impact of sample drying. [C] Post-conditioning Boom Clay, consolidated to COVRA repository depths.

2.2 *Conditioning Run 1*

The first conditioning run took place over 141 days. The axial pressure was increased to 15.5MPa and the porewater pressure was set to 1MPa. The pressures stayed constant throughout the consolidation and conditioning run and the flowrates were continuously monitored using data logging software. The test was complete and could be terminated once the cumulative flow from the porewater pressure pump had reached an asymptote and no further flow was occurring (**Figure 2-5 A**). In addition, an LVDT measuring the vertical displacement indicated that no further vertical motion was occurring after 50 days (**Figure 2-5 B**). It is interesting to note that the X-ray imaging of the core before consolidation (**Figure 2-3 A**) showed linear striations that did not appear on the X-ray image post-consolidation (**Figure 2-3 B**). These may have represented micro-fractures that had opened after the initial sampling and storage, and that were closed by the sample conditioning.

Figure 2-5 shows a hiatus in the data between 55 and 70 days resulting in a reduced flow and temporary decrease in the displacement rate shown on the LVDT. This occurred due to a fault with the air conditioning in the temperature controlled room resulting in a temporarily elevated ambient temperature of <2°. The temporarily raised temperature caused deviations in the porewater and axial ram flow rates and a small deflection in the LVDT measurements. However, fitting the LVDT displacements (**Figure 2-5 B**) shows that the conditioning had taken place in the first 50 days. The LVDT data were fitted using an exponential of the form f(x) = a*exp(b*x) + c*exp(d*x), where the coefficients and their 95% confidence intervals were equal to: a) 0.0008486 (0.0008334, 0.0008638), b) -0.07311 (-0.07459, -0.07163), c) 0.00434 (0.004317, 0.004363) and d) -1.158 (-1.173, -1.144). The fit had an R^2 value of 0.9961.

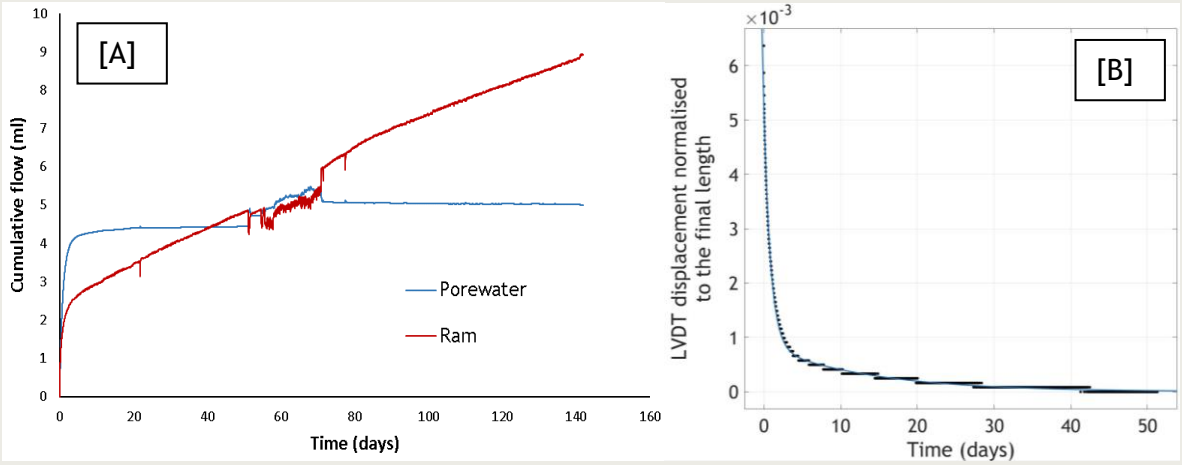

Figure 2-5: Conditioning run 1. [A] The cumulative flow from the syringe pump controlling the porewater pressure (blue) and the axial ram (red). The test was completed when the porewater flow had reached an asymptote. [B] The axial displacement measured by the LVDT normalised to the final length measurement (black dots) fitted by an exponential function with two terms.

2.3 *Conditioning Run 2*

The second conditioning run duration was 113 days. As with conditioning run 1, for conditioning run 2 the axial ram pressure was set to 15.5MPa and the porewater pressure was set to 1MPa. For the first 5 days, the porewater and ram flow rates were high, reducing after this time (**Figure 2-6 A**). The flow rate to the axial ram remained constant for the rest of the run. The porewater pressure pump flow rate slowly reached an asymptote. The axial displacement recorded by the LVDT showed a large change in the first 5 days from 143mm down to 127mm; after 50 days there was almost no axial displacement recorded (**Figure 2-6 B**). As with consolidation run 1, the LVDT data were fitted using an exponential of the form f(x) = a*exp(b*x) + c*exp(d*x), where the coefficients and their 95% confidence intervals were equal to: a) 0.008539 (0.008503, 0.008574), b) -1.086 (-1.096, -1.076), c) 0.000789 (0.0007657, 0.0008123) and d) -0.07267 (-0.07506, -0.07028). The fit had an R^2 value of 0.9969.

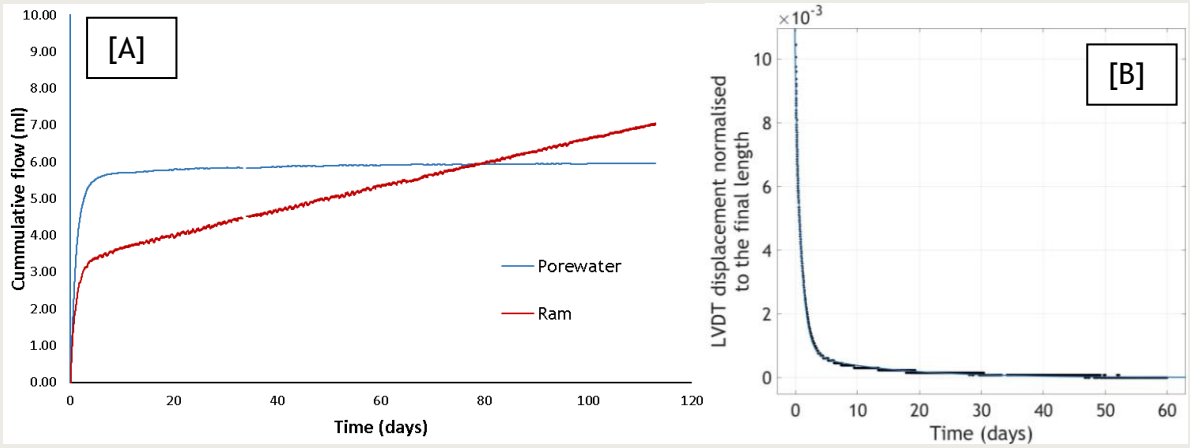

Figure 2-6: Conditioning run 2. [A] The cumulative flow from the syringe pump controlling the porewater pressure (blue) and the axial ram (red). The porewater flow reached an asymptote at ~110 days. [B] The normalised axial displacement recorded by the LVDT over the duration of the experiment (black dots) fitted by an exponential function with 2 terms (blue line).

2.4 *Modelling of Consolidation*

As will be described in further detail in the next Chapter, here the standard Biot's model is considered to derive the values of the permeability and the Young's modulus. The data for the flow of porewater from the sample during testing are compared with the output from the elastic model (**Figure 2-7**).

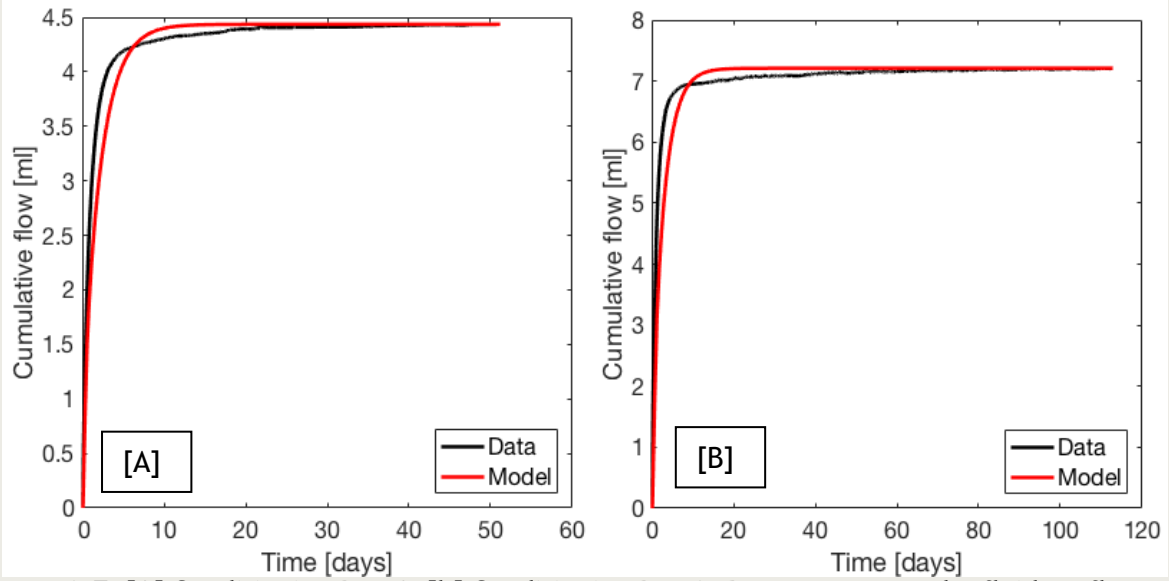

Figure 2-7: [A] Conditioning Run 1. [b] Conditioning Run 2. Data represents the fluid outflow volume from the sample over time (black line). The model curve (red line) is the output from the elastic model.

Using the model fittings, the predicted permeability and Young's Modulus values are estimated as follows:

Consolidation Run 1:

- Predicted permeability value: 3.42 x 10^{-19} m^2
- Predicted Young's Modulus: 7.22 GPa

Consolidation Run 2:

- Predicted permeability value: 3.74 x 10^{-19} m^2
- Predicted Young's Modulus: 5.46 GPa

2.5 *Sample Preparation*

Once the conditioning run had been completed and the clay cores had been consolidated to depths representative of the Netherlands repository concept, the cores were removed from the consolidation apparatus and divided to provide samples for the testing program. Samples were tessellated to ensure that there was minimum wastage of the consolidated core and an optimum number of samples could be obtained. These were then taken from the consolidated core using a circular saw and machine lathe, working as quickly as possible to minimise moisture loss from the clay.

3 Consolidation and hydraulic behaviour

3.1 *The role of effective stress*

For porous materials, the influence of effective stress is key to determining their physical properties. In the case of an argillaceous clay or rock, burial and exhumation history can have a profound influence on the hydro-mechanical properties of the material (Bjerrum, 1967). During burial of a sediment, the resulting increase in effective stress leads to consolidation, by way of compaction and dewatering, resulting in a reduction in both porosity and volume. The importance of this relationship for clay rich materials is described in greater detail by Wiseall and co-workers (2015). In soil mechanics, the influence of effective stress is generally considered in terms of its influence on the void ratio, *e*, of the material, where:

$$e = \frac{\emptyset}{1-\emptyset} \tag{3-1}$$

and $\emptyset$ is a function of the porosity.

Sample response to compression is typically described in e-log(P') space (where e is void ratio and P' is effective stress). An idealised response is shown in **Figure 3-1**. On initial compression, the void ratio of a normally consolidated clay will decrease linearly with increasing effective stress; this is known as the Virgin Compression Line (VCL). An overconsolidated clay (for a given effective stress) will plot on the Recompression/Rebound Line (RRL) (also referred to as the expansion/swelling line) as effective stress is relieved. On recompression, the clay state will ultimately re-join the VCL. Experimentally derived e-log(P_{eff}) curves are also used to estimate the maximum effective stress that the formation has previously been subjected to, generally termed the preconsolidation pressure, Pc. This provides a simple estimate of stress history and can be used to determine the over consolidation ratio (OCR).

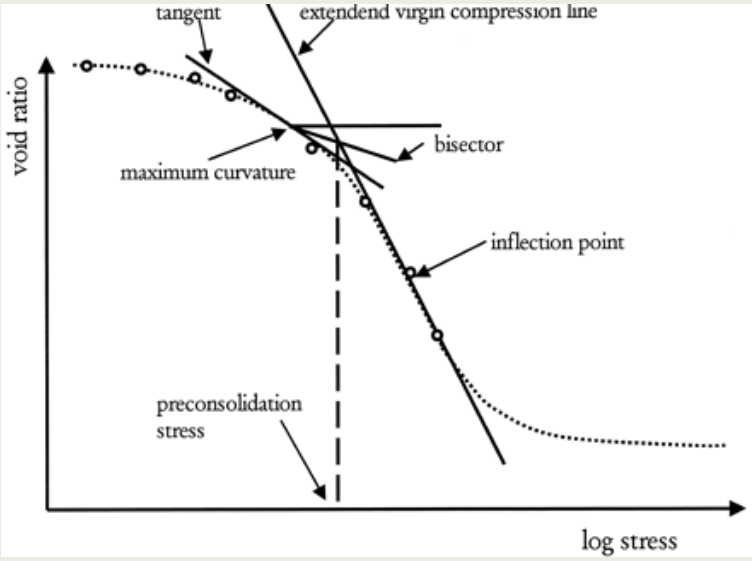

Figure 3-1: An idealised schematic showing the impact of increasing effective stress on void ratio during consolidation of a clay.

Wiseall et al., (2015) give a detailed account of previous consolidation studies conducted on Boom clay. The Boom Clay, in the Belgian context, is generally described as being a lightly overconsolidated material (Horseman et al., 1987; Horseman et al., 1993; Bernier et al., 1996). Estimated values for the vertical preconsolidation pressure, Pc', of the Boom

Clay taken from HADES generally range from between ~5 and 6 MPa, leading to an OCR at *in situ* conditions of ~2 – 3, though there is some debate relating to these values. Nevertheless, the most commonly adopted value within literature appears to be an OCR of 2.4. In this chapter, we present findings of a consolidation test conducted on Boom clay material taken from HADES, in order to determine whether typical consolidation behaviour is observed. In the following scoping experiments it is therefore expected that a similar response will occur when this test material is consolidated to conditions of relevance to the Netherlands Boom Clay disposal concept.

3.2 *Experimental set-up*

A cylindrical sample taken from the HADES URL (core reference: CGR 76/77D 6.02-6.52m), was produced with a 50 mm steel former with a diameter of approximately 50mm and a length of 43cm. Sample ends were faced-off perpendicular to the cylinder length, with the core axis parallel to the intended flow direction. Care was taken to work as quickly as possible, in order to reduce the impact of sample drying. The test sample, Covra-1, was produced such that flow was perpendicular to bedding within the clay. Basic geotechnical properties are presented in **Table 3-1**, with post-test measurements based on an estimation for the change in sample volume derived from the difference in mass between start and finish weights. This was necessary as it wasn't possible to accurately determine post-test sample volume due to deformation of the sample caused during testing.

	Sample No.	Reference (m)	Water content (%)	Bulk density (g/cm^3)	Porosity (%)	Saturation (%)
Pre-test	Covra-1	CGR76/77D 6.02-6.52	22.1	2.05	37.2	100
Post-test	Covra-1	CGR76/77D 6.02-6.52	20.2	20.8	35.1	100

Table 3-1: Basic pre- and post-test properties of specimen Covra-1. An assumed specific gravity for the mineral phases of 2.67 $Mg.m^{-3}$ (Wiseall et al., 2015) was used in these calculations. Post-test measurements are approximate as they are based on an estimated sampled volume.

A significant amount of data is available on the consolidation properties of the Boom Clay (Wiseall et al., 2015). However, before conducting the additional scoping tests planned in this experimental programme it was first necessary to determine that the consolidation properties of the core material collected from Mol was consistent with that tested in previous programmes. The experimental approach for this involved the use of a standard BGS isotropic permeameter apparatus (**Figure 3-2**). The basic permeameter design is described in some detail by Harrington and Horseman (1999) and consists of five main components: (1) a specimen assembly, (2) a 70 MPa rated pressure vessel and associated confining pressure system, (3) a fluid injection system, (4) a backpressure system, and (5) a National Instruments data acquisition system. The specimen is subject to an isotropic confining stress. The permeant can be changed at any time during an experiment. Independent pore pressure transducers are placed on the injection and backpressure lines to allow the system to be monitored for drift.

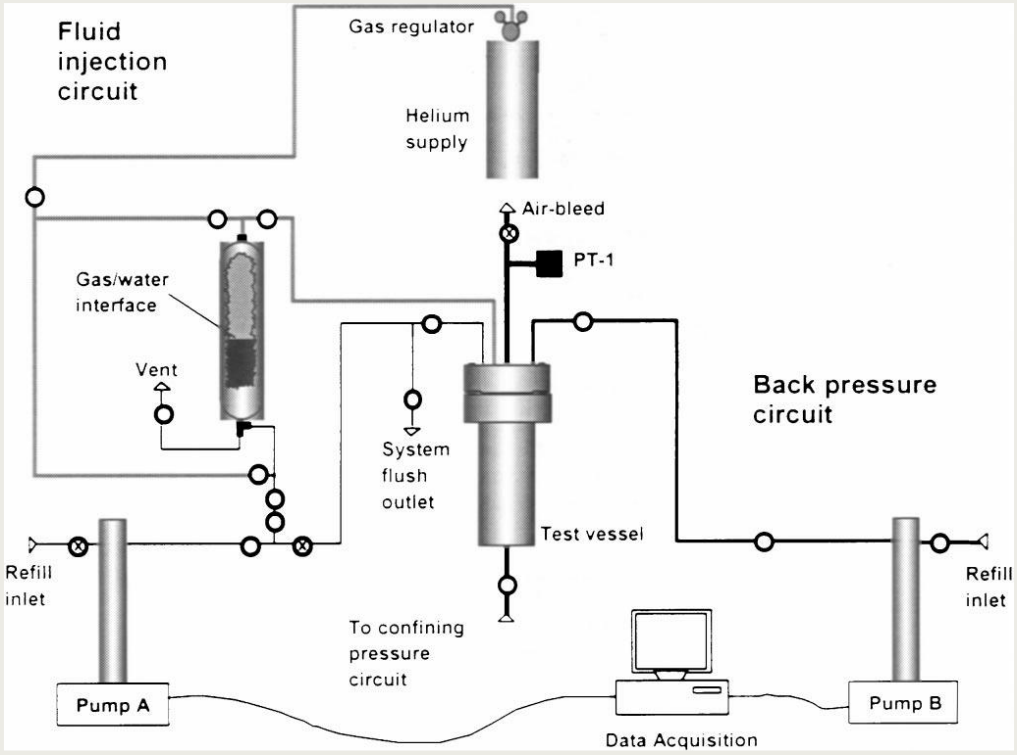

Figure 3-2: Schematic of a standard BGS isotropic permeameter apparatus.

Figure 3-3: Isotropic test assembly, containing a sample of Boom Clay.

The cylindrical rock specimen is sandwiched between two end-caps and jacketed in heat-shrink Teflon to exclude confining fluid. A unique 'lock-ring' arrangement (**Figure 3-3**) is then placed over the jacketed specimen, so as to provide a leak-tight seal. The inlet and outlet zones for permeant flow through the specimen are provided by porous filter discs, 50 mm in diameter, which rest on the bearing surface of the end-caps. During hydraulic testing, all the filters are saturated with a synthetic porewater solution, based on the pore fluid chemistry at HADES URL (see Section 1-1).

Volumetric flow rates are controlled or monitored using a pair of high-precision ISCO syringe pumps, operated by two digital control units. These pumps are calibrated in advance of testing, using a Druck PTX610 pressure transmitter. The ISCO pump controller has an RS232 serial port that allows volume and pressure data to be transmitted to a high specification National Instruments data acquisition. All pump data, as well as data from the independent pore-pressure transducers is logged at two minutes intervals. Testing is performed in an air-conditioned laboratory at a temperature of 20 ± 0.3 ºC. This approach reduces environmental impacts on flow data and allows exceptionally small flows to be measured within leak-tight apparatuses.

Testing was initiated by allowing the sample to rehydrate under a confining stress of 4.4MPa and a pore fluid pressure of 2.2MPa, applied at both the injection and backpressure ends of the sample. These conditions were selected as the *in situ* pressure conditions at the sampling location/depth at the HADES URL (see Chapter 1). This stage was conducted to ensure the sample was fully saturated under prior *in situ* conditions before consolidation testing. A hydraulic gradient of 0.5MPa was next applied across the sample, allowing hydraulic conductivity to be determined from the resulting outflow. This gradient was maintained during consolidation testing, during which time the confining pressure was increased in stepwise increments, thereby also allowing the examination of the impact of effective stress on hydraulic properties. Net flow of fluid out of the sample was monitored during each step, allowing changes in sample void ratio to be estimated during consolidation. The full experimental test history is given in **Table 3-2**.

Stage	Type	Injection pressure (MPa)	Back pressure (MPa)	Confining pressure (MPa)	Ave. effective pressure (MPa)	Applied pore-pressure gradient (MPa)
1	Hydration	2.2	2.2	4.4	2.20	0.0
2	Hydraulic CPT	2.7	2.2	4.4	1.95	0.5
3	Consolidation	2.7	2.2	6.4	3.95	0.5
4	Consolidation	2.7	2.2	8.4	5.95	0.5
5	Consolidation	2.7	2.2	10.4	7.95	0.5
6	Unload	2.7	2.2	8.4	5.95	0.5
7	Unload	2.7	2.2	6.4	3.95	0.5
8	Unload	2.7	2.2	4.4	1.95	0.5
9	Reload	2.7	2.2	6.4	3.95	0.5
10	Reload	2.7	2.2	8.4	5.95	0.5
11	Reload	2.7	2.2	10.4	7.95	0.5
12	Reload	2.7	2.2	12.4	9.95	0.5

Table 3-2: Experimental test history for sample COVRA-1.

3.3 *Results*

3.3.1 Hydration and initial hydraulic testing

Initial hydration of the sample was observed to occur over a period of around 4 days (**Figure 3-4**), before inflow rates were seen to become negligible at both sample ends. This reasonably rapid hydration response suggests only limited sample swelling occurred during this time, indicating that the sample had remained well-hydrated during excavation, transportation and preparation and that the applied synthetic pore fluid composition was consistent with that experienced by the core material *in situ* at the HADES URL.

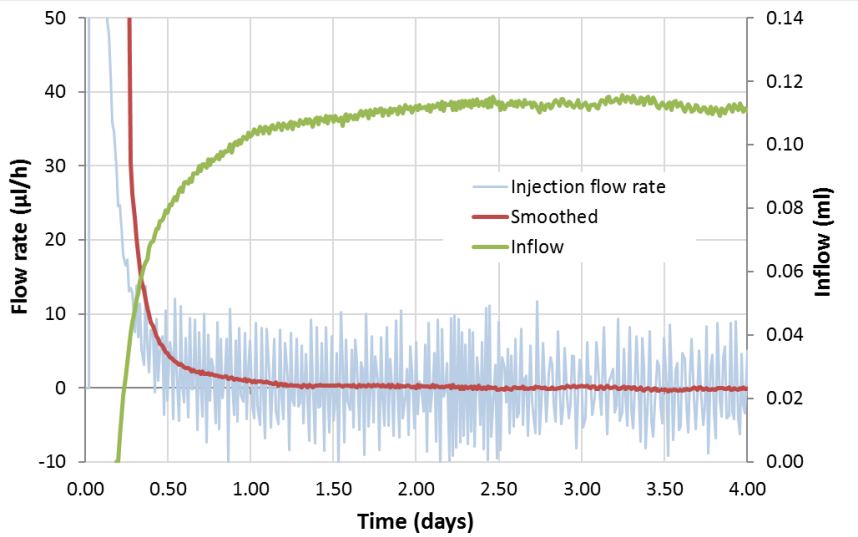

Figure 3-4: Inflow response during hydration at the sample injection end.

The sample response on hydraulic permeability testing is shown in **Figure 3-5**. Steady-state flow, with close matching and inflow and outflow was achieved within a period of around 7 days. Assuming Darcy's law, a 1-D analysis of the resulting data yields a hydraulic permeability of ≈ 1.6×10^{-19} m^2, under HADES URL stress conditions. This is consistent with values previously reported at Mol (Wiseall et al., 2015), suggesting recovered core has typical hydraulic properties for that location.

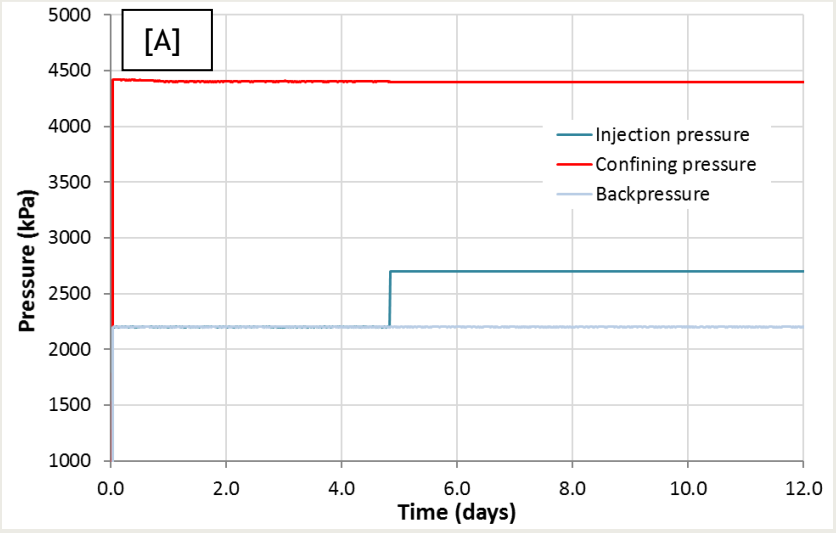

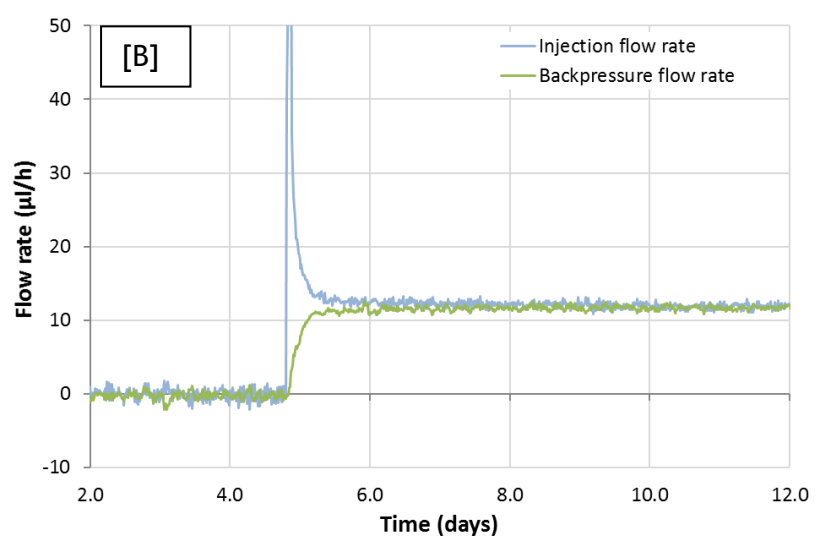

Figure 3-5: [A] Applied pressure conditions during initial rehydration and hydraulic permeability testing. [B] Inflow and outflow rates at the sample injection and backpressure ends, during hydraulic permeability testing.

3.3.2 Consolidation behaviour

During consolidation testing, increments/decrements in confining pressure were applied whilst maintaining a constant pore pressure gradient across the sample. This included loading, unloading and reloading the sample, so as to examine any potential hysteresis. The resultant changes in net fluid flow were then monitored (**Figure 3-6**) and used to calculate the reduction in void ratio, e, as a function of applied effective stress (**Figure 3-7**). A number of techniques are available to determine the point of yield in e-log P_{eff} space. Given the available number of data points available, rigorous statistical fitting through the linear segments of the loading curve is not viable. However, a linear fit through the initial and virgin consolidation slopes, yields an intersection point of approximately 5.05 MPa, i.e. an over-consolidation ratio of around 2.3. This can be equated to the effective preconsolidation pressure of the clay and denotes the point at which yield begins. This value is consistent with previous observations for Boom Clay taken from the same depth interval at the HADES URL (Wiseall et al., 2015) and, as with hydraulic measurements, indicates a reasonably typical response. Calculated values for the Bulk, Young's and Shear moduli of the clay are also given in **Table 3-3**, as a function of effective stress. Observations indicate a notable reduction in void ratio and the elastic moduli are likely to occur, when the Boom Clay is taken to effective stress conditions of relevance to the Netherlands (Section 1-3).

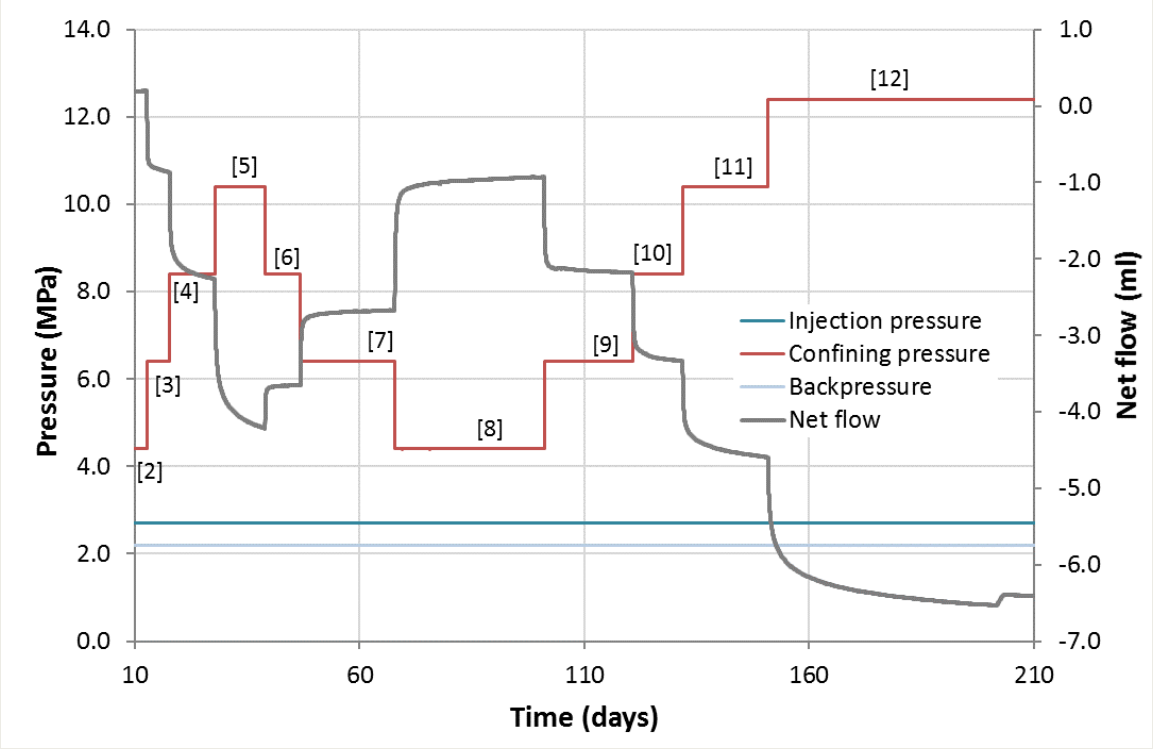

Figure 3-6: Changes in net flow as Boom Clay sample COVRA-1 is subject to loading, unloading and reloading. Parentheses denote test stage numbers.

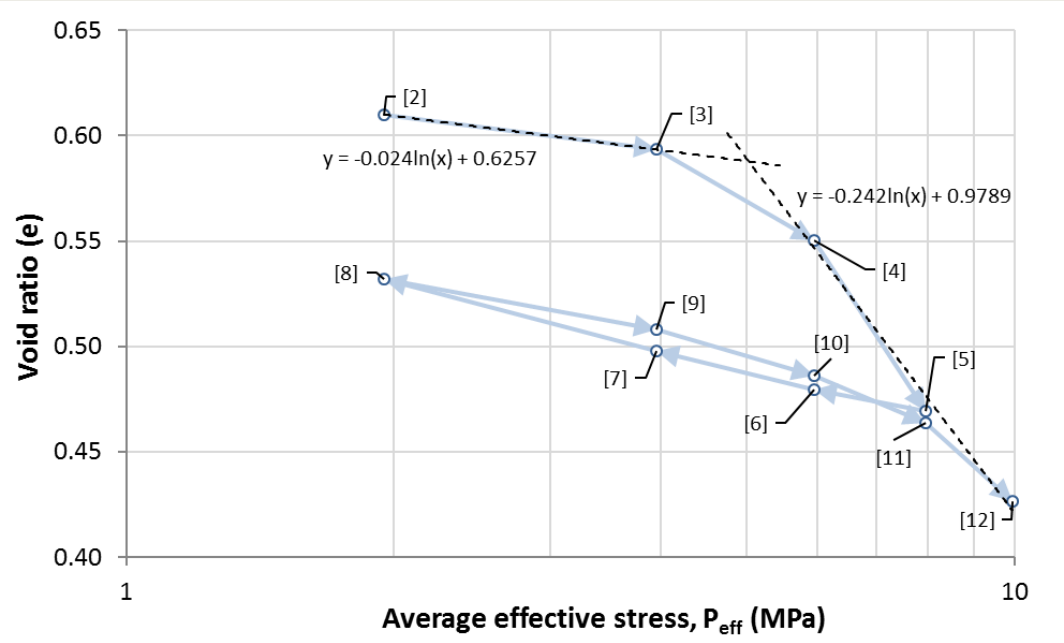

Figure 3-7: Change in void ratio with log(P_{eff}) during consolidation testing in the isotropic permeameter. Parentheses denote stage numbers. Intersection of the dotted lines gives an effective preconsolidation pressure of around 5.1 MPa.

Stage	Ave. P_{eff} (MPa)	Ave. hydraulic conductivity $x10^{-12}$ (m/s)	Ave. hydraulic permeability $x10^{-19}$ (m^2)	Bulk modulus, K_d (MPa)	Young's modulus, E_d (MPa)	Shear Modulus, G_d (MPa)
2	1.95	1.40	1.43			
3	3.95	1.25	1.28	194	436	194
4	5.95	1.02	1.05	74	166	74
5	7.95	0.73	7.42	38	86	38
6	5.95	0.79	8.06	282	635	282
7	3.95	0.90	9.16	162	365	162
8	1.95	1.09	1.12	88	197	88
9	3.95	0.97	0.99	129	289	129
10	5.95	0.84	0.86	138	310	138
11	7.95	0.71	0.72	131	295	131
12	9.95	0.50	0.51	79	178	79

Table 3-3: Calculated values for hydraulic conductivity and elastic moduli, as function of effective stress. Calculations are based on a Poisson's ratio of 0.125 (Barnichon and Volckaert, 2003; Bernier et al., 2007).

3.3.3 Hydraulic response to consolidation

Values for hydraulic conductivity at different effective stresses are given in **Table 3-3**. Plotting hydraulic conductivity values measured during consolidation against effective stress (**Figure 3-8**) demonstrates that a significant reduction is likely at effective stress conditions appropriate to the Netherlands (**Table 1-1**). When considering the direct influence of void ratio on hydraulic conductivity (**Figure 3-8**, **Figure 3-9**) it is apparent that a linear relationship is likely, once the preconsolidation pressure of the clay has been reached. However, it should be noted that this value may differ in a Netherlands location that has experienced any significant differences in burial history, from that experienced in Belgium. Further clarity on this would be achieved by testing core from any candidate location in the Netherlands sampled from prospective repository depths.

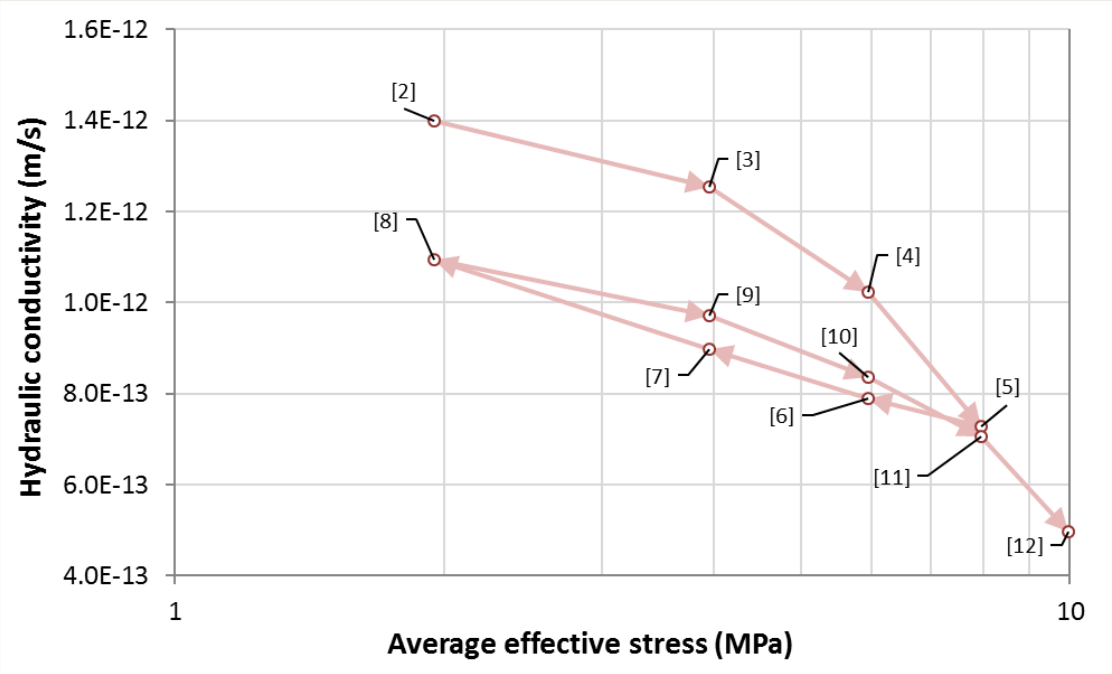

Figure 3-8: Sensitivity of hydraulic permeability to changes in effective stress.

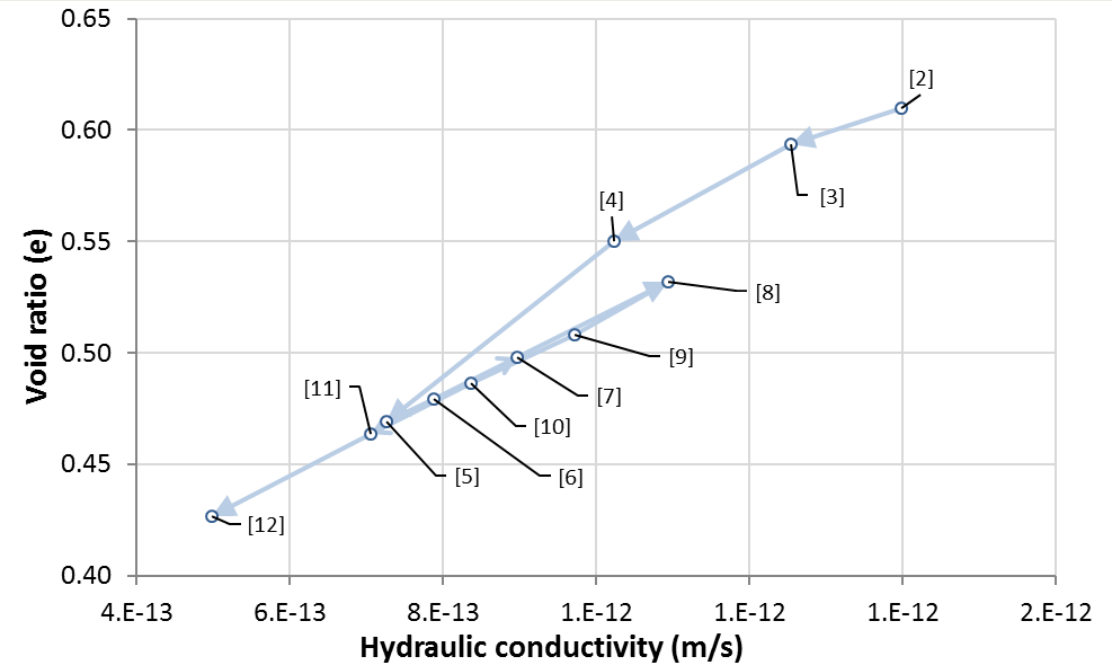

Figure 3-9: Sensitivity of hydraulic conductivity to changes in void ratio on consolidation.

3.3.4 Modelling of consolidation

The fluid flow through a compressible porous medium may be described by the Biot's model (Biot 1941), where the governing equation for flow is obtained by combining Darcy's law with the mass conservation equation, thus leading to

$$\nabla \cdot \left(\frac{k}{\mu}\nabla p\right) = \phi\beta\frac{\partial p}{\partial t} + \frac{\partial}{\partial t}(\nabla \cdot \boldsymbol{u}) \tag{3-2}$$

where $\boldsymbol{u}$ is the solid displacement [m], p is the fluid pressure [Pa], k is the intrinsic permeability [m^2], μ is the dynamic viscosity of the fluid [Pa·s], ϕ is the porosity [-] and β is the compressibility of the fluid [Pa^{-1}]. Note that an isotropic permeability, represented by the scalar k, is here assumed.

Equation (3-2) is coupled to the mechanical equilibrium equation

$$\nabla \cdot \boldsymbol{\tau} + \boldsymbol{f} = \mathbf{0} \tag{3-3}$$

where $\boldsymbol{f}$ is the body force per unit volume of the medium [N/m^2] and $\boldsymbol{\tau}$ is the total stress on the medium [Pa], which can be expressed as

$$\boldsymbol{\tau} = \boldsymbol{p}' - \alpha p\mathbf{I} \tag{3-4}$$

where $\boldsymbol{p}'$ is the effective stress (or pressure) tensor [Pa], α is the Biot's coefficient [-] and $\mathbf{I}$ is the identity tensor. Here, the standard Biot's model is assumed. Thus, an isotropic linear elastic matrix is considered and hence, under the assumption of small strains, the effective stress tensor takes the form

$$\boldsymbol{p}' = \lambda tr(\boldsymbol{\varepsilon})\mathbf{I} + 2G\boldsymbol{\varepsilon} \tag{3-5}$$

where λ is the first Lamé's constant [Pa], G is the shear modulus [Pa] and tr stands for the trace operator. For the sake of simplicity, $\alpha = 1$ is here considered. This is a reasonable assumption for a saturated porous medium and leads to the equation

$$\frac{E}{2(1+\nu)(1-2\nu)}\nabla(\nabla\cdot\boldsymbol{u}) + \frac{E}{2(1+\nu)}\nabla^2\boldsymbol{u} - \nabla p = -\boldsymbol{f} \tag{3-6}$$

where E is the Young's modulus [Pa] and ν is the Poisson's coefficient [-]. Note that the relationships $\boldsymbol{\varepsilon} = \nabla^s\boldsymbol{u}$, $\lambda = \frac{E\nu}{(1+\nu)(1-2\nu)}$ and $G = \frac{E}{2(1+\nu)}$ have here been used.

In order to estimate the values of the permeability k and the Young's Modulus E of the Boom Clay sample, the coupled system formed by Equations (3-1) and (3-5) is here numerically solved. Following standard procedures, these equations are discretized in space using the finite element method and in time using the finite difference method, see Harrington et al., (2017) for a detailed description of the fitting procedure. As shown by Horseman et al., (2005), the model is unable to represent multiple testing stages from a single set of material values. Thus, each consolidation stage is here treated as separate tests. The geometrical and material parameters of **Table 3-4** are used. As seen, the Poisson's coefficient reported by Barnichon and Volckaert (2003) and Bésuelle et al., (2013) is here used.

The fitting results are shown in **Figure 3-10**. As seen, the Biot's model (blue-dashed curve) performs well in some consolidation stages (see for instance, stages 4 and 7). However, it is not able to represent the time-dependent behaviour observed experimentally in some stages.

3.3.5 Numerical model: time-dependent skeleton deformation

As performed in Tamayo-Mas et al., (in press), the extended Biot's general consolidation theory is here assumed to include the creep effect observed in experimental tests. This enhanced model assumes a viscoelastic deformation of the matrix. In particular, the sample is modelled as a purely elastic spring connected in series with a Kelvin-Voigt model (another elastic spring connected in parallel with a dashpot of viscosity η). For the sake of simplicity, the elastic moduli of the two springs are here assumed to be equal (E) and hence, the Young's modulus of Equation (3-6) is replaced by the time-dependent Young's modulus

$$E(t) = \frac{E}{2-e^{-at}} \tag{3-7}$$

where $a := \eta/E$ [s^{-1}]. That is, compared to the standard Biot's consolidation model, only one extra fitting parameter (a) is needed.

BOOM CLAY SAMPLE		
Meaning	**Symbol [units]**	**Value**
Radius of the sample	r [mm]	24.96
Length of the sample	L [mm]	42.67
Poisson's coefficient	ν [-]	0.125
Dynamic viscosity	μ [Pa · s]	2.32×10^{-3}

Table 3-4: Geometrical and material parameters used in the numerical fittings for the Boom Clay specimen.

As done for the classical Biot's model, the equations with the time-dependent stiffness are discretised in space using the finite element method and in time using the finite difference method (see Tamayo-Mas et al., (in press) for a detailed description of the fitting procedure). Again, each consolidation stage is treated here as a separate test and parameters of **Table 3-4** are used.

The fitting results are also shown in **Figure 3-10**. As seen, laboratory data fit better with the proposed viscoelastic model (red-continuous curve). The fitted parameters obtained with both models are listed in **Table 3-5** and **Figure 3-11**. As seen, the two models lead to a similar Young's modulus. However, the new model does lead to significantly better permeability value predictions, especially for those stages where the confining pressure decreased.

BOOM CLAY SAMPLE						
Stage number	EXPERIMENTAL		FITTED			
			ELASTIC SKELETAL DEFORMATION		VISCOELASTIC SKELETAL DEFORMATION	
	Permeability [m^2]	Young's Modulus [MPa]	Permeability [m^2]	Young's Modulus [MPa]	Permeability [m^2]	(Averaged) Young's Modulus [MPa]
3	1.44×10^{-19}	581.82	7.73×10^{-20}	351.10	3.44×10^{-19}	413.29
4	1.17×10^{-19}	221.01	4.92×10^{-20}	276.83	1.71×10^{-19}	321.85
5	8.33×10^{-19}	114.84	7.34×10^{-20}	171.15	1.77×10^{-19}	192.93
6	9.04×10^{-20}	846.02	5.77×10^{-20}	908.58	8.65×10^{-20}	950.87
7	1.03×10^{-19}	486.29	2.31×10^{-20}	467.43	1.00×10^{-19}	533.69
8	1.25×10^{-19}	263.08	2.43×10^{-20}	268.06	1.60×10^{-19}	316.09
9	1.11×10^{-19}	385.61	4.91×10^{-20}	315.51	1.94×10^{-19}	357.87
10	9.59×10^{-20}	413.78	3.37×10^{-20}	334.20	7.43×10^{-20}	363.93
11	8.09×10^{-20}	393.46	1.37×10^{-20}	262.60	3.73×10^{-20}	292.92
12	5.70×10^{-20}	236.86	1.76×10^{-20}	192.40	3.62×10^{-20}	211.45

Table 3-5: Parameter values determined for each stage.

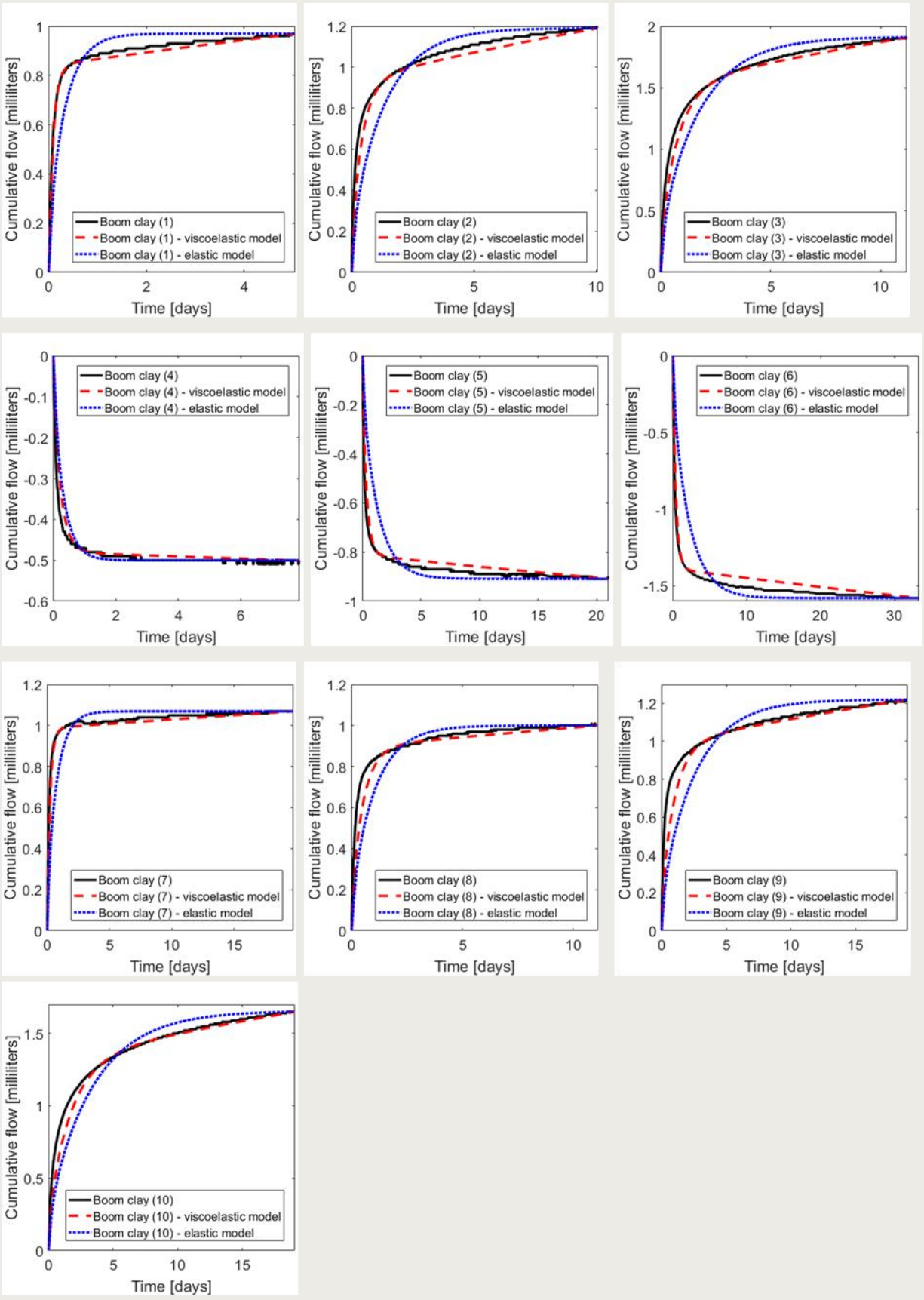

Figure 3-10: Comparison of model to flow data obtained by assuming both an elastic (blue-dashed curve) and a viscoelastic (red-continuous curve) model.

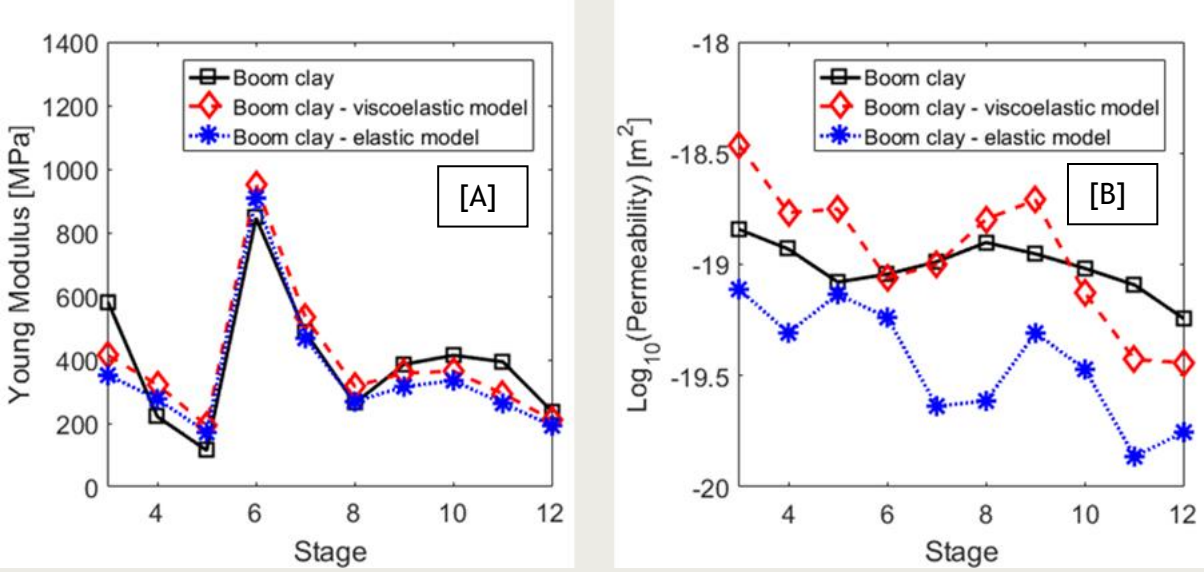

Figure 3-11: Parameter values determined for each stage. [A] Young's Modulus. [B] Permeability.

3.4 *Summary*

A detailed consolidation test, amenable to numerical analysis, has been performed on a sample of Boom Clay retrieved from the HADES URL. Analysis of the data shows that the Boom Clay has an initial OCR of 2.3, equating to an effective preconsolidation stress of 5.05 MPa. Transition from elastic to plastic behaviour (i.e. yield) is clearly visible in **Figure 3-8** as the slope of the void ratio-effective stress plot increases. These changes in void ratio are accompanied by systematic reductions in permeability and a drop in elastic moduli as the Boom Clay yields and moves to the normally consolidated line (NCL). On unloading, the plastic strain induced by the previous increments in confining pressure is non-recoverable. This results in the Boom Clay moving along a new rebound-reconsolidation line, which, because of the elastic response of the material during this phase of unloading, results in an increase in elastic moduli. In **Figure 3-9** permeability exhibits a general linear response shoring a strong correlation with void ratio and therefore effective stress.

Modelling of the data using a standard poroelastic approach generally provides a poor fit to the data. However, the introduction of time-dependent skeletal deformation significantly improves the fit to the data. Unsurprisingly this has little effect on the estimation of Young's modulus, **Figure 3-11**, as this term is defined by the asymptote of the curves, a parameter fixed within the model. However, the estimation of permeability, which defines the shape of the transient response in **Figure 3-11** is relatively sensitive to the change in model. Assuming the viscoelastic model provides a better representation for the bulk hydraulic properties of the Boom Clay, then a relatively good fit to the experimental is obtained. Minor discrepancies between measured and modelled response may relate either the localisation of flow within the clay or to minor errors in the constitutive foundation of the model.

The data clearly shows that Boom Clay is sensitive to burial history. From the Netherlands perspective, it is important to recognise that if the Boom Clay has been subject to a different burial history (to that at HADES), then the values presented in this Section may differ. Testing on material from a candidate site within the Netherlands is therefore required to reduce uncertainty in the estimation of consolidation and hydraulic parameters.

Outcomes:

1. An effective preconsolidation pressure of around 5.1 MPa was observed for Boom Clay material taken from the HADES URL.
2. Permeability and elastic moduli are sensitive to changes in both confining pressure and burial history.
3. As Boom Clay approaches yield, elastic moduli reduce.
4. As volumetric strain is only partially recovered on unloading, the elastic properties increase in value.
5. At HADES, an over consolidation ratio of around 2.3 is observed.
6. A poroelastic model is unable to adequately represent deformation of Boom Clay. A model using time-dependent skeletal deformation provides a better representation of the data.

Recommendations:

1. Because of the sensitivity of the Boom Clay to burial history testing should be broadened to examine the response to Boom Clay which has been subject to different burial and uplift scenarios.
2. The coupling between consolidation behaviour to other repository stimuli e.g. thermal loading, has not been examined. Further work is required, on preconditioned material, to explore these relationships in full

4 Swelling behaviour

The swelling of a clay-rich material, such as the Boom Clay, is controlled by a number of factors. Principally swelling is a physico-chemical interaction between the pore water and the clay minerals of the material. However, the propensity to swell will also be controlled by factors such as stress state and clay fabric. It is therefore thought that the consolidation of the material would be likely to impact the fabric of the clay, which this may have an effect on the anisotropy of swelling. This may have consequences on the hydraulic properties of the material, e.g. the hydraulic conductivity.

Only a limited number of studies have directly measured the swelling properties of the Boom Clay. Horseman et al., (1987; 1993) conducted a standard 1 dimensional oedometer testing on samples retrieved from Hades and measured a resulting swelling pressure of 0.82-0.92 MPa. Volckaert et al., (1995) also report a swelling pressure of 0.9 MPa, though the associated experimental data is not provided. A free-swelling approach was taken by Sultan et al., (2010), leading to a slightly lower value of 0.48 MPa. Whilst these findings demonstrate the capacity for the Boom Clay to swell, it should be noted that such pressures are significantly lower than those generated by engineered clay barrier materials such as MX80 bentonite (Graham et al., 2015). However, this does not impact the clay's propensity to self-seal, which is primarily driven by its exceptional propensity to creep, leading to closure of voids and fissures over very short timescales. Only a small amount of literature is available on the swelling properties of the Boom Clay, especially with relation to the effect of consolidation. Therefore, this study aims to quantify the main swelling properties of the Boom Clay at 223m and then study the effect that burial to 500 m depth would have on these properties.

Two main methods can be employed to measure the swelling properties of materials. One to measure the swelling potential and another to measures the swelling pressure; that being the stress required to prevent swelling. Swelling potential, $\Delta h/h$, is a measure of the change in shape of the material as a result of wetting. Swelling pressure is defined as that required to maintain a constant sample volume during wetting. Both of these parameters have been studied experimentally for this study.

To study the swelling potential a three-dimensional free swelling rig was developed. This measures the change in shape of a cubic sample in three axes. This allows us to observe anisotropic swelling which is likely due to the clay fabric of the Boom Clay. Two of these tests were carried out; one using core from Mol depth (223 m) and another test using the consolidated core which was buried to 500 m depth in the laboratory. To measure the swelling pressure of the Boom Clay a constant volume apparatus was used. The sample used was from Mol depth (223 m) and the sample was subject to a pore pressure cycle up to the estimated pore pressure at 500 m depth. The apparatus measured the swelling pressure using a combination of axial load cells and radial pore pressure transducers.

The results of these experiments will be discussed below. These results will then be discussed and compared to those in the literature, the implications of these results will also be presented as will recommendations for further work.

4.1 *Swelling under free conditions*

4.1.1 Experimental set-up

Two three-dimensional free swelling tests were ran on Boom Clay samples; one using core from a depth of 223m and one test from a core which had been further consolidated to 500 m depth.

The 3D swell apparatus consisted of a three-sided triangular dish, in which a cubic sample of material sits (**Figure 4-1**). Three-dimensional swelling was measured using three Mitutoyo digital dial gauges, these were arranged perpendicularly to each other to measure swelling in three dimensions. Sample preparation was carried out carefully in order to ensure that one of the dial gauges was set up to measure swelling perpendicular to bedding. The rod of the dial gauge was in constant contact with the face of the sample. The cubic sample was placed in the centre of the triangular dish and the dial gauges were set to zero. The dish was then flooded with the SCKCEN pore fluid (see Section 1) until the sample was fully submerged. Swelling was measured over time using a bespoke version of LabVIEW™ logging software. Tests ran until swelling was no longer observed, however some tests would swell for extended periods so tests were terminated when no more swelling was observed.

A total of two tests were ran for this study. The first test was ran on core from Mol depth, 223 m. The core was cut using diamond tipped blades to form a 50 mm cube, the faces of the cube were then squared off to ensure each face was completely flat and orthogonal to the adjacent face. The second test was ran on material from the material consolidated to 500 m depth. The sample was cut using the same technique from the first core to be consolidated. However, due to constraints on the core size and the need to maximise the number of samples from this core the sample was only prepared as a 40 mm cube.

Figure 4-1: Free swell apparatus.

The two free swell tests were ran for an extended amount of time. The aim was to run until no further swelling occurred. However, the first sample swelled so much the cube became too large to be constantly submerged, meaning the test was terminated. The second test ran for over 3 months until almost no swelling was observed.

4.1.2 Results

The results of the three-dimensional swelling tests will be presented below. A comparison between samples from 223 m depth and 500 m depth will be carried out.

Figure 4-2 A shows the data from the test carried out using a sample from a depth of 223 m, the sample used was a 50 mm cube. The most obvious result from this is the obvious anisotropy between the readings. Reading 1 has swelled by over 15 mm, whereas readings 2 and 3 are slightly above 4 mm by the end of the test. Reading 1 is measuring the swelling perpendicular to the bedding, whereas readings 2 and 3 are parallel to bedding. There is a swelling anisotropy ratio of almost 4:1 in this test. The reason for this is likely to be due to the bedding and clay fabric (see **Figure 4-3**). The microfabric provides the framework for both water absorption and osmotic pressure to develop. This, along with, osmosis and water hydration causes the swelling of the clay and expansion of the interlamellar structure.

In reading 1 the swelling occurs exponentially, however it appears that the swelling is beginning to slow down towards the end of the test. Unfortunately, the test had to be terminated as the sample had swelled out of the confinement of the dish, meaning the whole sample could no longer be submerged. The results of this test clearly show the anisotropic nature of the swelling behaviour of the Boom Clay.

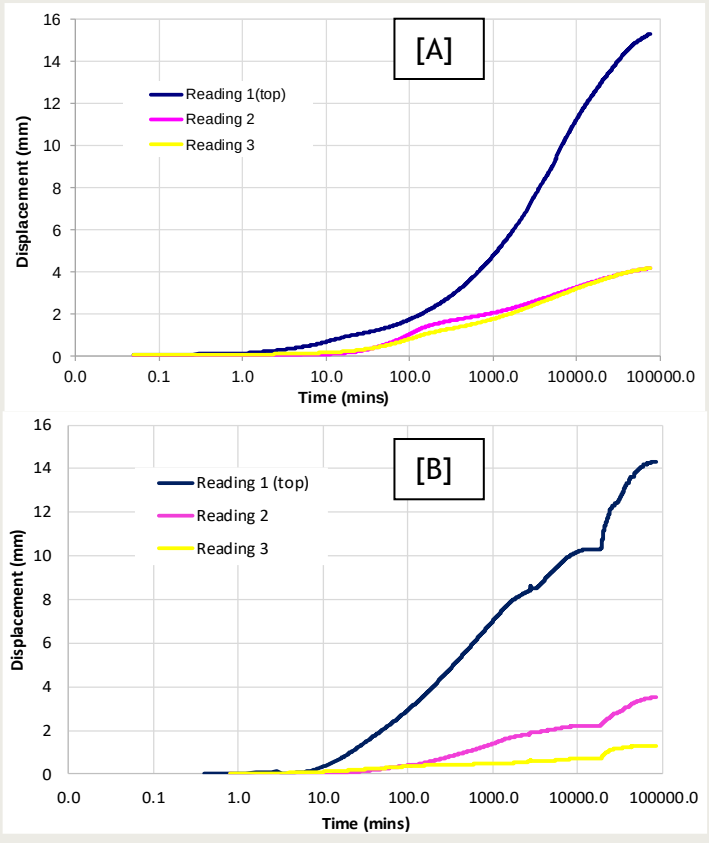

Figure 4-2: 3-dimensional free swell displacements. [A] First swell test carried out on material from the Mol repository depth. [B] Second swell test carried out on the Netherlands depth material.

Figure 4-2 B shows the 3-dimensional swell response from the second swell test, this used a 40 mm sample from the first consolidation test. This material was artificially buried to a depth of 500 m. **Figure 4-2 B** shows a similar anisotropic response to the sample from 223

m depth. It must be pointed out that the small drop in swelling seen in all three axes at around 12,000 minutes occurred due to the water drying out over a weekend. This was a mistake in the running of the test. However, once the test dish was refilled with pore water the material re-swelled. The swelling was not affected by this as the sample recovered back to a straight line of swelling after several days.

Figure 4-2 B shows that the axes perpendicular to bedding measures over 14 mm of swelling. It must be noted that it is difficult to directly compare the amount of swelling between the two tests due to the differing sample sizes used in each test. The readings from the axes parallel to bedding measure different values, this is in contrast to the test at Mol depth where the readings are the same throughout the test. The test in **Figure 4-2 B** was also run for a longer period of time than the test on the material from Mol. This is due to the smaller samples size used, therefore the sample did not swell out of the dish. Towards the end of the test in **Figure 4-2 B** the swelling has begun to slow down and reach a constant rate. This is the beginning of a secondary phase of swelling at a much slower rate.

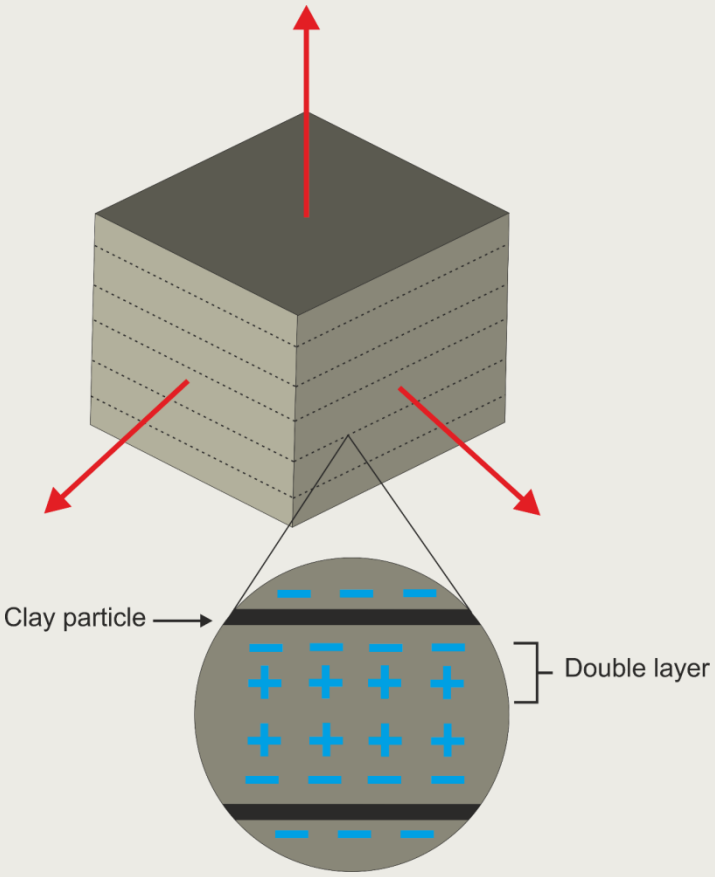

Figure 4-3: Schematic diagram explaining anisotropic swelling.

There are two significant differences between the two tests; the shape of the swelling curve and the difference in the horizontal swelling axes in the consolidated sample.

The swelling curve for the top axis in **Figure 4-2 A** is a concave shape, meaning swelling occurs exponentially. This occurs because as the sample swells the surface area exposed to the pore water becomes greater, meaning swelling can occur at an ever faster rate. This is not the case in **Figure 4-2B**, where the top axes seems to swell at a more constant rate. The reason for this could be due to the consolidation of the core to a depth of 500 m. After the consolidation of the sample many of the bedding parallel fractures closed (**Figure 2-3**).

Fracture closure makes it harder for water to infiltrate into the sample and therefore we do not see such rapid swelling rate. The Boom Clay is however still a highly swelling material when consolidated to 500 m and this test shows that in free swell conditions there is still a high degree of anisotropy. This is likely down to the laminations in the formation and also the relatively high clay content.

An easier way to compare the relative amount each sample has swelled is to study the total strain each sample has incorporated into its structure. Using this method we can now disregard the difference in sample size. **Figure 4-4** shows the total strain measurements for both free swell tests. The initial response in the first 10 minutes is similar however after this the two tests follow separate paths. The test ran using the consolidated sample has exhibited a greater amount of strain over the period of the test. The drop in the total strain is attributed to the test drying out, as explained above. If it was not for this it is predicted that the total strain for the consolidated sample would have been constantly over that of the sample from Mol depth. From comparing the data in **Figure 4-2 A and B** the higher strain value for the 500 m depth sample must come from additional vertical swelling. **Figure 4-2 B** shows that the horizontal swelling is still relatively low and close to that of **Figure 4-2 A. H**owever the vertical swelling in **Figure 4-2 B** is slightly higher than that of **Figure 4-2 A**, especially when accounting for the smaller sample size. During consolidation to 500 m the core was loaded axially, therefore once the sample is taken out of this higher stress condition the sample may rebound slightly. This may be the reason for the higher vertical swelling seen in **Figure 4-2 B**.

The sample from the consolidated core has a much more linear secondary swelling curve. The sample from Mol depth has a more convex secondary swelling. The reasons for this are unclear, however it could be associated with the consolidation of the core. In Chapter 2 of this report **Figure 2-3** shows the x-ray of the consolidated core before and after consolidation. In the pre consolidation x ray the sample has many bedding parallel cracks, however after consolidation these are no longer visible. Therefore, the material used for the test at 223 m in this core may also have bedding parallel cracks. These cracks could allow the infiltration of water and therefore change the shape of the curve. In the sample at 500 m the x-ray shows no visible cracks, therefore meaning the swelling is at a constant rate.

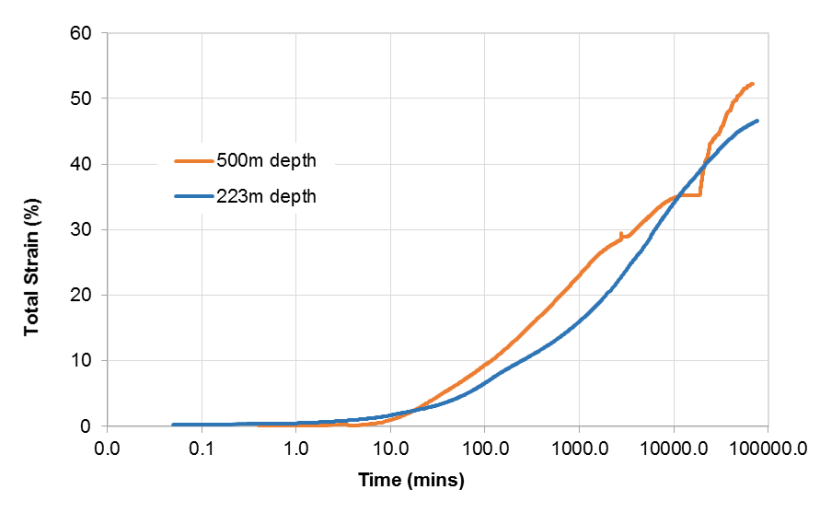

Figure 4-4: Total strain comparison between material from the two proposed repository depths.

The curves in **Figure 4-4** can be split into two distinct sections. There is an initial phase where almost no swelling occurs, however this only lasts for approximately 10 minutes in

both tests. After this period the primary phase of swelling begins. **Figure 4-5** shows the evolution of the primary swelling phase in more detail for both the 500 m and 223 m depth material. The equations on **Figure 4-5** describe the rate of swelling during the primary swelling phase. The rate of swelling is described using a power law for each test. However, the test carried out on consolidated material has a small drop in the strain data, which was an experimental error. This has affected the power law and we would expect the curve to be less convex if this experimental error was removed.

Towards the end of both curves the gradient begins to decrease, it is believed that this is the start of the secondary phase of swelling. This change in slope does not occur until a total strain of over 40% is achieved in the test on Mol depth material, whereas it takes to 50 % for the consolidated material to progress to secondary swelling. The secondary swelling phase is expected to occur at a much slower rate, as indicated by the change in slope. Unfortunately, the test on the material from 223 m was terminated so the secondary swelling phase cannot be interpreted. However, the test on the 500 m depth material is ongoing and observations will continue to be made to characterise the secondary swelling characteristics of the Boom Clay.

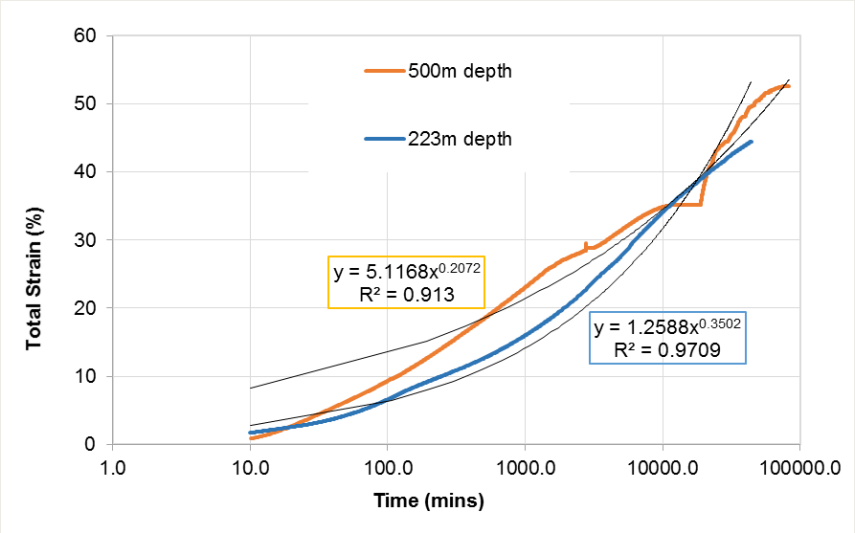

Figure 4-5: Primary swelling response for swelling tests at the Mol (blue line) and Netherlands (orange line) depths.

Very little data is available on the swelling properties of the Boom Clay, especially under free swelling conditions. There is also little data on the anisotropy of swelling; this test has clearly shown that the Boom Clay is an anisotropic highly swelling clay.

Further testing is required on a longer time line, for this we would use smaller samples. It would also be of interest to use samples from The Netherlands to see how this may vary. These samples, would also contain a porewater with a composition representative of the Netherlands within in the pore space, instead of using samples from Mol which contain a Belgian pore water composition. These results can now be compared against those gained in the constant volume conditions.

4.2 *Swelling under constant volume conditions*

4.2.1 Experimental set-up

To measure the swelling pressure of the Boom Clay a modified Constant Volume Radial Flow (CVRF) apparatus was used (**Figure 4-6**). The CVRF cell had been modified to measure axial strain and the radial pore pressure distribution. The apparatus consisted of: (a) a

thick-walled stainless steel pressure vessel; (b) a fluid injection system; (c) two axial load cells to measure axial strain; (d) three radial pore pressure transducers at consistent intervals down the length of the pressure vessel and (e) a logging system. **Figure 4-6** shows the arrangement of the sample, pressure vessel and corresponding sensors.

The sample used in this test was a 100 mm length sample with a diameter of 30 mm. The sample was prepared from core taken from the HADES research laboratory in Mol, Belgium at a depth of 223 m. The sample was prepared so the length of the sample was perpendicular to bedding. It was important that the sample was carefully prepared to the exact dimensions required for the pressure vessel. This would ensure that the sample would not swell during the testing and if it did it would be recorded by the sensor arrangement.

The pore pressure transducers along the length of the sample were GEMS 3100 transducers, arranged to measure the distribution of pore pressure down the length of the sample. The axial strain was measured using button load cells. These were in contact with the face of the sample using an in house steel-push rod with an o ring seal.

Pore pressure was applied to the sample by the injection and backpressure ports as seen in **Figure 4-6**. The pore fluid is supplied by two Teledyne Isco 260D syringe pumps. These pumps were filled with the reference pore fluid as discussed in Chapter 1. The sample was subjected to a pore pressure ramp from 1 MPa to 5 MPa and back down in 500 KPa steps. The syringe pumps were set to constant pressure mode and there was no pressure gradient over the length of the sample. The syringe pumps have an RS232 serial port, which allows volume, pressures and flow rates to transmitted back to a bespoke LabView™ logging system; this logging system also logged all other data outputs for this test, including temperature. Data was collected every 2 minutes for the whole period of the test.

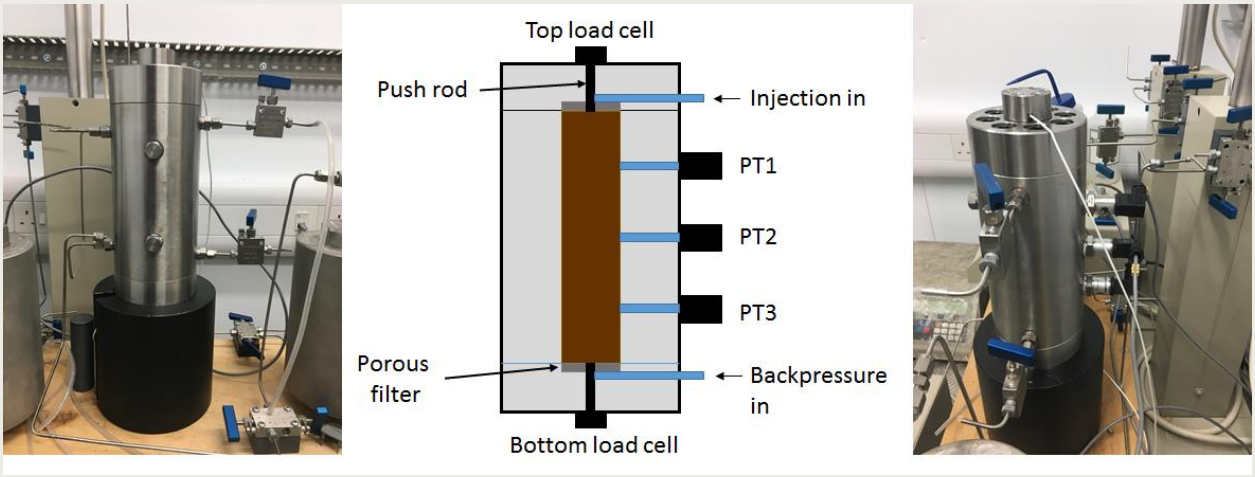

Figure 4-6: Illustration of the constant volume (CVRF) apparatus set-up. Note location of the top and bottom load cells and pressure transducers (PT1-3).

The test was conducted in a temperature controlled laboratory which is kept at a constant temperature of 21°C. The test is still ongoing, this is partly due to the nature of the test and also due to a period of time when the laboratory air conditioning was not working as it should, which had a knock on effect on the test. We did not set a time period for each period of constant pore pressure. Instead we would increase the pore pressure when we were sure that the pore pressures and axial loads had equilibrated to the new pressure. Once we were sure equilibrium had been reached we would increase the pore pressure to begin the next phase of the test.

Figure 4-7 shows the pore pressure cycle and the temperature profile for the laboratory. As can be seen the longer time steps correspond to the time period when the laboratory air conditioning was not working appropriately, this led to extended time periods for some phases. Unfortunately, this means that the test is still ongoing, however we believe it is more important to get high quality results than to prematurely finish the test.

4.2.2 Results

In this section the effects of a pore pressure ramp, ranging from 1 to 5 MPa and back down, on the swelling pressure of the Boom Clay are described. The pore pressure ramp the sample was subjected to is shown in **Figure 4-7 A** and is also described in **Table 4-1**. As can be seen the time steps are inconsistent for each stage, this was due to faults in the air conditioning, as shown by the temperature profile in **Figure 4-7 B**; the reasoning for this is explained above.

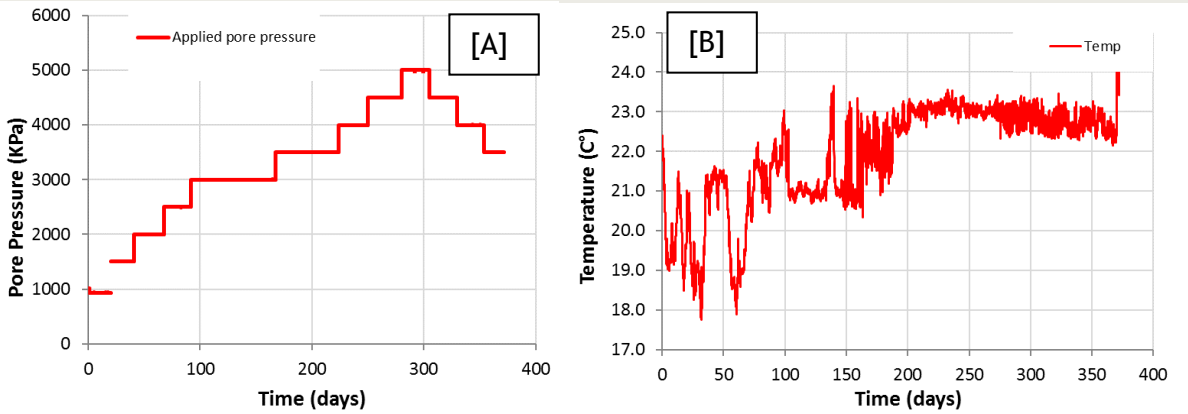

Figure 4-7: [A] Applied pore pressure ramp experienced by the sample. [B] Temperature.

As can be seen in **Figure 4-7 A** the increase in pore pressure was instantaneous and when first studying it appears that the pore pressure along the sample also increased instantaneously. As discussed above the pore pressure transducers (PT 1-3 in **Figure 4-6**) were arranged along the length of the sample, with PT 1 at the injection end and PT 3 at the backpressure end. If we zoom in on one of the pore pressure increases (**Figure 4-8**) we can see that the increase in pore pressure is not instantaneous down the length of the sample. The pore pressure at PT 1 and 3 increase very quickly over the period of slightly under 2 hours, however PT 3 in the middle of the sample takes nearly 9 hours to increase to the new pore pressure for the next phase of testing. This behaviour is linked to the permeability of the sample and the anisotropy of hydraulic conductivity. This has been discussed in detail in Chapter 3 of this report.

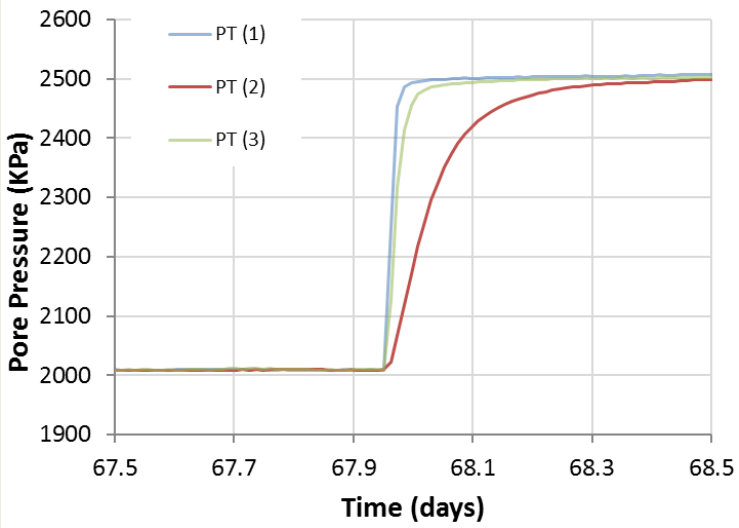

Figure 4-8: The pore pressure transducer response along the long-axis of the sample between 67.5 and 68.5 days.

The relationship between pore pressure and the vertical load applied to the two load cells is shown in **Figure 4-9**. The two load cells measured the swelling of the sample in a vertical axis, they were placed at the top and bottom of the sample as shown in the experimental set up **(Figure 4-6)**. A clear relationship between pore pressure and vertical load can be seen. As pore pressure increases so does the vertical load measured by the load cells. Initially the amount of axial stress measured at the top and bottom of the sample is above that of the applied pore pressure. However, once the pore pressure is raised to 3 MPa the bottom load cell reads approximately the same as the pore pressure. During the next stage we see a sudden decay in the load cell values. It is believed that this drop is associated with the large temperature flux that occurs around day 190 (**Figure 4-7**). After this point the bottom load cell remains below the applied pore pressure until the pore pressure begins to decrease. We have a large amount of confidence in the data up to approximately day 190, where the confidence in the results decreases.

Stage	Starting day	Average pore pressure (KPa)	Average stress on sample (KPa)	Swelling pressure (KPa)
1	19	974	1511	536
2	39	1499	1991	491
3	67	2000	2384	385
4	91	2500	2944	444
5	166	2999	3401	402
6	223	3500	3791	291
7	249	3999	4004	5
8	285	4498	4520	21
9	308	5000	4972	-28
10	329	4500	4741	241
11	358	3999	4345	346

Table 4-1: shows the length of each stage, the average pore pressure, sample stress and resulting swelling pressure.

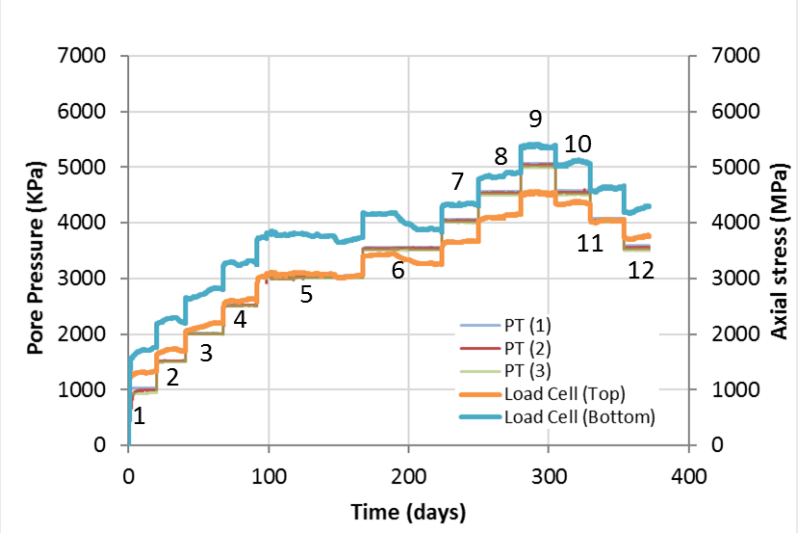

Figure 4-9: Relationship between applied pore pressure and axial stress. Note numbers apply to stages described in Table 4-1.

The difference between the average sample load (red in **Figure 4-9**) and the applied pore pressure equates to the swelling pressure. **Figure 4-10** shows the evolution of swelling pressure with the applied pore pressure. An initial swelling pressure of 536 KPa is observed at 1 MPa pore pressure. After this point the swelling pressure is observed to decrease as the pore pressure is increased during each stage. As mentioned previously there is a drop in the average load on the sample during stage 6 after which point we have less confidence in the load cell data. Thus, we are less confident in the swelling pressures at elevated pore pressures. However, it is likely that the swelling pressure will have continued to decrease overall as was observed during stages 1-5.

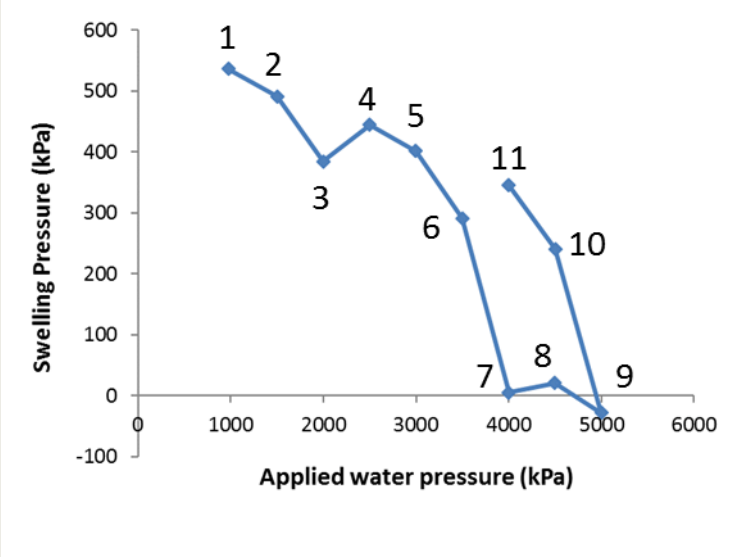

Figure 4-10: The effect of variation in porewater pressure on Swelling pressure evolution

This is an on-going test and the pore pressure will reduce back to zero. We expect the swelling pressure to carry on dropping as it is in **Figure 4-10**. However, we expect there to be an element of hysteresis as shown in the first two stages of reducing the pore pressure.

4.3 *Discussion*

This experimental programme has studied the Boom Clays swelling response to an elevated pore pressure cycle from 1 to 5 MPa. Due to the sensitive nature of the testing method and our desire to ensure the results are as accurate and reliable as possible this experimental programme is still on going. However, several key findings have been made and these can be compared against previous measurements of the swelling characteristics of the Boom Clay.

Only a small number of studies have measured the swelling pressure of the Boom Clay and none of these are under constant volume conditions. Many tests measure the swelling pressure using the oedometer method. Horseman et al., (1987; 1993) recorded a swelling pressure of 0.82-0.92 MPa. However, measurements were also made of up to 1.7 MPa from 1-D consolidation tests. Volckaert et al., (1995) report a swelling pressure of 0.9 MPa, however their experimental approach is not provided. These values are all above the measured swelling pressure of 536 KPa measured during this test. However, Sultan et al., (2010) measured a swelling pressure of 0.48 MPa using a free swelling method. In general there is a variation in our measured data compared to those in the literature. This variation could be due to a number of reasons, e.g. experimental method and sample preparation. We have taken great care to ensure that our samples are vacuum packed and stored under cold conditions to ensure the samples do not dry out. Then during the sample preparation much care is taken to avoid any damage to the sample or drying out. In order to test the reliability and accuracy of our results however another test programme would need to be carried out. Another reason for this variation could be due to the samples used in this study having a differing mineralogical content. Swelling properties are very dependent on mineralogical content, for example an increase in smectite content could have a significant effect on the swelling pressure.

In Section 7-2 of this report the swelling pressure is again measured during a separate CVRF gas injection test. During this test a swelling pressure of 0.5 MPa was generated, this is well matched to the value recorded during this study and gives us greater confidence in the values produced from this test.

The pressure transducers show that the pore water pressure is well distributed in the sample. The injection of the pore pressure has resulted in elevated axial loads at each end of the sample. When combining this knowledge with that of the free swell tests, this is further evidence of anisotropic swelling of the Boom Clay. This is due to both the laminations of the Boom Clay and also the clay fabric. For further testing it would be useful to measure radial swelling in a constant volume cell, this would enable us to be able to quantify anisotropy under both free swell and confined conditions.

The main aim of this entire study is to study the effect of consolidation to 500 m on the properties of the Boom Clay. With respect to that we can say that at elevated pore pressures the swelling pressure is likely to reduce go down, as shown in **Figure 4-10**. However, due to variations in laboratory temperature the data after 3.5 MPa may not be accurate. As a result of this further testing is required to fully understand the evolution of swelling pressures at elevated pore pressures. Furthermore, this experimental apparatus only uses axial load sensors either end of a 100 mm long sample. Therefore, in future tests radial measurements of load would be useful as they would provide a more accurate value for the sample pressure. In turn this would also provide us with knowledge on how anisotropic the swelling pressure may be. The free swell tests suggest that the Boom Clay is relatively anisotropic. This anisotropy would likely have an effect on the hydro-mechanics of the sample.

Outcomes:

1. The Boom Clay is shown to be a highly swelling clay, this is due to the interaction of the pore water with high swelling minerals such as smectite which are found in the Boom Clay
2. Free swelling tests showed that the Boom Clay exhibits a relatively large degree of anisotropy.
3. The swelling pressure of the Boom Clay was defined as 0.536 MPa.
4. Swelling pressure of the Boom Clay decreases as pore pressure increases.

Recommendations:

1. Further testing is required to fully understand the evolution of swelling pressure at elevated pore pressures
2. Further testing using an apparatus capable of measuring radial strain will also allow a more accurate reading of the swelling pressure. This will also give a greater insight into the anisotropy of the swelling behaviour under constant volume conditions.
3. The constant volume test continue to run and complete the pore pressure cycle. Enabling us to more accurately quantify the relationship between pore pressure and swelling pressure.
4. Further free swell tests should be conducted using different pore water solutions with varying chemical composition representative of the evolution in near-field conditions. This will test the sensitivity of swelling to pore fluid chemistry.

5 Influence of thermal load on hydraulic permeability

In a clay-based repository for heat emitting waste, thermal loading of the engineered barrier and surrounding rock mass can affect pore water pressure (Chen et al., 2011; Cui et al., 2009; François et al., 2009; Li, 2013; Monfared et al., 2012), mean effective stress (Chen et al., 2011; François et al., 2009; Monfared et al., 2012), pore structure (Li, 2013), pore water viscosity (Monfared et al., 2012), friction angle and shear strength (Cui and Tang, 2013; Monfared et al., 2012), and unit volume (Cui and Tang, 2013; Cui et al., 2009; François et al., 2009). These processes can perturb the stress state, permeability field, fabric and microstructure as well as the mechanical properties of the material (Wiseall et al., 2015).

The coupling of processes generated during the application of thermal load result in complex behaviour which, due to the physico-chemical nature of clays, is strongly linked to burial history. Data from Francois et al., (2009) nicely demonstrate this coupling couple, presenting results which show that volume change induced by thermal loading is linked to the over consolidation ratio (OCR)[a]. As such, clays with a low OCR value exhibit a reduction (contraction) in volume when heated, opposed to clays with high OCR values which exhibit a volume expansion (dilation). The magnitude of the volume change appears to increase as OCR ratio decreases and that very little, if any, of the volumetric strain induced during thermal loading is recoverable. While high OCR clays exhibit some hysteresis, the degree of non-recoverability is significantly less, as are the absolute magnitude of the strains induced. This suggests that in clays which are lightly overconsolidated, the change in porewater pressure and viscosity induced by thermal loading is sufficient to cause thermally induced consolidation. Abuel-Naga et al., (2007) present results from a series of tests examining thermally induced volume change and changes in porewater pressure in Bangkok clay. Like Francois et al., (2009), Abuel-Naga and colleagues show that temperature induced volume change is directly linked to stress history. They also show that the degree of volume change is controlled by the plasticity index (a parameter representing the upper and lower bounds of the plastic state) and that volume change behaviour can be related to thermal effects on the physico-chemical interparticle forces operating within the clay (Horseman et al., 1996).

5.1 *Experimental set-up and test procedure*

To examine if Boom clay exhibits thermally induced dilation or contraction on heating at representative depths of a Netherlands repository, a specimen of clay taken from the Hades underground laboratory was subject to an ascending history of thermal load. The apparatus used for this study was, in principal, exactly the same as that described in Chapter 3, with the exception that the pressure vessel and sample assembly were housed within a MMM Venticell 222 fan-assisted oven that had a temperature range of 5°C above room temperature to 300°C (**Figure 5-1**).

[a] Defined as the ratio between current and previous maximum depth of burial.

Figure 5-1: Photo showing pressure vessel and associated tubing located within a MMM Venticell 222 fan-assisted oven.

As before the cylindrical specimen cut perpendicular to bedding, designated Covra-1 (taken from core 76/77D), was sandwiched between two end-caps and jacketed in heat-shrink Teflon to exclude confining fluid. Volumetric flow rates were controlled or monitored using a pair of high-precision ISCO 260-D syringe pumps, operated by a digital control unit. Confining pressure was applied using a third ISCO pump connected to the same digital control unit. Each pump was calibrated using a Druck PTX610 pressure transmitter in ascending-descending increments to delineate potential hysteresis. The flow direction was from top to bottom across the sample.

The basic geotechnical properties for sample Covra-1 are presented in **Table 5-1**.

Specimen	Length (mm)	Diameter (mm)	Moisture content (%)	Bulk density (Mg m^{-3})	Dry density (Mg m^{-3})	Porosity (%)	Saturation (%)
Covra-1	49.9	50.3	23.6	2.05	1.66	37.8	>100

Table 5-1: Basic pre-test properties of specimen Covra-1. An assumed specific gravity for the mineral phases of 2.67 $Mg.m^{-3}$ (Wiseall et al., 2015) was used in these calculations. The saturation value greater than 1 suggests the value chosen for specific gravity is slightly low, reflecting possible heterogeneity within the Boom Clay. No post-test data is available due to failure of the O-ring seal on the pressure vessel.

Testing was initiated by allowing the sample to equilibrate under its original in situ stress of 4.4 MPa and a porewater pressure and 2.2 MPa, applied to both the injection and backpressure ends of the sample. As mentioned before, these conditions were selected as the *in-situ* pressure conditions at the sampling location/depth at the HADES URL (see Chapter 1). This stage was conducted to ensure the sample was fully saturated before consolidation testing. However, a very small cross-flow of between 0.7 and 1.1 μl/h between the injection and backpressure systems was observed during the hydration stage, suggestive of a minor discrepancy in the calibrated pump pressures. To remedy the situation, the pressure datum on each pump was reset to zero (at atmospheric pressure), the backpressure pump was recalibrated and the test restarted.

Once primary hydration was complete, marked by an absence of in/outflow from the core, a hydraulic gradient of 0.4MPa was applied across the sample, stage [2], allowing hydraulic conductivity to be determined from the resulting flow. In stage [3], confining stress and backpressure were both increased to 10.0 and 4.9 MPa reflecting the probable conditions likely to be encountered at a repository depth of 500m. Injection pressure was also increased to 5.5 MPa yielding a gradient of 0.6 MPa. The increase in gradient was applied to compensate for the reduction in permeability likely to be induced as the sample consolidated. This gradient was then maintained for the duration of the test while the temperature within the oven was incremented/decremented (**Table 5-2**). Net flow through the sample was monitored during each step, allowing changes in sample void ratio to be estimated during consolidation.

Note, testing was momentarily interrupted during stage 4 and stage 7 when the flexible Teflon sheath which excluded the confining fluid was accidently pierced as the sheath deformed in and around a carbonate feature, shown in **Figure 5-2**. After each event, the sample was re-jacketed, the test permeants replaced with new synthetic porewater solution and the test stage repeated. Following the second jacket failure during Stage 7, the void was infilled with a low swelling clay to prevent further jacketing problems. The full experimental test history is given in **Table 5-2**.

Stage	Type	Injection pressure (MPa)	Back pressure (MPa)	Confining pressure (MPa)	Ave. Eff. pressure (MPa)	Oven temp. (C)
1	Hydration/equilibration	2.2	2.2	4.4	2.2	30
2	Hydraulic CPT	2.6	2.2	4.4	2.0	30
3	Hydraulic CPT	5.5	4.9	10.0	4.8	30
4	Thermal	5.5	4.9	10.0	4.8	62
5	Thermal (jacket failure)	5.5	4.9	10.0	4.8	92
6	Thermal unload	5.5	4.9	10.0	4.8	62
7	Thermal	5.5	4.9	10.0	4.8	93
6	Thermal (jacket failure)	5.5	4.9	10.0	4.8	124
7	Thermal unload	5.5	4.9	10.0	4.8	93
8	Thermal load	5.5	4.9	10.0	4.8	124
9	Thermal unload	5.5	4.9	10.0	4.8	93
10	Thermal load	5.5	4.9	10.0	4.8	124
11	Thermal load	5.5	4.9	10.0	4.8	155
12	Thermal load	5.5	4.9	10.0	4.8	185

Table 5-2: Experimental test history for sample COVRA-1.

Figure 5-2: Photo of sample Covra-1 (CGR 76/77D) showing the carbonate feature and resulting void, which is thought to have caused the leakage problems noted in test Stages 4 and 7.

5.2 *Results*

Initial hydration of the sample occurred over a 42 day period. This was significantly longer than in previous tests reflecting the minor issues associated with the cross-flow noted in Section 5.1. Applying a correction to the data suggests a small quantity of fluid may have entered the sample during hydration. However, this will have been small given the high start saturation of the sample (**Table 5-1**).

A hydraulic gradient was then imposed across the sample at the start of Stage [2]. Flow-rate in and out of the specimen are plotted as a function of time in **Figure 5-3**. The gaps in the data during test stages [5] and [8] were caused by the sheath failures noted in Section 5.1. Assuming Darcy's law, a 1-D analysis of the resulting data yields a hydraulic permeability of $1.3x10^{-19}$ m^2, for Boom Clay under HADES URL stress conditions (**Table 5-3)**. This value is close to the value obtained in Section 3.3.3, suggesting a similar hydraulic behaviour between samples.

Confining stress, injection pressure and backpressure were then increased to values equivalent of 500 m depth of burial, Stage [3] (**Table 5-2)**. While flux across the sample remained similar to that of Stage [2], permeability decreased to $1.0x10^{-19}$ m^2 (**Figure 5-4**) due to the small increase in differential pressure imposed to offset the likely reduction in permeability caused by the application of the higher confining stress. That said, the value obtained is in line with that observed in Section 3.3.3, suggesting minimal hydraulic variance between samples.

Oven temperature was then incremented to 62°C while fluxes into and out of the sample were monitored with time, test stage [4]. This lead to a minor increase in flux (**Figure 5-3)** and a slight increase in permeability (**Figure 5-4)**. The increase in temperature to 92°C imposed during stage [5], yielded no useful data due to jacketing problems with the sample discussed Section 5.1. To ascertain if this had a deleterious effect on the hydraulic properties of the sample, temperature was reduced back to 62°C and the permeability re-measured, test stage [6]. Data from both **Figure 5-3** and **Figure 5-4** clearly show no significant change in behaviour had occurred as a result of the jacket failure.

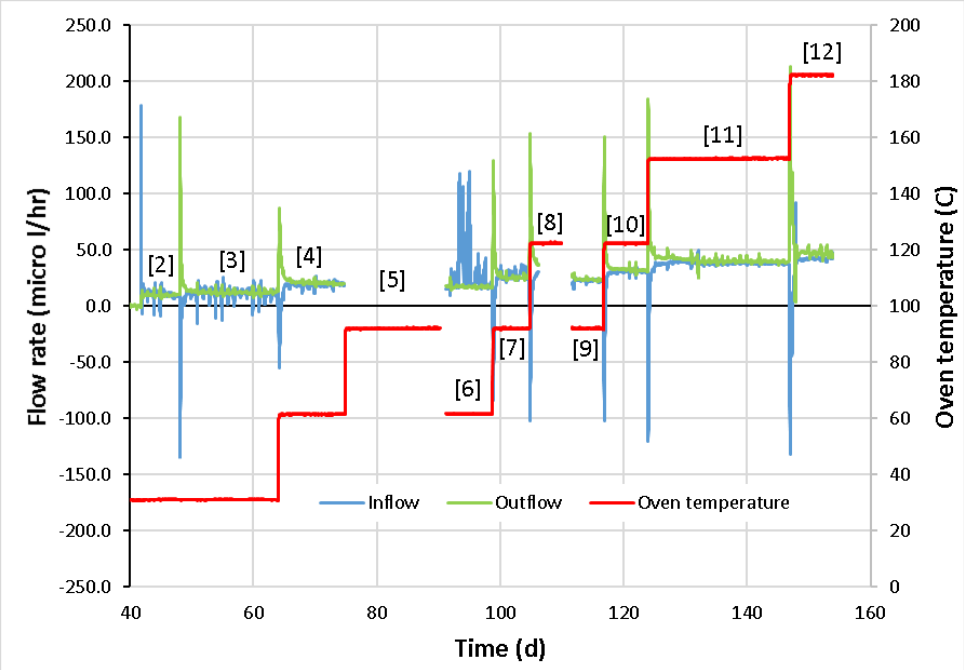

Figure 5-3: In- and outflow data as a function of time for different thermal loads applied to the sample. The gaps in the flow data during stages [5] and [8] were caused by failure of the confining sheath. Values in parentheses reflect test stage numbers.

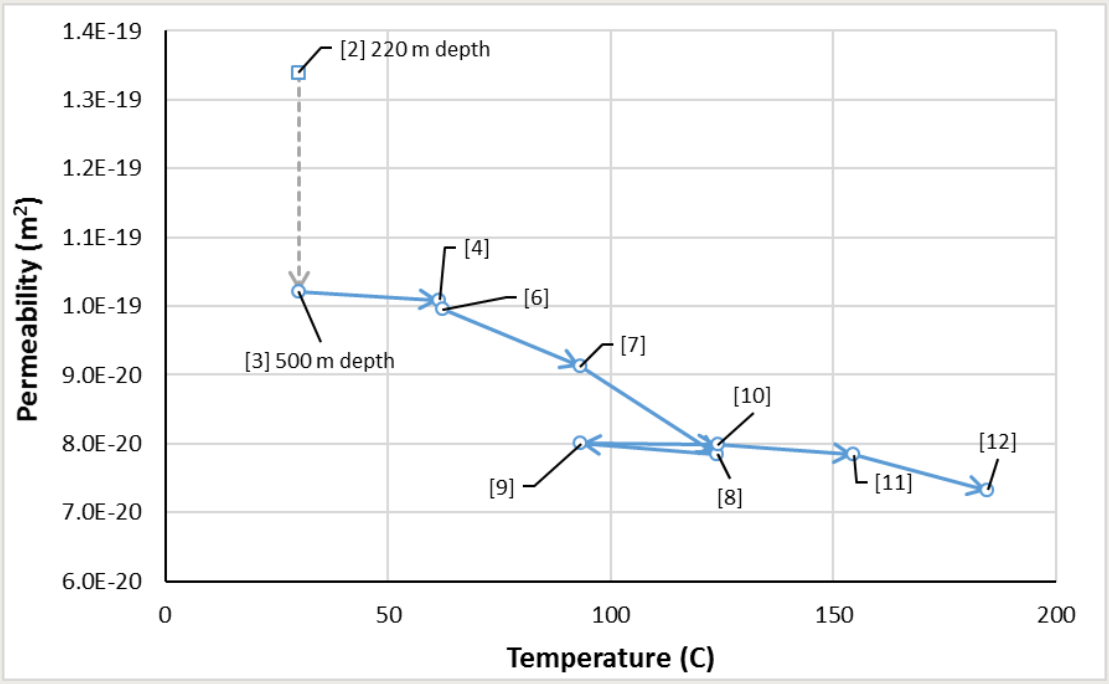

Figure 5-4: Cross-plot of intrinsic permeability against temperature for test stages [2] to [12] inclusive.

In stages [7] and [8][b] testing continued with temperature increased to 93 and 124°C respectively. Flux in and out of the sample again increased, which, when corrected for viscosity and water density changes due to the change in temperature (**Figure 5-5**),

[b] While stage [8] finished prematurely due to a second jacketing issue, Section 5.1, sufficient data was obtain with which to estimate permeability.

resulted in a significant reduction in permeability (**Figure 5-4**). This result suggests that the Boom Clay, under repository conditions likely within a Netherlands disposal facility, would exhibit thermally contractive behaviour across this temperature range. This observation is in line with results from both Francois et al., (2009) and Abuel-Naga et al., (2007) who also observed thermal contraction in lightly overconsolidated clay.

Stage	Temperature (°C)	Viscosity (Pa^{-1})	Density (Mg/m^3)	Permeability (m^2)
1	30	8.00E-04	998	-
2	30	8.00E-04	998	1.3E-19
3	30	8.00E-04	998	1.0E-19
4	62	4.55E-04	984	1.0E-19
5	92	3.11E-04	966	-
6	62	4.50E-04	984	9.9E-20
7	93	3.07E-04	965	9.1E-20
8	124	2.25E-04	942	7.8E-20
9	93	3.06E-04	965	8.0E-20
10	124	2.25E-04	942	8.0E-20
11	155	1.77E-04	915	7.8E-20
12	185	1.45E-04	884	7.3E-20

Table 5-3: Temperature, viscosity, density and permeability data for each test stage.

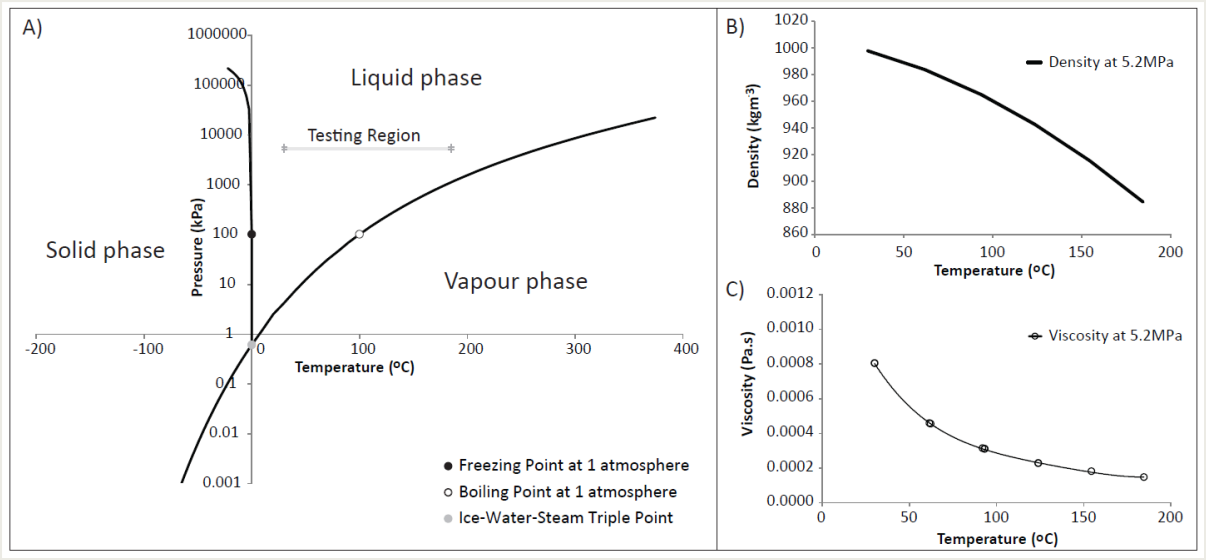

Figure 5-5: Phase diagram for water. Data clearly demonstrates that the synthetic solution remains as a liquid phase throughout the test duration (adapted from Daniels et al., 2017).

To examine the recoverability of any thermally induced contraction, the temperature during stage [9] was decreased to 93°C. **Figure 5-4** clearly shows that while permeability increases slightly between stages [8] and [9], the vast majority of the permeability change observed between test stages [7] and [9] remains non-recoverable. The similarity in form between the data presented in **Figure 5-4** and that of the consolidation response in **Figure 3-8** further supports the hypothesis for thermal contraction of the clay under these test conditions. Indeed, the degree of hysteresis evident in the data suggests thermal conditioning of the clay is an important consideration in a future Netherlands repository.

To further examine the coupling between thermal load and permeability, temperature was incremented in a series of steps, stages [10] through [12], to a final value of 185°C. While this latter value is outside the current range for most repository designs, it provides an

important end-member value for Boom Clay behaviour across a broad range of conditions. Inspection of the phase diagram (**Figure 5-5)** also shows that the synthetic porewater solution remains within the liquid boundary under these test conditions.

Figure 5-4 shows a general trend of decreasing permeability with increasing temperature. In stage [10], temperature was returned to the same value as that in test stage [8], yielding near identical values of permeability. This behaviour is similar in form to that of **Figure 3-8** and can be viewed as movement of the clay along the rebound reconsolidation line of consolidation theory (i.e. a predominantly elastic response). As temperature is further increased, stages [11] and [12], an inflection in the temperature-permeability response is observed (**Figure 5-4),** symptomatic of the clay moving back to the virgin consolidation line.

By enhancing the classical relationship between specific storage, and the water and solid-phase compressibilities, it is possible to estimate a temperature dependent storage coefficient. In the classical relationship,

$$S_s = \rho g(\alpha + \phi\beta) \tag{5-1}$$

where S_s is the specific storage [m^{-1}], ρ is the water density [kg/m^3], α is the solid-phase compressibility, ϕ is the porosity [-] and β is the water compressibility [Pa^{-1}]. This relationship can be simply extended to include temperature dependence leading to,

$$S_s(T) = \rho(T)g(\alpha(T) + \phi\beta(T)) \tag{5-2}$$

where T is the temperature [°C]. For the sake of simplicity (and in the absence of data), the solid-phase compressibility $\alpha(T)$ is assumed to be one order of magnitude smaller than the water compressibility. Thus, assuming a porosity value ϕ = 0.387 (**Table 5-1**), the water density values presented in **Figure 5-5 B** and the fluid compressibilities reported in Kell (1975), the temperature-dependent specific storages can be estimated, and are listed in **Table 5-4**. While these values should be treated with caution they are in general agreement with those reported by Wiseall et al., (2015). At some point in the future more thorough numerical analysis of the data may be warranted in which solid phase compressibility is more accurately represented and porosity is a variable linked to the thermally induced volume change.

At the end of stage [12], the high temperature seal on the pressure vessel failed and the test was terminated.

T [° C]	ρ [Kg/m^3] [1]	$10^{10} \times \beta$ [1/Pa] [2]	$10^6 \times S_s$ [1/m] [Eq. (2)]	T [° C]	ρ [Kg/m^3] [1]	$10^{10} \times \beta$ [1/Pa] [2]	$10^6 \times S_s$ [1/m] [Eq. (2)]
20	1000.09	4.59	2.19	90	967.38	4.74	2.19
25	998.95	4.52	2.16	95	963.97	4.82	2.22
30	997.58	4.48	2.13	100	960.46	4.90	2.25
35	995.98	4.44	2.11	105	956.83	4.99	2.28
40	994.18	4.42	2.10	110	953.10	5.09	2.32
45	992.19	4.42	2.09	115	949.26	5.20	2.36
50	990.02	4.42	2.09	120	945.31	5.32	2.40
55	987.69	4.43	2.09	125	941.26	5.44	2.45
60	985.20	4.45	2.09	130	937.10	5.58	2.50
65	982.56	4.48	2.10	135	932.84	5.72	2.55
70	979.79	4.52	2.11	140	928.47	5.88	2.61
75	976.87	4.56	2.13	145	924.00	6.05	2.67
80	973.83	4.61	2.14	150	919.43	6.23	2.73
85	970.66	4.67	2.17				

Table 5-4: Water density values, values of water compressibility and corresponding estimates for storage coefficients as a function of temperature assuming a constant porosity ϕ =0.387.

5.2.1 Disassembly of apparatus

Upon termination of the test, the oven was switched off and the temperature allowed to decay for around 2.5 hours, at which point the sample assembly (while still very hot) was carefully removed from the pressure vessel while wearing oven gloves. The loss in confining pressure associated with the seal failure resulted in uncontrolled swelling of the clay. This meant it was not possible to determine either post-test sample volume or basic geotechnical properties.

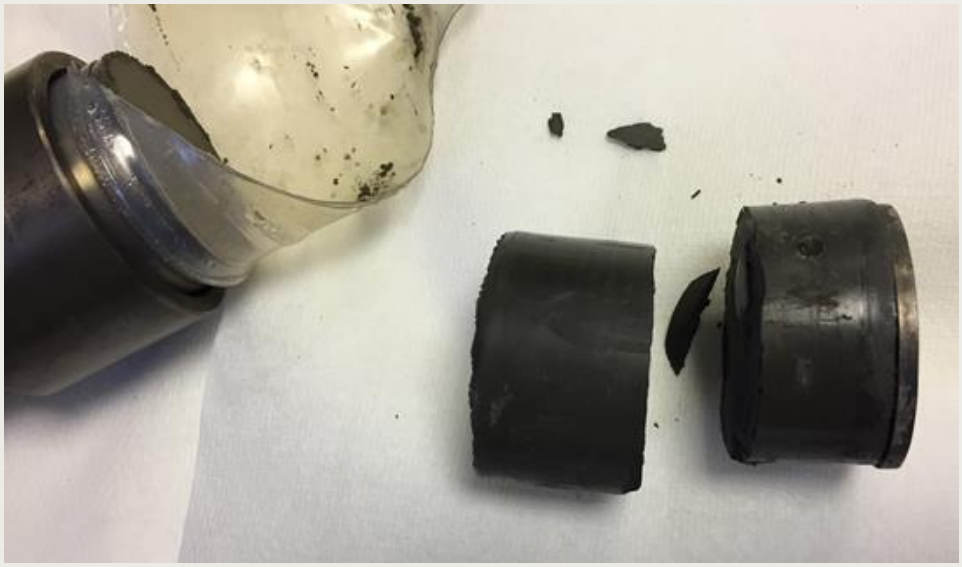

Figure 5-6: Post-test image of sample Covra-1 immediately after removal from the sample assembly.

However, the sample exhibited some interesting behaviour when removed from the sample assembly. **Figure 5-6** shows the sample immediately after removal having spontaneously fissured part-way along the axis of the core. This process rapidly continued as the thermal energy stored within the clay lead to further drying, cracking and fragmentation of the

core (**Figure 5-7)**. While cracking is predominantly focussed along the bedding planes, some fractures were observed cross-cutting the fabric.

Figure 5-7 shows that under the conditions of this test and the subsequent removal of the sample, significant thermally induced damage can occur to Boom Clay when subject to high temperature conditions. While this damage is an artefact of sample drying, the potential for moisture redistribution under a thermal gradient (rather than the isothermal loading imposed during this scoping study) remains entirely possible, and could lead to similar cracking under *in-situ* conditions.

Figure 5-7: Post-test image of sample Covra-1 shortly after removal from the apparatus. Rapid drying of the sample due to the thermal energy stored within the clay has resulted in cracking and fragmentation of the sample.

5.3 *Summary*

As part of this scoping study a sample of Boom Clay has been subject to a complex thermal history in order to examine the coupling between permeability and temperature and to ascertain if clay, at repository depths of interest to Covra, exhibits thermally contractive or dilatant behaviour. Data presented in **Figure 5-4** clearly show that intrinsic permeability is strongly dependent on the temperature applied to the clay. As thermal load increases, permeability exhibits a negative trend, decreasing by around $2.2x10^{-22}m^2/°C$. However, if temperature is subsequently decreased, much of the induced reduction in permeability remains and appears non-recoverable. Upon additional heating, further reductions in permeability continue once the temperature has exceeded the maximum value previously applied to the clay.

Although volumetric strain was not directly measured within this study, the reduction in permeability observed during thermal loading strongly indicates that Boom Clay, at an equivalent depth of burial of 500 m, thermally contracts on heating. This behaviour is in line with previous research by various authors (Francois et al., 2009 and Abuel-Naga et al., 2007) on a variety of clays at different states of consolidation which also exhibited thermal consolidation when over-consolidation ratios were small. This test was performed under isothermal conditions i.e. no thermal gradient, however it is highly probable that the latter would result in the redistribution of interstitial water within the clay. This may lead to thermally induced damage, similar in nature (though far less extreme) to that observed in **Figure 5-7**. The recoverability of any such damage and its impact on permeability and mechanical behaviour remains unclear.

The permeability data would appear to suggest that any mineral alteration of the Boom Clay across the temperature range of this study, has minimal impact on the hydraulic behaviour of the sample. That said, the duration of these tests (158 days) was relatively short and under repository conditions and timescales with variable near-field chemistry, reaction rates may differ. Further work is required to understand what, if any, changes occur during the heat emitting phase of the repository lifecycle.

Outcomes:

1. Under *in-situ* conditions relevant to a Netherlands repository, Boom Clay appears to thermally contract (i.e. consolidate) on heating.
2. Analysis of permeability data suggest volume change induced during thermal loading is non-recoverable when temperature is decreased.
3. Intrinsic permeability shows a marked sensitivity to changes in temperature, with increases in thermal load resulting in a permeability reduction.
4. Reductions in permeability caused during heating are, for the most part, non-recoverable.
5. Analysis of permeability data suggest mineral alteration of the clay was minimal under the test conditions examined within this study.

Recommendations:

1. Undertake additional experiments to better understand the impact of natural heterogeneity on the thermal behaviour of Boom Clay.
2. Examine the influence of thermal loading on hydraulic anisotropy to ascertain its relative importance for flow parallel and perpendicular to bedding.
3. Directly measure strain during thermal loading to confirm consolidation response and to quantify evolution in hydromechanical properties.
4. Perform elevated temperature tests under different thermal gradients to examine potential drying, thermally induced damage and rehydration/self-sealing properties after thermal loading.
5. Undertake long-term elevated temperature tests to assess reaction rates and possible mineralogical alteration due to variable near-field geochemical conditions.

6 Sensitivity of permeability to changes in hydrochemistry

Questions relating to the validity of Darcy's law when applied to clays have been around since the 1960's (Oakes, 1960; Hansbo, 1960, 1973; Kutelek, 1969) and the existence of possible 'thresholds' proposed as an explanation for departures between observation and theory (Miller and Low, 1963). While some authors suggest such departures stem from experimental errors, internal consolidation/swelling effects, particulate migration, or even bacterial growth (Mitchell, 1976), there is now a growing body of evidence in the literature that suggests argillaceous rocks can act as a semipermeable membrane capable of supporting an osmotic flux of groundwater (Hanshaw, 1962; Kemper and Evans, 1963; Young and Low, 1965; Kemper and Rollins, 1966; Fritz and Marine, 1983; Fritz, 1986; Neuzil, 1994; Wong and Heidug, 1994 and Van Oort, 1994).

Heister et al., (2006) measured the membrane potential of reconstituted Boom Clay discs, demonstrating the presence of an osmotically driven flow under such conditions. In these tests, membrane potential was coupled to the salt concentration gradient across the disc, which was observed to decrease over time due to the backflow of ions arising from the semipermeable nature of the membrane. However, the main uncertainty concerning osmosis under *in-situ* conditions is whether or not the membrane is rendered ineffective by the presence of fractures (Hanor, 1984). By reconstituting the clay, Heister et al., removed all such considerations, rendering the role of bedding, anisotropy, heterogeneity and fractures obsolete. In contrast, membrane experiments performed on Opalinus Clay under *in-situ* conditions by Horseman et al., (2007), yielded very small osmotic efficiencies typically ranging from 1% to 6% (with a mean value of around 4%). However, the high compressibility coefficient and low membrane efficiency revealed by these experiments can be explained by a number of factors from sample damage to chemically induced swelling.

6.1 *Experimental set-up and test procedure*

In an attempt to measure the membrane efficiency of Boom Clay and its sensitivity to changes in the molar concentration of the test permeant, a scoping test was initiated. As before, the apparatus used for this study was, in principal, exactly the same as that described in Chapter 3, with tests performed in an environmental room to minimise thermal noise (+/- 0.2°C). **Figure 6-1** shows a photo of the permeameter used for this study.

As in previous tests, a cylindrical specimen of Boom Clay was cut perpendicular to bedding, from core barrel 76/77D-2.58-2.83 through a combination of machine lathing and diamond cutting. The sample was designated Covra-2. Sample assembly and calibration of the apparatus is described in full in Section 3.2.

The test procedure comprised 8 stages (**Table 6-1**). Following equilibration and hydration of the sample, the intrinsic permeability of the core was measured, stage [2]. The synthetic solution was then flushed from the apparatus and replaced with NaCl solution whose osmotic pressure and salt fraction increased in a stepwise manner in test stages [3] through [9]. The exception was stage [5] when confining stress was increased to near Covra stress conditions.

Figure 6-1: Photo showing pressure vessel, connecting tubes and the three control pumps used to monitor inflow (left pump), outflow (right pump) and maintain confining pressure (centre pump).

Stage	Type	Permeant	Salt fraction	Injection pressure (MPa)	Back pressure (MPa)	Confining pressure (MPa)
1	EQ	Synthetic	0.0002	2.2	2.2	4.4
2	CPTH	Synthetic	0.0002	2.6	2.2	4.4
3	CPTH	NaCl (350 kPa)	0.0013	2.7[#]	2.2	4.4
4	CPTH	NaCl (700 kPa)	0.0025	2.6	2.2	4.4
5	Loading	NaCl (700 kPa)	0.0025	2.6	2.2	6.7
6	CPTH	NaCl (1,400 kPa)	0.0051	2.6	2.2	6.7
7	CPTH	NaCl (5,600 kPa)	0.0202	2.6	2.2	6.7
8	CPTH	NaCl (11,200 kPa)	0.0397	2.6	2.2	6.7
9	CPTH	NaCl (22,400 kPa)	0.0764	2.6	2.2	6.7

Table 6-1: Experimental history for sample Covra-2. EQ = equilibration stage; CPTH = constant pressure hydraulic test. Values in parentheses represent the osmotic pressure of the solutions. [#]injection pressure was 2.65 MPa due to a slight drift in the pump datum.

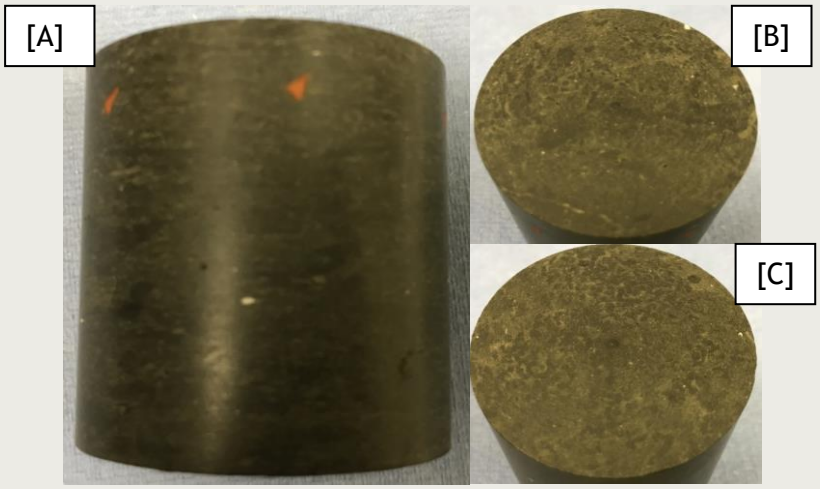

Figure 6-2: Sample Covra-2 taken from core barrel CGR76/77D-2.58-2.83m. [A] Side view of core with the red dots marking the injection end of the sample. [B] and [C] are the injection and backpressure faces respectively.

An estimate of the basic geotechnical properties for the Covra-2 sample (**Figure 6-2**) are presented in **Table 6-2**. These values should be treated with caution, as post-test sample volume and mass measurements were not available at the time of writing. As such, values are based on the pre-test moisture content of sample Covra-1.

Specimen	Length (mm)	Diameter (mm)	Moisture content (%)	Bulk density (Mg m^{-3})	Dry density (Mg m^{-3})	Porosity (%)	Saturation (%)
Covra-2	49.9	50.3	23.6	2.05	1.66	37.8	>1

Table 6-2: Basic pre-test properties of specimen Covra-2. An assumed specific gravity for the mineral phases of 2.67 $Mg.m^{-3}$ (Wiseall et al., 2015) was used in these calculations. The saturation value greater than 1 suggests the value chosen for specific gravity is slightly low, reflecting possible heterogeneity within the Boom Clay. No post-test data is available due to failure of the O-ring seal on the pressure vessel.

6.2 *Results*

Upon assembly and pressurisation of the apparatus, stage [1], a very small cross-flow of synthetic water was noted between the injection and backpressure systems. In an attempt to remedy the situation, the backpressure pump was isolated and its pressure datum checked. Under atmospheric conditions the pump had drifted to read -17 kPa, which would appear to be sufficient to generate a measureable flux across the specimen. It therefore became apparent that measuring the membrane properties of natural material was not going to be feasible using the current sample or apparatus. Indeed, given the permeability of Boom Clay and the apparent ease with which solvent could migrate through the clay, it suggested that for natural (non-reconstituted) material, membrane efficiencies are likely to be very low under normal testing conditions. That said, only one test was attempted within the scope of the project and further work is required to quantify these processes fully.

At day 14, test stage [2], a hydraulic gradient was imposed across the sample and flux in and out of the core measured as a function of time (**Figure 6-3**). Inspection of the data shows that flux rapidly evolved to a quasi-steady state condition, yielding an intrinsic

permeability of 1.6 $x10^{-19}$ m^2 by the end of the test stage, **Table 6-3**. Based on the cross-flow in stage [1] at minimal hydraulic gradient and the relatively high permeability of the specimen compared to more indurated mudrocks, the membrane efficiency of this core is likely to be very low. Given this response, the focus of the test evolved and it was decided to examine the sensitivity of intrinsic permeability to changes in molar concentration of the test permeant.

In stage [3] the permeants in both injection and backpressure reservoirs were changed for a simple NaCl solution with a salt fraction of 0.0013. This equated to a six fold increase in the salt concentration (and the osmotic pressure of the solution) compared to that of the synthetic interstitial fluid. To remove the latter from the tube work and sintered discs, a minimum of 100ml of NaCl was carefully flushed through the injection and backpressure circuits, while maintaining (as close as possible) the porewater pressure within each test system. The hydraulic gradient of 0.4 MPa was maintained constant through the test history.

Inspection of **Figure 6-3** indicates a small but measurable increase in flow following the introduction of NaCl, test stage [3]. However, at the start of stage [4], it was noted that the pressure datum of the injection pump had drifted again, which when corrected, yields a permeability value close to that of the previous stage (**Figure 6-4**). Following the increase in confining stress, in order to better reflect conditions in a Netherlands repository, flux across the sample decreased, indicative of consolidation and a reduction in sample volume. In stages [6] through [9] the salt fraction of the NaCl solution was progressively increased in a stepwise manner to a final value of 0.07639. This was over 280 times larger than the equivalent value for the starting synthetic fluid. As evidenced in **Figure 6-3**, the increase in salt concentration through test stages [6] to [8] had no significant effect on the mass flux of fluid through the clay. Even allowing for minor errors caused by mixing of the permeants during flushing, the data seems remarkably consistent. However, when the permeant is changed in step [9], flux out of the sample begins to decrease (**Figure 6-3)**. While this test stage is incomplete at the time of writing, an estimate of its asymptote can be made and plotted in **Figure 6-4**. Once permeability is corrected for viscosity and density changes of the NaCl solution, a reduction in permeability, compared to the previous stage [8], is observed. The size of the change is relatively large and can be considered a true response of the sample.

Stage	Salt fraction	Viscosity (Pa^{-1})	Density (Mg/m^3)	Ave.permeability (m^2)
2	0.00027	0.0010025	989.2	1.64E-19
3	0.00129	0.0010041	989.8	1.65E-19
4	0.00258	0.0010060	990.7	1.64E-19
5	0.00514	0.0010100	992.3	-
6	0.02026	0.0010349	1002.2	1.39E-19
7	0.03971	0.0010708	1015.2	1.44E-19
8	0.07639	0.0011503	1040.4	1.50E-19
9	0.00027	0.0010025	989.2	1.41E-19

Table 6-3: Salt fraction, viscosity, density and permeability data for each test stage.

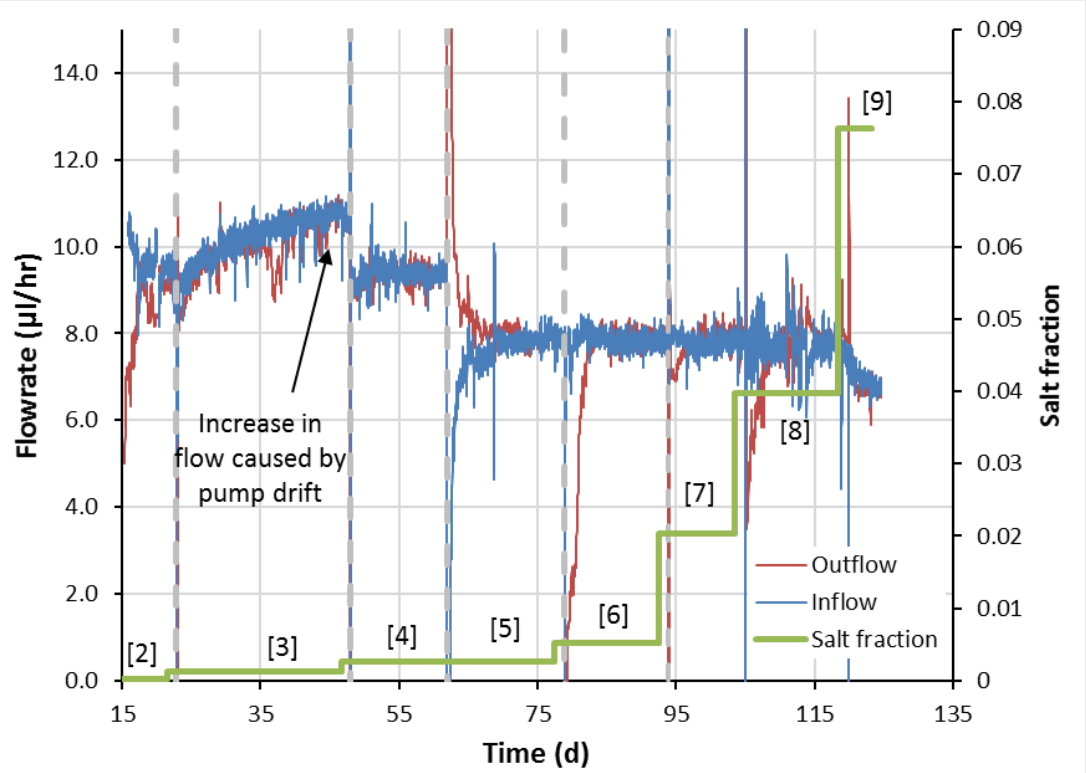

Figure 6-3: Flux in and out of sample Covra-2 as the salt fraction of the permeant is increased. Values in parentheses represent test stage numbers.

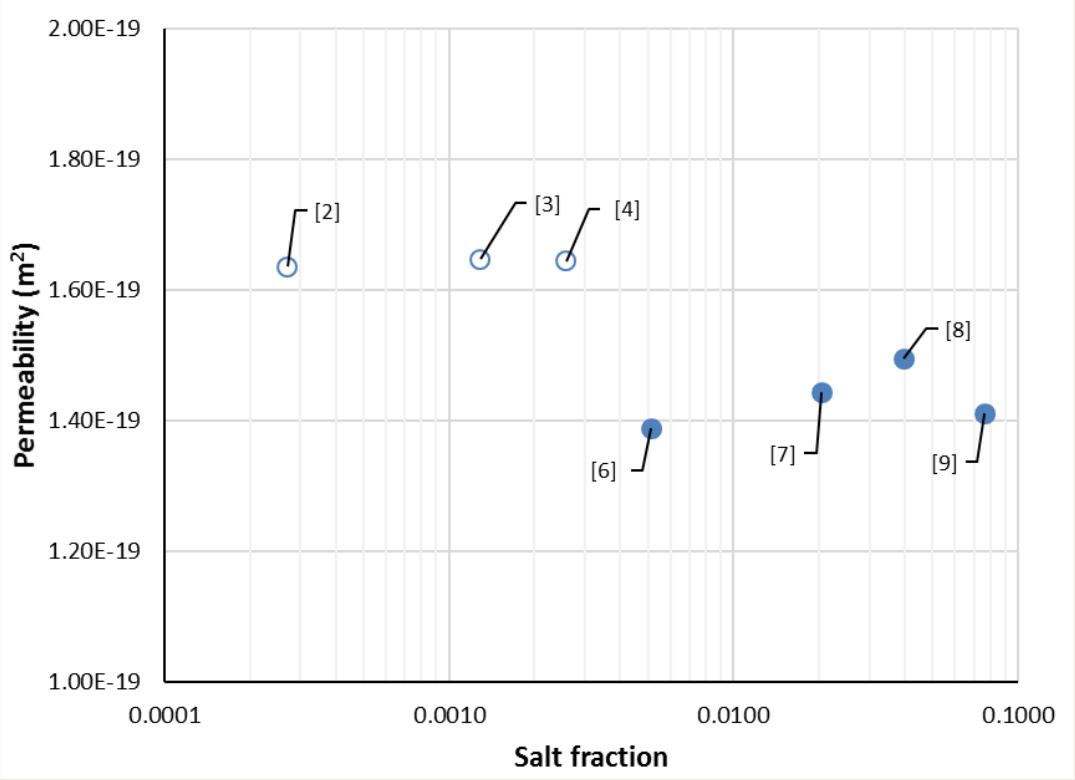

Figure 6-4: Permeability plotted as a function of salt fraction. Hollow symbols represent data for stress conditions at Mol, while solid symbols reflect stress conditions close to those expected in a Netherlands repository. Values in parentheses represent test stage numbers.

6.3 *Discussion*

In total, six different fluid salinities ranging in salt fraction from 0.0002 to 0.03971 have been injected through a sample of Boom Clay subject to two confining stresses. While permeability was observed to decrease between stages [4] and [6] (**Figure 6-4**), this was purely a mechanical effect caused by the increase in confining stress imposed during stage [5]. The permeability data before the increase in stress shows no obvious sensitivity to changes in fluid salinity. Even allowing for unrealistically large errors potentially introduced through mixing of the test permeants, the apparent lack of any sensitivity in the permeability response is a little surprising.

However, as the salt fraction increases significantly, stages [6] through [8], a consistent trend of permeability increase is observed. This seems somewhat counter-intuitive as the increase in salinity, and subsequent cation concentration within the clay, should lead to a reduction in pore volume as cations displace water as charge neutrality across the interlayer spacing is maintained. That said, stage [9] appears to be consistent with this hypothesis as permeability of the sample significantly decreases, compared to the previous stage [8], as the sample is exposed to the high salinity solution. Clearly, further testing is required to better understand this behaviour and in addition preclude sources of error, in particular, the composition of test fluids which should be tracked as a function of time using Inductively Couple Plasma (ICP) analysis. However, what is not clear, is, whether the increase in permeability trend observed from stage [6] through [8] would have occurred at low salinities, test stages [2] through [4], if the sample had been consolidated to Covra depths of interest at the start of testing. Further testing is required to address this uncertainty.

While it was not possible to directly measure the membrane properties of Boom Clay as part of this study, the ease with which fluids migrated through the clay, combined with its natural heterogeneity and minor sensitivity to large changes in NaCl salinity, suggests membrane efficiencies for this material are likely to be low. Conductive natural features and bedding planes may well render membrane potential ineffective through the backflow of solutes through the clay. As such, more complex tests are therefore required on longer length samples of representative volume, using differential pressure transducers to eliminate hydraulic gradients across the sample, in order to accurately quantify the osmotic potential of the Boom Clay.

In addition, such tests should also consider the impact of more complex fluid chemistries on both membrane efficiency and on the composition, structure and permeability of the clay. Further work is therefore required to examine the chemical coupling between porewater composition and the hydromechanical properties of the Boom Clay.

Outcomes:

1. Permeability appears to increase at elevated salinities. However, the lack of sensitivity between permeability and salinity at low salt fractions may be impacted by the low effective stress used during these measurements.
2. While it was not possible within this study to define the osmotic potential of unworked/natural Boom Clay, the ease at which fluids were able to migrate through the clay combined with the apparent minimal sensitivity of the system to minor changes in salinity, suggest low membrane efficiencies.

Recommendations:

1. Perform additional tests on samples of appropriate dimension to examine osmotic potential and membrane efficiency of Boom Clay samples consolidated to repository depths of interest to Covra.
2. Examine the influence of representative geochemical solutions on intrinsic permeability, mineral composition and stability and pore structure.

7 Gas migration behaviour

7.1 *Testing in a triaxial arrangement*

An experimental programme was designed to investigate the hydraulic and gas properties of Boom Clay under stress conditions representative of the Belgian and Netherlands disposal concepts. The Belgian depth tests were undertaken to gain comparative results with previous work and to allow direct comparison to be made with Boom Clay conditioned to a stress state representative of the Netherlands.

Two experiments were conducted using the triaxial Stress Path Permeameter (SPP) apparatus; this would give two measurements of hydraulic flow properties and four gas injection tests. The use of triaxial apparatus would allow the role of the intermediate principal stress to be investigated.

7.1.1 The Stress-path permeameter (SPP) apparatus

The stress-path permeameter (SPP) was designed to investigate stresses appropriate to radioactive waste disposal. The SPP was specifically designed to resolve very small volumetric (axial and radial) strains potentially associated with the onset of gas flow. The apparatus has been used on several experimental programmes, most notably experiments conducted on Callovo-Oxfordian Claystone, which demonstrated that sample dilation occurred at the onset of gas flow (Cuss et al., 2014; Cuss et al., 2012). A schematic of the SPP is shown in **Figure 7-1 A**, along with a photograph in **Figure 7-1 B**. The SPP comprised 6 main components:

1) The specimen, surrounded by a modified flexible Hoek sleeve (**Figure 7-2 B**) and main pressure vessel body.
2) Three dash-pots (**Figure 7-2 C**) that were mounted along the radial mid-plane of the sample which directly measured the radial strain of the sample. The dash pots were pressure balanced in order to reduce the force imposed upon the sample and to make sure the push-rods were not simply pushed out of the pressure vessel.
3) An axial load system comprised of an Enerpac single acting hydraulic ram (see **Figure 7-1 B**) pressurised by an ISCO-500 series D syringe pump. This was connected via an axial strain jig to a Global Digital Systems optical encoder for measuring linear displacement accurate to 0.003 mm. Miniature load cells were located at the piston ends to measure stress at the sample ends.
4) A confining pressure system using an ISCO-500 series D syringe pump and glycerol confining medium allowing radial strain measurements to be calculated through volume change.
5) A pore-pressure system comprised of two ISCO-100 series D syringe pumps to create pore fluid pressure and monitor back-pressure. The injection media could be either water or gas (helium).
6) A state-of-the-art custom designed data acquisition system facilitating the remote monitoring and control of all experimental parameters.

A cylindrical sample of Boom Clay was positioned between two stainless steel platens and jacketed in a flexible Hoek sleeve (**Figure 7-2 B**) to exclude the confining fluid. The inlet and outlet zones for water flow[c] to and from the specimen were provided by stainless-steel discs, nominally 20 mm in diameter and 3 mm depth. Guard-rings of 6 mm thickness and 2

[c] A synthetic pore fluid representative of the Netherlands was used, see Chapter 1

mm depth were located on the outer diameter of the platens, allowing pore-pressure to be measured in two locations on the faces of the sample.

The stainless steel load platens were in direct contact with the sample transmitting the axial force generated by the Enerpac ram directly to the specimen. Each platen had two ports facilitating flushing of the system and the removal of residual air prior to testing. Retaining collars and axial tie-rods locked the system components together to provide a rigid test rig, these were pre-tensioned at 300 Nm.

Axial displacement was measured using the GDS optical encoder connected to stainless steel push rods terminating a short distance behind the load-bearing face of each platen to minimise compliance effects. Data from the optical encoder was processed through a multiplexer to provide a continuous measure of axial strain.

Three pressure balanced dash-pots (**Figure 7-2 C**) were located around the radial mid-plane of the specimen. Brass push-rods were in direct contact with the outer diameter of the Hoek sleeve. Three 10 × 10 mm brass plates were cemented to the outer edge of the Hoek sleeve (**Figure 7-2 B**) in order to reduce the force the push-rods imposed on the sample surface. The push rods extended to the outside of the pressure vessel, where high precision LVDTs were used to measure the displacement of the sample diameter.

One experimental uncertainty in transport testing is the short-circuiting of the flow system along the jacket of the test sample. The addition of a 6 mm wide, 2mm deep, porous stainless-steel annular filter along the outer edge of each platen (**Figure 7-2 A**) allowed pore-water pressure to be monitored so that unwanted sidewall flow could be discounted. These two guard-rings (Harrington et al., 2003) were each connected to a pressure transducer and the complete guard-ring system (filter, pipework and pressure sensor) was saturated with water and flushed in order to eliminate gas from the system. The inlet/outlet filter was made up of a porous disc 20 mm in diameter and 2 mm depth. The control board of the apparatus allowed the guard-rings to be either connected to the injection system to assist in hydration, or isolated to give an independent measure of pore-pressure. As well as being able to eliminate side-wall flow as a possible transport mechanism, the guard-rings meant pore-pressure was measured at four different points on the test sample (injection pressure, injection guard-ring pressure, back-pressure, back guard-ring pressure) providing data on the hydraulic anisotropy within the sample.

7.1.1.1 Measured parameters

The logging software directly recorded the following parameters every 2 minutes: SPP injection circuit pump (pressure, flow and volume); SPP back-pressure circuit pump (pressure, flow and volume); SPP axial load pump (pressure, flow and volume); SPP confining pressure pump (pressure, flow and volume); Load cell on the injection platen; Load cell on the back-pressure platen; Radial displacement of the sample mid-plane (Radial 1, Radial 2 & Radial 3); Axial displacement of the sample; Temperature (vessel, laboratory low level and laboratory high level).

From the measured parameters, the following calculated parameters were determined: Axial strain of the sample; Radial strain of the sample; Volumetric strain of the sample (from direct measurements on the sample and from displacement of confining fluid); Permeability and storage capacity; Stress state. In addition to these parameters, physical properties were also recorded.

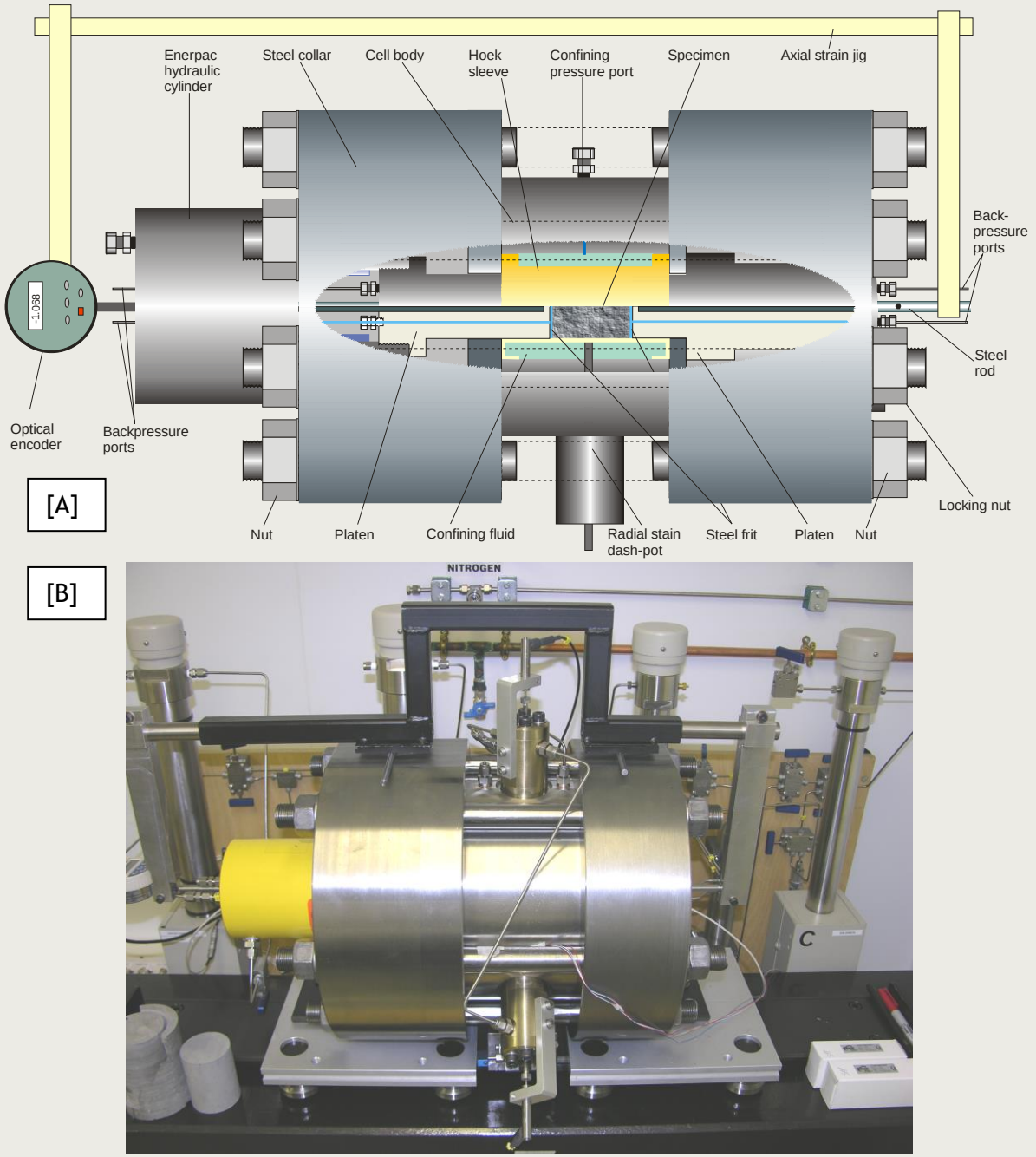

Figure 7-1: The stress path permeameter (SPP). [A] Schematic and [B] photograph showing the hydraulic ram (yellow), along with the dash-pots used to measure radial deformation of the jacketed samples.

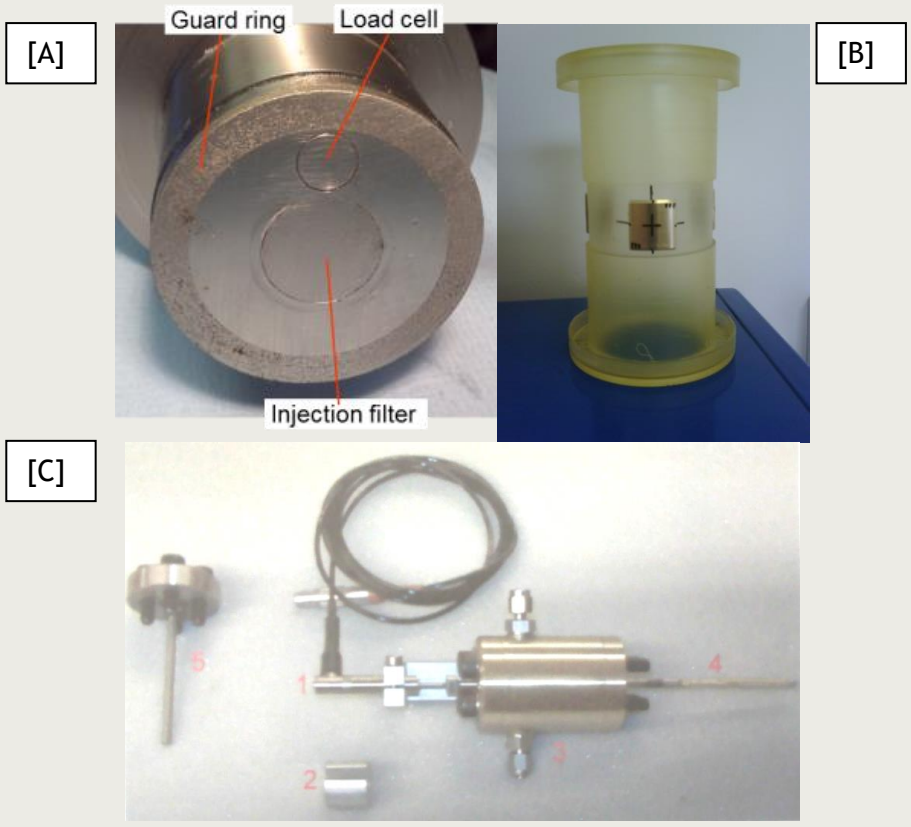

Figure 7-2: Components of the SPP. [A] Photo of the end platen showing the injection filter and guard-ring arrangement. [B] Modified Hoek sleeve with brass additions that are in direct contact with the arms of the dash-pot arrangement. [C] Pressure balanced dash-pot system. The dashpot arm [4] is in direct contact with the outside of the sample jacket. The movement of this arm is recorded by a high-precision LVDT [1]. The dashpot is pressure balanced through the pressure ports marked [3].

7.1.2 Basic physical properties

The starting samples were measured five times for length and nine times for diameter. The sample was weighed, which allowed bulk density to be determined. **Table 7-1** shows the pre-test physical properties of the specimens.

	Units	Value	Value
Sample reference		OPERA_SPP-1	OPERA_SPP-2
Location		Mol URL, Belgium	Mol URL, Belgium
Core direction		Perpendicular to bedding	Perpendicular to bedding
Average length	mm	89.89 ± 0.04	79.73 ± 0.04
Average diameter	mm	56.39 ± 0.01	56.01 ± 0.06
Volume	m^3	2.245×10^{-4}	1.964×10^{-4}
Average weight	g	475.89	400.41
Density	$g.cc^{-1}$	2.12	2.04

Table 7-1: Dimensions and basic properties of the Boom Clay test material (samples OPERA_SPP-1 and OPERA_SPP-2).

7.1.3 Test OPERA_SPP-1

The aim of test OPERA_SPP-1 was to determine the hydraulic and gas transport properties of the Boom Clay at stresses representative of the in situ stresses that the cores were taken from, i.e. the stress state at the Mol URL in Belgium. The test aimed to perform a two-stage test. In the first stage, a two-step hydraulic head test was performed. In the second, a gas-ramp injection test was performed up to a condition where gas flow would be initiated. The following sections outline the experimental results in detail.

7.1.3.1 Complete test history

Test OPERA_SPP-1 lasted a total of 278 days, with **Figure 7-3** showing the test result data for the complete test history and **Table 7-2** summarising the individual test stages and events. The three stages of the test can be seen (initial swelling stage and equilibration at *in situ* conditions, hydraulic testing and gas injection testing). The gas injection testing can be further split into stages of (i) gas injection at boundary condition A, (ii) gas injection at boundary condition B, (iii) gas shut-in. Results for each section are introduced in the following sections.

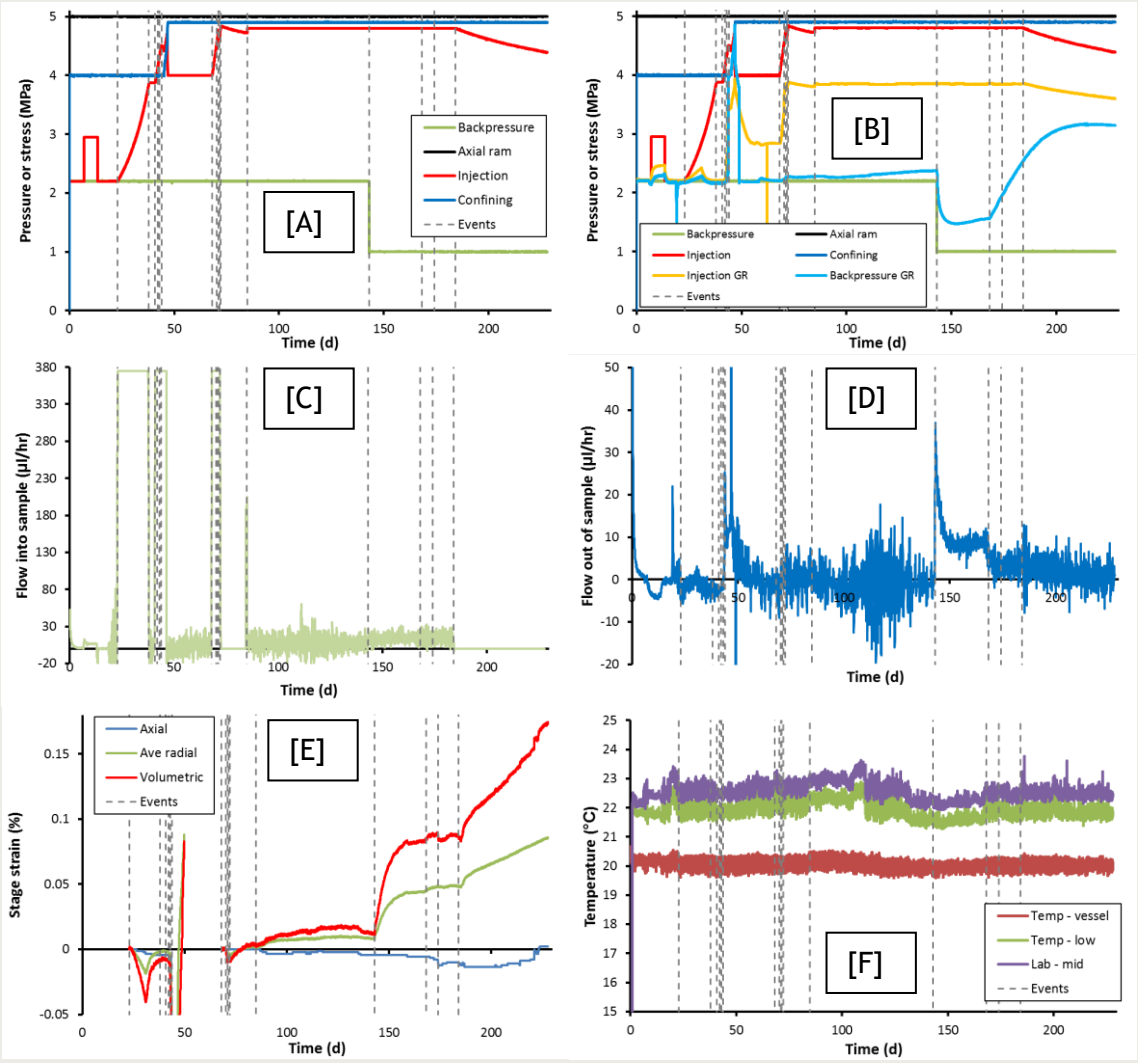

Figure 7-3: Data for the complete test history of test OPERA_SPP-1. [A] Pressure history (boundary conditions). [B] Full pressure history with guard-ring pressures. [C] Flow into sample. [D] Flow out of the sample. [E] Radial and axial displacement. [F] Temperature. Dashed lines represent events of note.

Stage	Time		Event	Stage length
1	0.00	Hyd	Start of the test and set-up of boundary conditions Confining = 4 MPa, Axial = 5 MPa, Pore pressure = 2.2 MPa	6.93
2a	6.93		Hydraulic test 1: Increase injection pressure to 3 MPa	16.01
2b	13.35		Hydraulic test 2: Reduce injection pressure to 2.2 MPa	
3a	22.94	Gas test 1	Gas injection 1: Start of gas injection ramp 1	17.93
3b	37.89		Gas injection 1: Start of constant pressure hold	
4a	40.87		Gas injection 2: Start of gas injection ramp 2	6.00
4b	42.13		Gas injection 2: increase in pressure at injection guard ring	
4c	43.00		Gas injection 2: Increase in pressure at guard-ring and increased injection	
4d	43.97		Gas injection 2: Peak gas pressure	
5	46.87		Increase in confining pressure to 4.9 Mpa Confining = 4.9 MPa, Axial = 5 MPa, Pore pressure = 2.2 MPa	21.26
6a	68.13	Gas test 2	Gas injection 3: Start of gas injection ramp	74.96
6b	70.30		Gas injection 3: Start of dilation	
6c	71.11		Gas injection 3: Gas peak pressure and start of compression	
6d	71.49		Gas injection 3: Gas pressure starts to rise again	
6e	72.25		Gas injection 3: Gas injection stopped at pressure limit	
6f	84.92		Gas injection 3: Switch to constant gas pressure	
7a	143.09		Gas injection 4: Reduction of back pressure to 1 MPa Confining = 4.9 MPa, Axial = 5 Mpa, Pore pressure = 1 Mpa	41.03
7b	168.26		Gas injection 4: Start of increase in back-end guard ring and reduction in flow out of the sample	
7c	174.11		Gas injection 4: Axial dilation of sample	
7d	184.12		Gas injection 4: End of gas injection	
8	227.89		End of test	43.77

Table 7-2: Summary of experimental history of test OPERA_SPP-1 showing stage number, description of stage/event, and boundary conditions.

7.1.3.2 Stage 1: Swelling and equilibration

The sample was loaded into the SPP and the boundary conditions were setup on the apparatus; confining pressure of 4 MPa, axial stress of 5 MPa, and pore pressure of 2.2 MPa. These conditions were set to be representative of the stress conditions of the sample when cored at the Mol URL. The boundary conditions were imposed carefully with a series of approximately 10 step changes up to the starting condition. Care was taken so as not to create an excessive axial load on the sample and for each increase in stepped stress to be minimal. At all times, axial stress was greater than confining pressure so as not to put the sample into extension. The initial stage lasted approximately 1 hour. Following the establishment of appropriate boundary conditions, the sample was monitored for swelling and equilibration. This lasted approximately 7 days.

Figure 7-4 shows the results for the seven day long stage. As can be seen in **Figure 7-4 C**, the sample initially contracted in response to the imposed boundary conditions. Approximately 0.05 % strain occurred in the first few hours of the stage. However, as the sample rehydrated and took on pore water, the sample dilated, which by the end of the stage had resulted in an approximate increase in sample volume of 0.4 %. As shown by **Figure 7-4 D**, all three radial strain sensors showed similar response, although a degree of anisotropy was observed. The flow into both ends of the sample showed an almost identical response, with an initial flow rate of 70 µl/h, which decayed to a negligible flow after five days. A total of 2.17 ml of water had been taken up by the sample during the

resaturation stage. No significant change in pore pressure was noted in the guard-rings (**Figure 7-4 B**). The hydraulic test was conducted (stage 2) once the sample had resaturated sufficiently determined by the strain and flow reaching an asymptote (day 7).

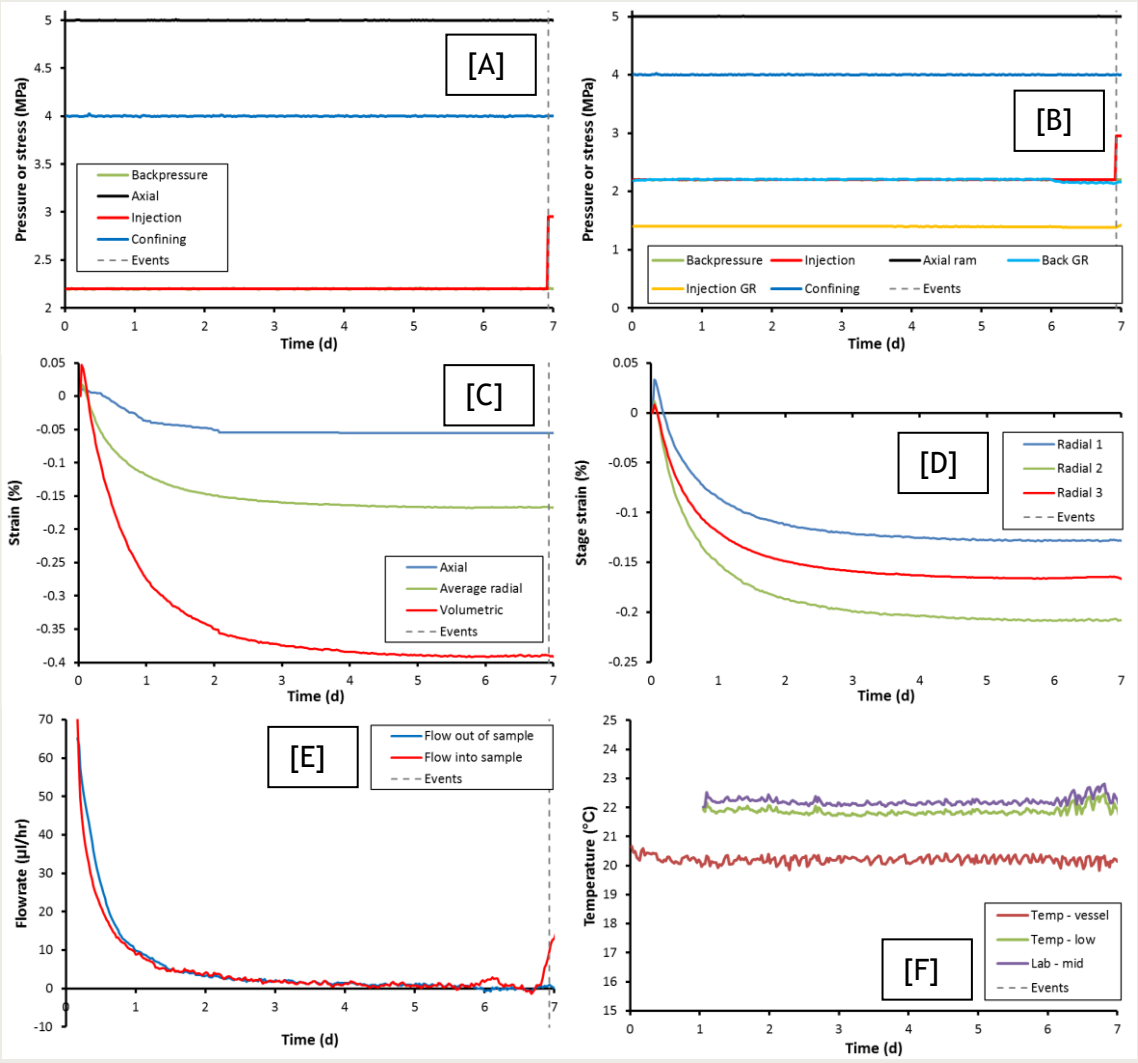

Figure 7-4: Data for the swelling and equilibration stage (1) of test OPERA_SPP-1. [A] Pressure history (boundary conditions). [B] Full pressure history with guard-ring pressures. [C] Radial, axial, and volumetric displacement. [D] Three radial displacement sensors. [E] Flow into sample. [F] Temperature.

Key observations of stage 1 (swelling and equilibration): a total of 0.4 % dilatant strain was measured; flow and strain equilibrated in approximately 5-7 days; a total of 2.17 ml of water was taken up; the sample showed a small degree of anisotropy.

7.1.3.3 Stage 2: Hydraulic two-stage constant head test

Following the swelling stage a two-stage constant head test was conducted, as shown in Figure 7-5. At the start of this test stage (2a) the injection pore-pressure was raised to 3 MPa with the guard-rings isolated (**Figure 7-5 A**). As a result the pore pressure in the guard-rings started to increase (**Figure 7-5 B**). The injection guard-ring pressure rose by 260 kPa during the stage, while the backpressure increased by 170 kPa. It has to be noted that the injection guard-ring pressure had equilibrated, whilst the back-pressure end appeared to equilibrate but started to increase in the final 24 hours of the high pressure

step. As a result of the increased pressure, the sample underwent 0.12 % dilatant strain (**Figure 7-5 C**). In the first 2 days of the stage, the average radial and axial strains were almost identical. However, axial strain reached a near asymptote whilst radial strain continued to increase. A degree of anisotropy was observed in the radial strain data (**Figure 7-5 D**), with Radial 2 > Radial 3 = Radial 1. Initially the elevated pore pressure resulted in an increased flow into the sample of about 15 µl/h, which over the course of 2 – 3 days reduced to approximately 7 µl/h. This resulted in a slowly increasing outflow from the sample, which reached asymptote at about 4 µl/h. This gives an average permeability into the sample of 6.93×10^{-19} m^2 and out of the sample of 2.7×10^{-19} m^2, giving an average permeability of 4.83×10^{-19} m^2 for sample OPERA_SPP-1.

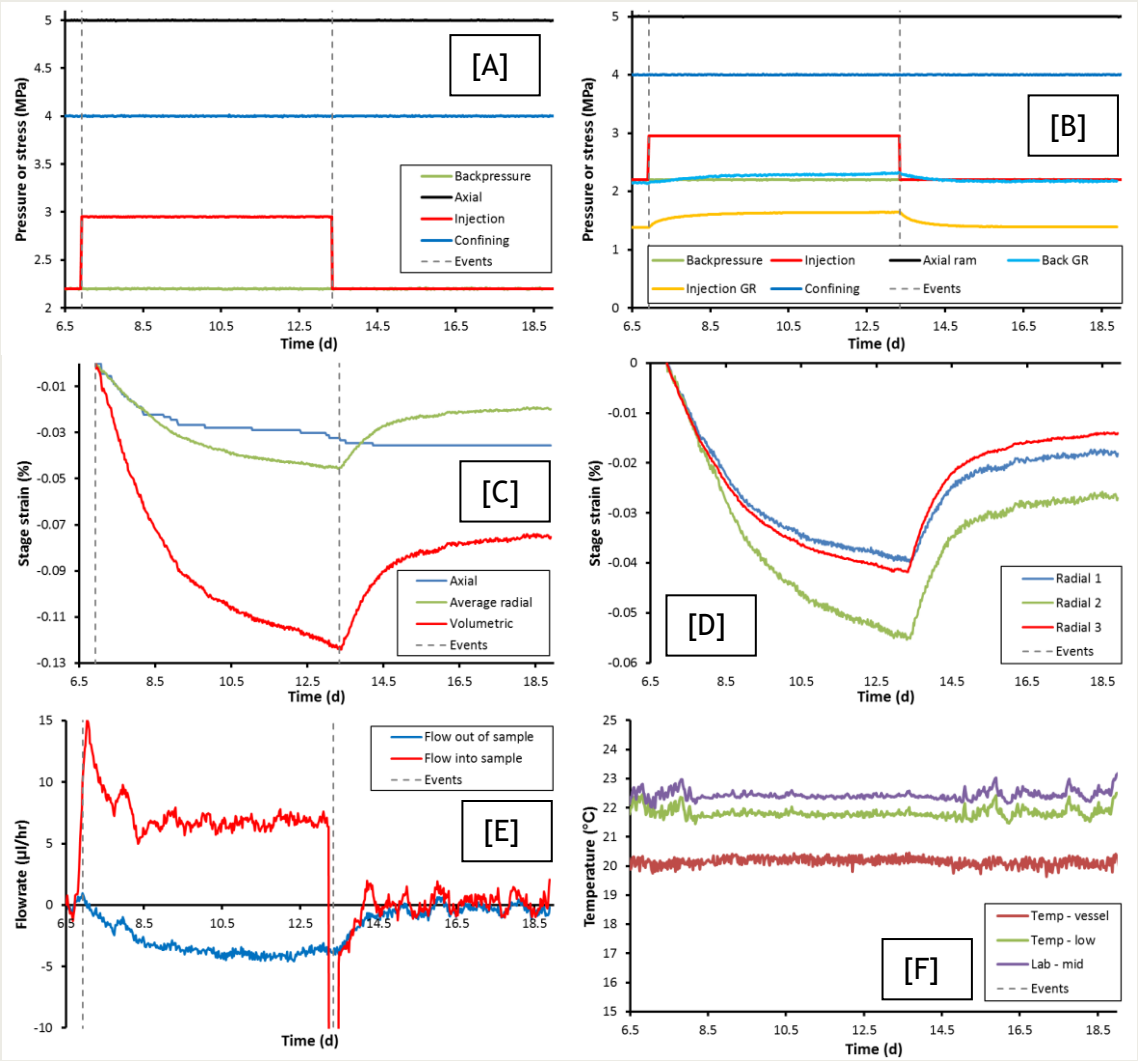

Figure 7-5: Data for the two-stage constant head test (stage 2) of test OPERA_SPP-1. [A] Pressure history (boundary conditions). [B] Full pressure history with guard-ring pressures. [C] Radial, axial, and volumetric displacement for the stage. [D] Three radial displacement sensors. [E] Flow into and out of sample. [F] Temperature.

Stage 2b of the two-step constant head test returned the injection pore pressure to 2.2 MPa (**Figure 7-5 A**). This resulted in the reduction of pore-pressure at both guard rings (**Figure 7-5 B**). The pressure within the injection guard ring returned to a level almost identical to that seen prior to the hydraulic test. The pressure at the back guard ring reduced to a level slightly higher than before the hydraulic test. However, an increase of the order of 25 kPa is not significant. It can be seen that both guard-ring pressures reduced within five days. The reduction in pore pressure resulted in only partial recovery of strain

(**Figure 7-5 C**). As can be seen, the radial strain recovered approximately half of its strain, but saw a final strain of 0.02 %. As shown in **Figure 7-5 D** this is consistent for all three radial strain measurements. Counterintuitively, axial strain continued to increase following the reduction in pore pressure. This was not expected and has not been seen in previous hydraulic tests. The cause for this is not known. Flow into and out of the sample quickly equilibrated on the reduction of pressure and within one day both show nominal flow. Both flow in and out show identical magnitudes, unlike during the high pressure stage when the injection flow was greater than the flow out of the sample.

Key observations of stage 2 (hydraulic test): the high pressure step resulted in 0.125 % dilatant strain and elevated guard-ring pressures; flow equilibrated within 2 – 3 days to give an average permeability of 4.83×10^{-19} m^2; the 2-stage head test resulted in some permanent (dilatant) strain of the sample; anisotropy seen in strain measurements.

7.1.3.4 Stage 3-4: Gas injection test 1

Figure 7-6 shows the results for gas injection test 1. This was conducted in two steps until breakthrough had occurred. The injection interface vessel was filled with approximately 300 ml of helium at a pressure of 2.2 MPa. This had been held for a prolonged period before the start of gas injection to ensure the water within the interface vessel was at full saturation with the helium. Gas injection was started at Day 22.94 by injecting water into the base of the interface vessel at a rate of 375 µl/h. This rate was deemed sufficient to raise the gas pressure sufficiently to initiate gas entry and breakthrough within 15 days.

Figure 7-6 A shows the pressure history of gas injection test 1. As can be seen, the gas pressure ramp resulted in the gas pressure getting close to the confining pressure, the least principal stress component. Should the injection pressure exceed the confining pressure then the jacket seal can fail and gas can escape from the injection circuit into the confining system. Previous testing (e.g. Harrington and Horseman, 1999) had shown gas flow at stresses lower than 3.785 MPa at which the gas pressure was held constant in the current test. By comparing the predicted gas pressure with the observed gas pressure it is possible to observe when gas entry occurs. This is seen as a deviation in the relationship. During gas injection ramp 1 there was no deviation and no flow out of the sample (**Figure 7-6 D**) and therefore it was concluded that gas entry had not occurred. Gas injection was paused for three days to observe whether gas entry was a time-dependent phenomena and again, no gas entry was observed.

Figure 7-6 B shows that the guard-ring pressures showed a response to the increase in gas pressure. This raised the injection guard ring by 200 kPa and the back pressure guard ring by 100 kPa. However, at Day 30.99 the pressures in the guard rings started to decay and reduced to the level of the starting pressure for the remainder of the pressure ramp. The reason for this reduction is unknown, but may be associated with water movement within the sample pressurizing the guard rings. The sample was seen to dilate at the same time as the guard ring pressure increased (**Figure 7-6 E**), suggesting that the increase in gas pressure was resulting in water movement and the sample swelling. It is possible that gas was migrating along the injection face into the guard ring and causing the guard ring to drain water into the sample. This would result in swelling and increase the pressure at the injection guard ring. However, the agreement between the prediction of gas pressure from the injection volume and the injection pressure suggests that no volume of gas was being lost to the guard rings and draining guard rings of water would not have resulted in a reduction of pore pressure. Therefore it is uncertain as to what these responses signify. As shown in **Figure 7-6 D**, no outflow from the sample was seen during gas injection ramp 1.

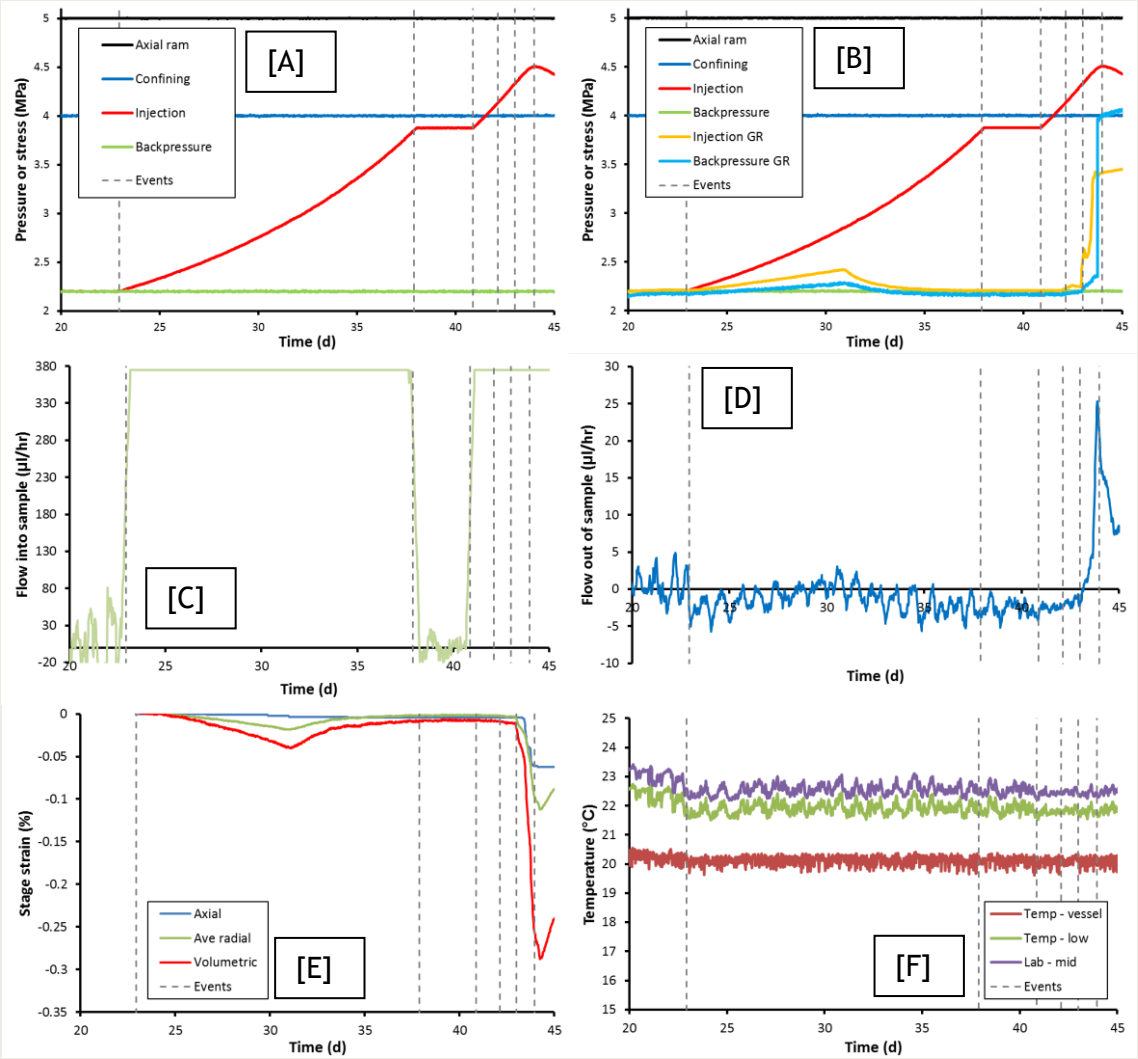

Figure 7-6: Data for gas injection test 1 of test OPERA_SPP-1. [A] Pressure history (boundary conditions). [B] Full pressure history with guard-ring pressures. [C] Flow into sample. [D] Flow out of the sample. [E] Radial and axial displacement. [F] Temperature. Dashed lines represent events of note.

The decision was taken to undergo a second gas pressure ramp until breakthrough occurred. This would require gas injection pressure to exceed the minimum principal stress (confining pressure) and could result in jacket leakage. The second ramp was initiated at Day 40.87 by restarted injection of water into the base of the interface vessel at a rate of 375 µl/h. At Day 42.91, when injection pressure was 4.31 MPa the first signs of gas mobility was noted. At this time the difference between the predicted and observed gas pressures started to diverge and the pressure in the injection-end guard-ring started to increase.

At Day 43 the pressure within the injection-end guard-ring jumped and dilation of the sample mid-plane was noted in two of the three sensors. At this time the injection pressure was 4.33 MPa. Therefore, this strong evidence for gas movement shows that the gas entry pressure was between 4.31 and 4.33 MPa. At this time it was also noted that flow out of the sample started to increase. This reached a peak of 25.3 µl/h when the peak gas pressure was experienced and when the pressure in the back-end guard-ring increased. Gas pressure peaked at 4.51 MPa and started to decay. The sample dilated a total of 0.29 % strain in response to the creation of dilatant pathways. As gas was still being injected, the injection pressure was dropping, the sample was beginning to contract, and the outflow was reducing, it can be inferred that the passage of gas to the back-end of the sample had

resulted in gas leaking from the jacket and into the confining system. Therefore this stage of the test was concluded.

Key observations of stages 3-4 (gas test 1): gas entry did not occur until the minimum principal stress had been exceeded; gas entry was between 4.31 and 4.33 MPa; the transport of gas was accompanied by the dilation of the sample by 0.29 %; gas pressure peaked at 4.51 MPa, at which point gas was able to escape the experimental apparatus.

7.1.3.5 Stage 5: Change of boundary conditions

A second gas entry experiment was performed by changing the boundary conditions of the test. In gas injection test 2 the confining pressure was increased to 4.9 MPa, just less than the 5 MPa axial stress. This aimed to remove the anisotropic stress and aimed to create a near-isotropic stress condition. The confining pressure was set at 0.1 MPa less than the axial stress to ensure that axial stress remained the maximum principal stress.

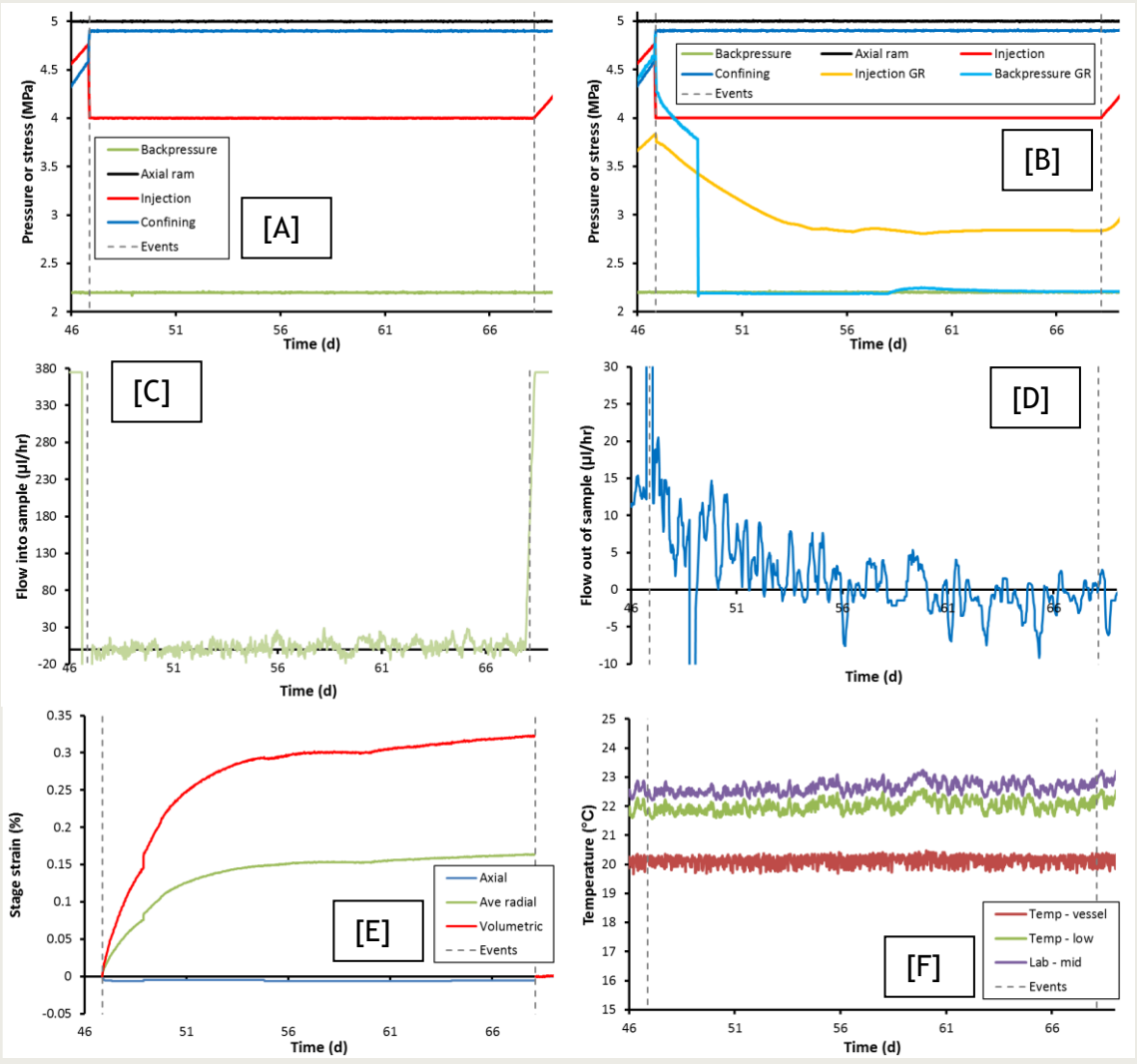

Figure 7-7: Data for stage 5 (change of boundary conditions) of test OPERA_SPP-1. [A] Pressure history (boundary conditions). [B] Full pressure history with guard-ring pressures. [C] Flow into sample. [D] Flow out of the sample. [E] Radial and axial displacement. [F] Temperature. Dashed lines represent events of note.

Figure 7-7 shows the data obtained for the 21 days that the sample was kept at the new boundary conditions to allow equilibration. At Day 46.87 the confining pressure was increased to 4.9 MPa and the injection pressure was reduced to 4 MPa. Initially all parameters were observed. However, it was apparent that the back-end guard-rings would take substantial time to reach an asymptote. Therefore at Day 48.88 the gas was drained from the guard-ring and the pressure lowered to 2.2 MPa. The guard-ring was then isolated.

As shown in **Figure 7-7 B** the pressure in the injection-end guard-ring took approximately 10 days to asymptote in response to the reduced injection gas pressure. Over this period flow out of the sample reduced from an initial 15 µl/h to a condition of no outflow. Throughout this stage the sample contracted by a total of 0.16 % in the radial direction, although no such contraction was seen in the axial strain. This resulted in a total volumetric contraction of 0.32 %.

Key observations of stage 5 (change in boundary condition): the sample took 10 days to settle following the changes in boundary conditions; the sample underwent 0.32 % volumetric contraction as a response to the change in boundary conditions.

7.1.3.6 Stages 6-7: Gas injection test 2

The second gas injection test also resulted in two stages in order to initiate gas flow in the sample. **Figure 7-8** shows the results for the first gas injection pressure ramp. As can be seen in **Figure 7-8 A**, the injection ramp was started at Day 68.13 by injecting water at a rate of 375 µl/h into the base of the gas interface vessel. This created the pressure ramp shown in **Figure 7-8 A**. As shown in **Figure 7-8 B**, the pressure in the injection-end guard-ring also increased, and showed a marked increase at Day 70.33, when the sample also started to dilate (**Figure 7-8 E**). A total of 0.01 % volumetric strain was observed as the gas pressure peaked at 4.77 MPa. This resulted in a reduction in gas pressure, injection-end guard-ring pressure, and contraction of the sample. No outflow was noted at this time (**Figure 7-8 D**) and therefore it can be assumed that gas was leaking from the Hoek-sleeve jacket. At Day 71.49 the pressure stopped decaying and started to rise again and this time reached the pressure limit of 4.8 MPa. Whilst it is evident that fluids (be these water or gas) are mobile in the system, there was no indication of outflow from the sample even when the gas pressure was greatly in excess of that seen in Gas test 1 and when its magnitude was close to that seen in the confining stress. As leakage between the Hoek-sleeve and injection platens had been inferred it was decided to switch to constant pressure and monitor the system.

As shown in **Figure 7-9**, the injection pump remained in constant pressure mode at 4.8 MPa for the rest of gas test 2 (up to Day 184.12). The boundary conditions remained constant until Day 143.09. During this period little of note happened. The back-end guard-ring slowly increased, whilst the injection-end one remained constant. Flow into the sample at the injection end remained low, with little flow at the back-end of the sample. The outflow became noisy about Day 107, although this is likely to be associated with temperature variations. Noise in the back-end flow can signify the expulsion of gas, in this instance this is not inferred.

At Day 143.09 the boundary conditions were altered in order to attempt to initiate gas flow. The back pressure was lowered to 1 MPa, giving an excess gas pressure of 3.9 MPa. It should be noted that lowering of back-pressure did not re-initiate flow in Callovo-Oxfordian claystone (Cuss & Harrington, 2012), although this is a lithified mudrock with a much higher over-consolidation ratio compared with Boom Clay. As can be seen in **Figure 7-9**, the reduction in back pressure resulted in a reduction in guard-ring pressure at the back-end of the sample, whilst in the injection end saw no change. The back-end guard-

ring reduced by 900 kPa in 10 days following back-pressure reduction. This resulted in a contraction on the sample (**Figure 7-9 E**) and an out flow from the sample (**Figure 7-9 D**). A marginal increase in inflow into the sample also occurred. Outflow resulted in 0.08 % sample contraction, and a consistent outflow of about 8 µl/h up until Day 168.26. At this point, the back-end guard-ring pressure started to rise and the outflow from the sample reduced to 3 µl/h. This resulted in further radial contraction and axial dilation.

Although fluid was draining from the sample in response to the change in back-pressure, this can all be explained as drainage of pore fluid. No evidence is apparent that suggests that gas has started to flow in the sample. Therefore an excess of pore pressure of 3.9 MPa is not sufficient to initiate gas flow if the gas pressure is lower than the minimum principal stress component.

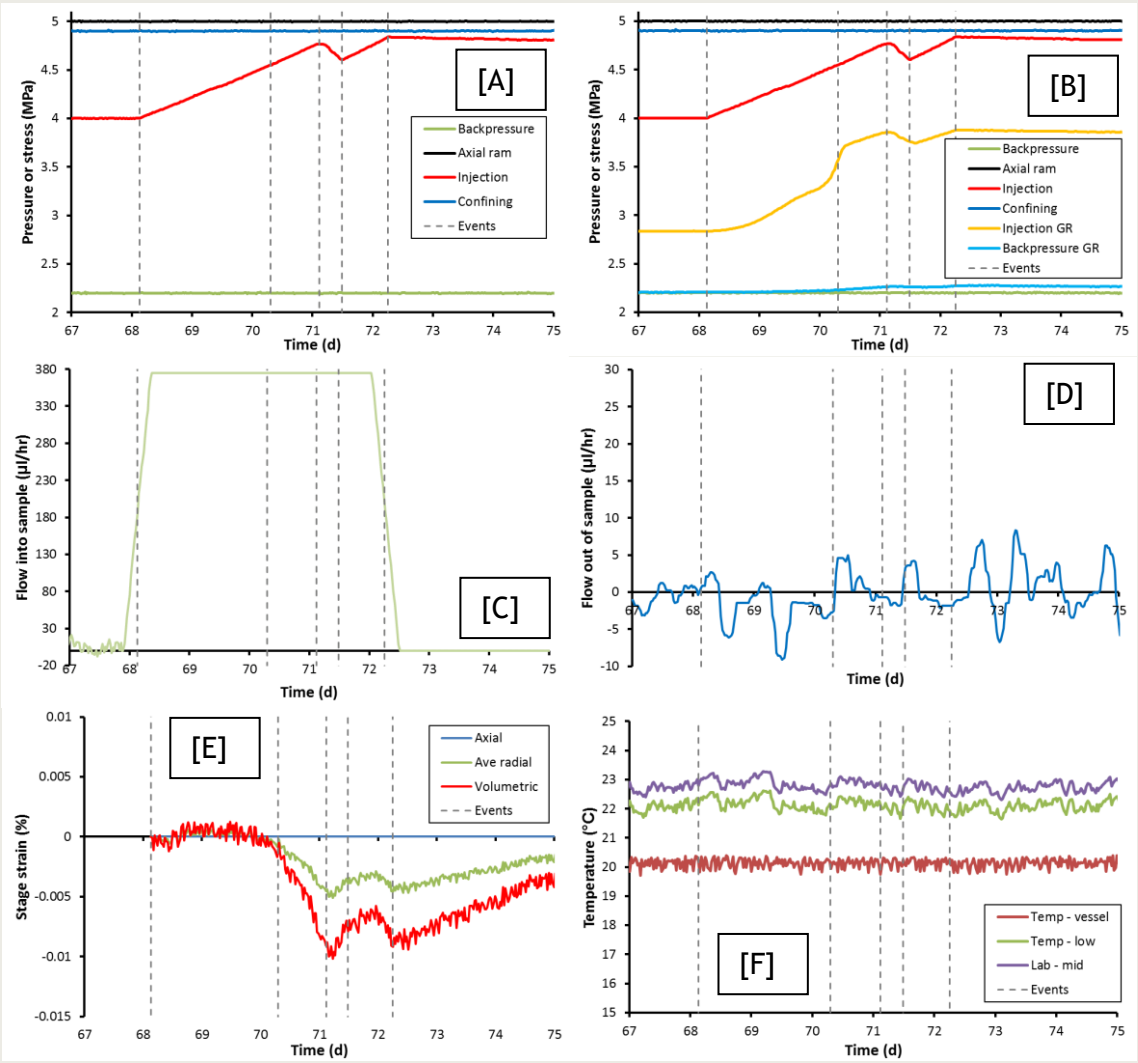

Figure 7-8: Data for Gas test 2, pressure ramp 1 (stage 6) of test OPERA_SPP-1. [A] Pressure history (boundary conditions). [B] Full pressure history with guard-ring pressures. [C] Flow into sample. [D] Flow out of the sample. [E] Radial and axial displacement. [F] Temperature. Dashed lines represent events of note.

Key observations of stages 6-7 (gas test 2): gas entry or breakthrough was not achieved even at an excess gas pressure of 2.6 MPa; possible leakage from the system was occurring resulting in the reduction of gas pressure; an excess gas pressure of 3.9 MPa was not sufficient to initiate gas flow if the gas pressure is lower than the minimum stress component; a reduction in back-pressure resulted in contraction as a result of pore fluid expulsion from the sample; no change in stress was seen at the injection-end guard-ring and therefore the injection point did not observe any changes as a result of back-pressure reduction.

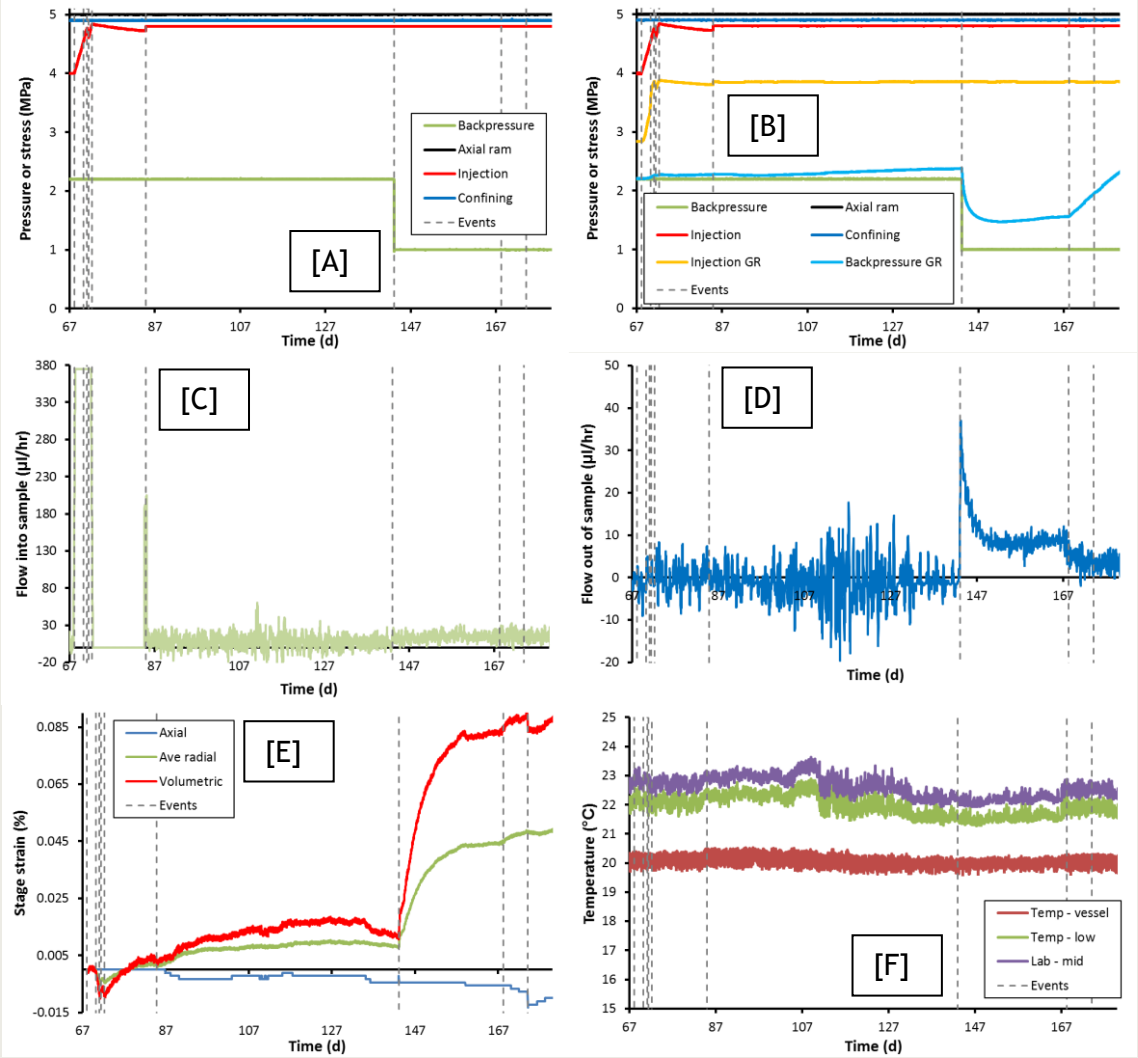

Figure 7-9: Data for Gas test 2 of test OPERA_SPP-1. [A] Pressure history (boundary conditions). [B] Full pressure history with guard-ring pressures. [C] Flow into sample. [D] Flow out of the sample. [E] Radial and axial displacement. [F] Temperature. Dashed lines represent events of note.

7.1.3.7 Stages 8: Gas shut-in

The final stage of test OPERA_SPP-1 was a 44 day-long gas shut in stage, as shown in **Figure 7-10**. At the end of stage 7d at Day 184.12, gas injection was stopped and all boundary conditions were kept static. This resulted in a slow decline of gas injection pressure (**Figure 7-10 A**), which resulted in a slow decline in injection-end guard-ring pressure (**Figure 7-10 B**). Injection pressure decreased by 0.41 MPa from an initial 4.8 to 4.39 MPa. Over the same period the injection-end guard-ring pressure reduced by only 0.25 MPa from 3.85 to 3.6 MPa. In contrast the back-end guard-ring pressure continued to

increase and reached an asymptote of 3.15 MPa, considerably higher than the back-pressure of 1 MPa. It can be seen that the cessation of injection and corresponding reduction in injection pressure had no influence on the rate of increase in pressure in the back-end guard-ring. Therefore the back-end and injection-end are largely independent of one another. Out flow from the sample (**Figure 7-10 D**) continued to decrease and by the end of the shut-in stage was negligible. However, the sample continued to contract and during the stage had contracted by 0.09 % volumetric strain. During the shut-in stage axial strain had also started to contract.

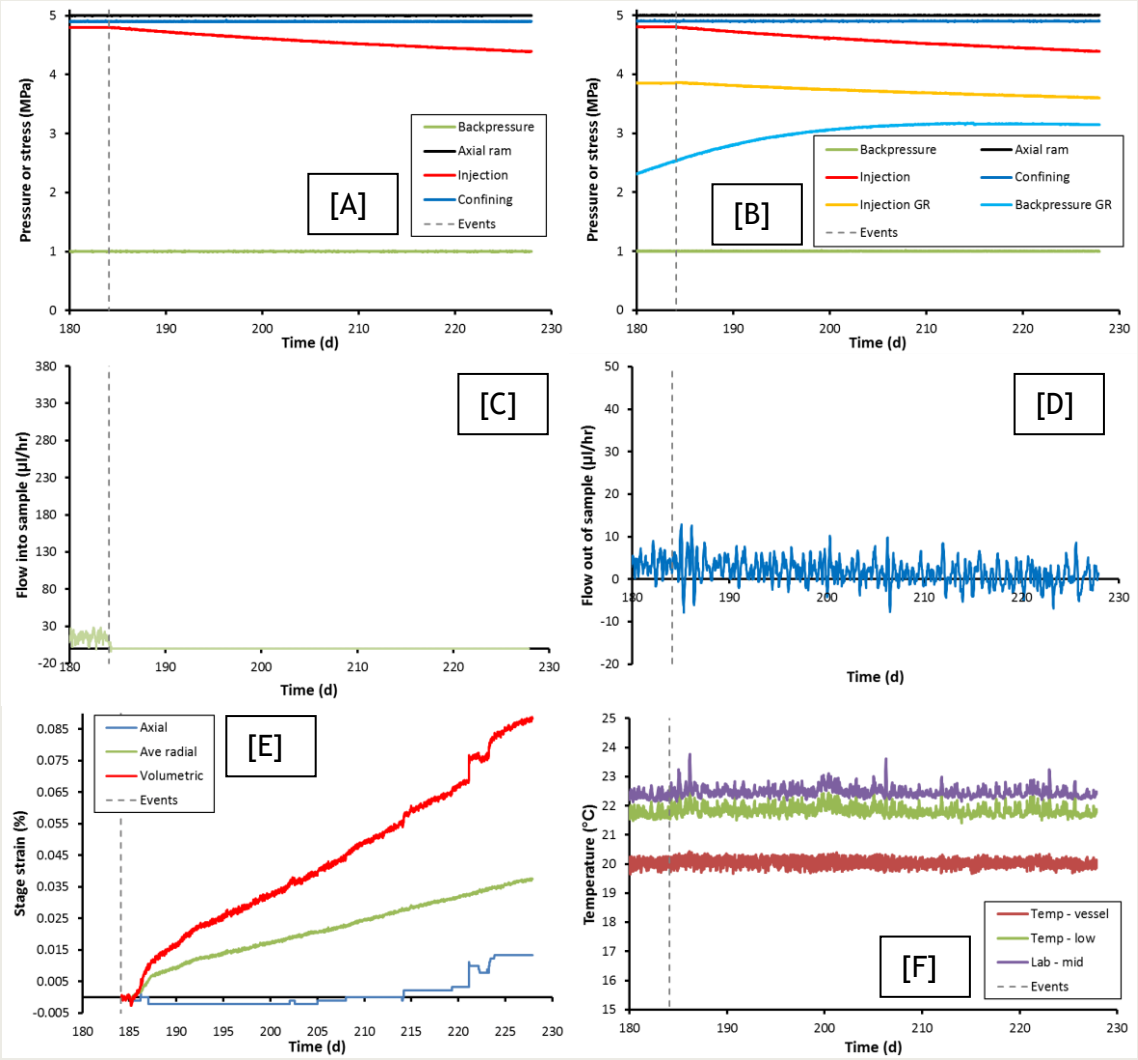

Figure 7-10: Data for the gas shut-in stage (8) of test OPERA_SPP-1. [A] Pressure history (boundary conditions). [B] Full pressure history with guard-ring pressures. [C] Flow into sample [D] Flow out of the sample. [E] Radial and axial displacement. [F] Temperature. Dashed lines represent events of note.

Key observations of stage 8 (gas shut-in): The back-end guard-ring continued to increase in pressure even though the injection pressure was reducing, suggesting that the two ends of the sample are separate from one another; the sample continued to contract; injection pressure, injection-end guard-ring pressure, and flow out of the sample all reduced during shut-in.

7.1.3.8 Observations of the final test sample

At the conclusion of the test, the apparatus was carefully de-pressurised in steps similar to those used at the start of the test. The apparatus was dismantled and the sample was removed in its Hoek-sleeve. **Figure 7-11** shows the sample following removal from the Hoek-sleeve.

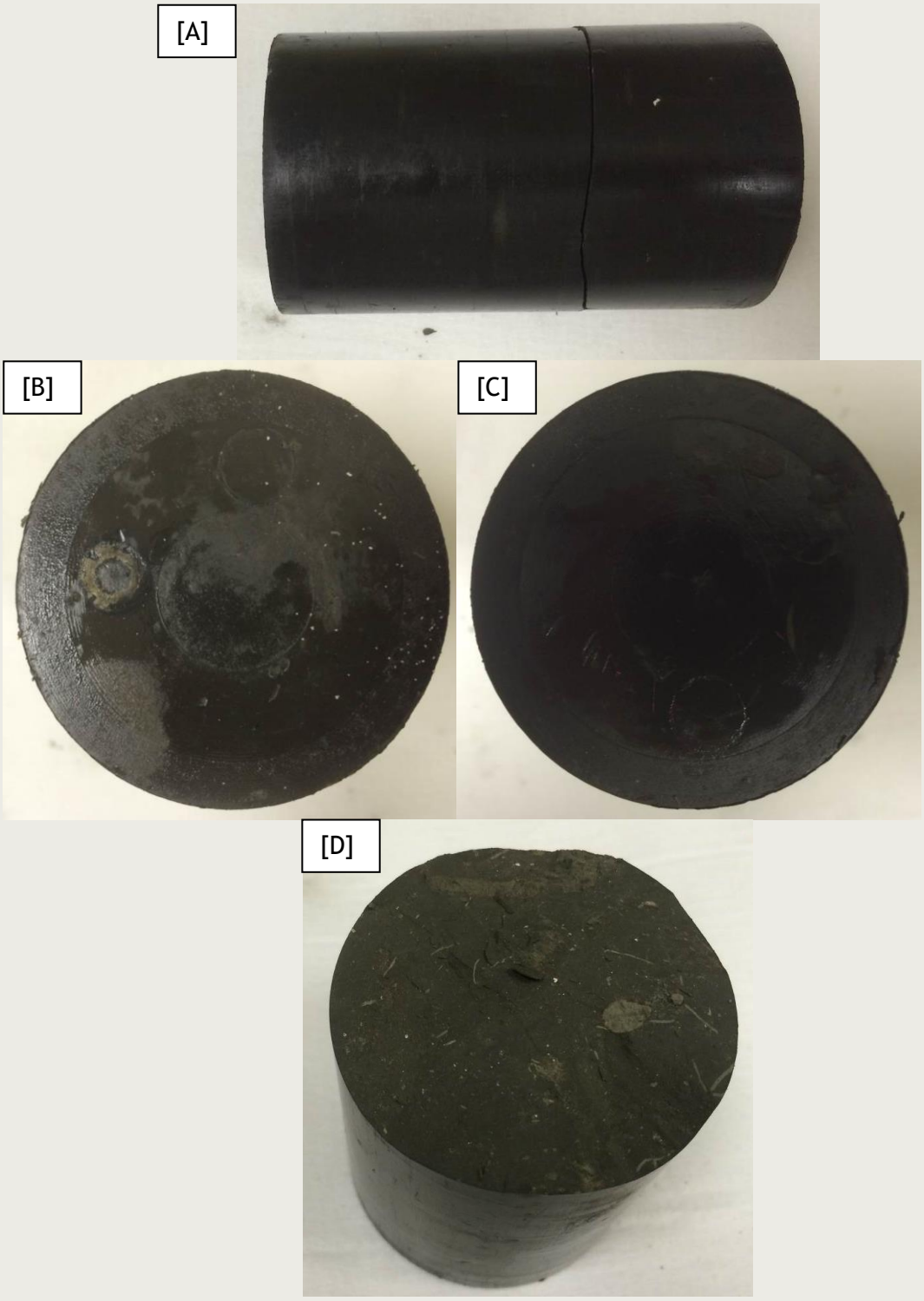

Figure 7-11: Observations of the final test sample. [A] Length of the test sample showing a fracture parallel with the sample ends. [B] Back-end of the sample. [C] Injection end of the sample. [D] Surface of the fracture.

The most prominent feature of note in **Figure 7-11 A** is the fracture seen that is parallel with the ends of the sample. It is believed that this formed either during depressurisation or on sample recovery. It is not thought that this feature was formed by the transport of gas through the sample. The surface of the fracture (**Figure 7-11 D**) appeared fresh and could possibly be the result of expanding gas within the sample. The ends of the sample (**Figure 7-11 B** and **C**) show indentations of the injection and guard-ring filters along with the load cell. Small cracks were apparent, but the timing of their formation is uncertain.

The sample was measured and was found to have a reduced average radius of 28 μm and an increased length of 88 μm, although it has to be noted that this measurement includes the radial crack. Unexpected was a change of mass. The sample lost 20 g in weight, a total of 4 % reduction. Whilst it was noted that mass was loss on sample recovery, it is unlikely that such a large amount had been lost.

Key observations of the test sample: a radial fracture was seen, although this was possibly formed during depressurisation or sample extraction; the sample saw negligible dimension change; sample lost 4 % weight during the test.

7.1.3.9 Summary of key observations of test OPERA_SPP-1

Test OPERA_SPP-1 was an 8 stage test that lasted a total of 277.89 days. During rehydration the sample underwent 0.4 % dilatant strain that equilibrated within 5 to 7 days. During this period a total of 2.17 ml of water was injected. The 2-stage hydraulic head test gave an average permeability of 4.83×10^{-19} m^2. The high pressure step resulted in 0.125 % dilatant strain and elevated guard-ring pressures. At the end of the hydraulic test some permanent dilatant strain of the sample was seen. The hydraulic phase of testing showed that the sample displayed anisotropic strains.

During gas test 1 gas entry did not occur until the minimum principal stress (confining pressure) was exceeded, giving a gas entry pressure of about 4.3 MPa. The movement of gas within the sample resulted in 0.29 % dilatant deformation. Gas pressure peaked at 4.51 MPa and may have resulted in jacket leakage. Gas pressure was lowered and the confining pressure was increased to be close to the axial stress. This resulted in 0.32 % consolidation of the sample. During gas test 2 it was not possible to reach gas entry as the gas pressure was held at a magnitude just below the minimum principal stress. The lowering of back pressure resulted in an excess gas pressure of 3.9 MPa. This was still insufficient to initiate gas entry. The sample underwent contraction as a result of the boundary condition change and the sample drained. During gas shut-in, the back-end continued to increase in pressure even though the injection pressure was reducing, suggesting that the two ends of the sample were not in full communication of one another. A radial fracture was seen in the final test sample, although this is believed to have formed during depressurisation of the sample at the end of the test. The sample saw little change in volume during the test, but did see a 4 % loss of weight, suggesting sample desaturation.

7.1.4 Test OPERA_SPP-2

The aim of test OPERA_SPP-2 was to determine the hydraulic and gas transport properties of the Boom Clay at stresses representative of the in situ stresses that the cores were taken from, i.e. the stress state at the Mol URL in Belgium. The sample was then consolidated in the apparatus to a stress representative of the Netherlands and a repeat gas injection test was conducted. This test would allow direct comparison between the Netherlands and Belgium disposal concepts. Test OPERA_SPP-2 aimed to perform a four-stage test. In the first stage, a two-step hydraulic head test was performed. In the second, a gas-ramp injection test was performed up to a condition where gas flow would be

initiated. The fourth stage consolidated the Boom Clay from a stress state representative of the Mol URL to a stress state representative of the Netherlands. The final stage performed a gas-ramp injection test up to a condition where gas flow would be initiated. The following sections outline the experimental results in detail.

7.1.4.1 Complete test history

Test OPERA_SPP-2 lasted a total of 322 days, with **Figure 7-12** showing the test result data for the complete test history and **Table 7-3** summarising the individual test stages.

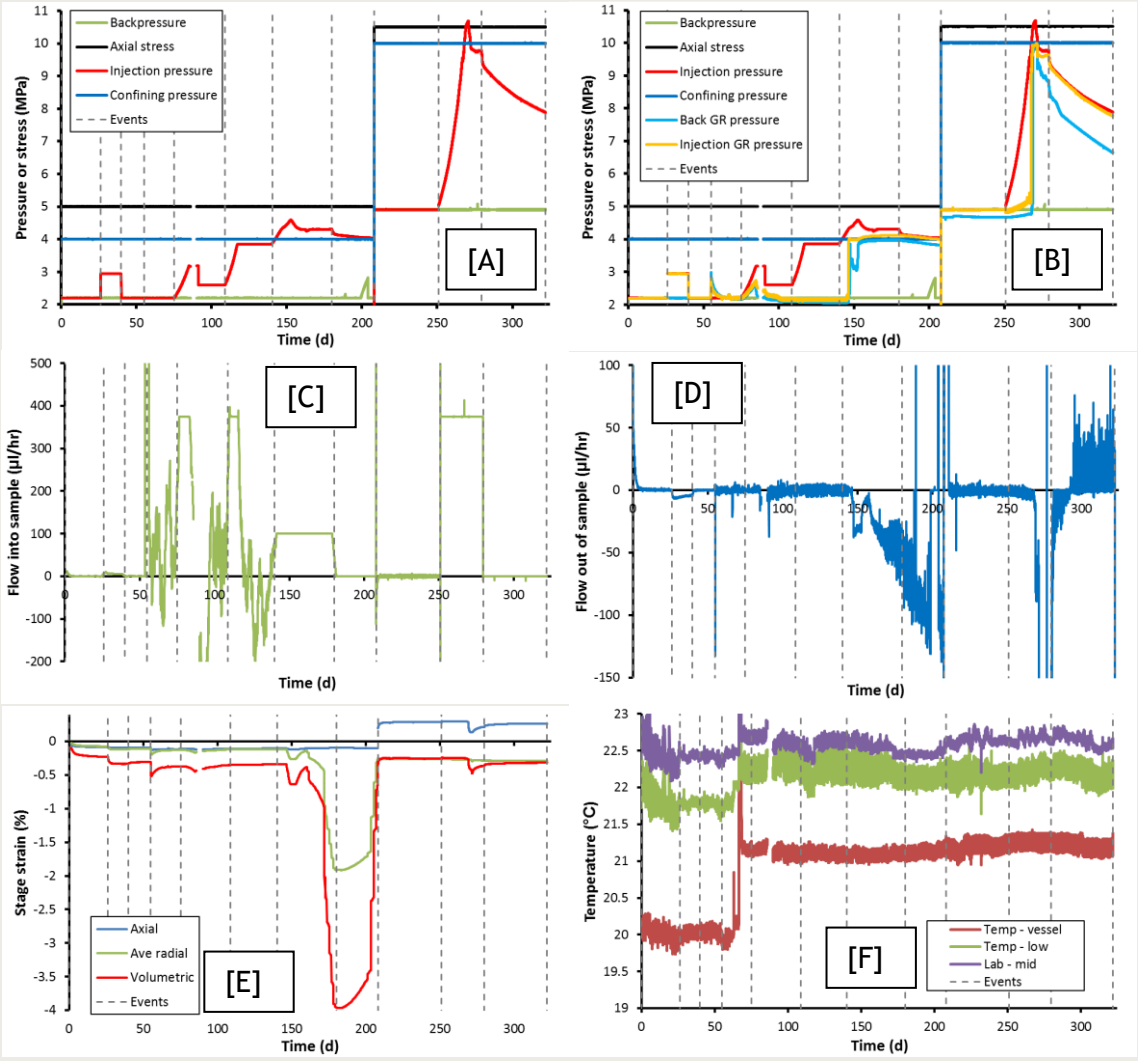

Figure 7-12: Data for the complete test history of test OPERA_SPP-2. [A] Pressure history (boundary conditions). [B] Full pressure history with guard-ring pressures. [C] Flow into sample. [D] Flow out of the sample. [E] Radial and axial displacement. [F] Temperature. Dashed lines represent events of note.

Stage	Time		Event	Stage length
1	0.00	Hydraulic	Start of the test and set-up of boundary conditions Confining = 4 MPa, Axial = 5 MPa, Pore pressure = 2.2 MPa	26.12
2a	26.12		Hydraulic test 1: Increase injection pressure to 3 MPa	48.97
2b	39.86		Hydraulic test 2: Reduce injection pressure to 2.2 MPa	
2c	54.91		Accidental pressurisation of guard-rings during gas filling	
2d	66.37		Start of gas pressure rise in guard rings	
3a	75.09	Gas test 1	Gas injection 1: Start of gas injection ramp 1	15.92
3b	84.85		Gas injection 1: End of gas injection ramp 1	
3c	91.01		Lowering of gas pressure following failure of logging system	17.79
3d	108.80		Gas injection 2: Start of gas injection ramp 1	31.44
3e	117.20		Gas injection 2: End of gas injection ramp 1	
3f	140.24		Gas injection 2: Start of gas injection ramp 2	47.97
3g	146.80		Gas injection 2: Start of increase in pressure in guard-rings	
3h	152.80		Gas injection 2: Gas peak pressure and Increase in BGR	
3i	160.00		Gas injection 2: Dilation strain of sample	
3j	161.50		Gas injection 2: Second dilation strain of sample	
3k	180.00		Gas injection 2: End of gas injection	
3l	188.21		Gas injection 2: Back-pressure pump full, increased BP	19.85
3m	189.10		Gas injection 2: Back-pressure pump emptied, re-started	
3n	199.18		Gas injection 2: Back-pressure pump full, increased BP	
3o	204.13		Gas injection 2: Back-pressure pump emptied, re-started	
4a	208.06	Consol	Consolidation phase; Confining = 10 MPa, Axial = 10.5 MPa, Pore pressure = 4.9 MPa	42.89
4b	211.06		Leak in back-pressure system fixed	
4c	250.00		End of consolidation stage	
5a	250.95	Gas test 2	Gas injection 3: Start of gas injection ramp	71.13
5b	254.16		Gas injection 3: Start of sample dilation	
5c	267.05		Gas injection 3: Lowering of injection pressure, lowering of guard-ring pressure and axial dilation of the sample	
5d	268.08		Gas injection 3: Axial dilation of sample, increase of injection and GR, start of outflow	
5e	269.01		Gas injection 3: Increase in outflow from sample, increase in back GR	
5f	270.77		Gas injection 3: Increase in radial dilation dilation and peak gas pressure	
5g	271.65		Gas injection 3: Maximum radial strain	
5h	272.06		Gas injection 3: Drop in guard-ring pressures and injection pressure, maximum outflow	
5i	272.85		Gas injection 3: Resumption of steady outflow from sample	
5j	276.69		Gas injection 3: Back-pressure pump full	
5k	276.84		Gas injection 3: Back-pressure pump emptied	
5l	279.62		Relaxation: Gas injection stopped	
5m	322.08		Relaxation: End of relaxation stage	
	322.08		End of test	

Table 7-3: Summary of experimental history of test OPERA_SPP-2 showing stage number, description of stage/event, and boundary conditions.

The five stages of the test can be seen in **Figure 7-12** (initial swelling stage and equilibration at *in situ* conditions, hydraulic testing, gas injection testing, consolidation to

stress state representative of the Netherlands, gas injection testing). Results for each section are introduced in the following sections.

7.1.4.2 Stage 1: Swelling and equilibration

The sample was loaded into the SPP and as with test OPERA_SPP-1 the boundary conditions were setup on the apparatus; confining pressure of 4 MPa, axial stress of 5 MPa, and pore pressure of 2.2 MPa. These conditions were set to be representative of the stress conditions of the sample when cored at the Mol URL. The boundary conditions were imposed carefully with a series of approximately 10 step changes up to the starting condition. Care was taken so as not to impose an excessive axial load on the sample and for each increase in stepped stress to be minimal. At all times, axial stress was greater than confining pressure so as not to put the sample into extension. The initial stage lasted approximately 1 hour. Following the establishment of appropriate boundary conditions, the sample was monitored for swelling and equilibration. This lasted approximately 26 days, as shown in **Figure 7-13.**

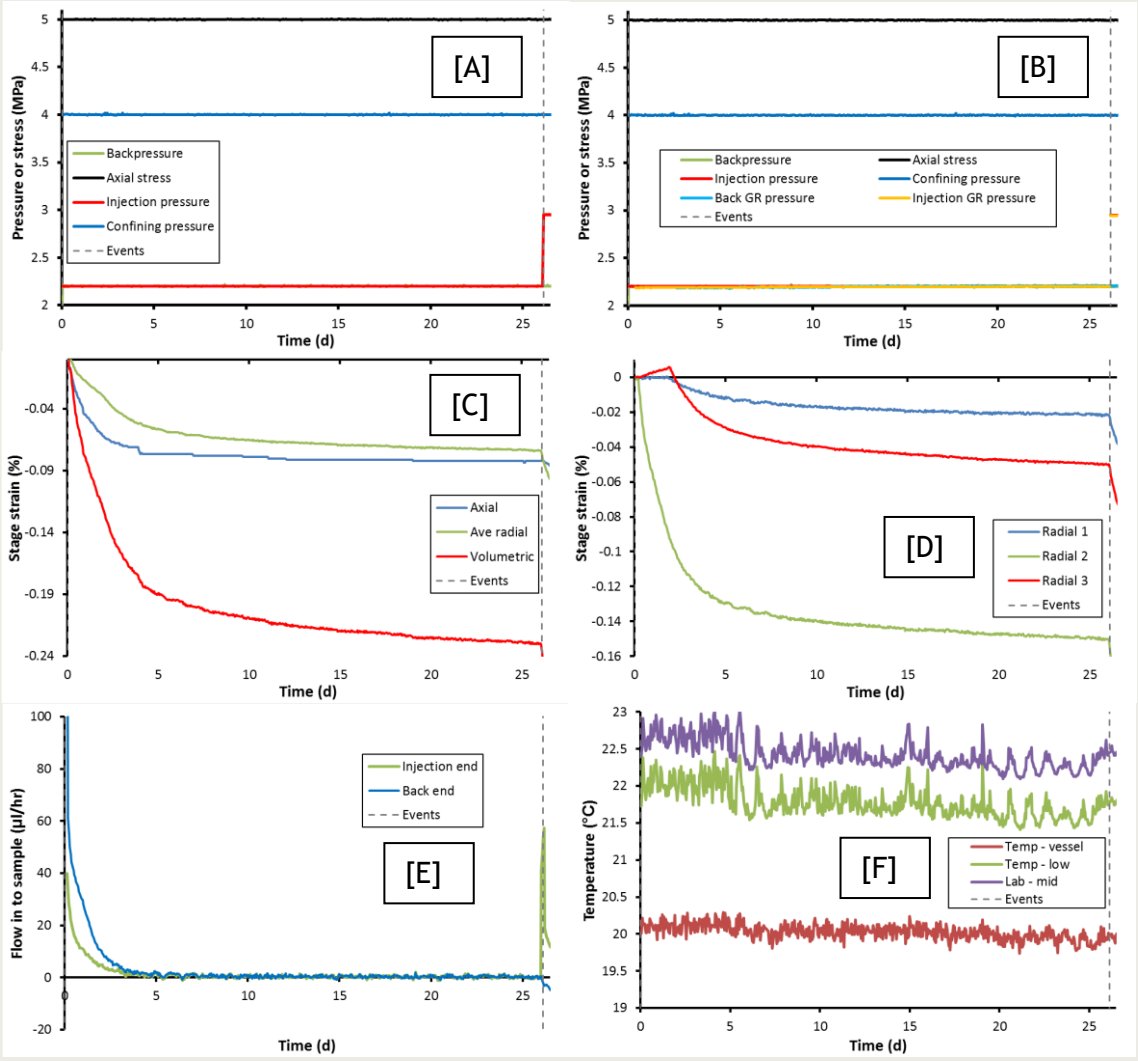

Figure 7-13: Data for the swelling and equilibration stage (1) of test OPERA_SPP-2. [A] Pressure history (boundary conditions). [B] Full pressure history with guard-ring pressures. [C] Radial, axial and volumetric displacement. [D] Three radial displacement sensors. [E] Flow into sample. [F] Temperature.

Figure 7-13 shows the results for the 26 day long stage. As can be seen in **Figure 7-13 D**, the sample initially showed complex behaviour. One of the radial strain sensors showed dilation, one initially showed no deformation, whilst the third showed contraction. This suggests that the sample had either been prepared without perfectly parallel faces or that the sample was not perfectly centred within the apparatus. Within three days all radial sensors showed dilation, although considerable anisotropy was observed. Radial 2 showed a total of 0.15 % dilation, whilst Radial 1 only recorded 0.03 % dilatant strain. This gave an average radial displacement of 0.07 % dilation, which was approximately half of the strain seen in test OPERA_SPP-1. Axial strain totalled 0.08 %, which is almost double that seen in OPERA_SPP-1. An overall volumetric strain of 0.23 % was observed, compared with 0.4 % in test OPERA_SPP-1. The flow into both ends of the sample showed a similar response, with an initial flow rate of 100 µl/h, which decayed to a negligible flow after five days. A total of 3.38 ml of water had been taken up by the sample during the resaturation stage. It should be noted that water uptake was nearly a factor of two greater at the back-end of the sample. No significant change in pore pressure was noted in the guard-rings (**Figure 7-13 B**). As strain and flow had reach asymptote by day 26 it was determined that the sample had resaturated sufficiently and that the hydraulic test could be conducted (stage 2). It can be seen that comparable results were noted for both sample OPERA_SPP-1 and OPERA_SPP-2.

Key observations of stage 1 (swelling and equilibration): a total of 0.23 % dilatant strain was measured; considerable anisotropy observed between the three radial strain measurements; flow and strain equilibrated in approximately 5-7 days; a total of 3.38 ml of water was taken up; the back-end of the sample had twice the uptake of water compared with the injection-end.

7.1.4.3 Stage 2: Hydraulic two-stage constant head test

Following the swelling stage a two-stage constant head test was conducted, as shown in **Figure 7-14**. At the start of this test stage (2a) the injection pore-pressure was raised to 3 MPa with the guard-rings open (**Figure 7-14 A**). This meant that the guard-ring pore pressure mimicked the injection and back pressure (**Figure 7-14 B**). As a result of the increased pressure, the sample underwent 0.1 % dilatant strain (**Figure 7-14 C**), comparable with test OPERA_SPP-1. Throughout the high-pressure stage, radial strain was a factor of nearly four greater than axial strain (**Figure 7-14 E**). A total of 0.1 % dilatant strain was caused by the raising of pore pressure at the injection end. Anisotropy was seen in the three radial strain readings (**Figure 7-14 F**), although two sensors (Radial 2 and 3) had almost identical responses. Initially the elevated pore pressure resulted in an increased flow into the sample of about 50 µl/h at the injection end (**Figure 7-14 C**), which over the course of 2 – 3 days reduced to approximately 7 µl/h (**Figure 7-14 D**). Over this same period, flow out of the sample increased and near matched inflow. Both inflow and outflow continued to evolve and reduce for the remainder of the high pressure-step and reduced to 5 µl/h. This gives a permeability into the sample of 1.73×10^{-19} m^2, out of the sample of 1.57×10^{-19} m^2, giving an average permeability of 1.65×10^{-19} m^2, less than that seen in test OPERA_SPP-1 (4.83×10^{-19} m^2).

Stage 2b of the two-step constant head test returned the injection pore pressure to 2.2 MPa (**Figure 7-14 A**). As the guard-rings were open, these mimicked injection and back-pressure (**Figure 7-14 B**). The reduction in pore pressure resulted in only partial recovery of strain (**Figure 7-14 F**). As can be seen, the radial strain recovered 31 % of the strain created by the raised pore pressure. This compares well with 30 % for volumetric strain, whilst axial strain recovered approximately 20 % of the strain. However, the full picture may be more complicated, as shown in (**Figure 7-14 F**). Radial 1 recovered the greatest strain (65 %), Radial 3 recovered 37 %, whilst Radial 2 only recovered 5 % and appears to be

influenced little by the reduction in pore pressure. Therefore there is considerable anisotropy not only in the total strain, but the degree of strain recovery on depressurisation. Flow into and out of the sample quickly equilibrated on the reduction of pressure and within one day both showed nominal flow (**Figure 7-14 C** and **D**). Flow data in test OPERA_SPP-2 correspond with inflow equal to outflow. This is dissimilar to test OPERA_SPP-1, which showed a greater flow into the sample than outflow.

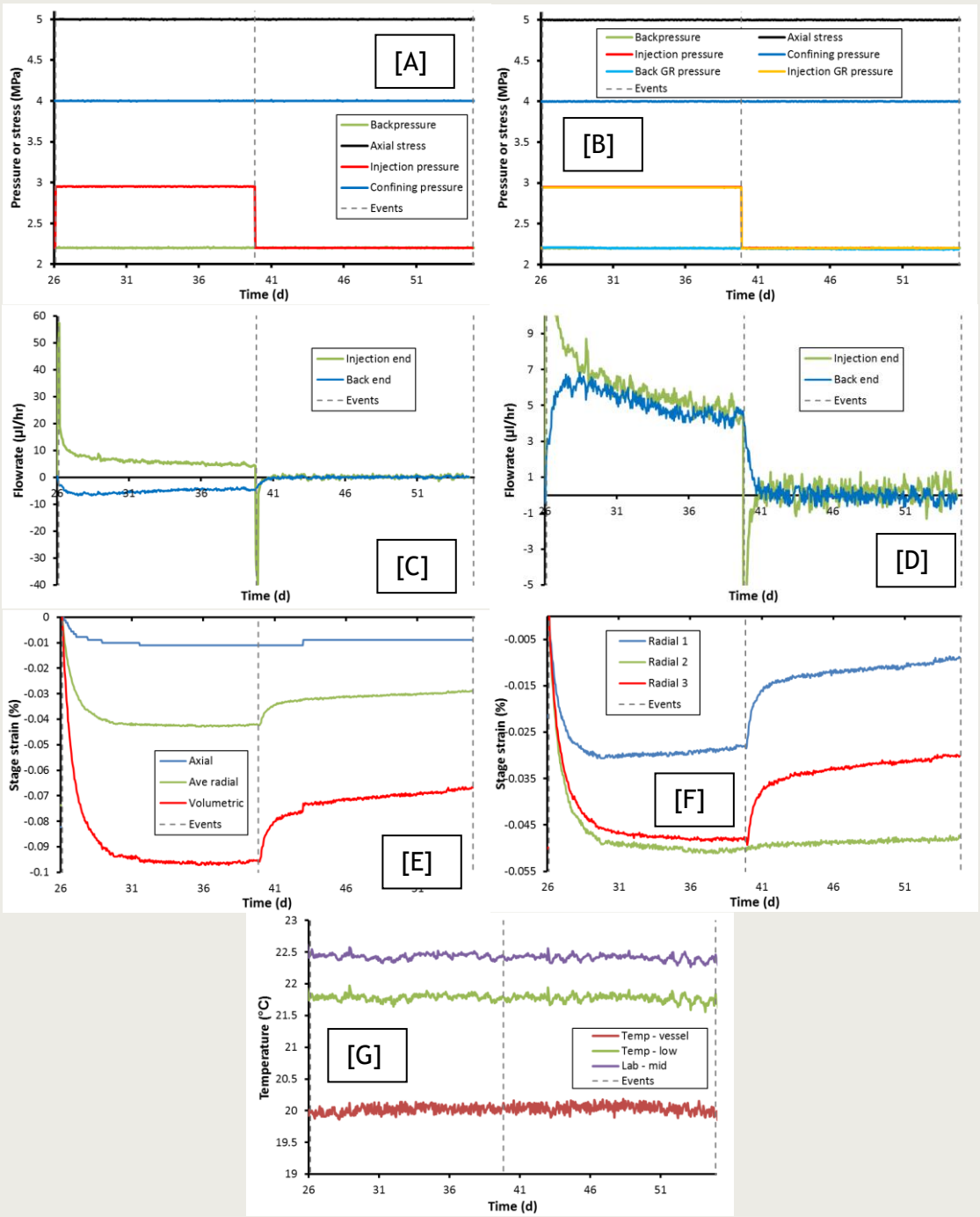

Figure 7-14: Data for the two-stage constant head test (stage 2) of test OPERA_SPP-1. [A] Pressure history (boundary conditions). [B] Full pressure history with guard-ring pressures. [C] Flow into and out of sample. [D] Detail of flow. [E] Radial, axial and volumetric displacement for the stage. [F] Three radial strain measurements. [G] Temperature.

Key observations of stage 2 (hydraulic test): the high pressure step resulted in 0.1 % dilatant strain; flow equilibrated within 2 – 3 days to give average permeability of 1.65 × 10-19 m2; inflow matched outflow with both evolving during the high-pressure stage; the 2-stage head test resulted in some permanent (dilatant) strain of the sample; anisotropy was seen not only in strain, but in the amount of strain recovery during depressurisation.

7.1.4.4 Stage 3a-3c: Gas ramp 1 of Gas test 1

Figure 7-15 shows the results for gas injection ramp 1 (stages 3a-3c, **Table 7-3**). The injection interface vessel was filled with approximately 280 ml of helium at a pressure of 2.2 MPa. This had been held for a prolonged period before the start of gas injection to ensure the water within the interface vessel was at full saturation with the helium. Gas injection was started at Day 75.09 by injecting water into the base of the interface vessel at a rate of 375 µl/h. This rate was deemed sufficient to raise the gas pressure sufficiently to initiate gas entry and breakthrough within approximately 15 days.

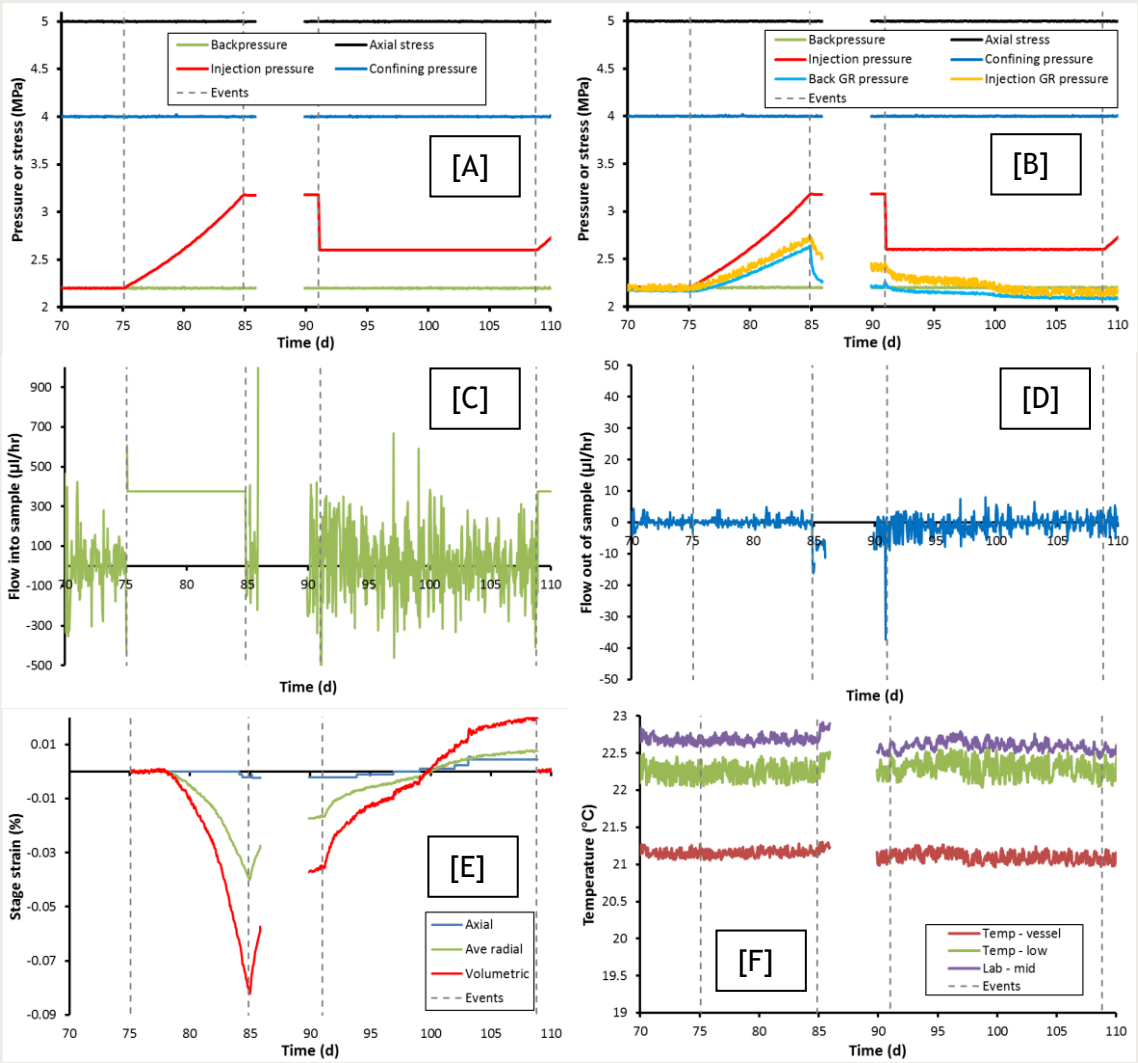

Figure 7-15: Data for the gas injection ramp 1 of test OPERA_SPP-2. [A] Pressure history (boundary conditions). [B] Full pressure history with guard-ring pressures. [C] Flow into sample. [D] Flow out of the sample. [E] Radial, axial and volumetric strain. [F] Temperature. Dashed lines represent events of note.

Figure 7-15 A shows the pressure ramp created during gas injection ramp 1. Pressure increased up to 3.175 MPa. The logging PC within the laboratory required maintenance and the decision was taken to switch the test to constant pressure as there was a high risk of gas entry during a period of the PC being offline. During the pressure ramp both the injection-end and back-end guard-rings showed a pressure increase (**Figure 7-15 B**). This was unusual and both quickly decayed once injection was halted. This potentially was caused by gas in the guard-rings. As shown in **Table 7-3**, at Day 54.91 the guard-rings were accidentally pressurised during filling of the gas interface vessel. Therefore the pressure response of the guard-rings is caused by this gas. During the pressure ramp a total of 0.08 % dilatant strain was observed (**Figure 7-15 E**). This quickly decayed once the test was switched to constant pressure. No flow out of the sample was evident (**Figure 7-15 D**), however, comparing the predicted gas pressure with observed pressure suggests that gas was mobile around Day 80.

During the routine maintenance, the laboratory PC was replaced, as shown by the break in data. A thorough evaluation of the data suggested that the gas within the guard-rings was problematic and there was communication between the injection port and guard-rings. Therefore the decision was taken to abandon the injection ramp. The injection pressure was lowered to 2.2 MPa at Day 91.01 and the system was monitored. Both guard-ring pressures decayed over the following 15 days (**Figure 7-15 B**) and the sample continued to contract (**Figure 7-15 E**). Just prior to starting gas injection ramp 2 at Day 108.8, the guard-rings were carefully bled of gas, still maintaining pressures of 2.2 MPa. This confirmed the presence of gas, which was fully flushed from the guard-rings.

Key observations of stage 3a-c (gas injection): test stage abandoned as gas had accidentally been filled in the guard-rings prior to the stage, this was influencing the test.

7.1.4.5 Stage 3d-3e Gas injection test 1

Figure 7-16 shows the results for gas injection test 1. The test started at 2.6 MPa by injecting water into the base of the interface vessel at a rate of 375 µl/h. This created a gas pressure ramp as shown in **Figure 7-16 A**. The gas pressure was raised to 3.9 MPa, 0.1 MPa below the confining pressure, and the test was switched to constant pressure mode to maintain pressure and monitor flow. No variation was seen in guard-ring pressure (**Figure 7-16 B**), flow into the sample (**Figure 7-16 C**), flow from the sample (**Figure 7-16 D**), or sample strain (**Figure 7-16 E**). Therefore it was concluded that gas entry had not occurred during the pressure ramp, nor during the constant pressure step. Therefore at Day 140.24 it was decided to perform a second gas ramp and to continue until breakthrough occurred.

As seen in **Figure 7-16 A** the second pressure ramp soon exceeded the minimum principal stress (confining pressure) and continued to increase. At approximately Day 146 significant changes occurred when the gas pressure was 4.3 MPa. The pressure in the guard-rings started to increase (**Figure 7-16 B**). At first a small perturbation of the injection-end guard-ring was noted. This was followed at Day 146.5 by a large increase in pressure, signifying that gas had reached the guard-ring. A hydrodynamic response was noted at the back-end guard-ring. The migration of gas to the injection-end guard-ring resulted in this filter filling with gas, which expelled water into the sample. This caused the sample to dilate (**Figure 7-16 E**). This characteristic "slug flow" is an artefact of the experimental geometry. At the time of the pressure increase in the guard-ring, a change in slope of the gas injection pressure can be seen and this is characteristic of gas flowing in the sample. Pressure in the guard-ring increased to match confining pressure, which might suggests that the Hoek-sleeve arrangement was leaking gas into the confining system. However, at Day 146.8 outflow from the sample (**Figure 7-16 D**) started and soon after (Day 147.4) the

pressure at the back-end guard-ring (**Figure 7-16 B**) increased to nearly equal the confining pressure. This pressure increase soon decayed.

The "clean" response of the outflow from the sample (**Figure 7-16 D**) suggests that water was being expelled at a constant rate, but this was potentially in response to gas movement in the sample. At Day 152.8 the gas pressure peaked at 4.59 MPa (**Figure 7-16 A**), this was accompanied by an increase in pressure at the back-end guard-ring (**Figure 7-16 B**) and a marked decay of outflow from the sample (**Figure 7-16 D**). This was followed by a decaying gas pressure (**Figure 7-16 A**) and contraction of the sample (**Figure 7-16 E**). However, around Day 157 outflow from the sample (**Figure 7-16 D**) started to increase and this time showed the characteristic "noise" that gas outflow displays. This was accompanied by the onset of dilational strain of the sample, suggesting that dilatant pathways were forming in the Boom Clay and these were transporting gas through the rock. The sample showed a total strain of 1.4 % (**Figure 7-16 E**). However, the lack of axial strain may suggest that this is an over-estimate and that a degree of side-wall flow was occurring.

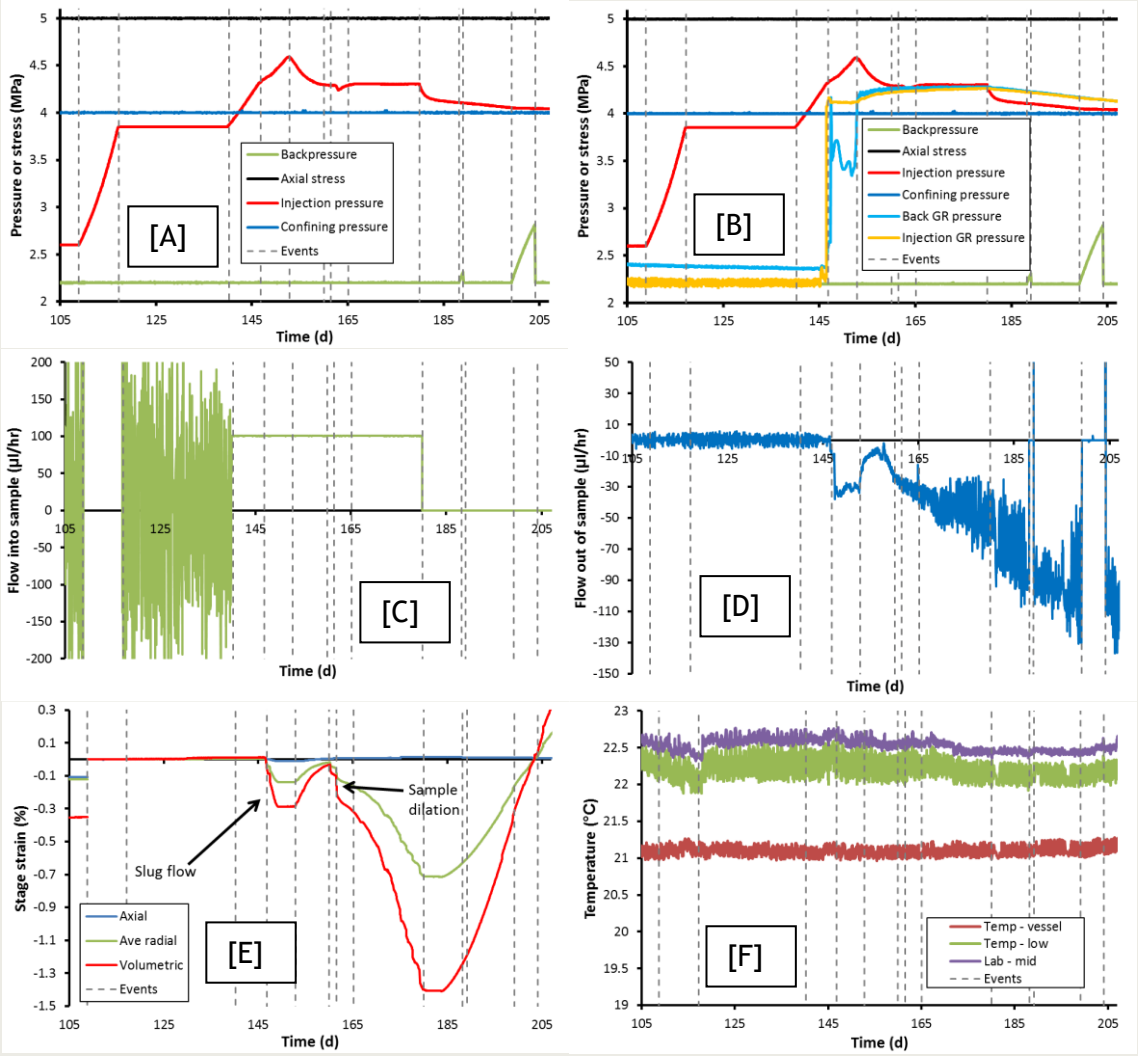

Figure 7-16: Data for the gas test 1 of test OPERA_SPP-2. [A] Pressure history (boundary conditions). [B] Full pressure history with guard-ring pressures. [C] Flow into sample. [D] Flow out of the sample. [E] Radial, axial and volumetric displacement. [F] Temperature. Dashed lines represent events of note.

Gas injection was stopped at Day 180.0, resulting in a reduction in injection pressure (**Figure 7-16 A**) for the remaining 24 days of the stage. Injection pressure reached an asymptote at a pressure close to the confining pressure, suggesting that leakage of the system was occurring. However, outflow from the sample (**Figure 7-16 D**) continued to increase, demonstrating that gas transport was still active within the sample. The cessation of gas injection resulted in a stabilised sample volume (**Figure 7-16 E**), although after a few days a long term contraction of the sample started, resulting in a final sample size smaller than at the start of the gas pressurisation (positive strain seen in **Figure 7-16 E**). It should be noted that the small volume of the backpressure pump resulted in the pump becoming full. This resulted in increased backpressure until the pump was emptied.

Key observations of stage 3 (gas injection): gas entry did not occur until the minimum principal stress had been exceed; gas entry pressure was approximately 4.3 MPa; transport of gas was accompanied by the dilation of the sample by 1.4 %, although this may include side-wall expansion of the jacket; gas pressure peaked at 4.59 MPa, at which point gas was able to reach break-through.

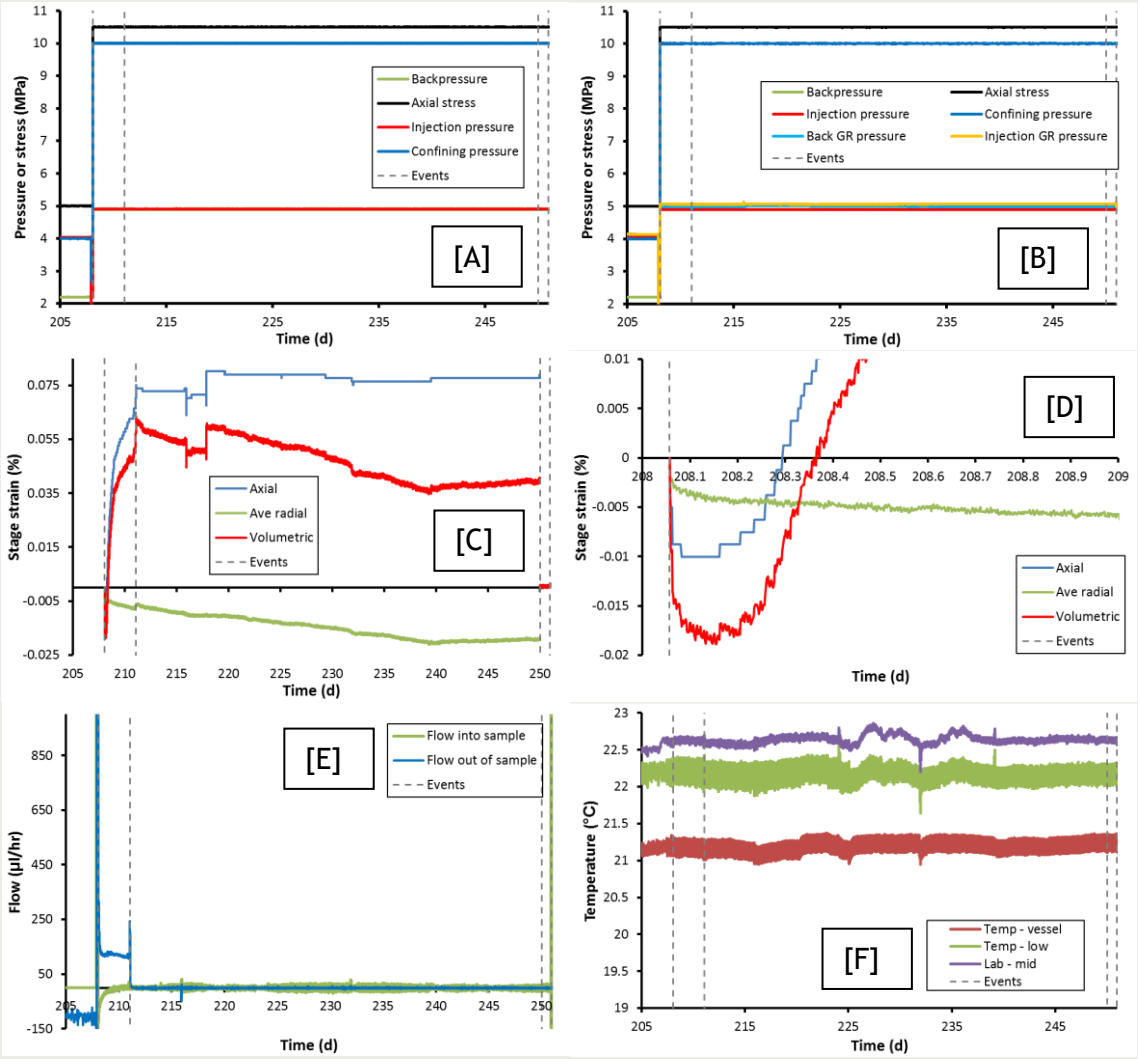

Figure 7-17: Data for the consolidation stage (4) of test OPERA_SPP-2. [A] Pressure history (boundary conditions). [B] Full pressure history with guard-ring pressures. [C] Radial, axial and volumetric strain. [D] Detail of initial strain. [E] Flow into and out of the sample. [F] Temperature. Dashed lines represent events of note.

7.1.4.6 Stage 4: Consolidation of the sample

At Day 208.06 the boundary conditions of the test were carefully altered to raise the stress-state of the sample to a condition representative of the Netherlands disposal concept, as shown in **Figure 7-17**. Axial stress was raised to 10.5 MPa, confining pressure to 10 MPa, and pore pressure to 4.9 MPa. This was done over a series of small steps for a total of one hour to reduce the likelihood of damaging the test sample. Once the test conditions were set the sample was monitored to observe the response of the sample to a raised stress condition. The consolidation step lasted a total of 42.89 days.

As the stress was increased the sample initially underwent dilatant strain (**Figure 7-17 D**), as seen in both axial and radial strains. However, axial strain quickly became contractive. Two competing processes were occurring. The raised pore pressure was causing swelling and sample dilation, whilst the increased stress on the sample was causing contraction and consolidation. These competing processes resulted in 0.08 % axial strain (contraction). In contrast, the radial strain continued to dilate, with a total of 0.02 %. Therefore in the radial direction the swelling of the sample in response to a raised pore pressure was stronger than the consolidation in response to a raised stress. Flow out of the sample suffered from leakage as the pore pressure was raised. Once this was remedied (Day 211.06) flow quickly reduced to near zero. Within two days of starting the consolidation stage the flow into the sample also reduced to near zero. Therefore the contraction in the axial direction and expansion in the radial direction was not accompanied by a measurable out flow from the sample. By Day 250 it was decided that consolidation had been completed and a second gas injection test could be undertaken.

Key observations of stage 4 (consolidation): two competing processes occurred on the changing of boundary conditions, the raising of pore pressure promoted swelling and dilation, whilst the increase in stress promoted contraction and consolidation; the axial direction resulted in 0.08 % contraction; the radial direction resulted in 0.02 % dilation; little flow into or out of the sample was detected; the contraction in the axial direction and expansion in the radial direction was not accompanied by a measurable out flow from the sample

7.1.4.7 Stage 5a-5k Gas injection test 2

In previous gas injection experiments a multi-stage approach had been adopted. For the final gas injection ramp it was decided to continue gas injection and not to pause when gas injection pressure was close to the minimum principal stress. Therefore at Day 250.95 the injection pump was set to a constant flow of 375 µl/h with a gas volume of approximately 295 ml at 4.9 MPa. This created the gas pressure ramp shown in **Figure 7-18**. As seen, injection pressure increased with only a small increase in guard-ring pressure (**Figure 7-18 B**) and small amounts of dilatant strain (**Figure 7-18 E**). No out flow from the sample was observed during this period. At Day 267.05 the test was interrupted for maintenance of the injection pump. This resulted in a small drop in injection pressure.

The sample underwent an axial dilation (**Figure 7-18 E**) at Day 268.08 when the gas injection pressure was 9.99 MPa. This is a condition when the injection pressure equalled the minimum principal stress component (confining pressure). At this time the pressure within the injection-end guard-ring rose several megapascals (**Figure 7-18 B**), the pressure at the back-end of the sample started to rise (**Figure 7-18**), and outflow from the sample started (**Figure 7-18 C** and **D**). This can be interpreted as gas entry, although the passage of gas was likely to be along the interface between the injection platen and the sample. Passage through the sample cannot be discounted.

Gas injection pressure continued to increase, with a significant event occurring at Day 269.01. At this time axial strain greatly increased (**Figure 7-18 E**), pressure in the back-end guard-ring significantly increased by several megapascal (**Figure 7-18 B**), and outflow from the sample increased (**Figure 7-18 C** and **D**). This occurred at a gas injection pressure of 10.48 MPa, a magnitude when gas pressure equalled axial stress. Therefore it can be concluded that gas movement in the sample, be it through the clay or along the edge of the sample, was solely controlled by the boundary conditions; i.e. gas flow is stress controlled.

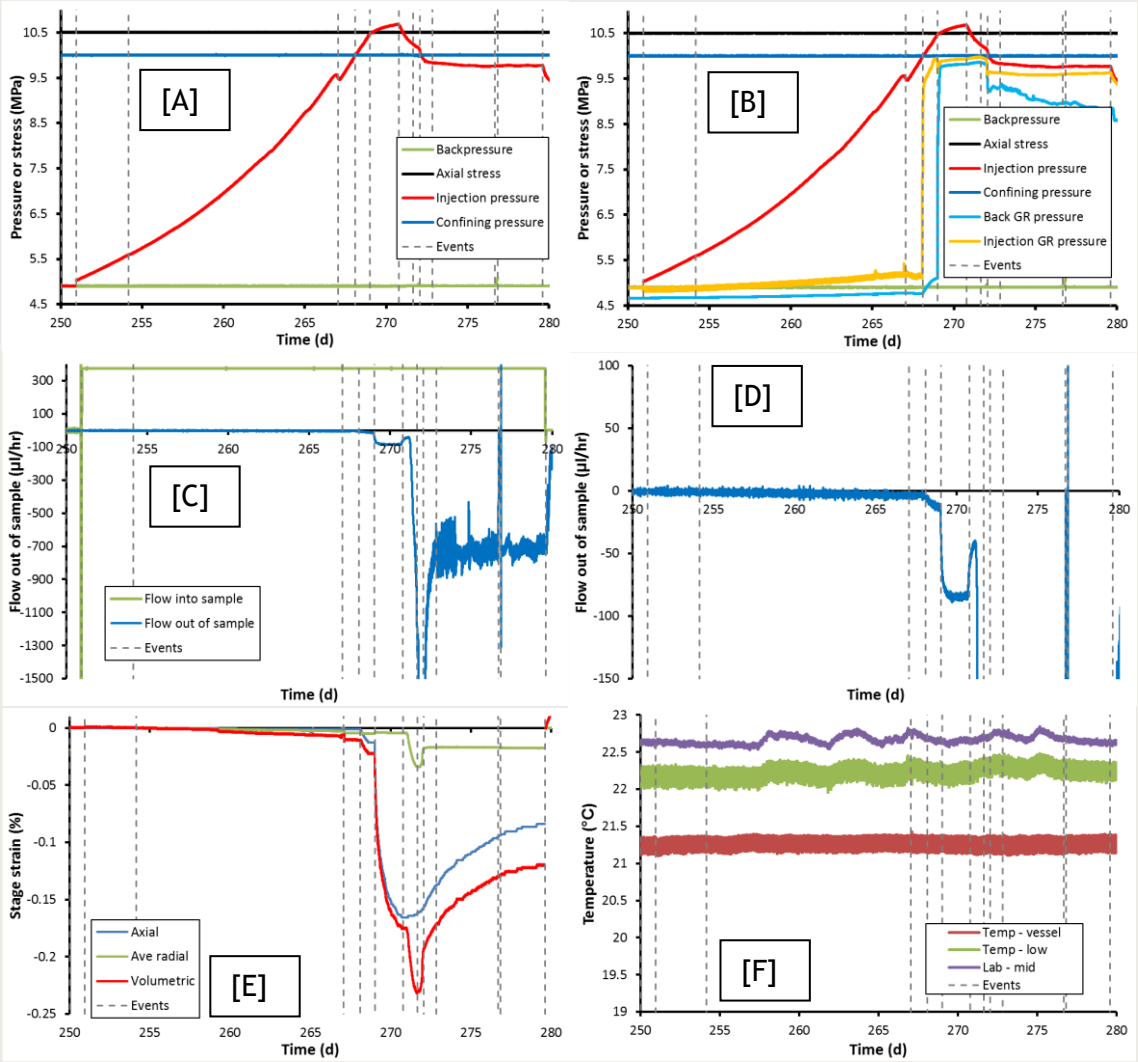

Figure 7-18: Data for the gas test 2 of test OPERA_SPP-2. [A] Pressure history (boundary conditions). [B] Full pressure history with guard-ring pressures. [C] Flow into and out of sample. [D] Detail of flow out of the sample. [E] Radial, axial and volumetric strain. [F] Temperature. Dashed lines represent events of note.

Gas pressure continued to rise until it reached a peak of 10.68 MPa at Day 270.77. At this time outflow from the sample greatly increased to attain a maximum of more than 2,000 µl/h, and then recovered to a steady 750 µl/h. At the time of gas peak the sample also started to dilate in the radial direction, whilst axial strain peaked at 0.16 % dilational strain. Following the peak in gas pressure the injection pressure slowly decayed until it reached a plateau of 9.6 MPa, a magnitude close to the confining pressure. At Day 272.06 outflow from the sample spiked, resulting in a drop in injection pressure, injection-end guard-ring pressure, and back-end guard-ring pressure. This also resulted in the

contraction of the radial direction of the sample. For the remainder of the test the back-end guard-ring pressure slowly reduced and the axial strain contracted.

Key observations of stage 5 (gas injection): gas did not become mobile until the minimum principal stress was reached (9.99 MPa); further gas movement occurred when gas pressure exceeded the maximum principal stress (10.48 MPa); gas movement in the sample, be it through the clay or along the edge of the sample, was solely controlled by the boundary conditions; i.e. gas flow is stress controlled; the sample dilated axially once gas became mobile; further axial dilation occurred once the maximum principal stress was exceeded; gas peak pressure (10.68 MPa) was followed by high outflow, axial contraction and radial dilation; gas injection reached an asymptote similar to the minimum principal stress component.

7.1.4.8 Stage 5l-5m Gas shut-in

Figure 7-19 summarises the data achieved for the 43 day shut-in period following the cessation of gas injection

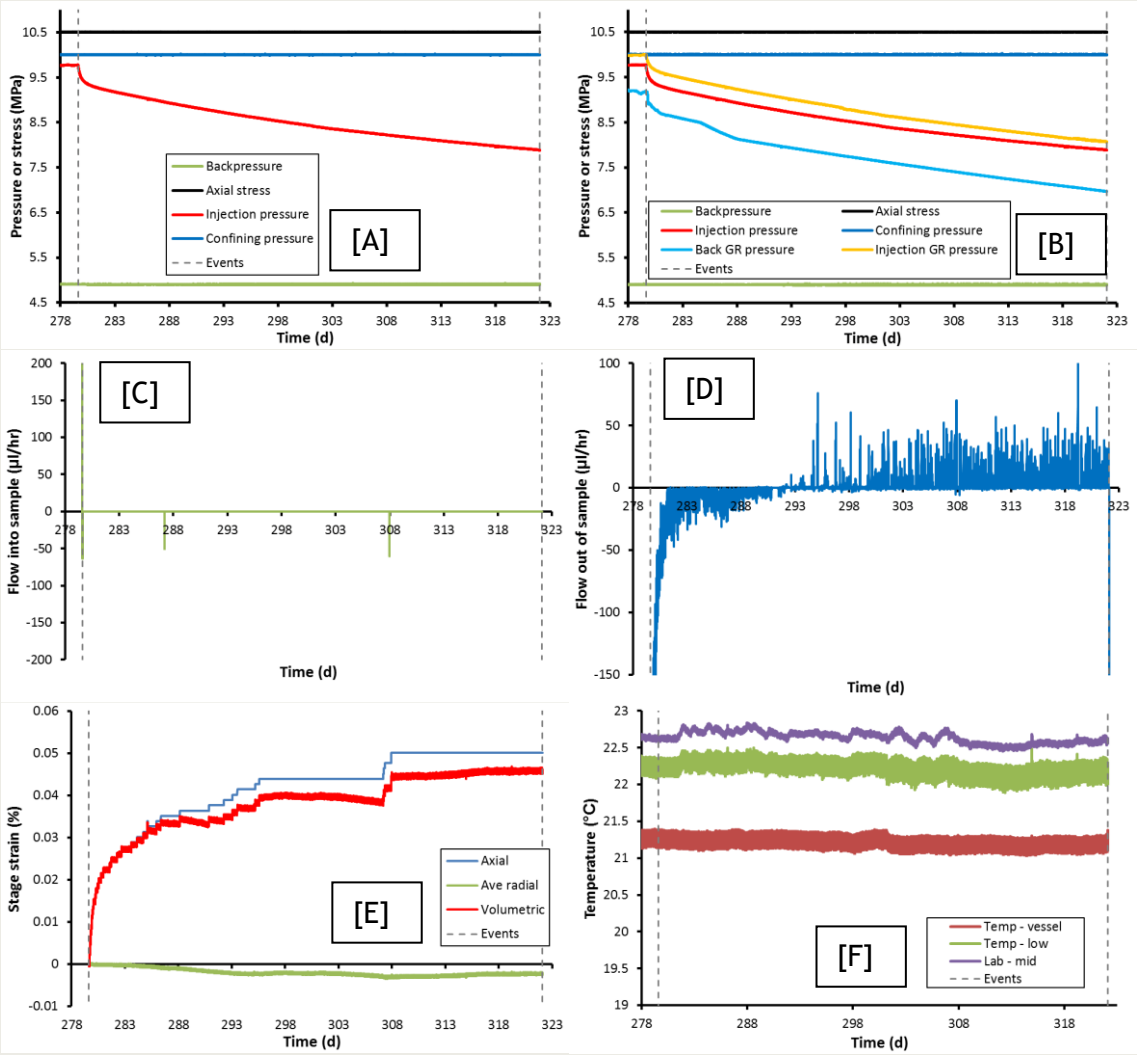

Figure 7-19: Data for the gas shut-in stage of test OPERA_SPP-2. [A] Pressure history (boundary conditions. [B] Full pressure history with guard-ring pressures. [C] Flow into sample. [D] Flow out of the sample. [E] Radial and axial displacement. [F] Temperature.

During the shut in period the injection pressure decreased (**Figure 7-19 A**). It was not possible to determine the capillary threshold pressure due to the slow decline of pressure. Both injection-end and back-end guard-ring pressures declined at a similar rate to the injection pressure. Once injection had been stopped the outflow from the sample decreased from an initial near 150 µl/h to a condition of no flow within 10 days. The noise within this data shows that gas was flowing out of the sample. During the shut-in period the radial strains continued to dilate, although only by a nominal 0.003 %. The sample contracted in the axial direction by a total of 0.05 %.

Key observations of stage 5 (gas shut-in): injection, injection-end guard-ring, and back-end guard-ring pressures all decayed during shut in at a similar rate; asymptote (capillary threshold pressure) was not reached; the sample contracted a total of 0.05 % in the axial direction.

7.1.4.9 Observations of the final test sample

At the conclusion of the test, the apparatus was carefully de-pressurised in steps similar to those used at the start of the test. The apparatus was dismantled and the sample was removed in its Hoek-sleeve. **Figure 7-20** shows the sample following removal from the Hoek-sleeve.

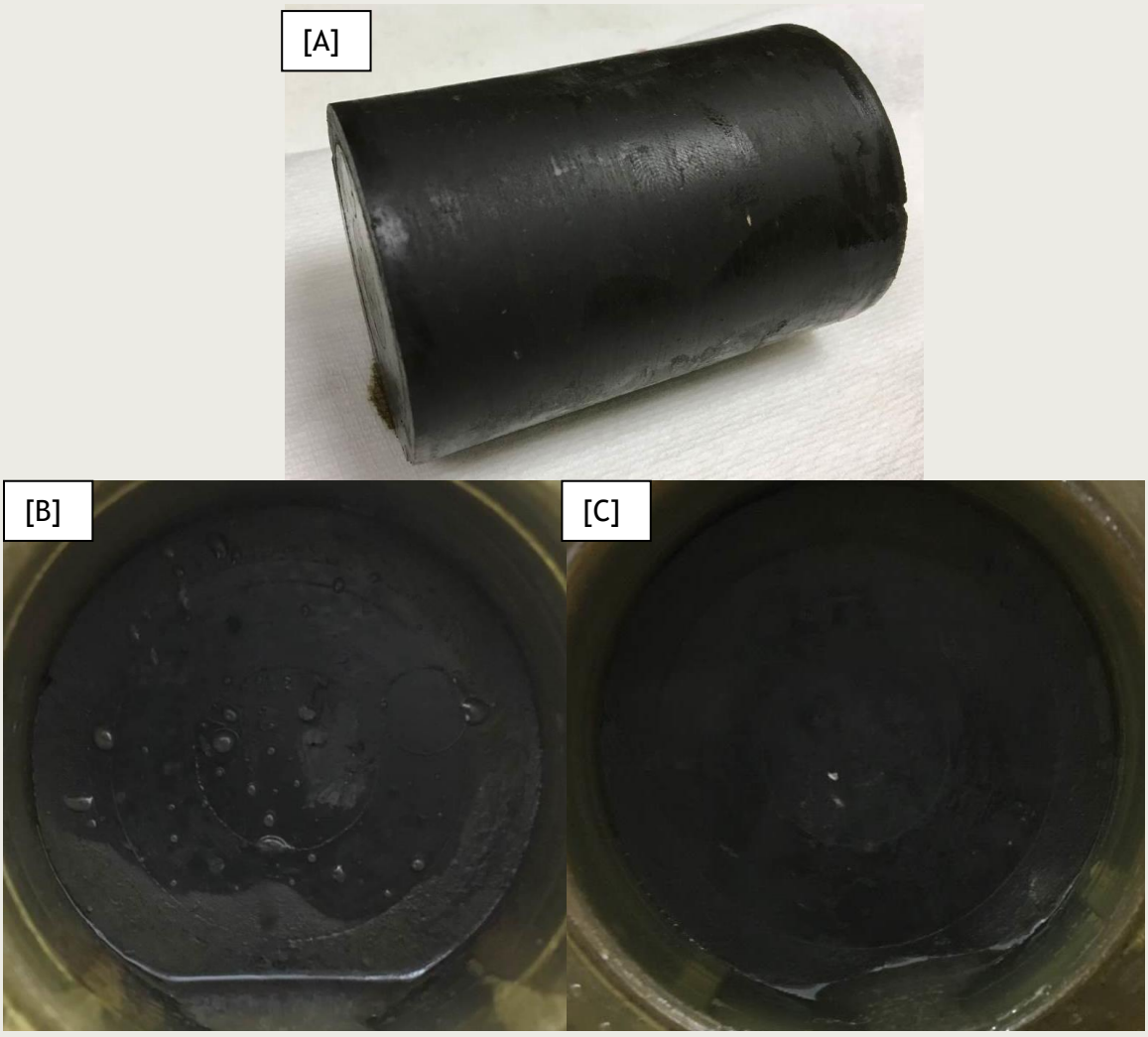

Figure 7-20 Observations of the final test sample OPERA_SPP-2. [A] Length of the test sample. [B] Back-end of the sample. [C] Injection end of the sample.

The ends of the sample (**Figure 7-20 B** and **C**) show indentations of the injection and guard-ring filters along with the load cell. Small cracks were apparent, but the timing of their formation is uncertain. The sample was measured and was found to have an increased average radius of 101 μm and an increased length of 224 μm, this meant an increase in volume of 1.26 cm^3. However, the sample had reduced by 3 g in weight, a reduction of 0.7 %. Overall, the sample had a 1.4 % decrease in bulk density. Therefore it can be concluded that the sample included a considerable quantity of trapped gas and the sample had been desaturated by gas migration.

Key observations of the test sample: the sample saw 1.26 cm^3 (0.64 %) increase in volume, a 0.75 % decrease in weight, resulting in a 1.4 % reduction in bulk density; sample included a considerable quantity of trapped gas; the sample had desaturated by gas migration.

7.1.4.10 Calculating gas permeability of test OPERA_SPP-2

Gas injection test 2 reached steady-state flow following gas breakthrough. Therefore it is possible to calculate the permeability of the Boom Clay at a depth equivalent of 500 m. The equation for steady state flow of gas as a single phase in a porous medium may be written by combining the mass continuity equation with a generalisation of Darcy's law:

$$\nabla.\left(\frac{\rho_g k_g}{\mu_g}\nabla\left(p_g\right)\right)=0 \qquad (7\text{-}1)$$

where p_g is the gas pressure (Pa), ρ_g is the gas density (kg.m^{-3}), k_g is the effective gas permeability (m^2), and μ_g is the gas viscosity (Pa.s). Assuming ideal gas behaviour and a constant value for k_g, equation (7-1) can be integrated along a 1D-flow path to obtain an expression for the flow rate at standard temperature and pressure (STP), Q_{st}, in terms of the pressures at either end of the path:

$$Q_{st}=\frac{v_{mst}k_g A}{2RT\mu_g L}\left(p_{gi}^2-p_{go}^2\right) \qquad (7\text{-}2)$$

where v_{mst} is the molar volume of the gas at STP, A is the specimen's cross-sectional area, L is the specimen length, R is the gas constant, T is the absolute temperature, p_{gi} is the gas pressure at injection, and p_{go} the pressure at outlet. Although gas pressure p_{go} cannot be measured directly in these experiments, it can be related to the backpressure of the water at the downstream end of the specimen, p_{wo}, by the relationship $p_{go} = p_{wo} + p_{co}$, where p_{co} is the apparent capillary threshold pressure. Based on the data from test OPERA_SPP-2, and assuming a value for p_{co} = 1.6 MPa, the effective gas permeability for Boom Clay is $2.3\text{x}10^{-20}$ m^2. However, given the uncertainty in p_{co}, it seems prudent to estimate permeability across a range of potential values, **Table 7-4**. This range in gas permeability agrees well with the results of Horseman & Harrington (2000), who report kg between 0.4 and ~10 × 10^{-20} m^2 for tests conducted at stresses representative of 220 m depth.

Capillary threshold pressure, p_{co} (MPa)	Effective gas permeability , k_g ($x10^{-20}$ m^2)
1.0	2.0
1.5	2.3
2.0	2.6
2.5	3.0

Table 7-4: Effective gas permeability calculated for a range in capillary threshold pressures.

7.1.4.11 Summary of key observations of test OPERA_SPP-2

The five stage triaxial test OPERA_SPP-2 lasted a total of 322 days. During initial swelling a total of 0.23 % dilatant strain was measured as a result of swelling. Considerable anisotropy was noted in the strain. A total of 3.4 ml of water was taken up, with flow and strain equilibrating in approximately 5 to 7 days. It should be noted that the back-end of the sample had twice the water uptake compared with the injection end. The hydraulic permeability of the sample was determined to be 1.65×10^{-19} m^2, although permeability was continuing to evolve at the end of the stage. The high pressure step of the 2-stage head test resulted in some permanent (dilatant) strain of the sample. Anisotropy was seen not only in strain but in the amount of strain recovery following depressurisation. Gas entry did not occur until the minimum principal stress had been exceeded at a gas pressure of 4.3 MPa (excess pressure of 2.1 MPa) at a stress condition representing Mol. Gas movement was accompanied by a total dilatant strain of 1.4 %. Gas pressure peaked at 4.59 MPa, at which point break-through was achieved.

The sample was consolidated to a stress state representative of the Netherlands. Two competing processes occurred; the raised pore pressure promoted swelling and dilatancy, whilst increased confining pressure promoted contraction and consolidation. The axial direction contracted by 0.08 %, with the radial direction only dilating by 0.02 %. Little flow into or out of the sample occurred. At a stress state representative of the Netherlands, gas did not become mobile until the minimum principal stress was reached (9.99 MPa, excess gas pressure of 5.1 MPa). Further gas migration was promoted when the gas pressure exceeded the maximum principal stress at 10.48 MPa (excess gas pressure of 5.58 MPa). Therefore gas movement was solely controlled by boundary conditions. The sample dilated axially once gas became mobile, with further dilation occurring once the maximum principal stress had been exceeded. Gas pressure peaked at 10.68 MPa (excess gas pressure of 5.78 MPa), resulting in high outflow, axial contraction and radial dilation. The effective gas permeability was calculated to be 2.3×10^{-20} m^2.

The final sample had a 0.64 % (1.26 cm^3) increase in volume and a 0.75 % decrease in weight. This resulted in a 1.4 % reduction in bulk density. It should be noted that this comparison is made after the sample had been consolidated to represent depth of the Netherlands. This shows that the sample included a considerable volume of trapped gas and that gas migration had resulted in desaturation of the Boom Clay.

7.1.5 Comparison of tests OPERA_SPP-1 and OPERA_SPP-2

All four gas injection tests conducted show a consistent physical driver of gas migration; gas does not become mobile (gas entry) until stresses that are close or above the local stress state are imposed. This relationship is shown in **Figure 7-21**. Gas entry has not occurred in any stages at a pressure lower than the confining pressure of the test, although Test stage 2 shows that entry occurred at a pressure just below confining pressure. The lowering of back pressure demonstrates that it is not excess pressure that dictates gas entry, as the lowering of pore pressure should have re-established gas flow. Therefore local stress is the primary control on gas entry and advective migration in Boom Clay. Therefore in the Netherlands advective gas migration will not occur until a gas pressure equal, or close to, the minimum principal stress.

Both tests resulted in a reduction of weight of the sample, whilst the volume of the sample increased. This shows that the samples included a considerable volume of trapped gas and that gas migration had resulted in desaturation of the Boom Clay.

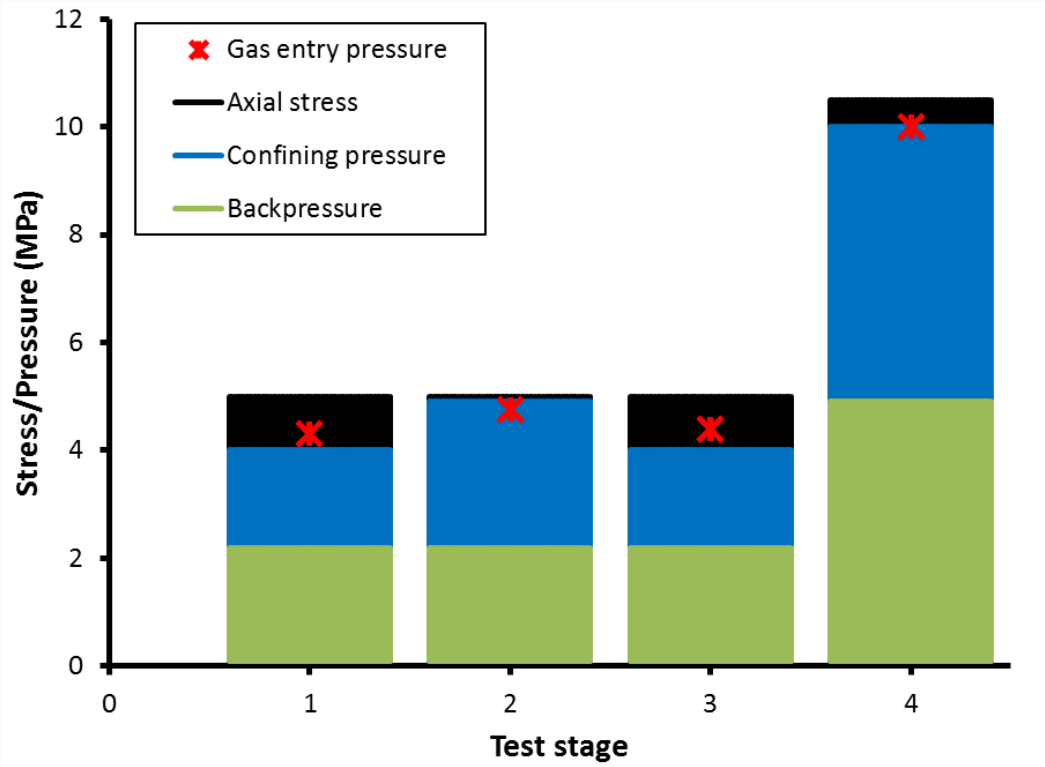

Figure 7-21: Comparison of boundary conditions with gas entry pressure for the four gas injection tests conducted. Test stages 1 and 2 represent test OPERA_SPP-1, stages 3 and 4 represent test OPERA_SPP-2.

Hydraulic properties were only determined for Boom Clay at a stress state representative of Mol. Permeability was determined to be 4.83×10^{-19} m^2 and 1.65×10^{-19} m^2 for tests OPERA_SPP-1 and OPERA_SPP-2 respectively. These can be seen to be consistent with one another. Both test samples showed anisotropy in strain and strain recovery.

Key observations comparing tests OPERA_SPP-1 and OPERA_SPP-2: All four gas tests showed that gas migration did not occur until gas pressure exceeded the minimum principal stress (confining pressure); lowering of back pressure showed that excess gas pressure is not the controlling parameter of gas entry; both tests saw a reduction in weight, and increase in volume; considerable quantity of gas trapped in the samples; gas migration resulted in sample desaturation; Permeability measurements agree (4.83×10^{-19} m^2 and 1.65×10^{-19} m^2); both samples showed anisotropy in strain and strain recovery.

Outcomes:

1. Two tests were conducted under triaxial conditions giving two measurements of hydraulic permeability at stresses representative of Mol, and four gas injection tests at stress conditions representative of both Mol and the Netherlands.
2. Boom Clay undergoes dilatant strain during re-hydration showing the sample swells.
3. Permeability was determined to be 4.83×10^{-19} m^2 and 1.65×10^{-19} m^2.
4. Boom Clay shows anisotropy in strain and strain recovery. Permanent dilatant deformation caused by the two-stage hydraulic test.
5. Gas migration did not occur until gas pressure exceeded the minimum principal stress (confining pressure), therefore the intermediate principal stress plays an important role on gas migration. The gas entry pressure was 4.3 MPa (excess pressure of 2.1 MPa) for both OPERA_SPP tests at stress conditions representative of Mol, and the gas pressures peaked at 4.51 MPa (excess pressure of 2.3 MPa) and 4.59 MPa (excess pressure of 2.4 MPa) for tests SPP-1 and SPP-2 respectively at Mol conditions.
6. The gas entry pressure was 9.99 MPa (excess pressure of 5.1 MPa) at stress conditions representing the Netherlands, further gas movement occurred when the maximum principal stress was reached (10.48 MPa, excess gas pressure of 5.58 MPa). Gas pressure peaked at 10.68 MPa (excess pressure of 5.78 MPa) at stress conditions representing the Netherlands. The effective gas permeability was 2.3×10^{-20} m^2.
7. Break-through occurred at peak gas pressure and the gas movement resulted in dilatant deformation and desaturation of the clay. The clay increased in volume and reduced in weight, showing considerable amounts of trapped gas within the sample.
8. Lowering of backpressure did not initiate gas entry in a test when gas pressure was just below confining pressure, i.e. excess pressure does not control gas entry.
9. During sample consolidation two competing processes occurred: the raised pore pressure promoted swelling and dilatancy, whilst increased confining pressure promoted contraction and consolidation. Sample consolidation resulted in contraction axially and dilation radially, with no flow into or out of the sample.
10. Gas shut-in behaviour suggested that the two ends of the sample were not in communication with one another.

Recommendations:

1. The anisotropy of strain seen during hydration and gas migration requires detailed investigation to ascertain its impact on the behaviour of the clay. This should include the recovery of strain during times of sample contraction.
2. A suite of hydraulics tests is required to describe the variation observed between samples, this should include testing cores taken at different heights within the full Boom Clay sequence.
3. The capillary threshold pressure requires defining under different stress states.
4. Whilst the current test showed that gas would not become mobile until the least principal stress was exceeded, the results were influenced by gas escaping the Hoek sleeve once gas pressure exceeded confining pressure. Further testing should be conducted in an experimental system where leakage is not possible to determine the gas transport behaviour at high pressures.
5. The role of the intermediate stress requires further investigation to determine the gas pressure at which entry occurs in a non-isotropic stress state.
6. Stress history created by tunnelling, back-fill, and rehydration can be complex and the role this plays on advective gas flow requires careful consideration.
7. The observed dehydration following gas migration requires further investigation and careful consideration. Desaturation will influence the mechanical response of Boom Clay and this too requires further investigation. Experiments are required to determine whether desaturation is a bulk rock phenomena, or whether localised regions of desaturation are created.

7.2 *Constant volume tests*

7.2.1 Experimental approach

To further investigate the coupling between gas pressure, total/effective stress and porewater pressure, two test histories were undertaken in which samples of Boom Clay were volumetrically constrained i.e. dilation of the sample was limited to the elasticity of the pressure vessel, a photo of which is shown in **Figure 7-22**. The apparatus was comprised of six main components: (1) a thick-walled stainless steel pressure vessel, (2) a fluid injection system, (3) a backpressure system, (4) five total stress sensors to measure radial and axial stress, (5) 13 independent porewater pressure sensors, and (6) a microcomputer-based data acquisition system.

The pressure vessel was comprised of a dual-closure tubular vessel manufactured from 316 stainless steel and pressure-tested at 69 MPa. Each end-closure was secured by twelve high tensile cap-screws which were used to apply a pre-stress to the specimen. The 60 mm internal bore of the pressure vessel was honed to give a polished surface, with all ports, except those for the direct measurement of stress, containing porous plugs. Total stress was measured through a series of load cells mounted on the outside of the vessel connected to the sample through high modulus tungsten carbide rods. Gas was injected in to the clay through a central filter embedded at the end of a 6.4 mm diameter stainless steel tube terminating at the mid-plane of the sample. The end of the filter was profiled to match a standard twist drill which was used to produce the hole in which the rod was located.

Volumetric flow rates into and out of the sample were controlled or monitored using a pair of high-precision ISCO-260, Series D, syringe pumps operated from a single digital control unit. The position of each pump piston was determined by a digital encoder with each step equivalent to a change in volume of 16.6 nL, yielding a flow accuracy of 0.5% of the set-point. Movement of the pump piston was controlled by a micro-processor, which continuously monitored and adjusted the rate of rotation of the encoded disc using a DC-motor connected to the piston assembly via a geared worm drive. This allowed each pump to operate in either constant pressure or constant flow modes.

Total stress and porewater pressure sensors were hard-wired directly to a National Instruments data acquisition system. A programme written in LabVIEW™ elicited data from the pump at pre-set time intervals of 2 minutes. The same data acquisition system systematically logs outputs from load cells and pressure transducers to provide a detailed time series dataset.

Significant care was taken in the design of the experimental system to minimise the chance of trapping residual gas within the tubework connecting each radial transducer to the vessel body. As can be seen in **Figure 7-22**, each transducer was fitted with a valve to allow venting of the system and the removal of residual gas prior to the start of testing. A cut-through of the vessel and schematics showing the relative positions of the filters (**Table 7-5**), and stress sensors is shown in **Figure 7-23**.

All hydraulic measurements were performed using a synthetic groundwater which was also used as the backpressuring fluid during gas injection tests. While hydrogen will be the primary gas generated in a geological disposal facility for high level waste and/or spent fuel, helium was selected as a safe substitute based on its inert nature and similar molecular diameter. The test history for each sample is presented in **Table 7-6**.

Array	Sensor name	Axial distance from injection face (mm)	Rotation around bore of vessel (degrees)
Total stress	Injection load cell	0	-
Total stress	Radial 1 load cell	15.2	0
Total stress	Radial 2 load cell	60	120
Total stress	Radial 3 load cell	104.8	240
Total stress	Backpressure load cell	120	-
Radial porewater array 1	Radial 1	38.6	330
	Radial 2	38.6	60
	Radial 3	38.6	150
	Radial 4	38.6	240
Radial porewater array 2	Radial 5	60	330
	Radial 6	60	60
	Radial 7	60	150
	Radial 8	60	240
Radial porewater array 3	Radial 9	81.4	330
	Radial 10	81.4	60
	Radial 11	81.4	150
	Radial 12	81.4	240
Central filter	Middle	60	-

Table 7-5: Relative positions of total stress and porewater pressure filters. Axial distance is to the centre point of each sensor. Angular rotation is anti-clockwise with the Zenith taken vertically at the top of the vessel at the Radial 1 load cell position, see Figure 7-23

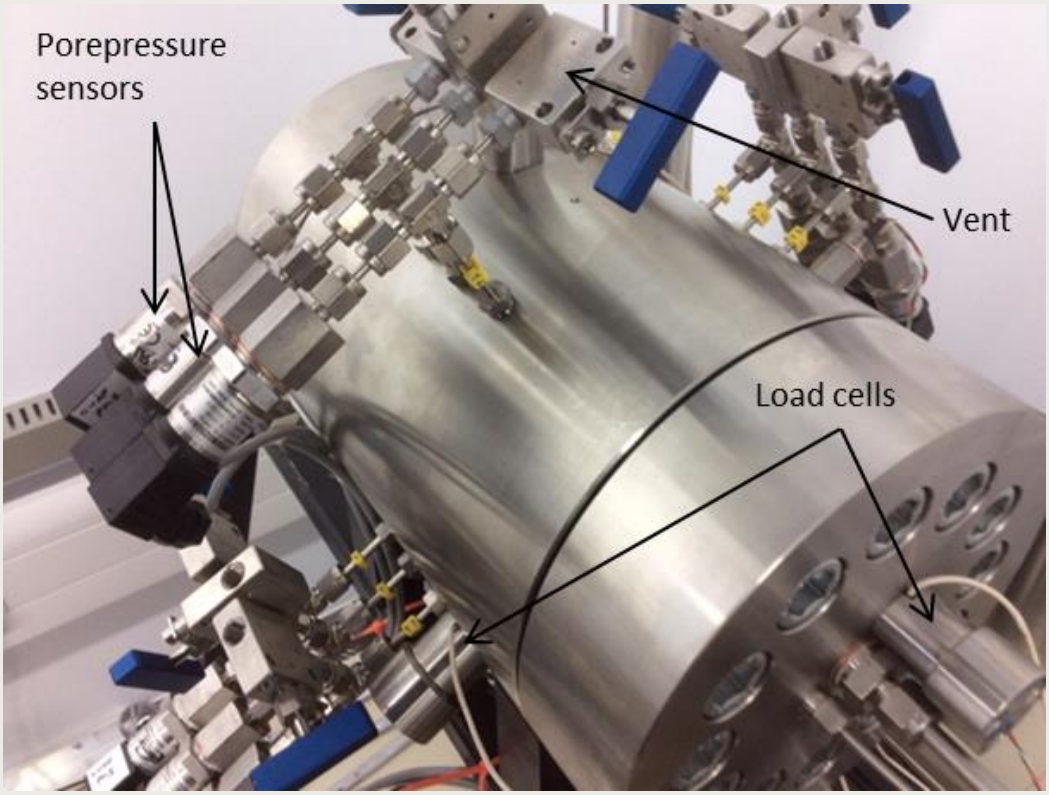

Figure 7-22: Photograph showing the main body of the constant volume cell. Radial porewater pressure sensors and their accompanying drains are visible around the periphery of the vessel.

Sample Covra-3	Stage	Type	Pressure Injection (MPa)	Backpressure (MPa)	Permeant
	1	EQ	-	-	Synthetic porewater
	2	EQ	1.0	1.0	Synthetic porewater
	3	CPH	1.5	1.0	Synthetic porewater
	4	EQ	1.0	1.0	Synthetic porewater
	5	CFRG	-	1.0	Helium

Table 7-6: Experimental test history for CVRF sample COVRA-3

7.2.2 Calibration and test material

All pressure transducers and load cells were calibrated for both ascending and descending pressure functions against a known laboratory standard, traceable back to National pressure standards. Hysteresis was therefore measured and multiplier and offset corrections calculated for each pressure device.

Test samples were prepared by a combination of band sawing and machine lathing. Samples were initially 'rough-cut' to approximately the correct length before machine lathing. In this way, moisture loss was kept to a minimum and a high quality test sample obtained with nominal dimensions of 120mm length and 60mm diameter. The cylindrical specimen, designated Covra-3, was prepared using core material from barrel CGR74/75-0.84-1.11m. Basic geotechnical properties are presented in **Table 7-7**.

Figure 7-24 shows a series of images taken of specimen Covra-3 prior to testing. In the x-ray image (**Figure 7-24 A**) a significant amount of heterogeneity is evident within the sample. While many features align with bedding (i.e. horizontal in the image presented), a number of cross-bedding features are clearly evident. However, none of these traverse the entire length of the core and therefore can be considered, for this phase of testing, as localised features only. Close examination of the images [A] through [D] (**Figure 7-24**) show no obvious signs of micro-cracking, supporting the assertion that this sample is suitable for gas testing.

	Sample No.	Reference (m)	Water content (%)	Bulk density (g/cm^3)	Porosity (%)	Saturation (%)
Pre-test	Covra-3	CGR74/750 84-1.11	23.4	2.026	38.5	99.7
Post-test	Covra-3	CGR74/750 84-1.11	24.0	2.019	39.0	100.0

Table 7-7: Basic geotechnical properties for sample Covra-3.

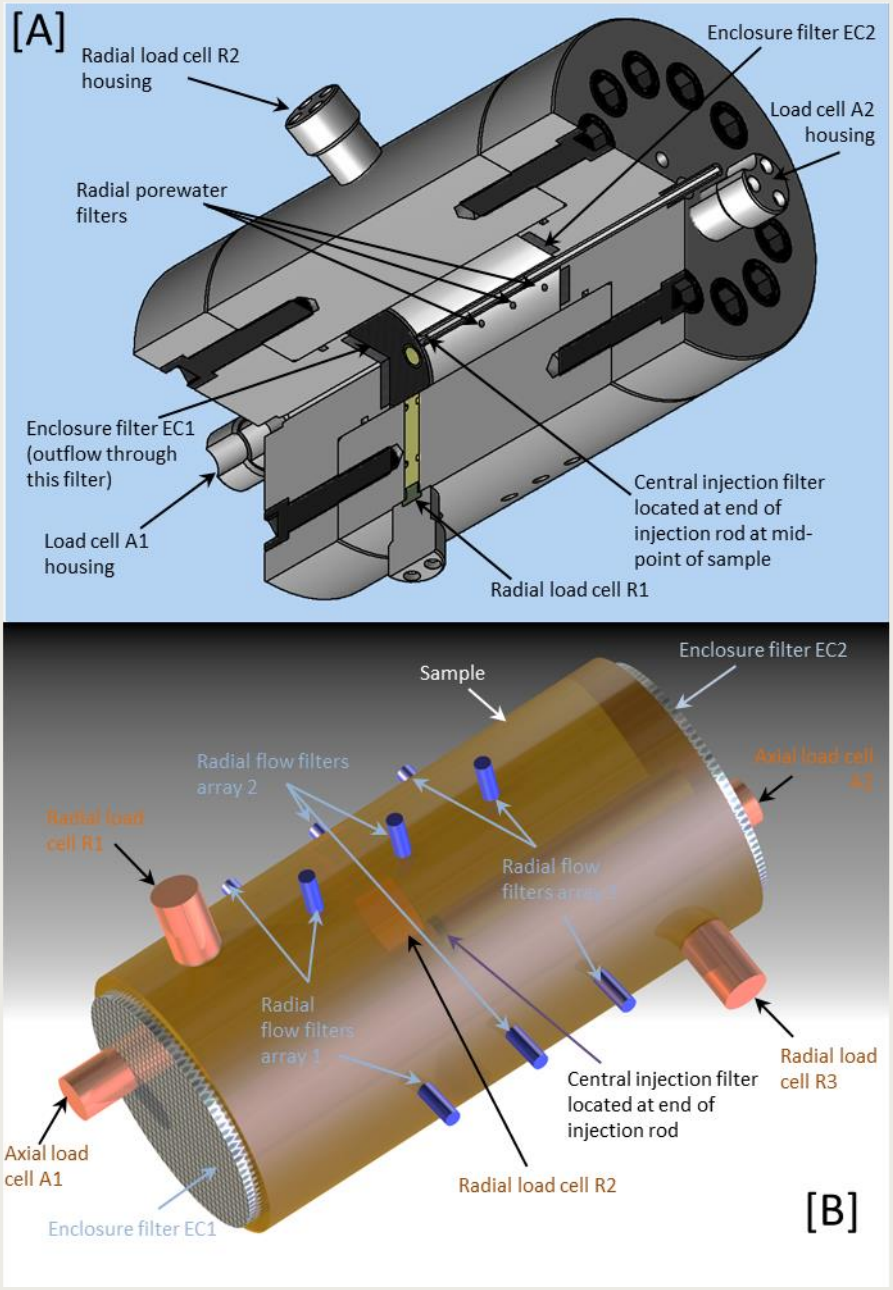

Figure 7-23: A) Cut-away diagram of the constant volume pressure vessel showing major experimental components. B) Rendered image of a sample showing the relative positions of the load cells and pore pressure filters.

Figure 7-24: Pre-test images of sample Covra-3. A) X-ray image of core (note the dark horizontal line around the mid-plane of the sample is an artefact of imaging). B) End-face showing central hole to accommodate the injection tube. C) Side view of core. D) Backpressure end-face. Minor shallow surface striations are evident in images [B], [C] and [D], which are caused when a hard nodule of material is 'plucked' by the lathe and dragged across the sample surface. However, these features are discontinuous, shallow, and do not have a deleterious effect on the sample properties (Table 7-6).

7.2.3 Results

The results from two highly-instrumented tests are described in the following sections, with each test providing insight into the temporal and spatial development of stress, porewater pressure and gas flow within Boom Clay.

7.2.3.1 Equilibration and hydraulic testing

Upon assembly of the apparatus, Stage [1], the sample was initially left to 'equilibrate' with synthetic water within all radial filter arrays as well as the large sintered discs mounted in the face of each end-closure (**Figure 7-23**)[d]. The purpose of this was two-fold. Firstly, by monitoring the pressure response of each individual filter it is possible to confirm that each array was saturated at the onset of testing, and secondly, to give the sample a chance to hydrate prior to the application of the backpressure, thereby reducing

[d] A small pre-stress applied to the sample during gentle tightening of the end-closure bolts was subtracted from the stress data presented in the subsequent graphs.

the chance of spontaneous piping. **Figure 7-25 A** shows a plot of porewater pressure against time. The gradual reduction of pressure in each array indicates uptake of water from the filters, evidence to the fact they were fully saturated at the onset of testing.

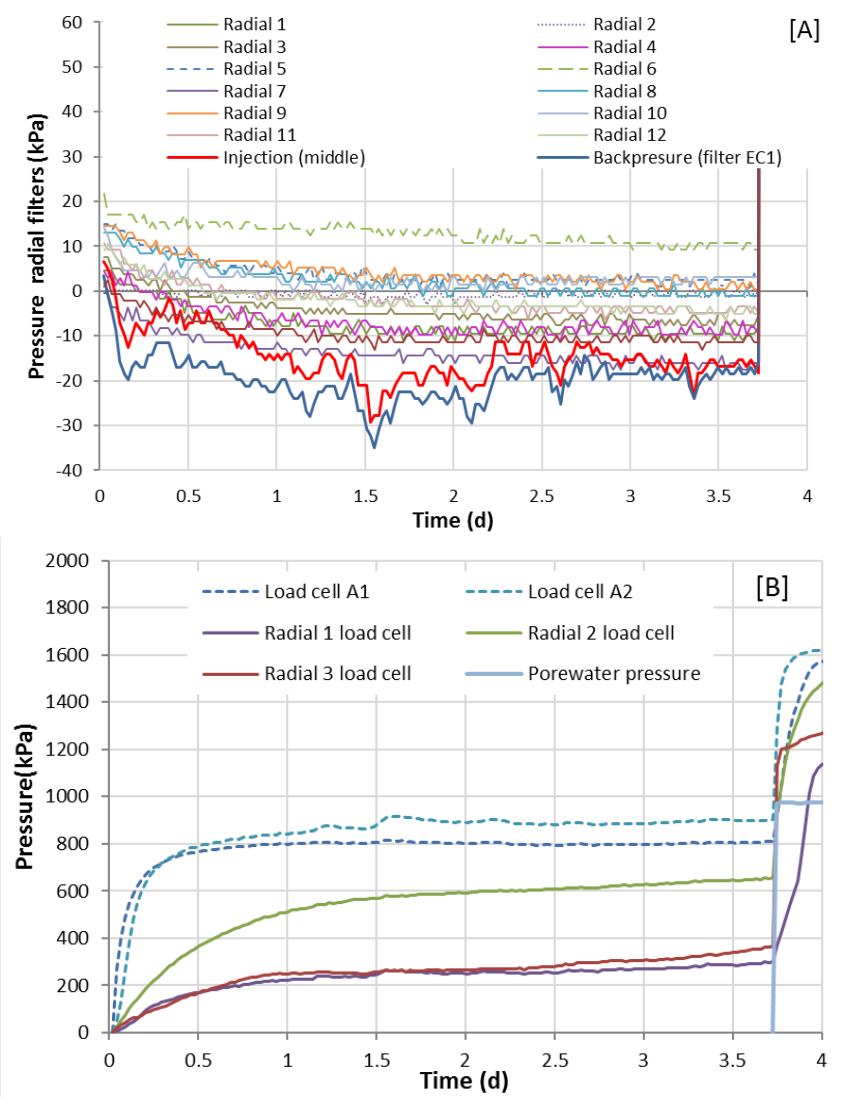

Figure 7-25: Initial equilibration of clay sample Covra-3. From 0 to 3.8 days, stage [1], the clay is passively hydrated through the uptake of water from the apparatus filters. From day 3.8 onwards, stage [2], backpressure was applied to the sample through all of the filters. The development of pore pressure [A] and stress [B] are presented.

However, the limited availability of water appears to have constrained the development of stress within the sample (**Figure 7-25 B**) and as such, pore pressure was increased in all filters to a value of 1000 kPa at day 3.8. Inspection of the data shows this had an immediate impact on the development of stress within the sample. Flux into the sample (**Figure 7-26**) indicates roughly equal inflow from either end of the core, suggesting minimal hydraulic variation in the axial plane.

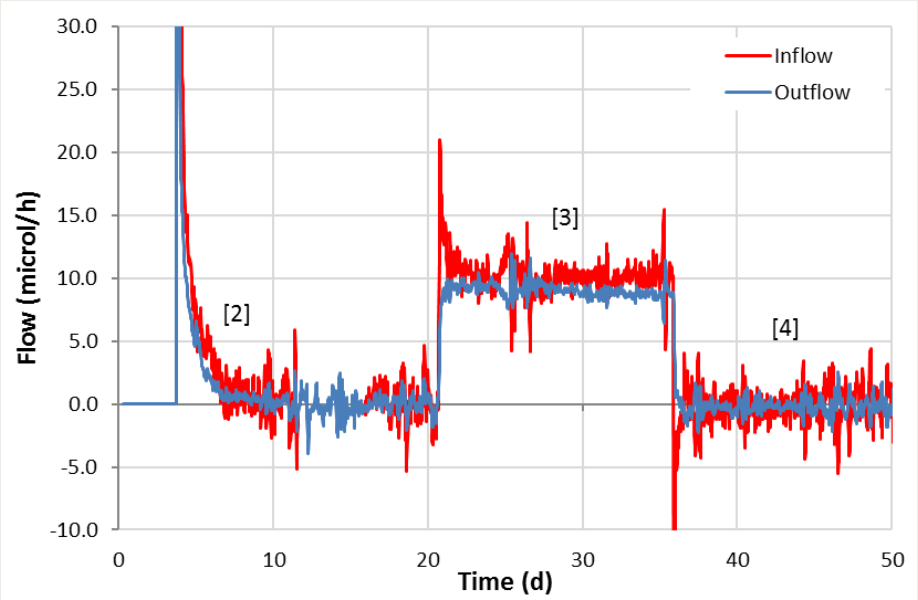

Figure 7-26: Flow rate into and out of sample during equilibration phases and hydraulic testing. Values in parentheses represent test stage numbers. Inflow rates have been corrected for a minor leak.

Not surprisingly the development of stress is initially biased towards the end-closure filters (**Figure 7-25 B)**, which register the highest increase in pressure. Interestingly radial pressure is highest at the mid-plane of the sample, suggesting a possible 'Poisson-type' effect as the swelling pressure preferentially developed at either end of the core is transmitted through the sample. While there is some noise in the data, by the end of stage [2] (**Figure 7-26 C)** an average total stress of around 1.5 MPa is observed in the data. Swelling pressure is obtained by subtraction of the backpressure, in this case 1.0 MPa, which yields a value of 0.5 MPa. While this is somewhat lower than would be expected, it lies within the range of values quoted by Wiseall et al., 2015.

At day 15.7 all radial filters (and the large axial EC-2 filter) were isolated from the backpressuring system, so that from this time forward each transducer can be considered to provide a measure of the local value for porewater pressure. Close inspection of the data in **Figure 7-26 A** and **B** shows some very minor variations in pressure ranging from +22 kPa to -47 kPa with an average change in pressure for the entire array of -7 kPa. As such, to all intents and purposes the sample can be considered to be in equilibrium prior to the start of baseline hydraulic testing.

At day 20.7 water pressure within the central injection filter was increased to 1.5 MPa. Outflow from the sample was only possible through the large axial filter EC-1. Examination of the data in **Figure 7-26** shows that flux in and out of the core quickly reached an asymptote at an average flux of around 9.4 μl/h. Because of the complex nature of the drainage boundary condition, it was not possible to calculate permeability using a simple analytical solution. Numerical modelling of the data will be necessary in the future in order to estimate permeability.

Inspection of data in **Figure 7-27 A**, shows a complex response to the increase in porewater pressure. As pressure is incremented in the central filter, all radial filters, with the exception of radial 2, rapidly increase, such that the transient phase lasts less than 24 hours. That said, there are a few notable exceptions. Radial filters 1 and 5 spontaneously increase to the same pressure as that in the centre of the sample, strongly indicating the presence of a hydraulic pathway between the filters. What is equally interesting, is that

shortly after the step in pressure, both filters exhibit a progressive decrease in pressure suggestive of pathway sealing. For the following 10 days pressure in both filters continues to decline. From around day 33 onwards, all transducers reach their final asymptote values and remain fairly static from that point forward.

The other notable exception is radial filter 2 which exhibits a high degree of time dependency compared to all other radial filters. The anomalous behaviour of this transducer may stem from issues with the filter restricting the ingress of water. All radial filters were therefore changed between tests Covra-3 and -4.

Figure 7-27 B shows a plot of average porewater pressure viewed longitudinally along the length of the sample. The anomalous response of radial filters 1 and 5 is clearly visible (dark red line) as an elevation in the distribution of pore pressure within the sample. However, the behaviour of radial filter 9 is similar to that of the other filters on the same plane viewed across the sample (i.e. filters 10, 11 and 12) suggesting a localised event/feature is responsible for the behaviour noted for filters 1 and 5. That said, by the end of the hydraulic test, significant variations in longitudinal porewater pressure value had disappeared, suggesting time dependent homogenisation of the sample. This is exemplified in **Figure 7-28** which is a plot of individual filter pressure (at day 35.9) as a function of axial distance along the core. Controlled backpressure (i.e. filter EC-1 through which outflow occurs) plots at 0 mm on the x-axis, while filter EC-2, at the opposite end of the core, plots at 120 mm. Inspection of the graph shows a linear distribution in porewater pressure emanating from either side of the central, mid-plane injection point suggesting a strong degree of hydraulic symmetry. However, the asymmetry in the linear fits (grey dashed lines) can be simply explained by the complex nature of the drainage boundary condition. Since flow is restricted to one end of the sample (through filter EC-1), the porewater pressure at the opposite end of the sample is free to evolve. This results in the asymmetry observed in the pressure response.

The total stress response during hydraulic testing and subsequent re-equilibration, stages [3] and [4], is presented in **Figure 7-27 C**. While there is some noise in the data, a general trend of increasing total stress is observed following the imposition of the hydraulic gradient at day 20.7. The development of stress is both complex and likely impacted by the drainage boundary condition imposed upon the sample. To better understand the observed deviations in stress, **Figure 7-29** shows the change in load cell response from day 20.6 (just before hydraulic testing began) compared to that at day 35.9 (at the end of the hydraulic test). A similar asymmetry in stress to that in **Figure 7-28** for porewater pressure is observed. Counter-intuitively the magnitude of the stress change is larger than that of the measured porewater pressure at a number of locations within the sample, however, the average change in stress is around 315 kPa (red dotted line) which is comparable with that of the average pore water pressure change of 304 kPa (dotted blue line, based on values from arrays 1, 2, 3 and filter EC2). The potential roles of side-wall friction and error within the stress measurement cannot be differentiated within the data.

In test stage [4] the injection pressure was returned to the reference value of 1.0 MPa and porewater pressures allowed to decay. With the exception of filter 2, the hydraulic transients lasted around 24 hours, similar in length to those observed following the increment in pressure at the start of stage [3]. Thereafter, the sample was allowed to equilibrate for a further 14 days to ensure all pressure transients had fully decayed prior to the onset of gas testing. However, inspection of the stress data in **Figure 7-27 C** suggests only a portion (around 55%) of the change in stress was actually recovered during stage [4]. That said, the magnitude of the stress changes are small (only a few hundred kPa), such that friction and experimental noise/error (in the measurement of stress) system impact the data.

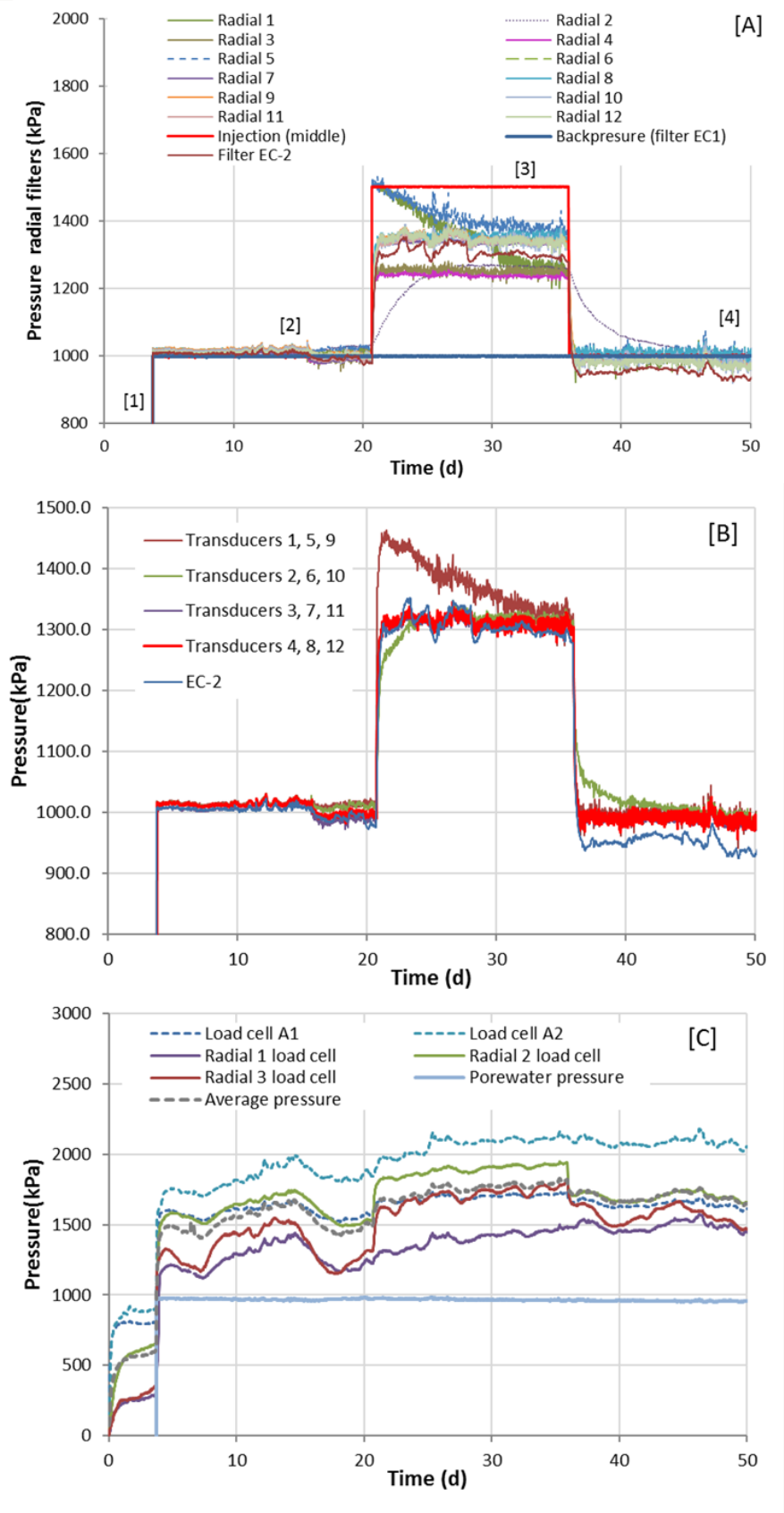

Figure 7-27: Porewater pressure, [A], average longitudinal porewater pressure [B], and load-cell data, [C], for sample Covra-3. Values in parentheses represent test stage numbers. In stage [3] a hydraulic test was performed on the sample and the distribution of porewater pressure and stress measured.

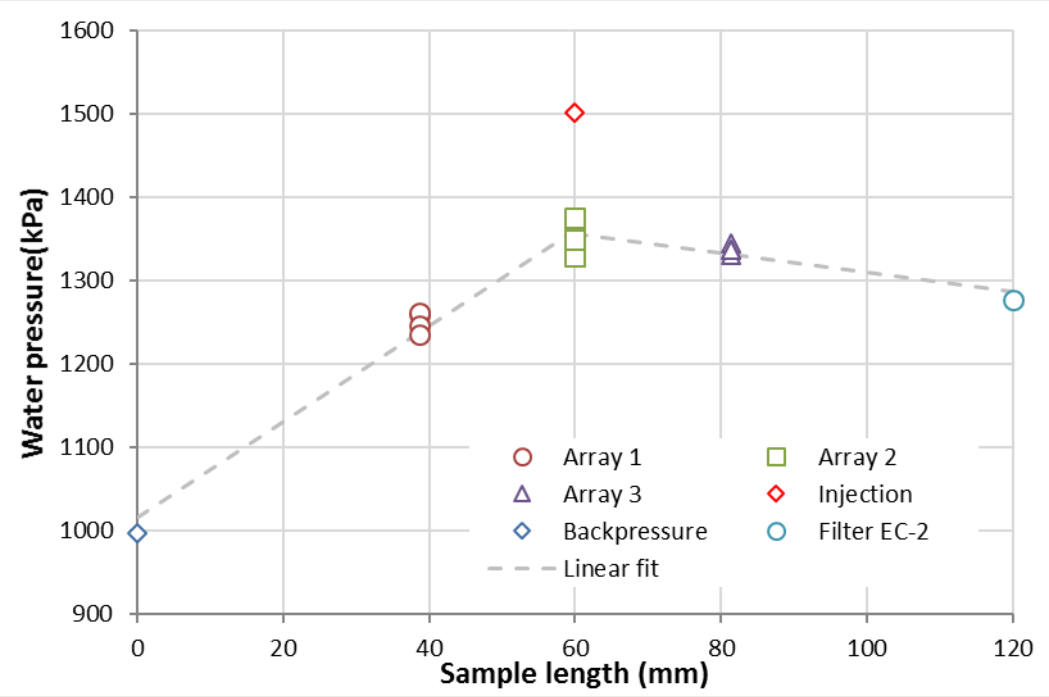

Figure 7-28: Distribution in porewater pressure at the end of hydraulic testing. The asymmetry in the pressure profile is caused by the complex drainage boundary condition.

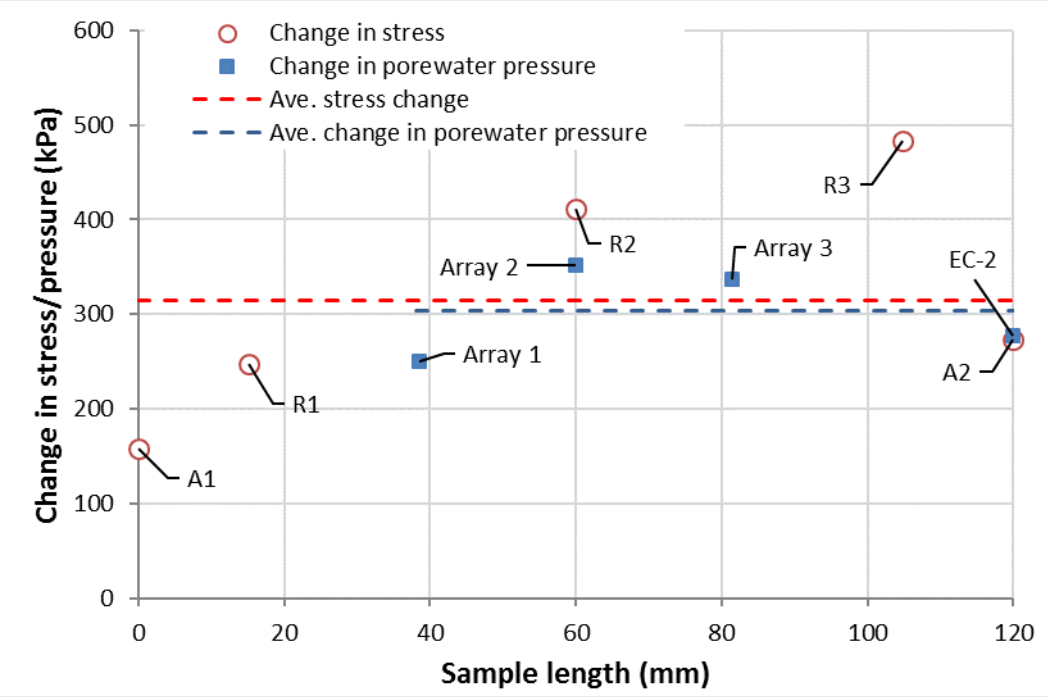

Figure 7-29: Changes in stress and porewater pressure observed during hydraulic testing.

7.2.3.2 Gas testing

To investigate the point at which gas becomes mobile in the clay, most of the synthetic porewater solution was removed from the injection pump and replaced with helium gas. This was then flushed through the pipework and central injection filter to remove as much of the synthetic solution as possible prior to the onset of gas testing. At day 51, the injection pump was switched to constant flow rate mode (at a nominal flux of 375 μl/h)

and the gas in the injection pump slowly raised in pressure. **Figure 7-30 A** shows the evolution in flow rate into the system and the accompanying flux out of the core. Major gas breakthrough is clearly evident at day 67.2, when flux out of the sample rapidly increases. As injection pressure subsequently decays and permeability develops within the sample, flux rapidly decreases towards a quasi-steady state condition.

However prior to the onset of major gas flow, two precursor events were visible in the data, **Figure 7-30 A** inset graph. As gas pressure begins to increase so does the water pressure in all of the radial (and EC-2) filters. This is interpreted as a simple hydrodynamic response, common in gas tests, caused by the displacement of residual water trapped within the injection system at the start of gas testing. It should not be confused with the onset of gas flow. Indeed, by day 55, most of the residual water had been displaced and porewater pressure and outflow begin to decay back to their pre-gas injection values.

As gas pressure continues to increase, a second precursor event is observed signified by the rapid increase in flux out of the core. This occurs at day 59.8 and is accompanied by incremental steps in all stress and radial filter pressures, though the magnitude of the individual responses is dependent on their location. This suggests a non-uniformly distributed response, indicative of a localised flow. While this event is accompanied by an increase in outflow rate, the composition of the flux is unclear. However, what is clear is that gas migration within the clay, associated with the second precursor event, only occurred when gas pressure exceeded the radial component of total stress. Careful analysis of the data suggests that a gas pressure around 0.2 MPa higher than the average total stress (including the axial component) was required to initiate gas flow. This can be construed as a measure of the tensile strength of the material and is in line with data presented by Dehandschutter et al., (2005) who suggest a value around 0.1 MPa.

To examine the temporal and spatial development of pore pressure during gas injection a number of simple spider plots (**Figure 7-31**) have been created. Here, the axes of the graph have been orientated with that of the sample, in effect, providing a perspective equivalent to that of looking along the major-axis of the core. Prior to gas entry, day 51.18, pore pressure is equally distributed both around the circumference of the core and along its axis, creating a regularly shaped plot. Shortly after initial gas entry at day 60.19, pore pressure within the clay increases and an anisotropy in the distribution of pressure is clearly observed. By day 65.08, the anisotropy has become more pronounced as pore pressure continues to non-uniformly increase. Not surprisingly, the largest values of pressure are located at the furthest point of measurement away from the backpressure filter EC-1. Following major gas breakthrough, the magnitude, distribution and anisotropy of pore pressure within the sample changes again with pressure rapidly increasing as gas penetrates individual radial filters.

In **Figure 7-30 B**, these events are clearly visible as rapid increases in filter pressure e.g. filter 9 at day 60.1. These are often correlated with changes in total stress as evidenced by the radial load cell 3 response for this example. That said, once penetrated by gas, the pressure within the filter closely mimics that of the injection system, indicating a minimal drop in gas pressure along the flow pathway. On the time scale of these observations, it also suggests that these pathways are relatively stable once formed and are able to conduct gas for the duration of the test.

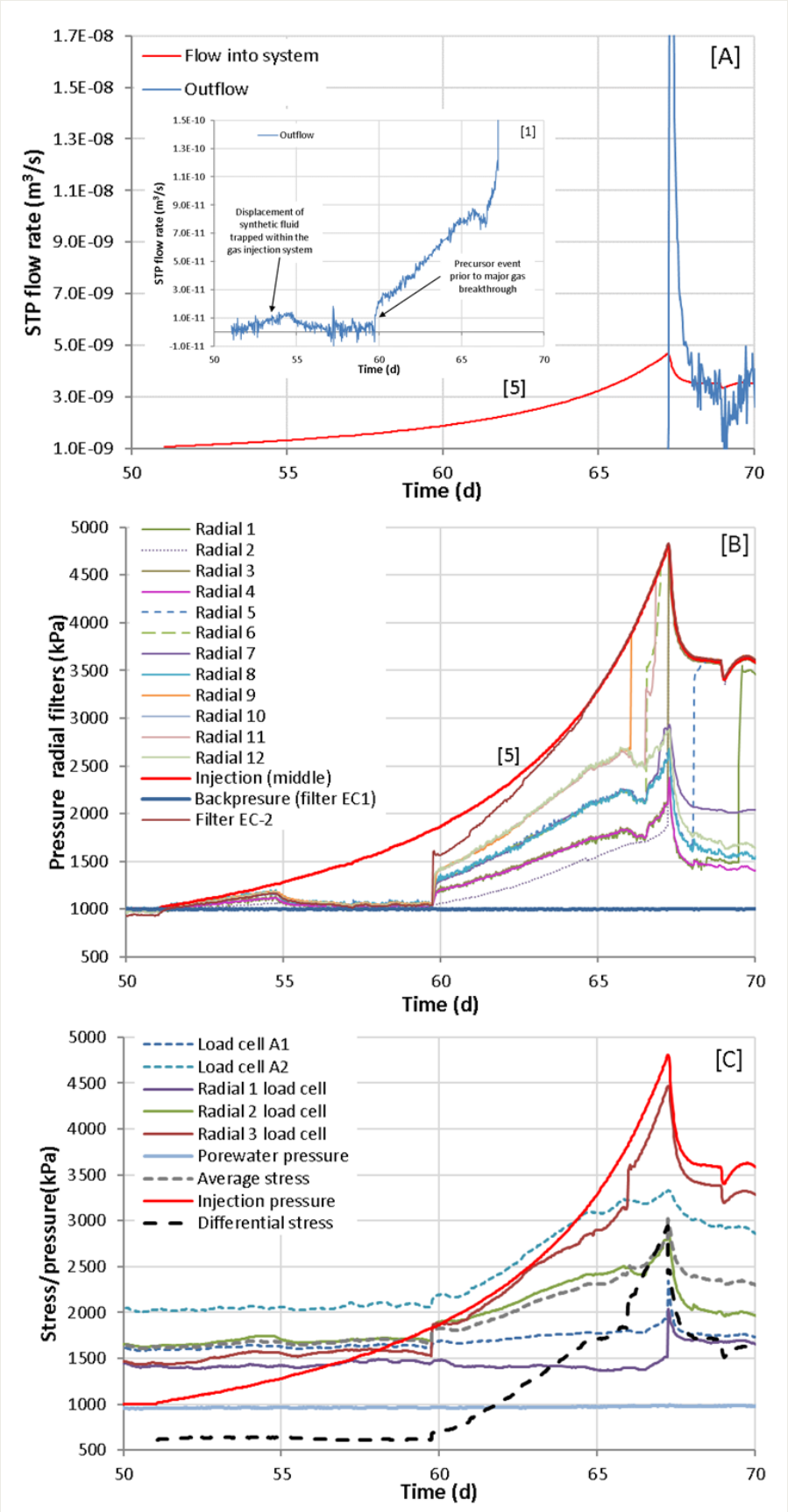

Figure 7-30: Data from gas injection test, sample Covra-3. [A] STP flow rate into system and out of core; [B], development of pore pressure around the sample; [C] evolution of total stress. Value in parentheses represent test stage numbers.

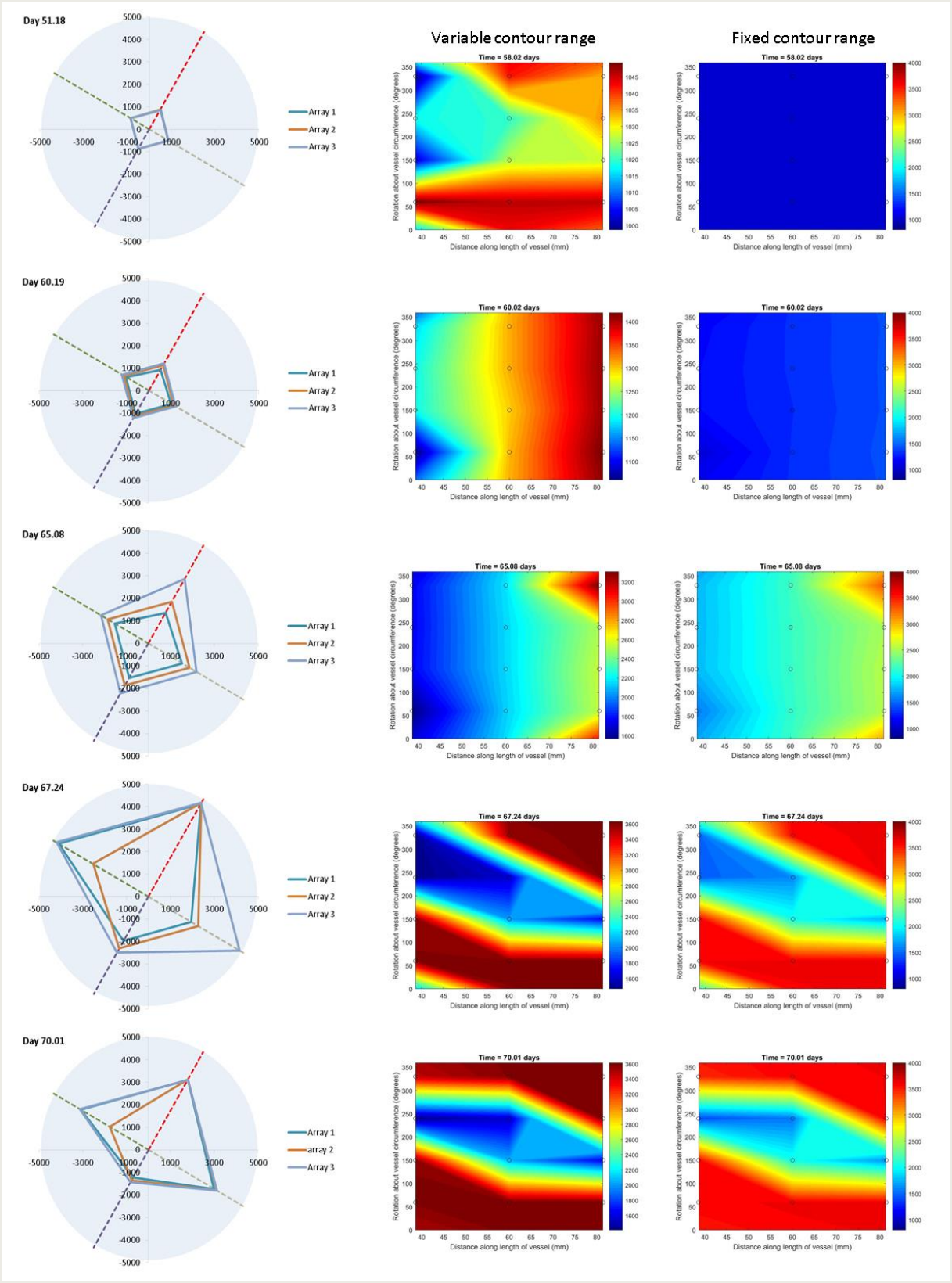

Figure 7-31: Spider and intensity plots showing the variation in pore pressure during gas injection. The anisotropy and localisation of gas flow becomes apparent in these plots.

Following the peak in gas pressure (**Figure 7-30 A**) gas pressure exhibits a spontaneous negative pressure transient approaching a quasi-steady state around day 68. However,

around day 68.9 the injection pressure and flux out of the sample spontaneously decrease. As outflow from the core declines, injection pressure begins to increase once again, leading to a second much smaller peak in gas pressure before returning to a value similar to that at day 68.

Figure 7-32 shows a series of spider plots illustrating the temporal and spatial development of radial stress within the sample. Prior to gas entry (day 58.01) stresses are approximately equal. However, as gas penetration of the sample continues (days 60.02 and 65.08), and outflow through EC-1 begins (day 67.25), an anisotropy in the pattern of radial stress develops. As with pore pressure, stress increases are biased towards the end of the sample furthest from the backpressure filter EC-1. However, it is not clear from the data if this is caused by the spatial distribution of gas pathways or the complex nature of the boundary condition imposed during this test. Either way, this behaviour induces relatively large differential stresses within the sample (**Figure 7-30 C**), which peak at a value around 2.9 MPa, coinciding with major gas breakthrough. Further work is therefore required to better understand the number, aperture and distribution functions for these features. Axial stress behaves in a similar fashion, exhibiting a pronounced sensitivity to the injection pressure following initial gas penetration of the clay. Unfortunately, the test was prematurely terminated at day 71 when synthetic water from the injection pump was accidently pumped into the sample at 375 μl/h.

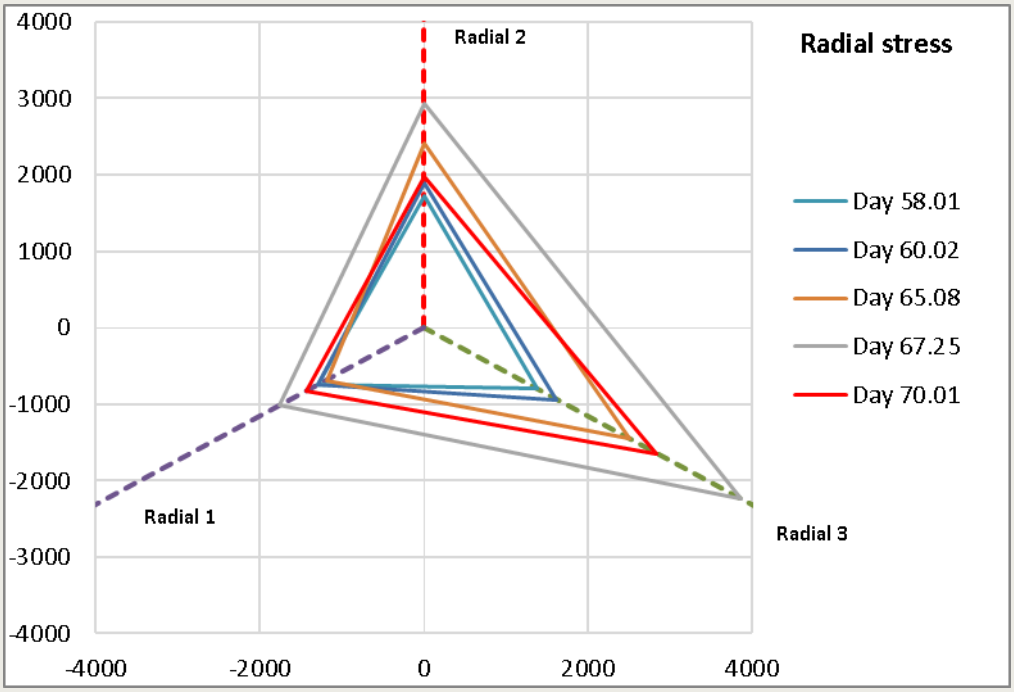

Figure 7-32: Spider plot showing the temporal development of radial stress within sample Covra-3. Radial 1, 2 and 3 are located closest to the backpressure filter (EC-1), sample mid-plane and end-closure (EC-2) respectively. Note, the magnitude of the stress response is denoted by the vector measured along the respective axis. When stress is equal at all points in the sample, the data plots as an equilateral triangle.

7.2.4 Discussion

Horseman and Harrington (1994) highlighted the potential importance of dilatancy as a fundamental process governing the advective movement of gas through Boom Clay. This work suggested that gas migration, stress and porewater pressure were integrally linked and that pore sizes within Boom Clay were of sufficiently small diameter to prevent

capillary entry, resulting in dilatant flow and the creation of new porosity. This hypothesis was further supported by Harrington et al., (2012), who following the injection of gold and titanium nano particles, observed aggregates of material encased within clay, confirming the presence of dilatant pathways during gas migration. In **Figure 7-30** initial gas entry occurs when gas pressure marginally exceeds the local value of total stress. The magnitude of these pressures is substantially less than those previously reported for gas flow under isotropic *in-situ* conditions, Horseman and Harrington (1994). However, this is not surprising as total stress, in the test geometry of a constant volume cell, is governed purely by the swelling potential of the clay. The capacity for the clay to utilise intergranular matrix support, in a standard poroelastic sense, is minimal as no external force is applied to the sample. As such, swelling pressure and the strength of the clay provide the only mechanisms through which the clay can withstand the force applied by the gas pressure.

Following gas entry, **Figure 7-27** demonstrates that further gas flow is strongly coupled to total stress and porewater pressure. As gas pressure continues to increase and conductive pathways develop, the asymmetry in stress and pore pressure distribution within the clay increase. This behaviour is indicative of localised gas flow. During this phase of migration, large differential stresses (i.e. maximum minus minimum stress) develop within the clay, peaking at 2.9 MPa, coincident with major gas breakthrough. These differential stresses are significantly larger than both the tensile and shear strengths reported for Boom Clay under Mol *in-situ* conditions (Wiseall et al., 2015). Clearly, some form of 'stress shielding' appears to be in operation within the clay during gas flow. While the mechanism providing this support is unclear, intergranular locking combined with the constant volume boundary condition, may help to explain this behaviour.

As gas further penetrates the clay, an increase in all pore pressure sensors is observed. While the rate of change in pressure varies from one location to the next, the composition and nature of the accompanying flux can be analysed. Based on an initial estimate of gas and water volumes (within the injection system), it is possible to estimate flux into the clay as a function of time, using a modified form of the ideal gas law corrected for the compressibility of the synthetic fluid and test apparatus. While the calculation is very sensitive to the assumed start volume of gas, it can be used to infer flux behaviour. **Figure 7-33 A** is a plot of flow into and out of the core corrected back to experimental conditions, thereby removing the compressibility of the permeant. In this way, if the flux was predominantly aqueous in nature, then in and outflow would coincide, plotting on top of each other. Inspection of the data indicates that as gas pressure exceeds the total stress and begins to propagate within the clay, porewater is slowly squeezed out of the sample as gas pressure continues to increase and new pathways form. Analysis of the data suggest that between 1.6 and 3.7 ml of water is displaced from the sample.

However, this value should be treated with caution and not necessarily viewed as classical 'desaturation' of the clay. Because large differential stresses are induced as the gas attempts to locate a suitable sink, the gas pressure exerts a force on the system, in effect, equivalent to an increment in total stress. In reality, it seems reasonable to assume that such behaviour will result in localised consolidation of the clay. However, this is not unexpected, as the complex nature of the drainage pattern combined with the unrealistic zero strain boundary condition imposed by the pressure vessel walls, create an environment amenable to the generation of artificially high gas pressures. In a Netherlands repository concept, hosted in deformable Boom Clay, the boundary condition would be fundamentally different, such that the clay would be able to dilate and thereby moderate the potential to generate high gas pressures.

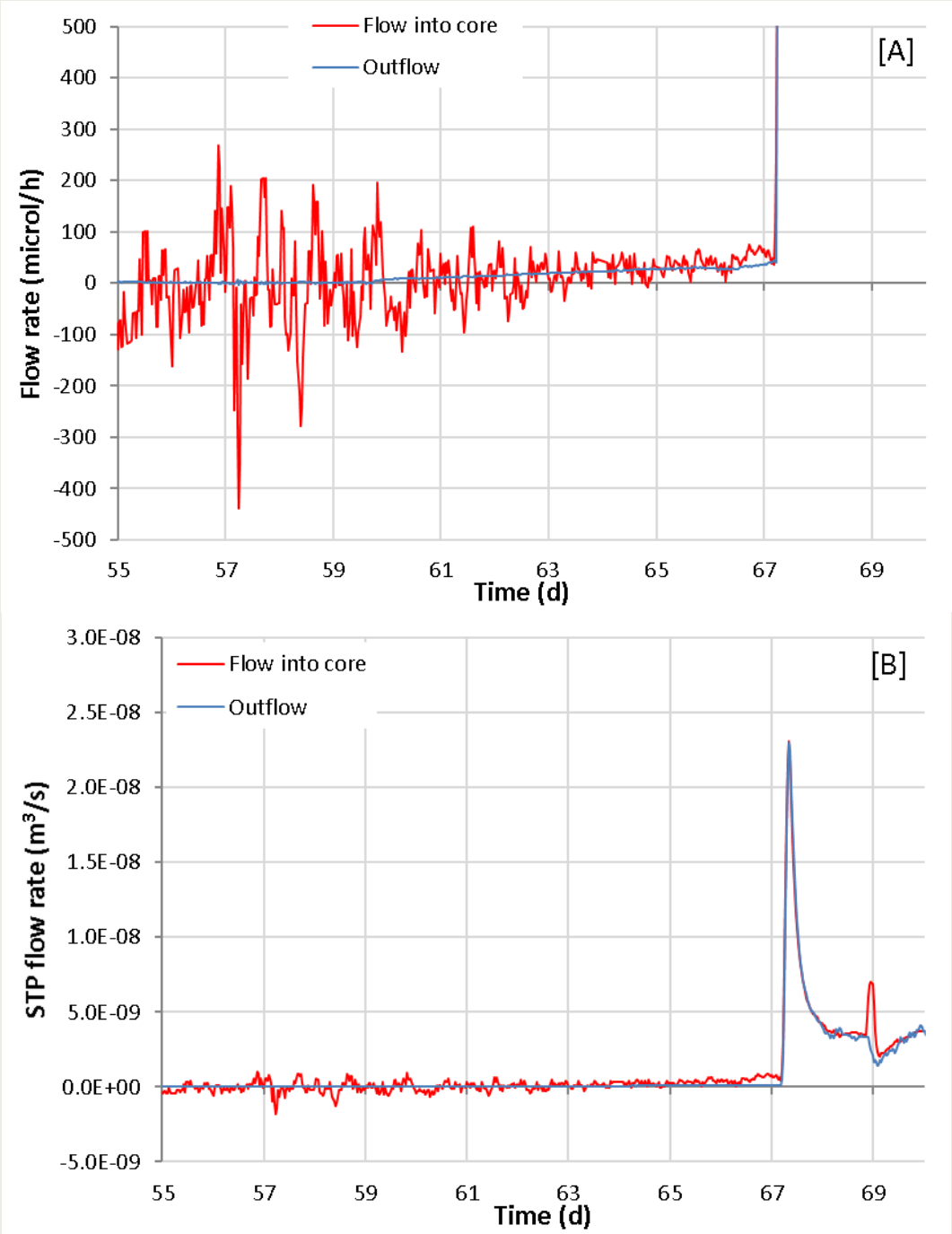

Figure 7-33: Plot of inflow and outflow from the clay during the precursor event prior to major gas breakthrough [A] and subsequent outflow [B]. Inflow to the clay is estimated using the ideal gas law modified to compensate for changes in volumetric flow rate due to compressibility of the synthetic solution and test apparatus. In [A] calculated values are converted back to experimental conditions to remove compressibility of the permeant from the equation. Under these conditions, if the flux is predominantly aqueous in nature then in and outflow will coincide.

Once major gas breakthrough occurs, **Figure 7-33 B** shows that flux in and out of the core are approximately equal at all times, suggesting that the volume of gas pathways remains approximately static. The exception to this observation is just before day 69 when inflow spontaneously increases and outflow decreases. The cause for this instability in the gas pathways is unclear.

Unlike previous tests performed on compact bentonite (Harrington et al., 2017; Graham et al., 2012; Harrington and Horseman, 2003), following major gas breakthrough total stress within the Boom Clay, is, on average, significantly lower than the value of gas pressure applied to the injection filter. This indicates only part of the gas pressure is transmitted to the surrounding clay, suggesting the presence of an intergranular stress. However, this cannot be the only cause for the behaviour noted, as radial load cell 3 (**Figure 7-30 C**) is similar in both magnitude and form to the gas injection pressure. This suggests that proximity of the gas pathways to the point of measurement may play an important role in the subsequent values measured, and given the variation in stresses observed, only a relatively small number of gas pathways may have formed.

Data also demonstrates that the drop in gas pressure along the conductive pathways from the central source to radial filters is very small (**Figure 7-30 B**) such that very high gas pressure gradients must therefore exist close to the sink filter. There is no evidence in the data for a significant pressure drop at the length-scales of the pathways generated within this test.

It is also worth noting that during the initial phase of hydraulic testing, two of the radial filters (numbers 1 and 5) appears to be in direct communication with the central injection filter (**Figure 7-27 A**) simultaneously registering the same value of pressure as that applied to the injection filter. However, as the test progresses, pressure in both filters decrease to values in line with those of the neighbouring transducers. In **Figure 2-3 A**, a series of linear micro-cracks are visible, raising the possibility that a similar feature(s) may have been present at the onset of hydraulic testing. This would certainly account for the rapid pressurisation of the radial filters, and as water moved along the micro-crack induce swelling of the clay. This hypothesis is supported by the data which exhibited a slow progressive decrease in pressure, symptomatic of a reduction in permeability linked to pathway self-sealing. If correct, it would suggest that micro-cracks within Boom Clay can remain conductive at total stresses around 1.5 MPa i.e. the swelling pressure + external porewater pressure (**Figure 7-26 C**).

That said, by the end of the hydraulic testing the sample exhibited a linear distribution in pore water pressure suggesting good hydraulic symmetry along the length of the core and potentially homogenous hydraulic properties. However, the complex nature of the drainage boundary condition means that further work is required to fully quantify hydraulic anisotropy and symmetry.

Outcomes:

1. Gas entry in Boom Clay occurred at a pressure marginally greater than the local total stress. This pressure was substantially lower than previous values due to the nature of the boundary conditions.
2. Following gas entry, gas flow is strongly coupled to total stress and porewater pressure.
3. As gas continues to penetrate the clay (prior to breakthrough), anisotropy in the distribution of stress and porewater pressure increases, varying temporally and spatially within the sample.
4. Prior to major gas breakthrough large differential stresses are generated within the clay. These are transmitted through the fabric and water expelled, most likely through localised consolidation of the clay.
5. Peak differential stress occurred at major gas breakthrough.
6. On the length scales of this test, data demonstrates a minimal drop in gas pressure along the conductive pathways, which once formed appear relatively stable. This may be linked to the localised consolidation described in bullet 4.
7. Shortly after breakthrough flux in and out of the core are approximately equal, suggesting the volume of gas pathways remains roughly static.
8. During hydraulic testing evidence for self-sealing of micro-cracks was observed.

Recommendations:

1. Additional tests, performed at repository depths of interest to Covra, are required to better understand the gas migration behaviour of Boom Clay and to reduce uncertainty through the acquisition of statistically meaningful high calibre data. Key questions to investigate include:
    a. What is the minimum pressure at which gas will become mobile and enter the clay?
    b. How much interstitial water is displaced as a direct consequence of gas flow either through visco-capillary type processes or compression of the surrounding clay matrix?
    c. What is the maximum gas pressure that can be developed and how sensitive is this parameter to the number and location of sinks?
    d. What is the nature of the observed couple between gas flow, gas pressure, total stress and porewater pressure, and what impact does this have on effective gas permeability?
    e. How stable are gas pathways once formed, both at steady state and at low volumetric flow rates close to the capillary threshold value?
    f. Is gas flow dispersed through the buffer or focused along a relatively small number of preferential pathways?
    g. What role, if any, do system interfaces (canister, engineering disturbed zone (EBS) and rock wall) have in governing the movement of gas in the EBS?
    h. What controls the direction of the gas flux?
    i. Do the processes outlined above temporally evolve resulting in a locus of parameters?
    j. Does gas have any long-term effects on barrier performance?
    k. What effect does the boundary condition (constant stress or constant volume) have on all of the above properties.

7.3 *Testing in an isotropic arrangement using nanoparticles*

A test in an isotropic configuration and using nanoparticles was conducted to depict gas migration pathways through the Boom Clay.

7.3.1 The isotropic apparatus and experimental methodology

A gas migration test using gold and titanium nanoparticles was conducted in an isotropically constrained sample of boom clay. The experimental apparatus is shown in **Figure 7-34**. The apparatus and methodology was similar to that of Harrington and co-workers (2012). The experimental apparatus used for isotropic confinement differed from the apparatus used for the constant volume tests presented in section 7.2 in a number of ways. The pressure vessel rested on its base, had only one end closure and the sample assembly was hung within a confining fluid from the underside of the removable end closure. The sample volume was not fixed; it could change over the duration of the experiment. The isotropic confining pressure was applied using a confining fluid, requiring 3 pumps to control the experiment (rather than 2 in the constant volume tests). The injection and backpressure systems were isolated from the confining system by means of a Teflon sheath and lock rings that surrounded the sample assembly. A recessed area in the injection platen placed against one end face of the cylindrical Boom Clay sample held gold and titanium nanoparticles (**Figure 7-35**). A mixture of gold and titanium nanoparticles were used because this has been found to prevent clustering of the nanoparticles allowing them to enter the clay more easily (Harrington et al., 2012). The Teflon wrapping the sample assembly was sealed to the sample using a silicone mastic to prevent the migration of fluid between the sample and the Teflon sheath.

At the start of the test, the sample assembly was prepared in a fume cupboard to contain the nanoparticles and, once sealed, was suspended in the confining fluid. Air was removed from the confining and backpressure systems by flushing with de-ionised water, and any water in the injection system pipework was removed by air flushing. The end closure was attached to the vessel using an o-ring and a push-fit of the lid, which was then supported with a large and especially made locking nut that screwed down onto the top of the vessel. The pipework was then connected up to the outside of the end closure. The pumps and the sample assembly were then leak tested to ensure that all of the connections were tight.

The pumps were calibrated and zeroed prior to the commencement of the test, and calibrated values of pressure were used to control the pumps. The injection pump was programmed to have a shut off pressure that was set just below (by ~120kPa) the confining pressure, so that the injection pressure could never exceed the confining pressure and allow gas to delaminate the Teflon sheath from the outside of the clay, thus bypassing the clay to get to the backpressure end of the sample. Using a shutoff pressure ensures that any fluid migration in the test must be occurring through the clay and not around it. The pump pressures and volumes were measured over the duration of the test period. The pressures were also independently measured by a pressure transducer connected to the pipework next to each pump. These independent transducers made sure that none of the pumps drifted over the course of the test. As with the previous tests, the experimental data were acquired using a microcomputer-based data acquisition system that took measurements every 60 seconds. The total test duration was 50 days.

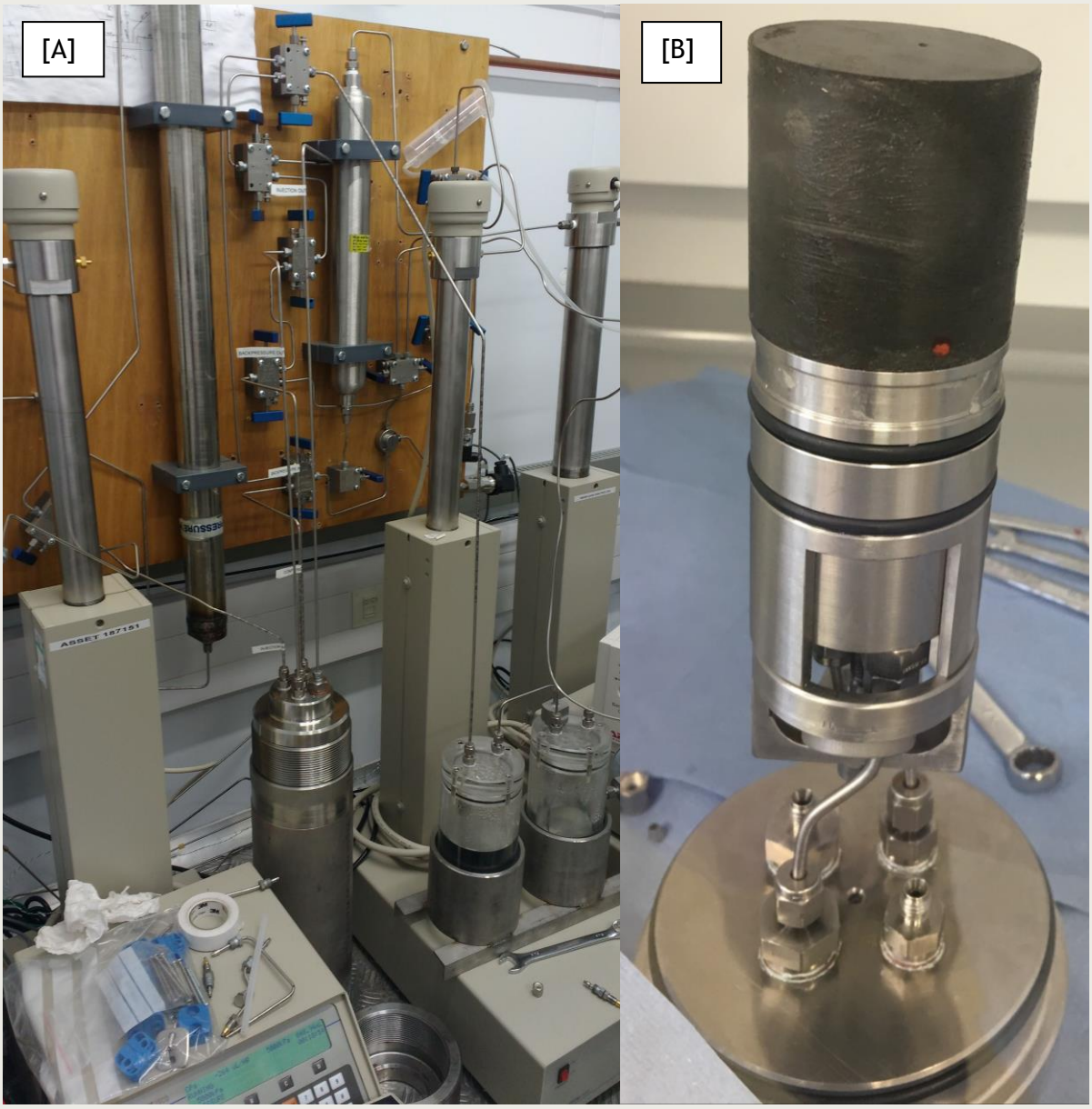

Figure 7-34: [A] Photograph of the experimental apparatus showing the steel pressure vessel, the confining, injection and backpressure pumps, the filtration system for the fluid outlet, the interface vessel for helium attached to a wooden board and the controlling values and pipework, also attached to the wooden board. [B] The sample resting on the first platen; part of the assembly to be suspended from the base of the end closure. A second platen will be fixed at the other end of the sample supplying the backpressure to the downstream end of the sample, and the assembly will be sealed inside a Teflon sheath.

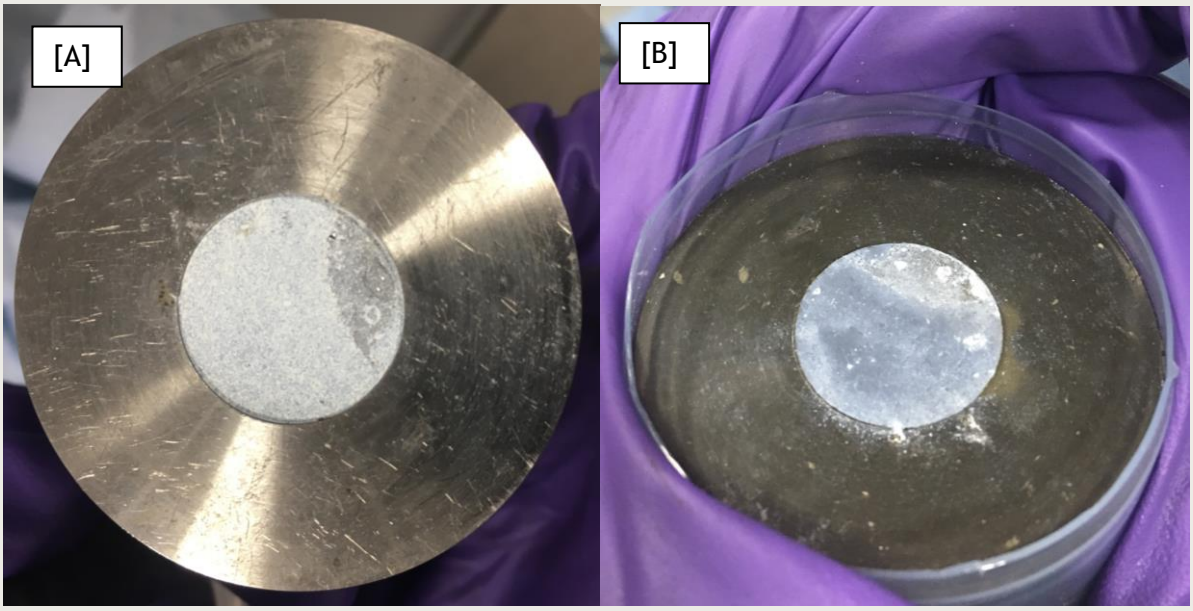

Figure 7-35: [A] The injection platen with gold and titanium nanoparticles filling a recess in the platen, behind which sits a filter that allows the gas pressure to reach the face of the sample. [B] The Boom Clay with a nanoparticle impregnated area originally touching the recessed region in the platen that held the nanoparticles at the start of the test. This is called the 'cake'.

Gas was pressurised at a known volume in an interface vessel at the injection side of the sample assembly. The injection pump was filled with deionised water which was used to control how much gas pressure the injection side of the sample experienced. The gas was injected into the clay through a central filter behind the nanoparticles in a recessed area of the injection platen (**Figure 7-35**). The pressures and volumes were measured at the far end of the sample by the backpressure pump.

7.3.2 Pressures and gas flow rates

At the start of the test, the confining pressure was set to 5MPa and the interface vessel was filled with 265ml of He at 1MPa gas pressure. The gas pressure at 1MPa was applied to the surface of the clay at the injection end of the sample. The backpressure pump was initially stopped and closed to the atmosphere for the first part of the test. The backpressure stayed at a low level (below 250kPa) and very gradually increased. At 26 days, the pressure at the downstream side of the sample started to rise more quickly and the valve was opened to the atmosphere to prevent the pressure from building up and reducing the pressure gradient across the sample (**Figure 7-36**).

The injection pump was set to a constant flowrate of 375µL per hour and the injection pressure increased until it reached the shutoff pressure of 4977.72kPa. At this point, the injection pump was switched to constant pressure mode and the pressure was maintained at the shutoff pressure. When the injection pump was switched to the constant pressure mode, the injection flowrate dropped to ~125kPa (**Figure 7-37**) and the flowrate very gradually decreased to a minimum of ~50kPa at 43 days. At this point, there was a slight increase in both the flowrate and the spread of the flowrate data about the average, indicating gas migration through the sample was occurring.

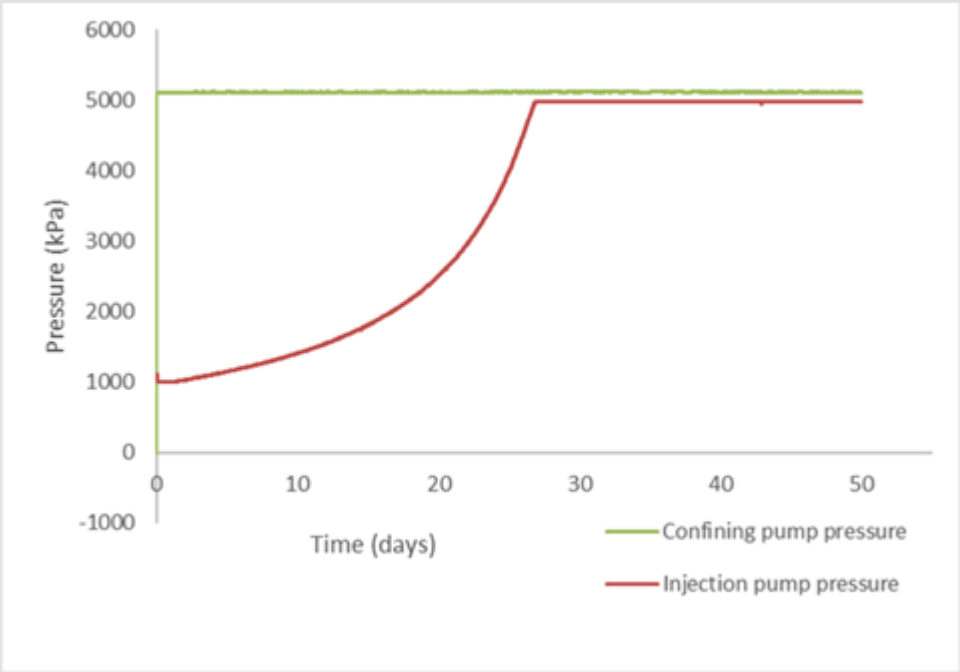

Figure 7-36: The confining (green), injection (red) and backpressure (blue) pump pressures for the duration of the experiment.

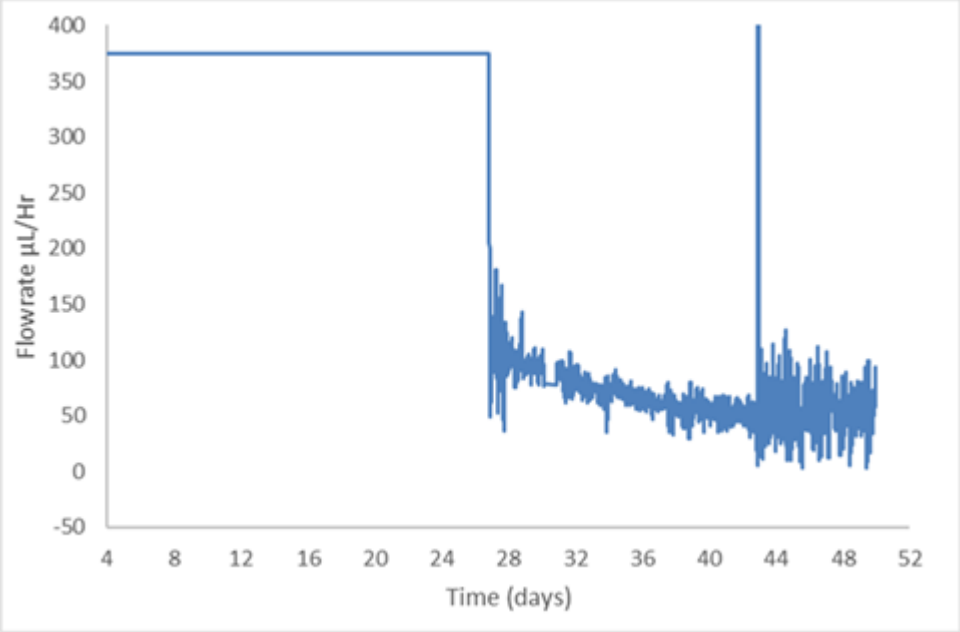

Figure 7-37: A 50 point moving average of the injection flowrate (µL/Hr) over the duration of the experiment (50 days). The moving average removes some of the noise in the data. For the first 26 days of the experiment, the injection flowrate was set to a constant 375µL/Hr. At this point, the injection pressure had almost reached the confining pressure and the injection pump was then set to constant pressure mode at 4977kPa.

7.3.3 X-Ray Computed Tomography scanning

7.3.3.1 Method

Two samples of Boom clay with identical dimensions were scanned by the Manufacturing Metrology Team at the University of Nottingham using a Nikon MCT225 high accuracy X-ray

CT scanner system. The X-ray CT data were acquired using an 180kV, 112µA source. The X-rays were captured on a flat panel Perkin Elmer an1620 detector with a detector pixel size of 0.2mm. One continuous complete rotation of the sample (360°) occurred allowing the capture of 3142 projections in a total scan time of 1.75 hours. All of the pixel data was used without binning, allowing the acquisition of higher resolution images, at the cost of longer exposures and higher scan times; however 2 frames for each projection were averaged. With a 50mm diameter sample, the maximum resolution achievable was 40µm voxel size, although for the smaller region of interest 20µm resolution was achieved. The practical limit for this machine was 2µm, which would have been possible with a much smaller sample size. No post processing occurred, instead a filter of 1mm thickness of pure copper was used to ensure that any artefacts in the data (e.g. beam hardening) were removed. Firstly, a control sample of Boom clay that had not been tested and contained no nanoparticles was scanned to act as a reference for comparison with the experimental test sample. The test sample containing Au and TiO_2 nanoparticles was subsequently scanned.

7.3.3.2 Results

The X-ray CT scanning was able to achieve good contrast scans with nice clear features shown in the clay samples. However, the detection of the infiltration of the nanoparticles into the sample was limited. Clusters of nanoparticles were seen on the top interface of the clay directly beneath the injection platen containing the nanoparticles. Where the Au nanoparticles occurred in the sample, they were shown as white (very high density) regions, distinct from the other features in the sample (such as pyrite) that showed as lighter shades of grey (**Figure 7-38** and **Figure 7-39**).

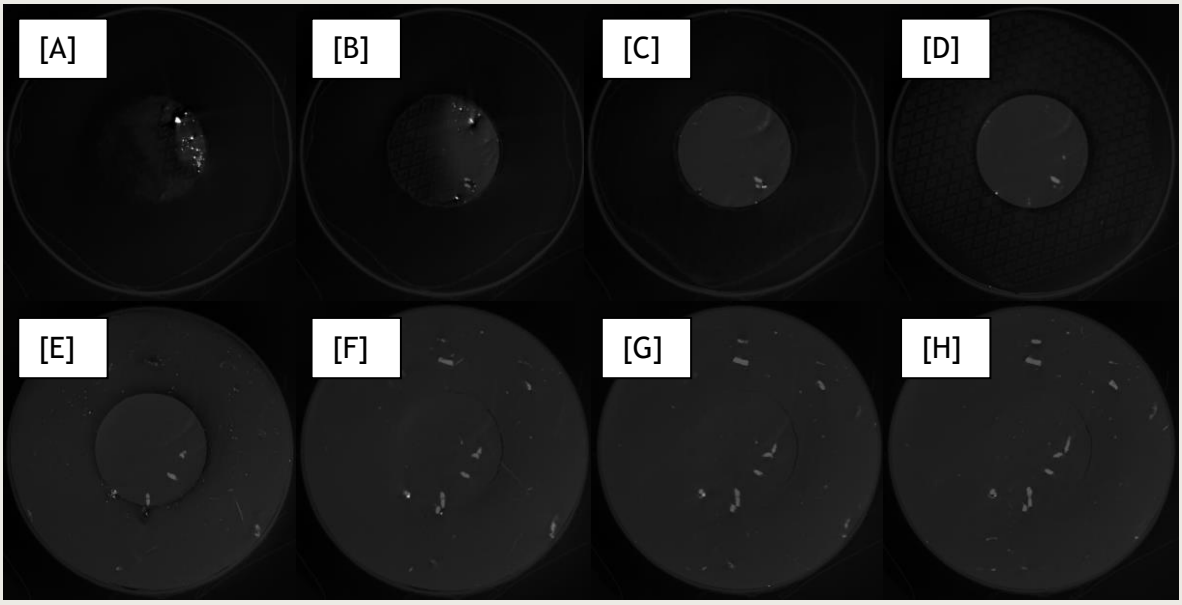

Figure 7-38: A series of 8 aerial-view X-ray CT images through the top section of the sample at 160µm intervals highlighting the nanoparticles (bright white) and the other structural and fabric features (pale shades of grey). The distribution of nanoparticles on the 'cake' can be seen. At the southwest edge of the cake (on images C-H), a bright region of nanoparticles next to a pale grey feature can be seen to descend a short distance into the clay away from the 'cake'.

The nanoparticles that were observed were confined to the topmost 3mm of the sample. They mostly occupied a thin layer at the interface between the injection platen containing the nanoparticles at the start of the test, and the contact with the clay injection surface. In two places, the nanoparticles were observed to descend into the clay beneath the surface. These two locations were at the edges of the nanoparticle 'cake' and are associated with other fabric features in the clay, mapped as a pale grey colour in the XCT

images (**Figure 7-38** and **Figure 7-39**), and as a darker grey colour than the background in the XCT reconstructions (**Figure 7-40**).

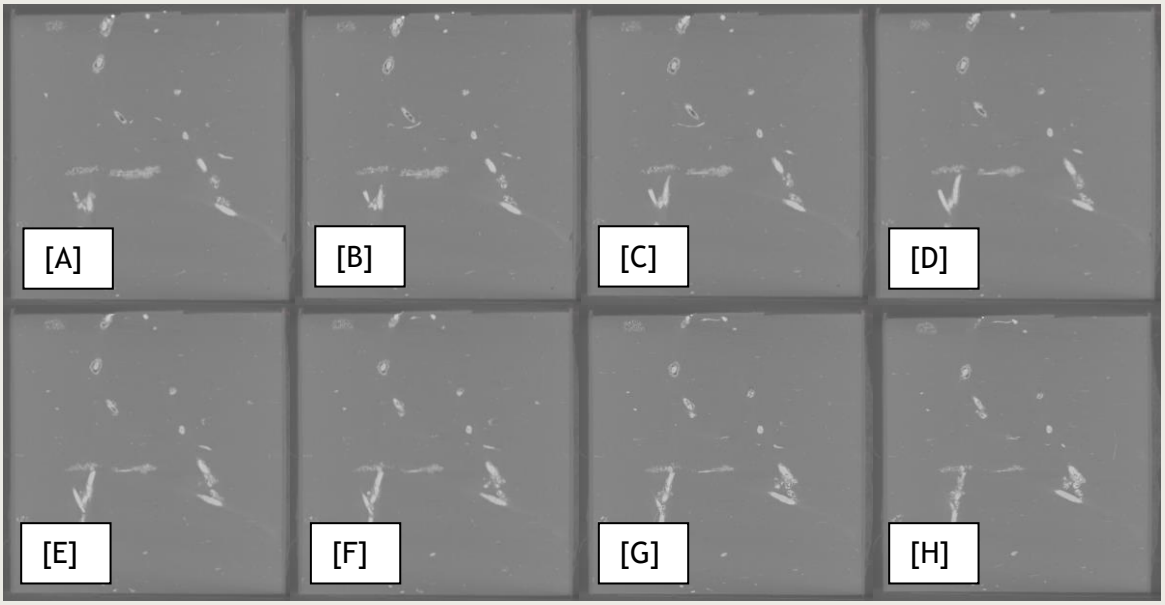

Figure 7-39: A series of 8 side-view X-ray CT images through the entire sample at 40m intervals. The thin layer of protruding clay at the top of the sample is the impression left in the clay due to the recess in the injection platen used to hold the nanoparticles. The nanoparticle 'cake' was observed along this interface. To the left hand side of the 'cake', a bright white region of nanoparticles can be seen extending down into the clay along the edge of a pale grey feature. The heterogeneous nature of the fabric can be seen through the presence of the lighter grey regions (likely pyrite) throughout the sample.

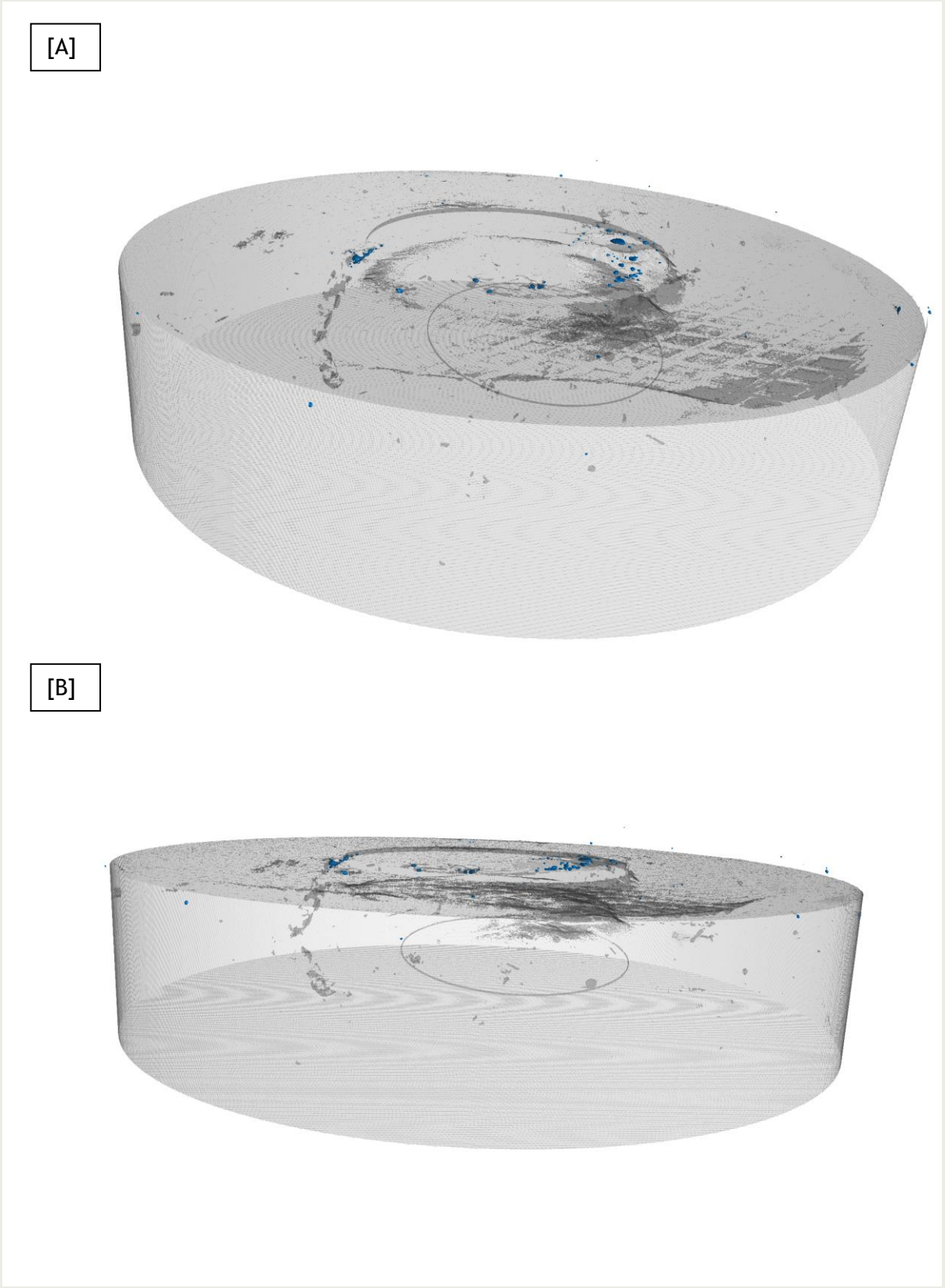

Figure 7-40: XCT reconstructions from two angles of the top most portion of the sample in full 3D geometry as transparent overlays on the imaged locations of the nanoparticle clusters (blue). Both images show nanoparticle clusters on the contact interface between the injection platen and the top surface of the clay where the nanoparticle 'cake' should be located. A higher density linear feature can be seen oriented vertically through the clay below the edge of the

'cake'; it is located on the left side of the images. The top part of this feature has trapped nanoparticles, and the nanoparticles at the greatest depth in the sample lie along this feature.

7.3.4 Environmental Scanning Electron Microscopy

7.3.4.1 Sample preparation

An FEI QUANTA 600 environmental scanning electron microscope (ESEM) equipped with an Oxford Instruments INCA Energy 450 energy-dispersive X-ray microanalysis (EDXA) system with a 50mm^2 X-Max silicon-drift detector was used to make high-resolution observations of the sample. The ESEM, low vacuum (0.98 Torr H_2O) mode was used with a 20kV beam to directly observe fracture surfaces, without a conductive coating in both secondary (SE) and backscattered electron imaging (BSE) modes.

Gold nanoparticles were identified in backscatter images by their elevated brightness caused by their very high backscattered electron coefficient, due to their large atomic number and high density. Identification was confirmed by EDXA, which was also used to map the fractured clay surface to determine the distribution of gold (Au) and titanium dioxide (TiO_2) nanoparticles.

To prepare the sample for SEM imaging it was submerged into liquid nitrogen, embrittling the clay (**Figure 7-41**). It was then axially cleaved using a hammer and chisel to reveal a longitudinal profile through the core. Bedding planes oriented parallel to the end of the cylindrical sample offered planes of weakness which meant that the sample did not break cleanly on the first attempt. Small pieces of clay initially broke off before the sample fractured axially along a clean surface parallel to the length of the cylinder; this enabled high quality imaging to be undertaken.

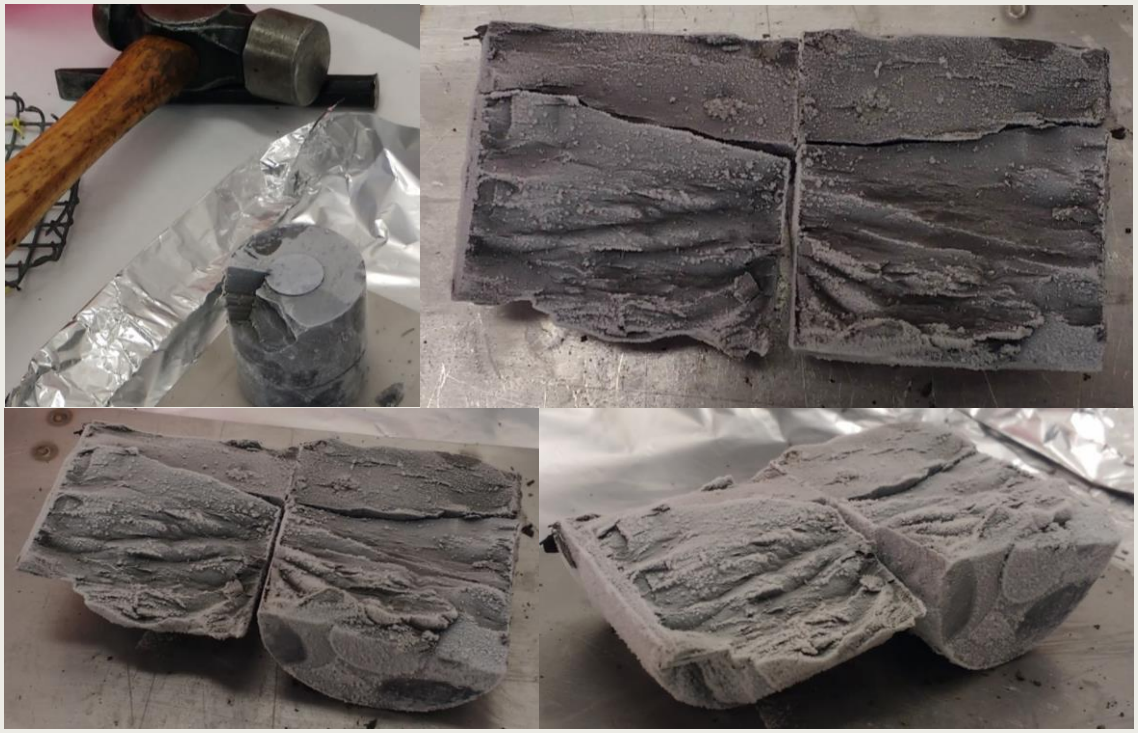

Figure 7-41: After submersion in liquid nitrogen, the frozen and embrittled clay was split axially parallel to its length using a hammer and chisel. Initially pieces broke off the clay, but then the sample split cleanly along a plane of weakness.

7.3.4.2 Gold nanoparticles

Very little gold was found to have been transmitted into the clay from the nanoparticle 'cake' at the injection end of the sample. SEM analysis found rare isolated particles and these were confined to a zone no more than 100 microns from the injection platen's interface with the clay. One of these particles was found to be contained within an aggravated partially healed micro-crack (**Figure 7-42 A**). No evidence of TiO_2 infiltration was found within the sample. The reason for the low Au nanoparticle infiltration can be seen when looking at the Au nanoparticle distribution on the 'cake'. Instead of there being an even distribution of TiO_2 and Au nanoparticles over the surface the Au is clumped together in aggregates, roughly 40 microns in size (**Figure 7-42 B**). Aggregates of this size would not be able to pass into the clay or through any micro-cracks that developed as a result of gas flow through the sample.

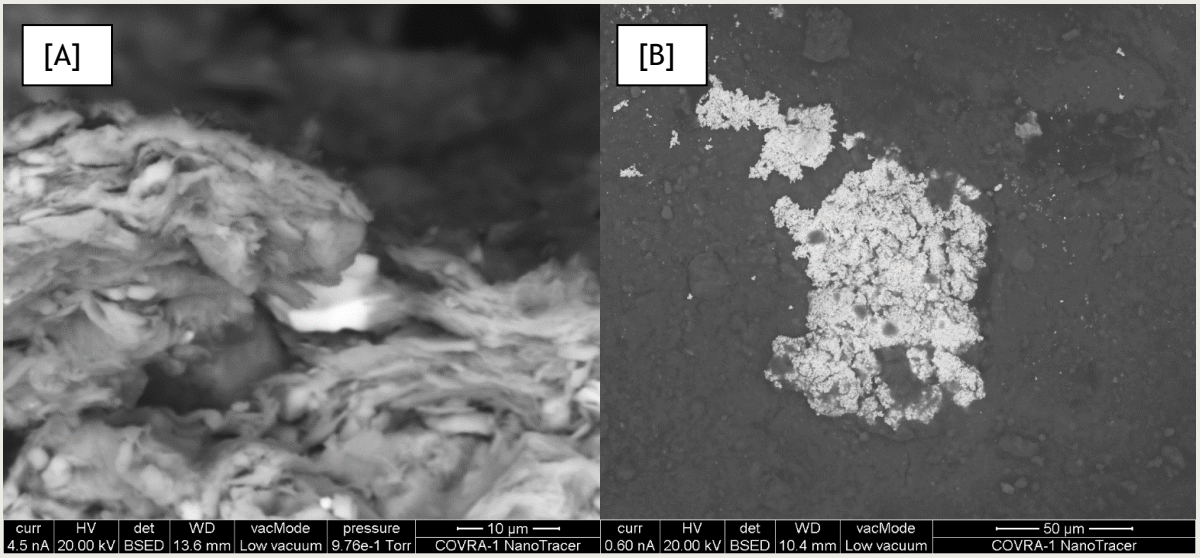

Figure 7-42: A) Au nanoparticle contained within a partially healed micro-crack. B) A clumped aggregate of Au nanoparticles.

7.3.4.3 Fracture framework and structural fabrics

Although few gold nanoparticles were seen within the clay, SEM analysis revealed that the clay fabric had been altered during the experimentation. Horizontal and more steeply (45° and vertical) inclined annealed and open fractures could be seen throughout the fabric. Both the fractures and the pore space will have been increased in size through freeze-drying related shrinkage, therefore care must be taken when interpreting these features. The vertical and horizontal open fractures were most likely formed, or certainly enhanced, by freeze-drying-related shrinkage and they gave the clay fabric a clotted aggregate texture (**Figure 7-43 A**). The 45° annealed fractures may represent fluid pathways within the clay fabric (**Figure 7-43 B**). Rarely some of the micro-fractures are surrounded by a darker coloured clay suggesting that the clay is hydrated; it is possible that later shrinkage has followed these hydrated horizons, although the cause for the hydration is unclear.

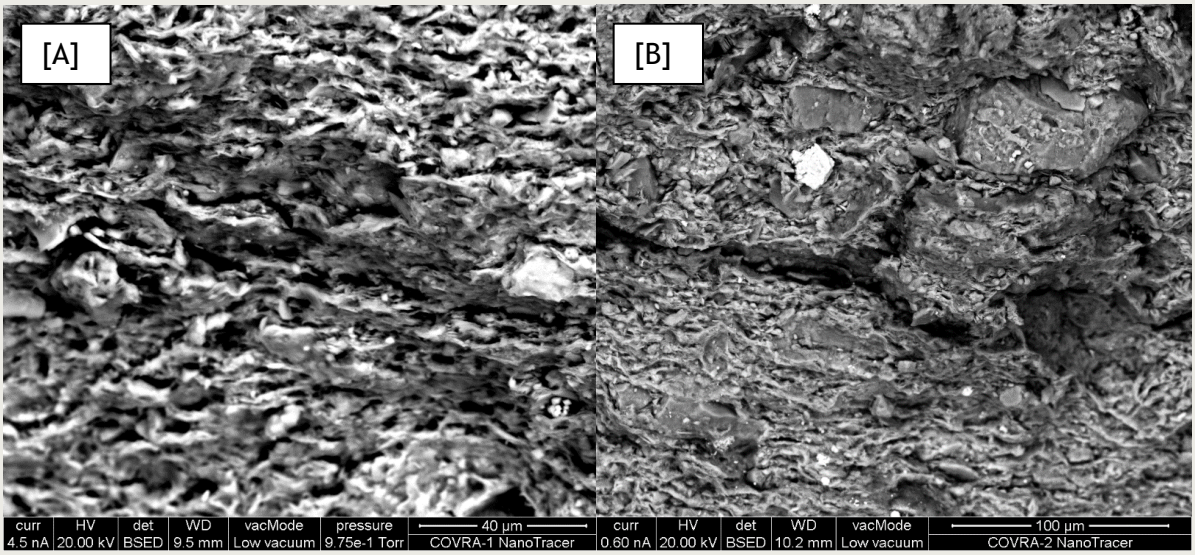

Figure 7-43: A) Clotted aggregate texture to the clay surface due to vertical or horizontal open fractures, formed or enhanced by freeze-drying-related shrinkage. B) 45° annealed fractures.

Pyrite is common throughout the sample as a framboidal-structured material. It is either isolated within the clay matrix as an early diagenetic phase or it is present along linear planes throughout the sample that represent pre-existing fractures (**Figure 7-44**). A few other fabrics of interest were observed within the clay matrix. The upper clay layer (5-10 microns) appeared damaged and liquefied; there were isolated, small and rare Au nanoparticles present in this layer. However, there was no structural relationship and very limited penetration (20 microns). The clay away from this fabric had a very strong horizontal fabric, emphasised by horizontal freeze-drying-related shrinkage cracks.

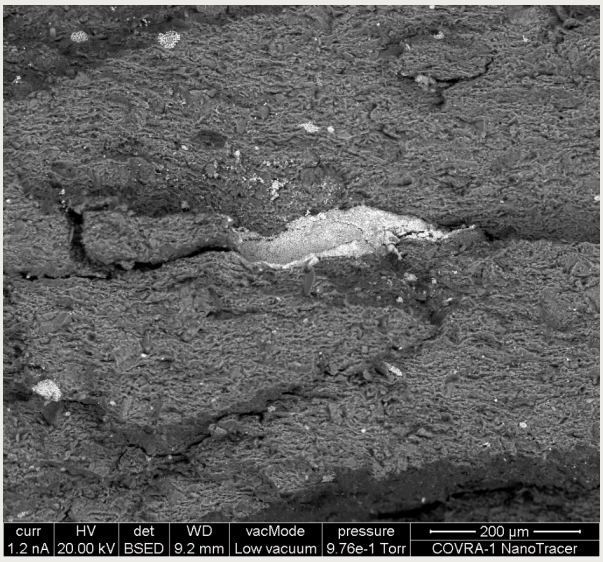

Figure 7-44: Pyrite present along a linear plane representing a pre-existing fracture.

7.3.5 Discussion

Previous studies have been able to use Au and TiO2 nanoparticles to highlight gas migration pathways that have resealed after the gas injection has ceased (Harrington et al., 2012, Wiseall et al., 2015). It was not possible in this study to recreate the technique to image fracture pathways within the Boom clay in detail.

The X-ray CT scanning highlighted some nanoparticles at the top of the sample, although the density recorded was not as high as was expected or as has previously been seen on the post-test sample. This was the first time that X-ray CT scanning had been used to detect the nanoparticles and it is possible that the resolution of the X-ray CT scan was too low to capture the size of the Au nanoparticles. The nanoparticles individually are on the order of a couple of μm across. The Nikon MCT225 machine used for the scanning has a maximum resolution of 20μm. Therefore unless significant numbers of Au nanoparticles were clustered together, it would be unlikely that the X-ray CT machine would be able to detect them. Instead, as each image is constructed from an average of the material at the voxel of interest, the signal would be lost in the background of clay. In addition, clumped nanoparticles would be too large to be carried into the micro-fractures opened by the gas migration, so if smaller clusters of Au nanoparticles were being trapped, they would not be resolved by the X-ray CT. In only two locations did the x-ray CT imaging locate nanoparticles that were beneath the top surface of the clay at the injection end of the sample. These two locations showed a pale grey feature in the clay that intersected the surface and penetrated downwards. It is probable that the heterogeneous fabric at these locations, combined with the proximity to the injection site, allowed larger clusters of nanoparticles to move a short distance through the clay before they became trapped.

A small number of Au nanoparticles were also seen using scanning electron microscopy to have penetrated the top part of the clay sample. However, the majority of the particles were clumped at the interface between the steel platen and the clay in the nanoparticle 'cake'. There are a number of possible reasons for this; one reason is that the nanoparticles got wet. Small amounts of water could have been present in the tubing through the injection platen, although the platens were thoroughly dried after cleaning so this seems unlikely. Alternatively, during loading of the clay with the confining pressure, moisture may have been forced from the clay into the nanoparticle 'cake'. If the gas pressurisation rate was too slow, there may have been time for water to condense on the nanoparticles; there was a time lapse of just over 1.5 hours between the increase of the confining pressure on the sample and the introduction of the gas to the injection end of the sample at 1MPa. Harrington and co-workers (2012) induced gas flow in Boom Clay and mapped the fracture pathways using an Au-TiO_2 nanoparticle mixture. In their test, the nanoparticles entered the sample and were distributed in a region ~20mm into the sample. However, the confining pressure for their test was lower (2.2MPa) and the injection flowrate was set to a constant 1650μL/Hr (4.4 times faster), which meant that the gas pressure at the injection end of the sample reached the confining pressure in a much shorter time. Although they found that adding TiO_2 to the Au nanoparticles, Harrington and co-workers (2012) still found that the Au nanoparticles aggregated and clumped, and were rarely found away from the nanoparticle 'cake' at the injection end of their sample. By contrast with this study however, they found that the TiO_2 was able to spread through the micro-fractures induced by the gas flow, and was located along both sub-horizontal channels in the broken core surface, and sub-vertical micro-fractures that intersected the bedding planes (Harrington et al., 2012).

The SEM imaging in this study has however shown that there are damage zones and fractures that have been induced by the gas flow, even though their pathways have not been recorded by the Au nanoparticles. The 45° annealed fractures represent fluid migration pathways that were active during gas flow and that resealed when the gas flow terminated. The Harrington et al., (2012) study demonstrated that the Boom Clay dilated to allow the gas migration to take place; there is now a wealth of work that supports dilation of fractures in clays as the main transport mechanism (e.g. Wiseall et al., 2015).

Outcomes:

1. Gas flow was induced through the Boom Clay. The gas flow did not occur until the injection pressure had increased to just below the confining pressure.
2. X-ray CT imaging of the sample highlighted areas where the nanoparticles were the most concentrated, but did not pick up nanoparticles throughout the interior of the sample. Rare nanoparticles were identified within the top couple of mm. However, the resolution of the XCT technique is about an order of magnitude greater than the size of individual nanoparticles, and it is therefore not possible to map individual particles with this technique when using a sample of the dimensions used in our testing program.
3. The ESEM and EXDA analysis showed that only rarely were nanoparticles identified within the sample; instead most of the nanoparticles were identified as larger clusters within the 'cake' on the injection end surface of the clay. It is likely that moisture caused the nanoparticles to clump and form aggregates, most of which were too large to fit into the micro-fractures induced by the gas migration.
4. The ESEM analysis has however identified 45° annealed fractures that were formed during the gas migration through the clay.

Recommendations:

1. Perform additional tests on samples of repository depth Boom Clay to further examine gas migration pathways. Improve the nanoparticle visualisation techniques used on the post-test samples.
2. Given the very high density of the Au nanoparticles and the high density contrast between the nanoparticles and the clay, dark field XCT imaging may provide additional insight into the distribution of Au nanoparticles within the complete post-test sample. Dark field imaging is a new technique that identifies radiation that has been scattered by an object, rather than that which passes directly through the sample. This has the advantage over SEM imaging because the sample would not need to be dissected.
3. Higher powered XCT imaging (as can be conducted at the Rutherford Appleton Laboratory) will provide improved resolution without needing to decrease the sample size.

8 Transport properties in fractures

8.1 *Testing in a shear-box arrangement*

A key contributor to the flow of fluids around a radioactive waste disposal facility will be discontinuities, be these fractures, faults or joints. Previous work at the BGS on Opalinus Clay (Cuss et al., 2011; 2014; Cuss & Harrington, 2014) showed that fracture transmissivity is not a static constant and shows considerable variation. For instance, Opalinus Clay undergoes one order of magnitude reduction in flow from wetting of the fracture and swelling of clay minerals alone. A second order of magnitude reduction was noted on shear, taking the flow properties to close of that of the intact rock. Continued shear resulted in increases of flow in a series of events, finally resulting in 4 orders of magnitude increase in flow. A programme of experiments was designed as part of OPERA to investigate the hydraulic flow characteristics of fractures in Boom Clay and to observe whether similar changes of flow are seen in plastic clay.

8.1.1 The Direct Shear Rig apparatus

The custom-made Direct Shear Rig (**Figure 8-1** and **Figure 8-2**) comprised six main components:

1. Rigid steel frame that had been designed with a bulk modulus of compressibility and shear modulus approximately 2 orders of magnitude greater than Boom Clay, resulting in minimal deformation of the apparatus compared to the test sample;
2. Vertical load system comprising an Enerpac hydraulic ram controlled by a Teledyne/ISCO 260D syringe pump, a rigid loading frame and an upper thrust block (up to 72 kN force). Vertical travel of the thrust block was measured by a high precision non-contact capacitance displacement transducer, which had a full range of ±0.5 mm and an accuracy of 0.06 µm;
3. Shear force actuator comprised of a modified and horizontally mounted Teledyne/ISCO 500D syringe pump designed to drive shear as slow as 14 microns a day at a constant rate (equivalent to 1 mm in 69 days) or as fast as 0.5 mm per second along a low friction bearing. The movement of the bottom-block was measured using a Mitutoyo Digimatic Indicator with a full range of 25 mm and an accuracy of 1 µm [tests OPEAR_Shear-1 and OPEAR_Shear-2], or a linear variable differential transformer (LVDT), which had a full range of ±25 mm and an accuracy of 0.5 µm [test OPERA_Shear-3];
4. Pore pressure system comprising a Teledyne/ISCO 500D syringe pump that could deliver water up to a pressure of 25.8 MPa;
5. A state-of-the-art custom designed data acquisition system using National Instruments LabVIEW™ software facilitating the remote monitoring and control of all experimental parameters;
6. A sample assembly comprising two sample holders, where the bottom block was actively sheared and the top block was connected through a linkage system to a force gauge measuring the shear stress along the slip plane. Vertical load was applied to the rock samples by means of a steel thrust block.

The rig was originally designed to achieve 10 MPa normal stress (36 kN force) on a sample 60 mm × 60 mm. At this normal load, it is expected that shear force will not exceed 25 kN. Normal load was imposed by a hydraulic ram that was pressurised using an ISCO/Teledyne, as shown in **Figure 8-2**b.

In 2016 the apparatus was modified to test cylindrical samples. This was primarily due to difficulties in preparing cubic samples of indurated clay-rich rocks. Therefore all tests in the current study were performed on cylindrical samples. Whilst this aids sample

preparation, it does have implications for normal load. The apparatus is designed to deliver a constant force onto the sample. As that sample fractures and slides the contact area between the two halves of the sample reduces. Scoping studies on cubic samples showed that restricting shear to a maximum of 10 % (0.1 strain) meant that the varying stress was not a significant concern. The sliding of circular surfaces past one another reduces contact area more quickly compared to a square surface. Therefore to minimise the effect of changing contact areas strain should be minimised to 5 mm, or 8 % (0.08 strain).

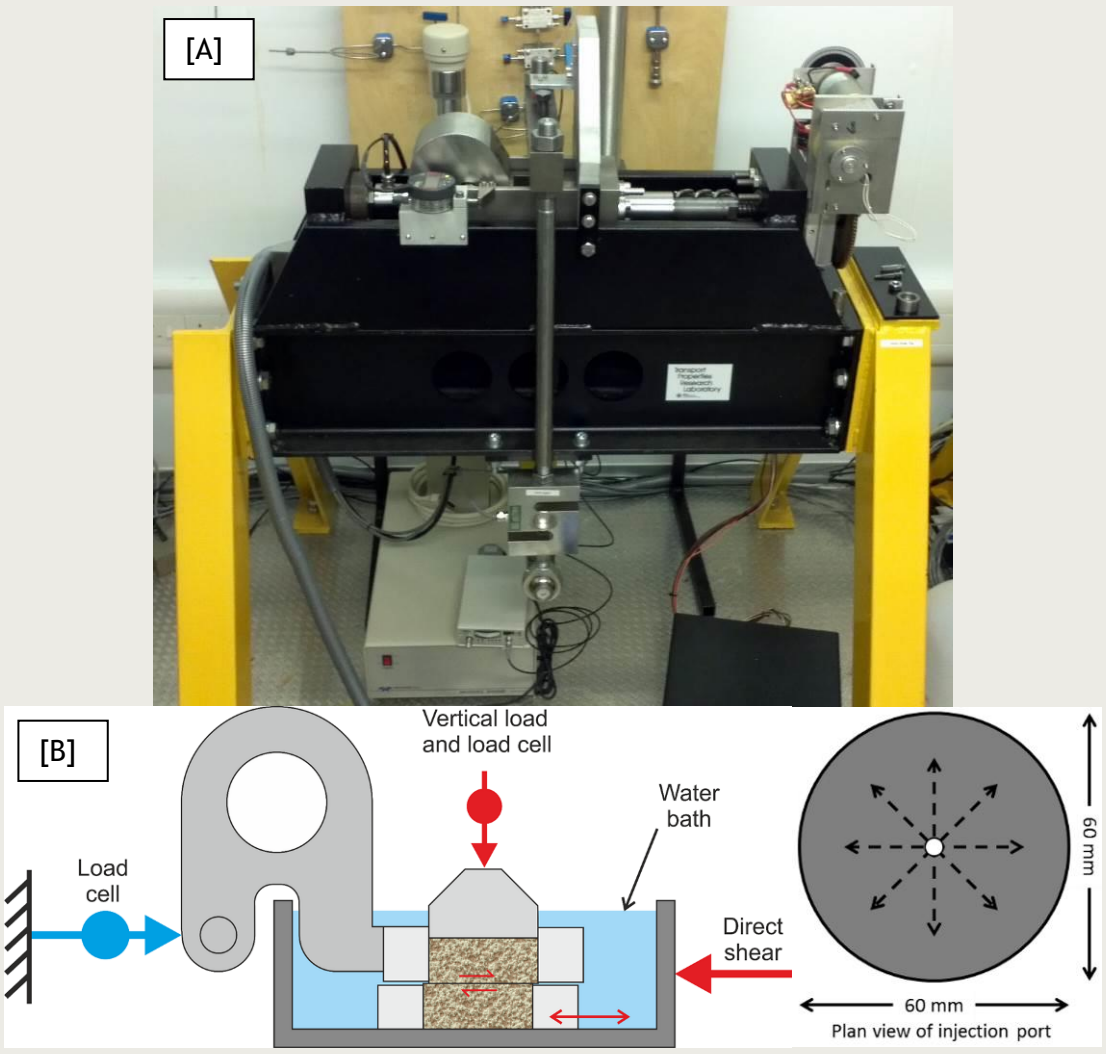

Figure 8-1: The direct shear rig. [A] Photograph and [B] schematic of the apparatus.

Three samples of Boom Clay were prepared, two of Belgian depth and one consolidated to the disposal concept of the Netherlands. These were prepared by machine lathing with a diameter of 60 mm and 53 mm height. The samples were wrapped in cling-film to reduce drying effects. For each sample, two 25 mm high collars were attached that were positioned to be flush with the ends of the sample, thus giving a 3 mm separation between the collars. Each collar then fitted snugly within a larger sample holder. A thrust block was attached to the top of the arrangement to allow normal load to be transmitted through the sample. Two different types of thrust block were used; initially a flat thrust block (as shown in **Figure 8-1 B** was used. For repeat testing a second arrangement was used that included a 4 mm diameter injection bore that delivered pore fluid directly to the fracture surface. The upper sample holder was attached to a linkage system (**Figure 8-1 B**, **Figure 8-2 A** and **C**) that measured shear load transmitted through the sample.

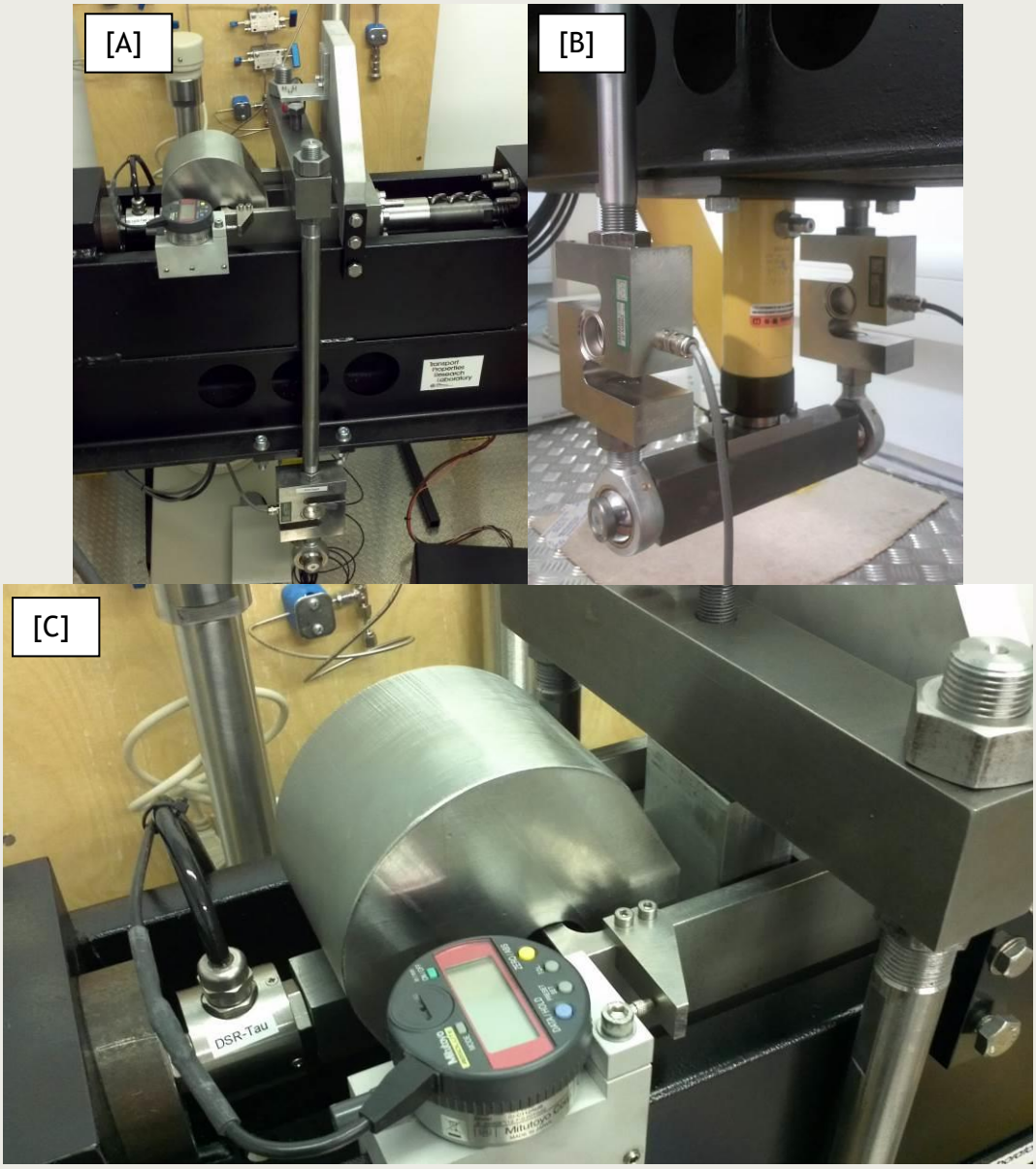

Figure 8-2: Components of the direct shear rig. [A] Loading frame with normal load cells at the bottom. [B] Normal load ram (yellow). [C] Sample assembly, shear load cell and Mitutoyo Digimatic Indicator.

All tests followed a similar protocol, with the only variation being the normal stress applied to the samples and the use of either unconditioned or conditioned Boom Clay:

- Part one of the test used the cylindrical intact samples. Normal load was imposed on the sample and the apparatus was set to constant shear. This subjected the intact Boom Clay to a shear force sufficient to result in failure and the formation of a fracture sub parallel with the shear direction. The test was conducted typically for 100 hours until failure was apparent. This was identified by achieving peak stress, or the reduction in stress to a residual stress condition. The normal load was reduced and the samples were extracted from the apparatus. Both fracture surfaces were scanned to determine fracture roughness (see Section 8.1.3) and a 4 mm diameter hole was drilled in the centre of the top block using a masonry drill. Care was taken that the drill-bit did not get too hot, which would desaturate and/or damage the sample.

- Part two conducted the flow part of the experiment. For this, the top block had the addition of a 4 mm diameter injection bore to deliver fluid directly to the fracture surface. The experiment was set-up so that the top and bottom blocks were in the same position as for the first part of the experiment; taking care that the shear directions were similar and that the two fracture surfaces were matched in profile. Normal load was established and a pore pressure of 250 or 500 kPa was initially established. Due to mismatch between the two fracture surfaces this resulted in high flow rates. To ensure that erosion did not occur the pore-pressure system was switched off and the water-wet fracture surface was allowed to self-seal. Within a few hours it was possible to establish a constant injection pressure of 500 kPa. The time-dependent evolution of this initial flow was monitored. Once flow had reached a steady level the apparatus was set to constant shear, slower than in Part One of the test. The test was conducted until peak or residual stress had been reached. Throughout the test the flow of injection fluid was monitored.

8.1.2 Calculation of fracture transmissivity

Fracture transmissivity was calculated assuming radial flow from the injection hole given the steady state fluid flow rate Q and the pressure head H at the injection point. Steady flow in a cylindrical geometry can be given by:

$$Q = \frac{2\pi T\left(h_i - h_0\right)}{\ln\left(r_o\right) - \ln\left(r_i\right)} \tag{8-1}$$

where T is the transmissivity, h_i is the head on the inner surface with radius r_i, and h_o is the head on the outer surface at radius r_o. Therefore fracture transmissivity is given by:

$$T = \frac{Q\ln\left(r_o\right) - \ln\left(r_i\right)}{2\pi\left(h_i - h_0\right)} \tag{8-2}$$

For the experimental setup r_0 = 30 mm, r_i = 1.96 mm, h_0 = 0.05 m and h_i ~ 100 m, transmissivity (m^2/s) can simply be calculated from:

$$T = 1.183\times10^{-12}\frac{Q}{P_p} \tag{8-3}$$

if the fluid flux (Q in μl/h) and pore pressure (P_p in kPa) are known. This relationship was used to calculate the transmissivity of the fracture throughout the experiment. A correction could be made for the change in contact area between the blocks, and hence the outer radius of the fracture, however scoping calculations demonstrated this had only a negligible effect on the overall calculation compared with the uncertainty of how the fracture contact area changed with time.

8.1.3 Quantification of fracture roughness

Understanding the topography of fracture surfaces (fracture roughness) is important in estimating the hydro-mechanical behaviour of discontinuities within a rock mass. Within a fracture aperture, mechanical properties will be affected by the spatial distribution of contact areas, which in turn affect the stress distribution and ensuing asperity damage during normal and shear loading. Hydraulic behaviour will be modified by the degree of connectivity and tortuosity within the fracture, which affect the permeability, and transmissivity of fluids.

In the present study, laser triangulation method was adopted, whereby the fracture surfaces were scanned using a NextEngine 3D Scanner HD, as shown in Figure 8-3. This produced a 3D mesh model of the fracture surface accurate within an error of ± 65 microns. Algorithms inbuilt within the data acquisition ScanStudio HD software produced clean surface data, which were used in subsequent empirical and statistical analysis.

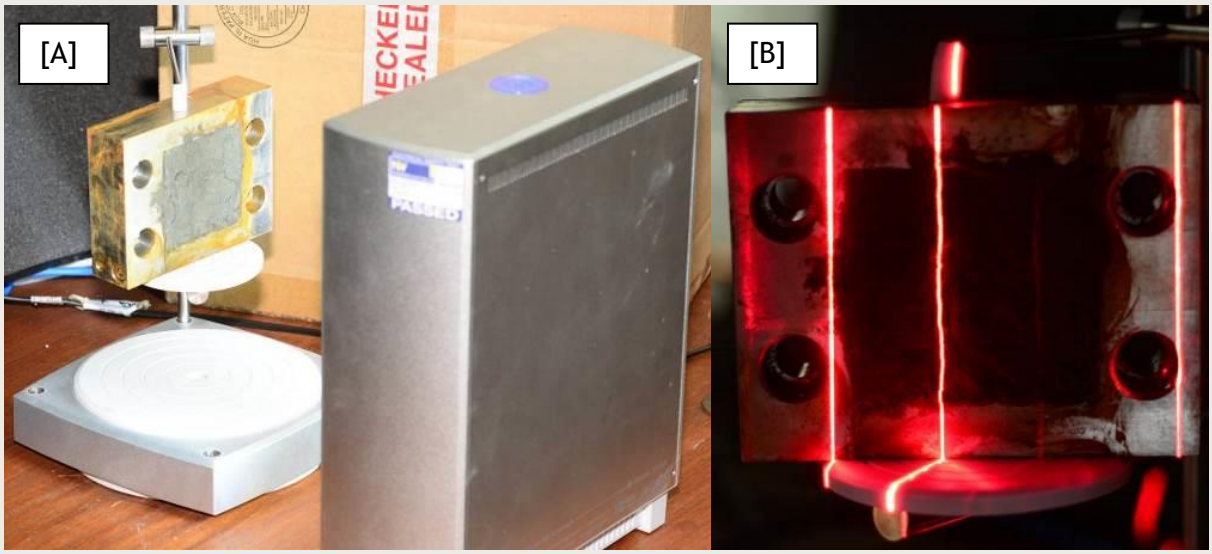

Figure 8-3: [A] NextEngine 3D Scanner with lower block sample. [B] Laser scanning in process.

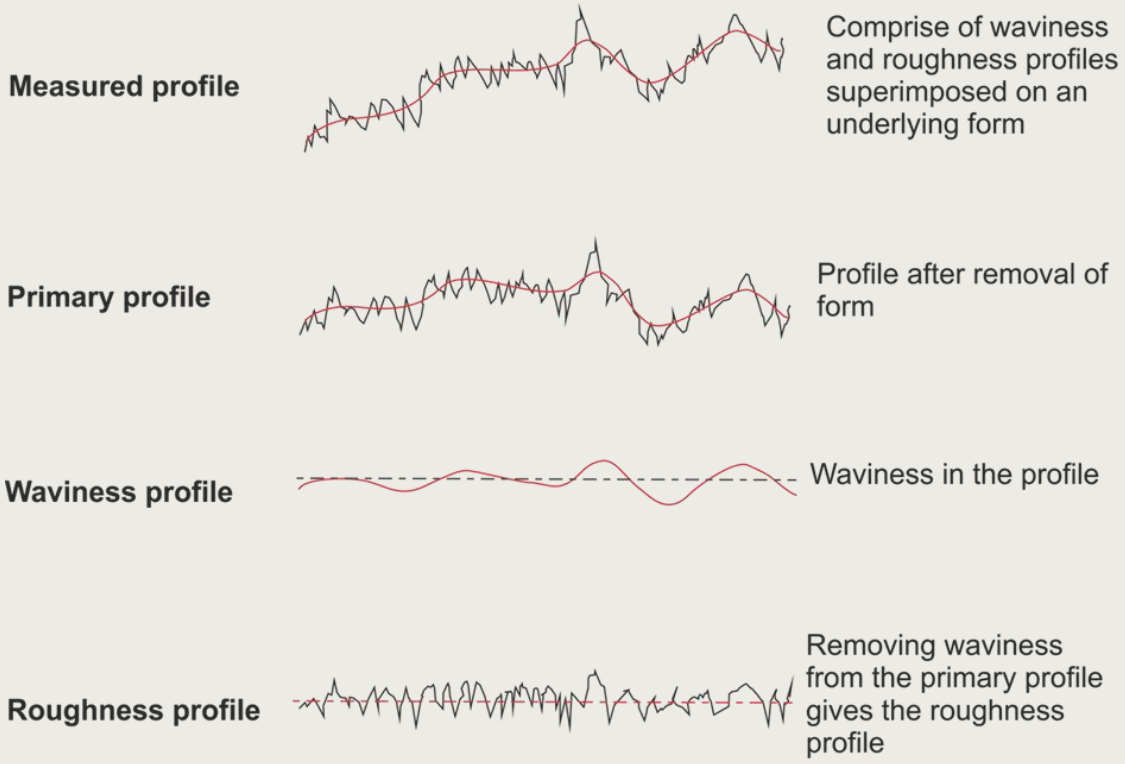

Figure 8-4: Summary of stages involved in analysis of measured profile to obtain a roughness profile (From ASTM standard, 2009).

The measured surface data is usually composed of three components: form, waviness and roughness. The form corresponds to the underlying shape and tilt of the surfaces with respect to the measuring platform. A "corrected" profile obtained by removing form from

the surface data can be used to obtain a 2-D profile that describes the surface texture. This profile after removal of form is usually referred to as the "primary profile". The stages are depicted in **Figure 8-4**.

From the primary profile, the waviness profile is removed by applying a band-pass filter. In theory, difference between the primary and waviness profile gives the roughness profile. However, in the present study no band-pass filters were applied due to lack of uniform waviness in the dataset. Hence, surface roughness calculations were performed on "primary profile" datasets spanning the entire fracture surface. All the data processing and surface parameter calculations were performed in TrueMap 5.0 surface topography software.

8.1.4 Profile and surface texture parameters

A range of parameters (**Table 8-1**) can be extracted from each profile generated from the 3D mesh model. The parameters can be conveniently subdivided into profile parameters (denoted *R*) and area parameters (denoted *S*).

Roughness Average (R_a; S_a)

The average roughness parameter for a profile (R_a) or surface (S_a) is the arithmetic mean or average of the absolute distances of the surface points from the mean plane/profile:

$$R_a = \frac{1}{N}\sum_{n=1}^{N}|r_n| \qquad S_a = \frac{1}{MN}\sum_{j=1}^{N}\sum_{i=1}^{M}|z|(x_i,y_i) \tag{8-4}$$

where *N* is the number of data points in the profile, r_n is the distance from a data point to the mean line, *M* is the number of columns in the surface and *N* is the number of rows in the surface.

Root Mean Square (RMS) Roughness (R_q; S_q)

The Root Mean Square (RMS) Roughness (R_q; S_q) is the square root of average squared absolute height values of the surface profile from the mean line. It is given by:

$$R_q = \sqrt{\frac{1}{N}\sum_{n=1}^{N} r_n^2} \qquad S_q = \sqrt{\frac{1}{MN}\sum_{j=1}^{N}\sum_{i=1}^{M} z^2(x_i,y_i)} \tag{8-5}$$

Peak Height (R_p; S_p), Valley Depth (R_v; S_v), Peak to Valley Height (R_t; S_t)

Peak Height (R_p; S_p) is the maximum height above the mean line/plane (**Figure 8-5**). Valley Depth (R_v; S_v) is the maximum depth below the mean line/plane (**Figure 8-5 A**). Peak to Valley Height (R_t; S_t) is the maximum peak to valley distance (**Figure 8-5**).

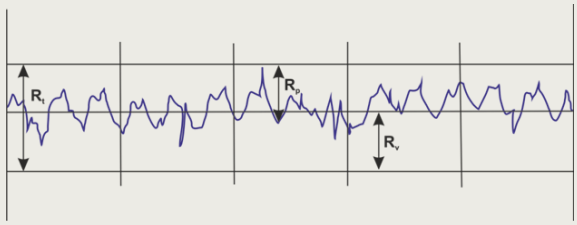

Figure 8-5: Profile Height and Depth parameters.

Kurtosis (R_{ku}; S_{ku}) and Skewness (R_{sk}; S_{sk})

Kurtosis (R_{ku}; S_{ku}) is a measure of the sharpness of the surface/profile. Skewness (R_{sk}; S_{sk}) measures the symmetry of the variation of a profile/surface about its mean line/plane. They are given by:

Kurtosis: $R_{ku} = \frac{1}{NR_q^4}\sum_{n=1}^{N} r_n^4$ $\quad S_{ku} = \frac{1}{MNS_q^4}\sum_{j=1}^{N}\sum_{i=1}^{M} z^4(x_i, y_i)$ (8-6)

Skewness: $R_{sk} = \frac{1}{NR_q^3}\sum_{n=1}^{N} r_n^3$ $\quad S_{sk} = \frac{1}{MNS_q^3}\sum_{j=1}^{N}\sum_{i=1}^{M} z^3(x_i, y_i)$ (8-7)

Gaussian surface has kurtosis value of 3. A surface that is centrally distributed has a kurtosis value greater than 3. A surface that has a well spread out distribution has a kurtosis value of less than 3. A Gaussian surface, having a symmetrical shape for the height distribution, has a skewness of zero. A plateau honed surface with predominant plateau and deep valleys will tend to have a negative skew, whereas a surface comprised of disproportionate number of peaks will have positive skew. By using a combination of the skewness and kurtosis values, it is possible to identify plateau honed surfaces that have relatively flat top, but contains deep valleys.

Texture Direction (S_{td})

Texture Direction (S_{td}) is used to quantify the lay direction of the texture of a surface with respect to the y-axis. The S_{td} parameter is only meaningful for a surface with a predominant texture direction. A good rule of thumb is that if the S_{td} parameter is greater than 0.5, this is an indication of a significant texture.

Texture Direction Index (S_{tdi})

Texture Direction Index (S_{tdi}) is a measure of how dominant the predominant direction is relative to the rest of the surface. The S_{tdi} value is always between 0 and 1. Surfaces with a very predominant texture direction will have a S_{tdi} value close to zero. If there is no significant lay to the surface, the S_{tdi} parameter is close to one. It should be noted that the software used to calculate the textural properties of the fracture surface give the above parameters, which are common in metrology. The parameters have not been converted to Joint Roughness Coefficient/Number commonly used in structural geology.

Parameter	Symbol	Description
Roughness average	R_a ; S_a	Arithmetic mean of the absolute distances of the surface points from the mean plane/profile
Root Mean Square (RMS) Roughness	R_q; S_q	Square root of average squared absolute height values of the surface profile from the mean line
Peak Height	R_p; S_p	Maximum height above the mean line/plane
Valley Depth	R_v; S_v	Maximum depth below the mean line/plane
Peak to Valley Height	R_t; S_t	Maximum peak to valley distance
Kurtosis	R_{ku}; S_{ku}	Measure of the sharpness of the surface/profile
Skewness	R_{sk}; S_{sk}	Measures the symmetry of the variation of a profile/surface about its mean line/plane
Texture Direction	S_{td}	Direction of the texture of a surface with respect to the y axis
Texture Direction Index	S_{tdi}	Measure of how dominant the predominant direction is relative to the rest of the surface

Table 8-1: List of parameters calculated to describe surface characteristics of the test fracture.

8.2 *Test OPERA_Shear-1*

Test OPERA_Shear-1 aimed to test Boom Clay at a stress condition representative of the Mol URL in Belgium, the state at which the material was cored. The shear apparatus is such that pore pressure within the rock is difficult to sustain. Therefore stresses are usually reduced to be representative of the effective stress state. The first shear test was designed to be conducted with a normal stress of 3 MPa with a pore pressure of 1 MPa imposed along the full top surface of the sample, giving an effective stress of about 2 MPa. However, the pore pressure injection system leaked and it wasn't possible to inject water at 1 MPa. In error, the normal stress was not lowered and the experiment was conducted at an effective stress of 3 MPa, higher than the stress state at Mol.

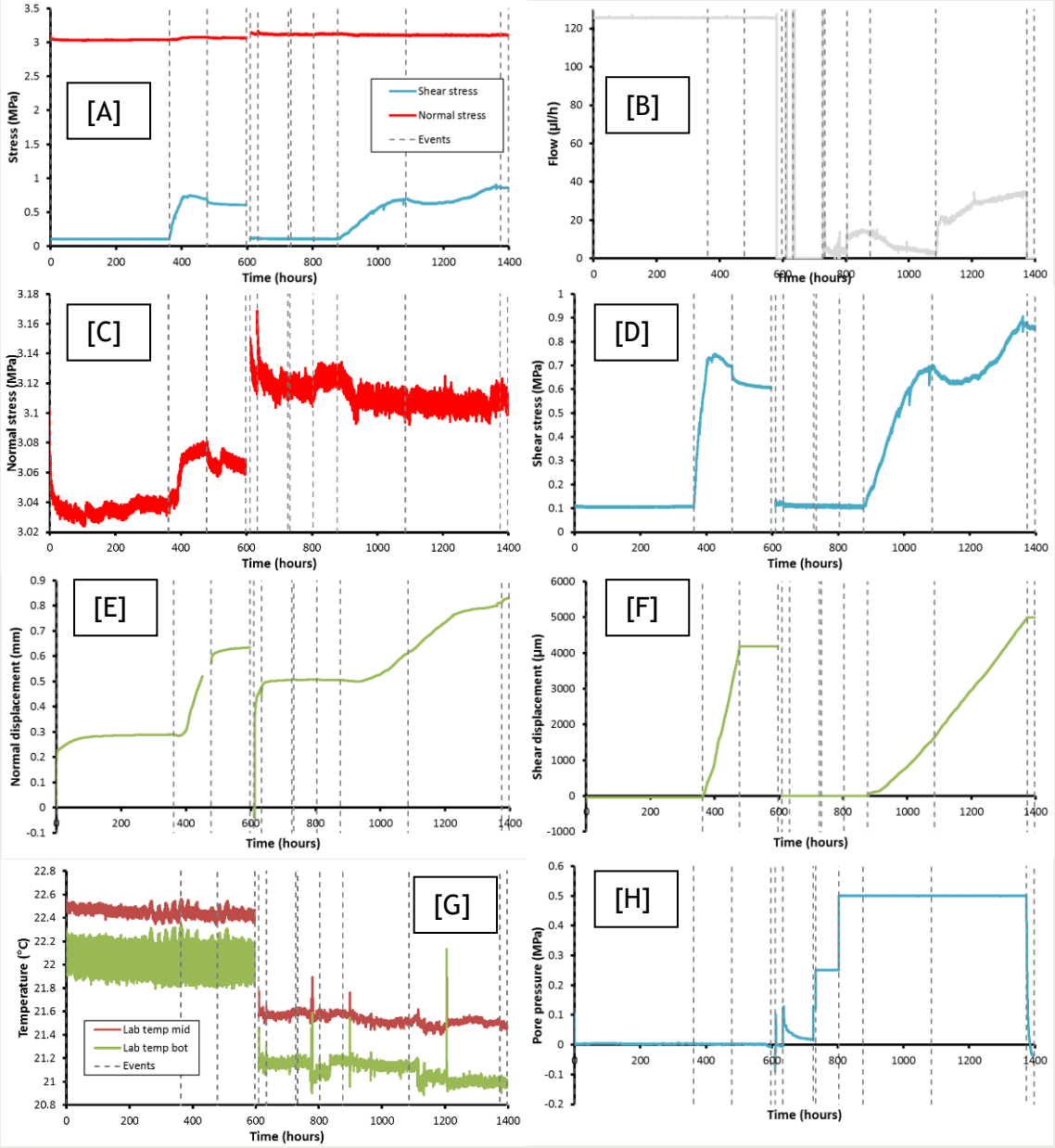

Figure 8-6: Data for the complete test history of test OPERA_Shear-1. [A] Stress history. [B] Flow into the sample. [C] Normal stress. [D] Resultant shear stress. [E] Normal displacement of the sample. [F] Shear displacement. [G] Temperature. [H] Pore pressure. Dashed lines represent events of note.

Test OPERA_Shear-1 lasted a total of 58.22 days (1397.34 hours), with **Figure 8-6** showing the test result data for the complete test history and **Table 8-2** summarising the individual test stages. The three phases of the test can be seen (initial hydration and swelling stage at *in situ* conditions, shear test 1, and shear test 2 – flow testing). This can be further sub-divided into 6 stages of testing, the results for each stage are introduced in the following sections.

Stage	Time (h)		Event	Stage length
1	0.00	Hyd	Start of test: Normal stress = 3 MPa, Injection = 125 µl/h	362.24
	362.24		End of hydration stage	
2	362.24	Shear test 1	Start of shearing of intact sample	115.51
	379.09		Drop in shear stress	
	385.40		Drop in shear stress	
	402.51		Drop in shear stress	
	424.94		Drop in shear stress	
	407.67		Peak shear stress	
	450.06		Normal displacement transducer out of range	
	477.75		End of shearing, stress relaxation stage Re-setting of normal displacement transducer	
3	597.19		End of relaxation stage Decommissioning of sample, laser scanning of surface	119.44
4	610.00	Shear test 2: Flow experiment	Set-up of test for flow experiment	266.53
	633.20		Pore pressure set to 125 kPa, but experienced high flow rate	
	726.33		Increase pore pressure to 125 kPa	
	732.87		Increase pore pressure to 250 kPa	
	779.45		Start of short-term temperature problem in laboratory	
	803.13		Increase pore pressure to 500 kPa	
5	876.53		Start of shear	497.71
	953.77		Small drop in shear stress	
	963.58		Drop in shear stress	
	984.43		Drop in shear stress	
	1016.26		Drop in shear stress	
	1076.68		Drop in shear stress	
	1085.43		Peak stress	
	1150.27		Residual stress	
	1205.11		Temperature event	
	1360.70		Shear stress movement	
6	1374.24		Stopping shear	23.1
	1397.34		End of test	

Table 8-2: Summary of experimental history of test OPERA_Shear-1 showing stage number, description of stage/event, and boundary conditions.

8.2.1 Stage 1: Sample hydration

The sample was loaded into the Direct Shear Rig and the boundary conditions were setup on the apparatus; normal stress of 3 MPa. The pore pressure system was set to 250 kPa. However it was immediately apparent that leakage was occurring through the join between the collars of the sample arrangement. It was decided to impose a nominal flow of 125 µl/h in order to saturate the sample and to see if the leakage would diminish with the

Boom Clay swelling. This stage of the test lasted 15 days (362.24 hours) and is summarised in **Figure 8-7**.

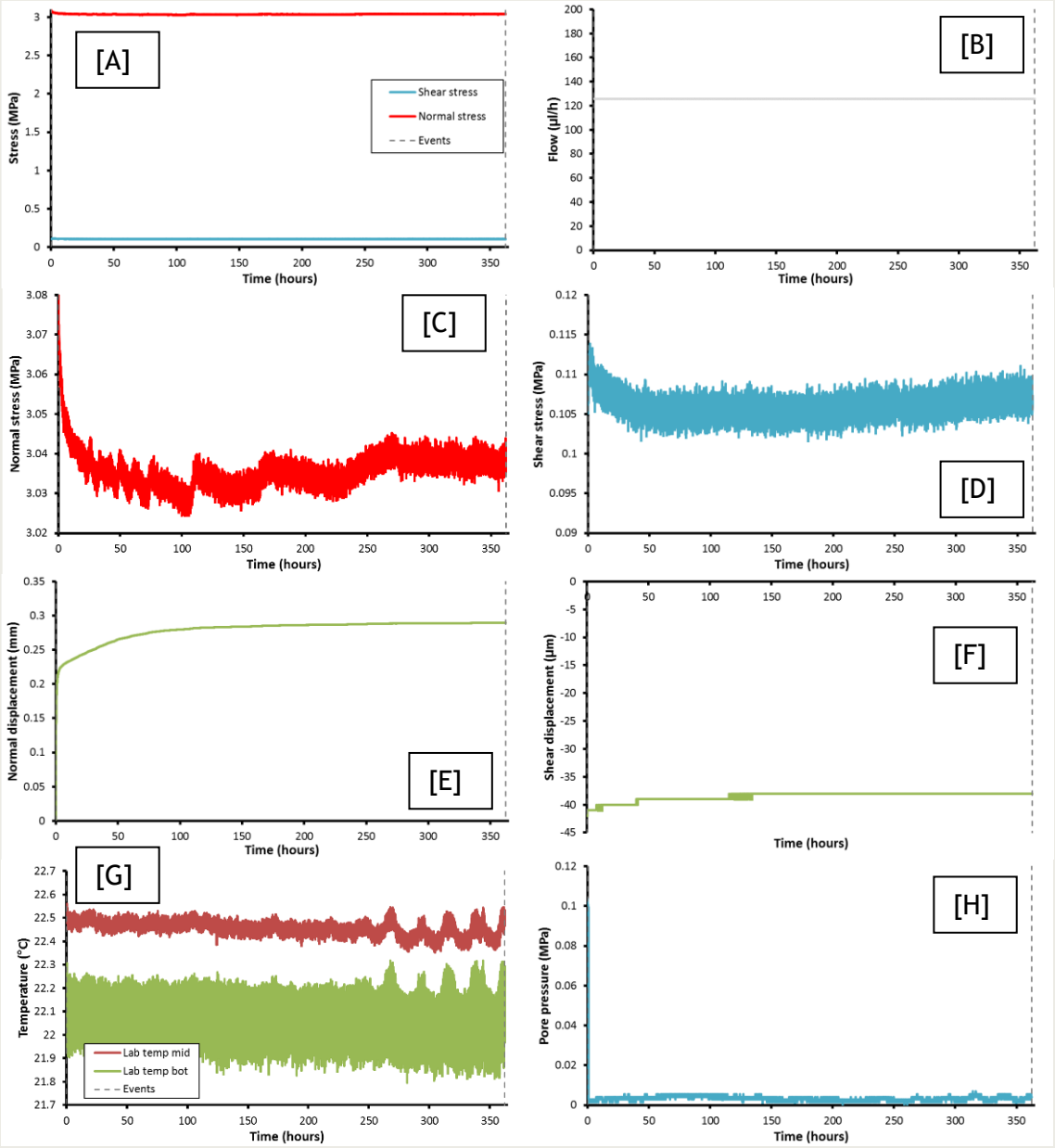

Figure 8-7: Data for the stage 1 (rehydration) of test OPERA_Shear-1. [A] Stress history. [B] Flow into the sample. [C] Normal stress. [D] Resultant shear stress [E] Normal displacement of the sample. [F] Shear displacement. [G] Temperature. [H] Pore pressure. Dashed lines represent events of note.

Figure 8-7 shows that little of note occurred during rehydration. The slow flow of water at 125 µl/h (**Figure 8-7 B**) did not result in an increase in pore pressure (**Figure 8-7 H**). The sample contracted in response to normal load (**Figure 8-7 E**). A total of 290 µm (0.005 strain) occurred, almost all occurring in the first few hours of the stage. It should be noted that the raising of pore fluid was attempted on two occasions during the stage, but the leak was still prominent.

Key observations of stage 1 (rehydration): a total of 0.005 contractive strain was measured; most of the reduction occurred in the first few hours of testing.

8.2.2 Stage 2: Shear test 1

The initial shearing phase of test OPERA_Shear-1 lasted a total of 115.51 and is summarised in **Figure 8-8**.

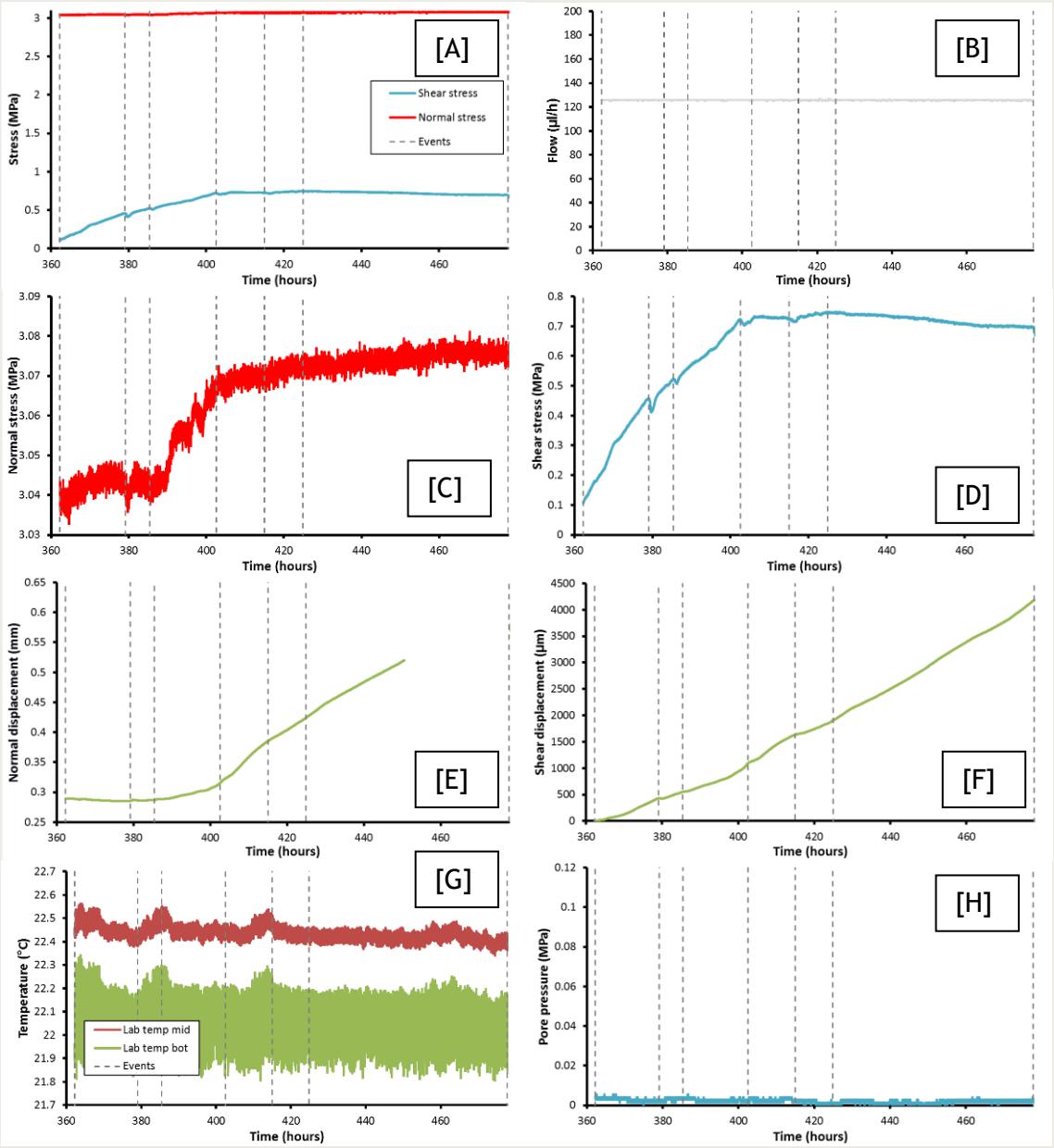

Figure 8-8: Data for the initial shearing of test OPERA_Shear-1. [A] Stress history. [B] Flow into the sample. [C] Normal stress. [D] Resultant shear stress. [E] Normal displacement of the sample. [F] Shear displacement. [G] Temperature. [H] Pore pressure. Dashed lines represent events of note.

As can be seen in **Figure 8-8 F**, a relatively linear shear rate was achieved. Calibration studies have shown that the modified ISCO pump achieves a linear displacement. However, the low-friction bearing that the shear arrangement is attached to allows small amounts of lateral movement. This results in the displacement data appearing non-linear at times as the measurement is made on one corner of the shear arrangement. This small lateral movement does not impact the sample.

The shearing of the sample resulted in an initial, near-linear, stress-strain response; this corresponds to the shear modulus of the sample. Stress increased until at 379.09 hours when shear stress was 0.49 MPa the shear stress dropped by 0.07 MPa (**Figure 8-8 D**). This event corresponds with a small amount of contraction of the sample and may represent enhanced contraction during fracture formation. A second stress drop of 0.02 MPa occurred at 385.4 hours when shear stress was 0.524 MPa. This event was also accompanied by a small amount of contraction. During this period of the test the normal stress on the sample (**Figure 8-8 C**) can be seen to increase by a small amount (0.03 MPa). This is the result of bending of the load-frame arrangement that does not result in a change in pressure within the normal load ram; therefore the normal load pump is not able to correct for it. Experience has shown that this bending moment is insignificant. The sample also started to slowly contract during this period (**Figure 8-8 E**), showing that the forming fractures were promoting consolidation.

Shear stress continued to increase until it reached a maximum (peak stress) of 0.734 MPa at a strain of 0.022 (407.67 hours). As can be seen in **Figure 8-8 D**, the stress around the time of peak stress was somewhat chaotic with at least two events with drops in shear stress. This suggests that stick-slip movement along the formed fracture was occurring. The release of only small amounts of shear stress indicates that movement was of the order of microns. At peak stress conditions, the sample had contracted 0.96 mm.

The sample sustained a constant shear stress with continued shear (**Figure 8-8 D**) until approximately 425 hours when shear stress slowly reduced due to strain weakening of the formed shear plane. Shear stress reached a minimum of 0.698 MPa (**Figure 8-8 D**) when shear was stopped at 477.75 hours, a total strain of 0.064.

Key observations of stage 2 (Shear test 1): Peak stress was 0.734 MPa at a strain of 0.022; stress drop when shear stress was 0.49 MPa signified the formation of the first fracture; residual stress of approximately 0.7 MPa; sample contracted as the shear fracture was formed; a series of stress drops showed the development of the shear zone; the sample was sheared for a total of 0.064.

8.2.3 Stage 3: Stress-relaxation; shear test 1

Shear displacement was halted and the time-dependent response of the shear stress transmitted through the fractured sample was investigated, as shown in **Figure 8-9**. During the 119.44 hours that the sample was held with constant boundary conditions, shear stress reduced by 0.09 MPa. This shows that the shear zone was creeping. The sample had not achieved an asymptote and the final stress would have been lower than the 0.61 MPa recorded. The sample was also continuing to contract, with 0.08 mm contraction occurring during the stage. At the end of Stage 3 the sample was extracted from the apparatus and was laser scanned to record the fracture topology.

Key observations of stage 3 (Stress relaxation; shear test 1): Shear stress reduced as the shear zone underwent creep; At least 0.09 MPa was relaxed, although shear stress had not achieved asymptote; prior to decommissioning, shear stress had decayed to 0.61 MPa; the sample continued to contract by 0.08 mm.

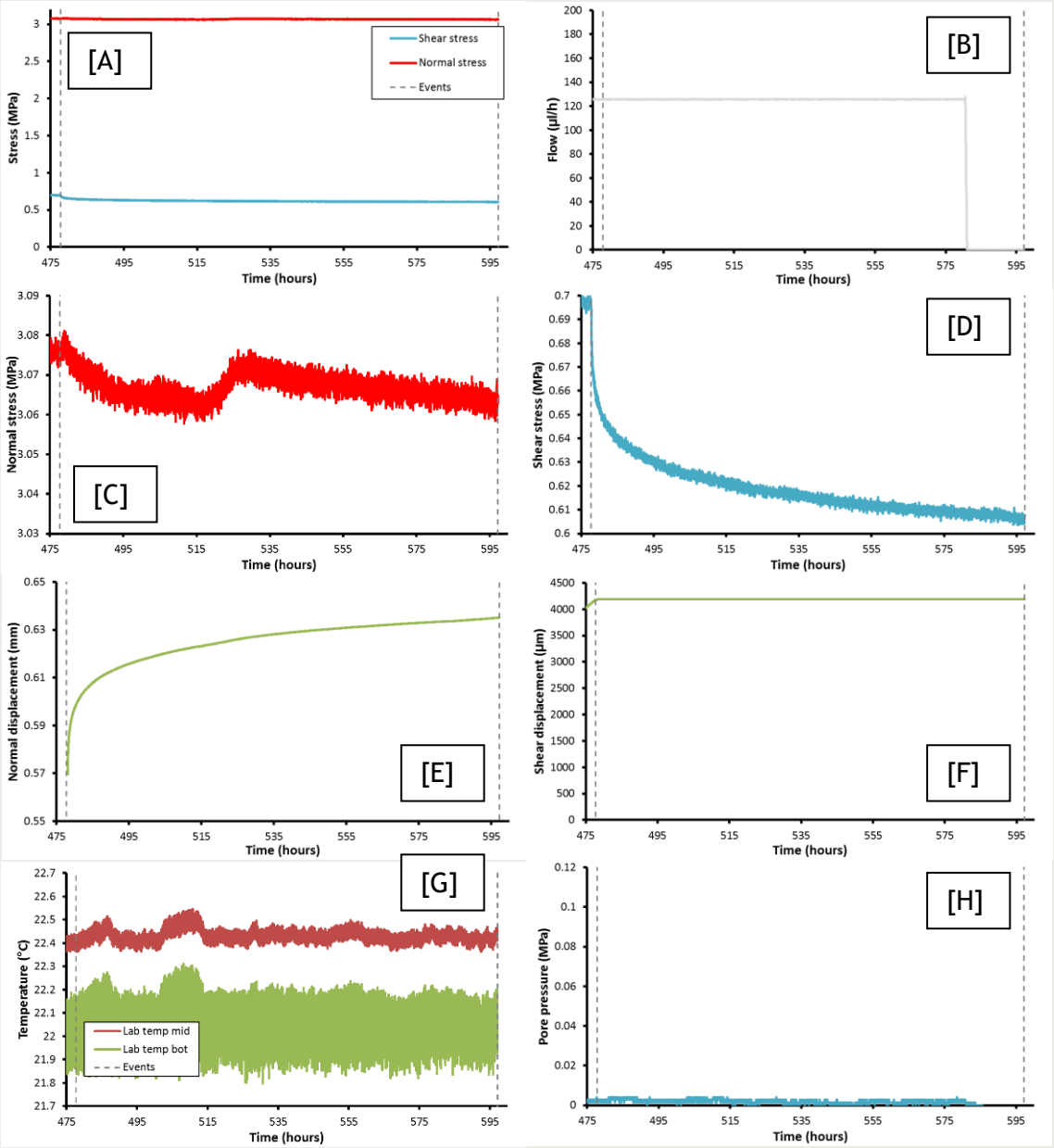

Figure 8-9: Data for the stress-relaxation stage (3) following shear of test OPERA_Shear-1. [A] Stress history. [B] Flow into the sample. [C] Normal stress. [D] Resultant shear stress. [E] Normal displacement of the sample. [F] Shear displacement. [G] Temperature. [H] Pore pressure. Dashed lines represent events of note.

8.2.4 Stage 4: Rehydration of the fracture surface

A 4 mm diameter hole was drilled into the centre of the top sample to allow an injection bore to be added. The length of the injection pipe was adjusted so that it sat flush with the fracture surface. The interface between the Boom Clay sample and top block was sealed using Mastic, whilst Mastic was also added to the injection pipe prior to insertion into the sample. The apparatus was reassembled and the same boundary conditions were imposed with a normal stress of 3 MPa, as shown in **Figure 8-10**.

As seen in **Figure 8-10 B**, the 11 day (266.53 hours) stage was dominated by trying to establish sufficient pore pressure injection without causing erosion of the fracture surfaces. Initially injection was set to 125 kPa and flow was seen to be too high resulting in a small volume of water injected and flooding the fracture faces. Injection was stopped and the

Boom Clay was allowed to swell and self-seal. At 633.2 hours pore pressure was again set to 125 kPa (**Figure 8-10 H**) and experienced high flow rates (**Figure 8-10 B**). Injection was stopped, but a pore pressure had been created within the sample, which took four days to decay. This suggested that the fracture was self-sealing. Pore pressure was increased to 125 kPa at 726.33 hours and a relatively low flow rate of around 10 µl/h (9.5×10^{-14} m^2/s) was achieved. Pore pressure was raised to 250 kPa at 732.87 hours with flow remaining at around 10 µl/h, but soon started to decay to reach approximately 3 µl/h (4.7×10^{-14} m^2/s). At 803.13 hours the pore pressure was set to 500 kPa, the target injection pore pressure. Flow increased to approximately 13 µl/h (3.1×10^{-14} m^2/s) and remained at this magnitude for the remaining time of the stage.

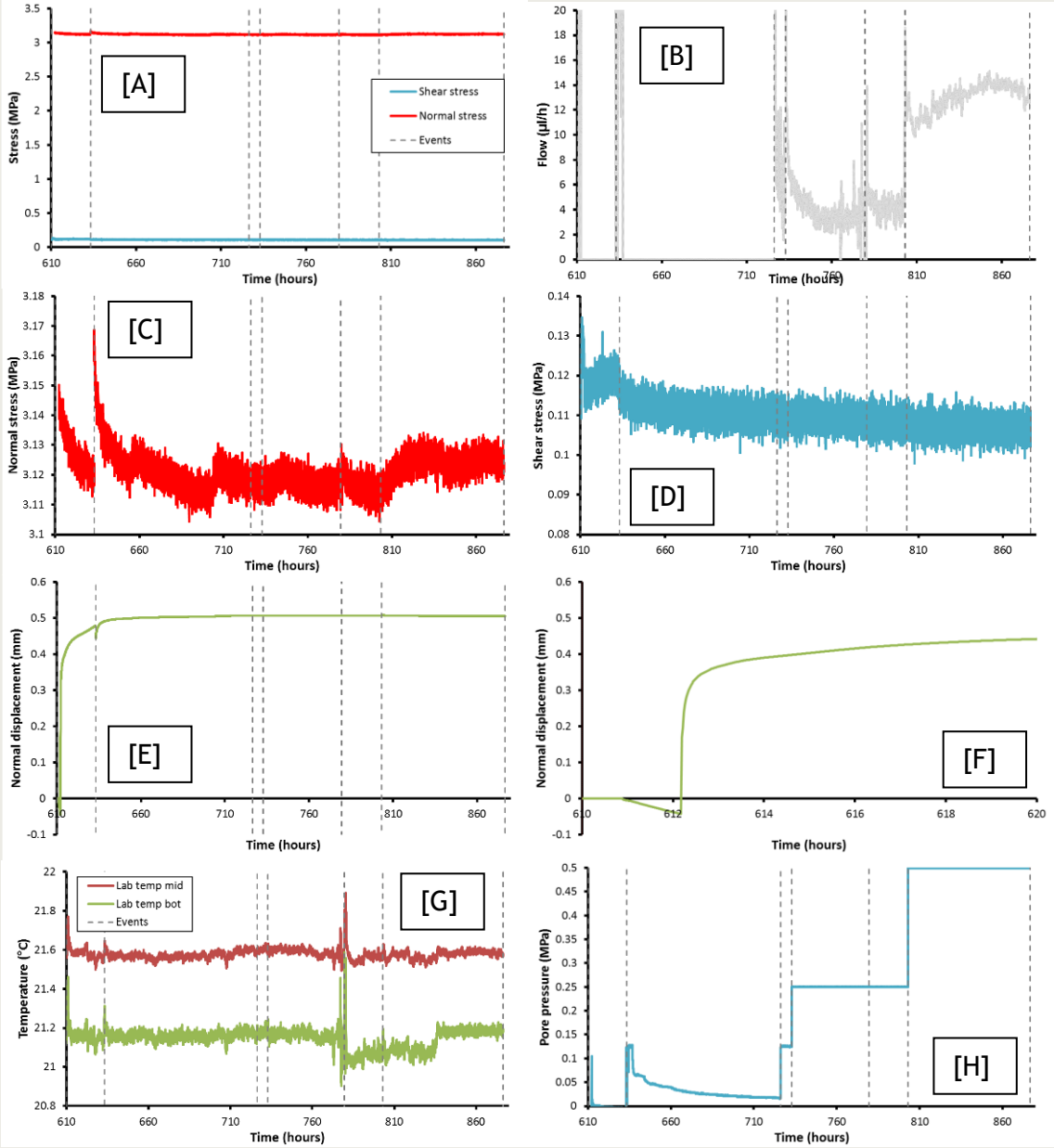

Figure 8-10: Data for the rehydration of the fracture stage (4) of test OPERA_Shear-1. [A] Stress history. [B] Flow into the sample. [C] Normal stress. [D] Resultant shear stress. [E] Normal displacement of the sample. [F] Detail of normal displacement. [G] Temperature. [H] Pore pressure. Dashed lines represent events of note.

Initially the sample started to dilate once fluid had been injected into the fracture (**Figure 8-10 F**). This was quickly superseded by contraction of the sample for the remaining time of the stage. A total of 0.5 mm of contraction occurred (~1 % strain). The injection of pore fluid at 125 kPa at 633.2 hours resulted in the sample initially dilating in response to a change in effective stress. However, this was short-lived and the sample continued to contract. Also of note is the experimental artefact experienced at 779.45 hours. During maintenance of the laboratory air conditioning unit there was a short-term increase in temperature of approximately 0.3-0.4° C (**Figure 8-10 G**). This only affected the injection pump, as seen by noise in the flow data (**Figure 8-10 B**).

Key observations of stage 4 (Rehydration of fracture surface): Initially it was difficult to sustain pore pressure within the fracture without excessive flow rates; the fracture self-sealed due to swelling and by the end of the stage sustained 0.5 MPa with a flow of 13 µl/h; initially the fracture started to dilate, but competing processes resulted in net contraction of fracture surface; Sample contracted by 1 %.

8.2.5 Stage 5: Shear test 2

Figure 8-11 summarises the results achieved for the repeat shear test for OPERA_Shear-1. The aim of the repeat shear test was to observe how fracture transmissivity altered during shearing and to compare the mechanical results with those achieved during shear test 1 on intact Boom Clay. Constant shear was started at 876.53 hours (**Figure 8-11 F**). The initial shear stress response was near-linear (**Figure 8-11 D**), resulting in a near-linear decline in flow (**Figure 8-11 B**), which reduced from 14 to 5 µl/h (3.3 to 1.2 × 10^{-14} m^2/s).

At 953.77 a small reduction in shear stress occurred when shear stress was 0.4 MPa. This signifies the first evidence of fracture movement and corresponds with a change in slope of the decrease of flow (**Figure 8-11 B**) and the start of contraction of the sample (**Figure 8-11 G**). Further small shear stress drops were noted at 963.58, 984.43, 1016.26 and 1076.68 hours, all probably due to movement along the pre-existing fracture or the formation of new fractures. During this period of time the flow into the fracture continued to reduce in a near-linear manner to reach a minimum of 2.7 µl/h (6.4 × 10^{-15} m^2/s).

The final stress drop at 1076.68 hours (shear stress of 0.7 MPa) resulted in a drop of 0.08 MPa (**Figure 8-11 D**) and the start of increased flow into the fracture (**Figure 8-11 B**). This event is accompanied by a small amount of dilation of the sample, not evident in **Figure 8-11 E**. Soon after at 1085.43 hours the sample reached a peak stress of 0.703 MPa at 0.028 strain. Over a period of a few hours, flow increased from 2.7 to 21.4 µl/h (0.6 to 5.1 × 10^{-14} m^2/s), a near order of magnitude increase. Therefore peak stress promoted the increase in flow. Following this shear stress was reducing as the shear surface strain weakened, resulting in a reduction in flow. However, continued shear resulting in further contraction of the sample (**Figure 8-11 E**) and increases in flow **(Figure 8-11 B**). A residual stress was reached at 1150.27 hours at a shear stress of 0.623 MPa at 0.044 strain.

Following residual stress conditions the shear plane started to work-harden, i.e. shear stress began to increase as it was becoming harder to shear. For the remaining time of active shear, the sample continued to contract (**Figure 8-11 E**), flow increased to a maximum of 35 µl/h (8.3 × 10^{-14} m^2/s; **Figure 8-11 B**) and shear stress reached a maximum of 0.88 MPa at a strain of 0.083. At 1360.7 hours shear was stopped and relaxation was monitored.

Key observations of stage 5 (Shear test 2): A peak stress of 0.703 MPa was achieved at 0.028 strain; A residual stress of 0.623 MPa was seen at 0.044 strain; the first indication of movement occurred at a shear stress of 0.4 MPa; shear reduced flow from 14 to 2.7 µl/h (3.3 to 0.6 × 10^{-14} m^2/s); peak stress resulted in flow increasing by nearly one order of magnitude from 2.7 to 21.4 µl/h (0.6 to 5.1 × 10^{-14} m^2/s); maximum flow at 0.083 strain was 35 µl/h (8.3 × 10^{-14} m^2/s) at a shear stress of 0.88 MPa; the sample dilated during the formation of fractures or the movement along pre-existing ones.

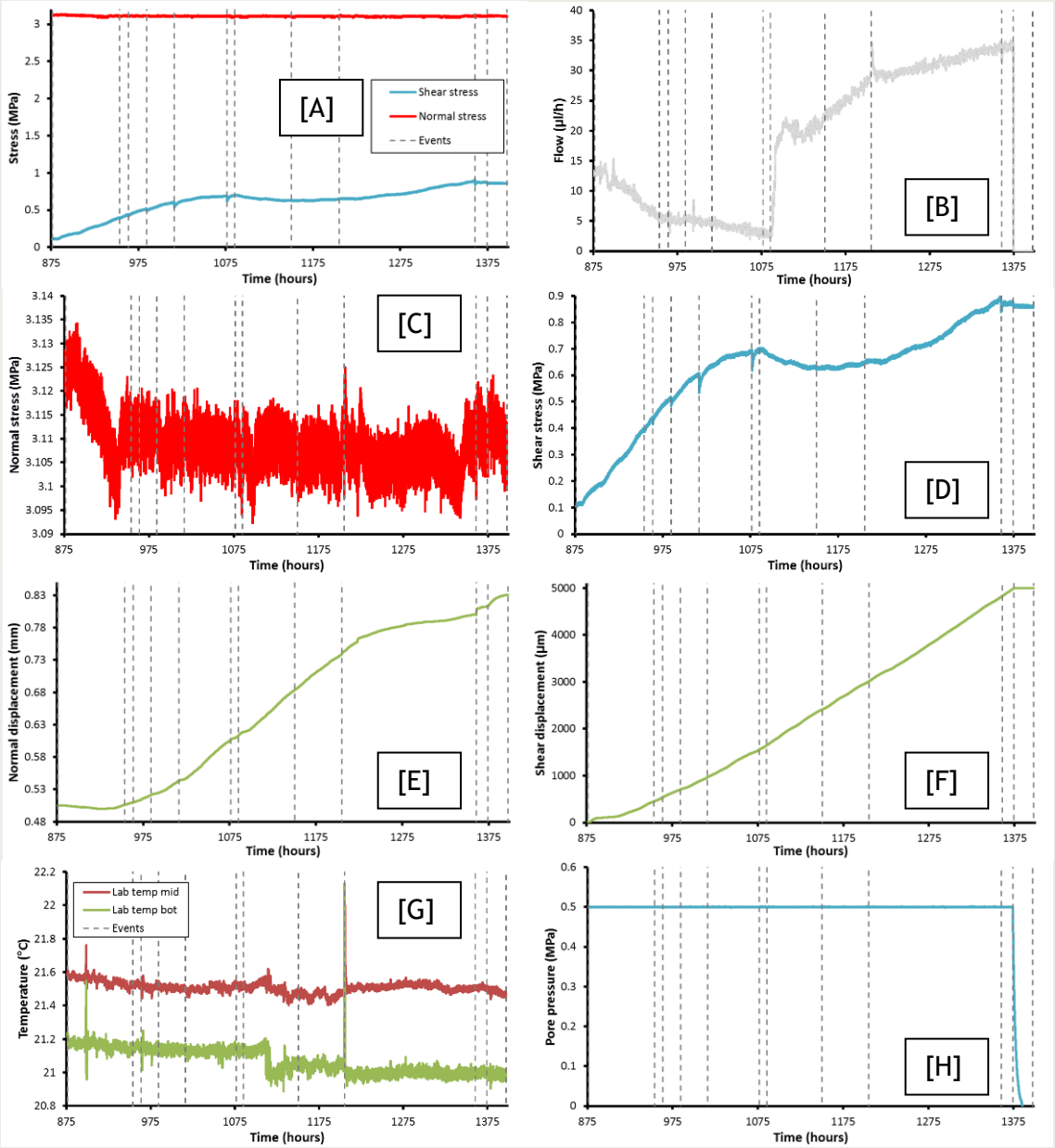

Figure 8-11: Data for shear test 2 of test OPERA_Shear-1. [A] Stress history. [B] Flow into the sample. [C] Normal stress. [D] Resultant shear stress. [E] Normal displacement of the sample. [F] Shear displacement. [G] Temperature. [H] Pore pressure. Dashed lines represent events of note.

8.2.6 Stage 6: Stress relaxation

A short 23 hours of stress relaxation was undertaken, as shown in **Figure 8-11**. Pore pressure took 11 hours to decay to zero pressure (**Figure 8-11 H**), indicating the fracture

remained conductive. Shear stress decayed to 0.86 MPa, only a 0.02 MPa reduction (**Figure 8-11 D**). During the relaxation stage the sample continued to contract (**Figure 8-11 E**).

Key observations of stage 6 (Stress relaxation): Pore pressure decayed within 11 hours showing that the fracture was still conductive; stress relaxed by only 0.02 MPa; the sample continued to contract.

8.2.7 Comparing shear tests 1 and 2

Figure 8-12 compares the mechanical results for shear tests 1 and 2 of test OPERA_Shear-1. Both tests have good linear regions, which give a slope of 30.076 MPa for shear test 1 (**Figure 8-12 A**) and 30.405 MPa for shear test 2 (**Figure 8-12 B**). These values correspond with the shear modulus of Boom Clay and show good agreement (**Figure 8-12 C**). Close agreement is also seen in peak stress, with shear test 1 giving 0.734 MPa and shear test 2 giving 0.703 MPa. These are remarkably similar, yet differences in the strain seen at peak stress were seen, with shear test 1 reaching peak stress at 0.022 and shear test 2 at 0.028. Differences are also seen post-peak, with shear test 1 showing stable sliding at residual stress, while shear test 2 resulted in an initial reduction in shear stress (strain softening), followed by work-hardening of the shear plane. It should be noted that normal stress was marginally greater in shear test 2.

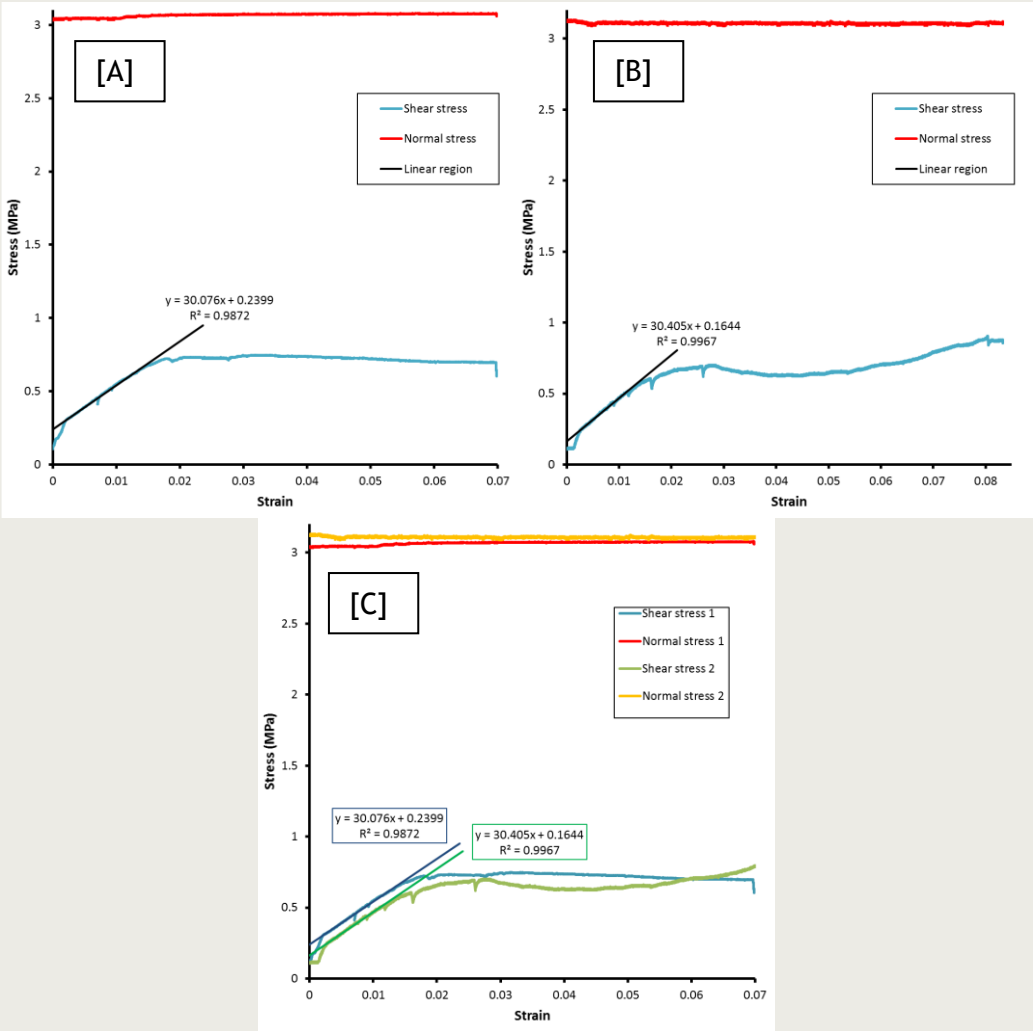

Figure 8-12: Stress-strain response of test OPERA_Shear-1. [A] Shear test 1. [B] Shear test 2. [C] Comparison of the shear tests.

The mechanical data from test OPERA_Shear-1 suggests that Boom Clay had self-healed. In previous testing of Opalinus Clay (Cuss et al., 2014; Cuss & Harrington, 2014) repeat testing resulted in a significantly reduced strength and change in shear modulus. In the current tests it appears that the fractured Boom Clay has similar mechanical properties to the intact rock. Therefore the reduction in flow properties prior to shearing (self-sealing) resulted in a degree of mechanical self-healing.

Key observations comparing shear test 1 and 2: Both tests have similar shear modulus and peak stress; differences seen in the strain at which peak stress was achieved; post-peak the two samples behaved differently; shear test 2 strain softened and then strain-hardened, shear test one underwent stable sliding; Boom Clay underwent self-healing.

8.2.8 Fracture topology

Figure 8-13 shows a series of photographs of the fracture surface at the end of shear test 1 and shear test 2 for comparison. As can be clearly seen, a continuous fracture surface was formed in the sample during the first shear test (**Figure 8-13 A** and **B**). This formed sub-parallel with the shear direction. Some polishing was observed, but generally the surface appeared a clean break in the Boom Clay.

Figure 8-13: Observations of fracture surfaces in test OPERA_Shear-1. [A] Shear test 1 top surface. [B] Shear test 2 bottom surface. [C] Shear test 2 bottom surface.

Following shear test 2 (**Figure 8-13 C**), the fracture surface was still clearly seen. However, the addition of water during this shear test resulted in a change of the Boom Clay fabric,

as seen by a change in colour, roughness and extrusion of clay between the two collars of the sample holder. A small fossil-like object can be seen in the centre of **Figure 8-13 C**, this was not apparent in **Figure 8-13 B** and may suggest that a new fracture surface formed.

The shear surfaces were scanned following shear test 1 and 2 using a NextEngine 3D Scanner HD, the results of which are shown in **Figure 8-14** and **Figure 8-15**. The upper images in each figure show the raw scanned surface height, whilst the lower images show this data following the removal of a 3rd order polynomial surface to remove the "form" of the fracture. Both **Figure 8-14** and **Figure 8-15** show the same general features of the fracture surfaces and show that the two halves of the test sample fit together, although areas of mismatch can be inferred.

Carefully comparing the two shear surfaces after tests 1 and 2 does not show the same general features (e.g. **Figure 8-14 A** and **B**). Even accounting for differences in form based on the samples being at different orientations within the scanner (e.g. **Figure 8-14 C** and **D**), there is little correlation between the results from shear test 1 and 2. This suggests that a new fracture surface formed between the two tests and that the prolonged injection of water at the start of shear test 2 resulted in the self-healing of the clay.

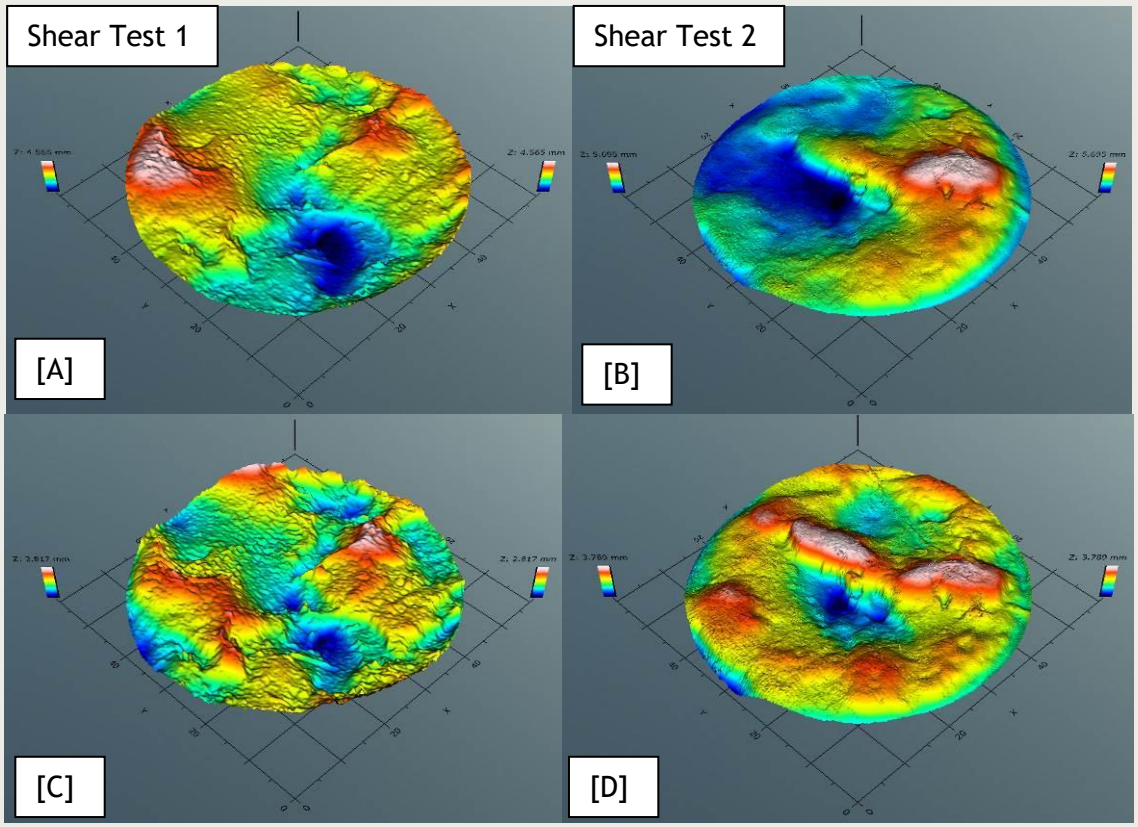

Figure 8-14: Surface topology of the bottom fracture surface following shear test 1 and 2 of test OPERA_Shear-1. [A] Shear test 1 bottom surface. [B] Shear test 2 bottom surface [C] Shear test 1 bottom surface following removal of surface form. [D] Shear test 2 bottom surface following removal of surface form.

Surface topology data was processed using TrueMap 5.0 software. This can determine gross surface data or can be used to define parameters along profiles. For the current study only surface results are considered, as summarised in **Table 8-3** and **Figure 8-16**. As can be seen, most parameters compare well between the top and bottom fracture surfaces. Significant differences are seen between shear test 1 and 2. For instance, average

roughness (S_a) increases from 0.371 to 0.485 mm between test 1 and 2, whilst the route mean squared roughness (S_q), peak to valley height (S_t) and texture direction index (S_{tdi}) all increased from 0.452 to 0.6205 mm, 3.001 to 4.221 mm, and 0.479 to 0.563 respectively. Therefore the fracture surface in shear test 2 has considerably greater roughness and may be a new fracture surface.

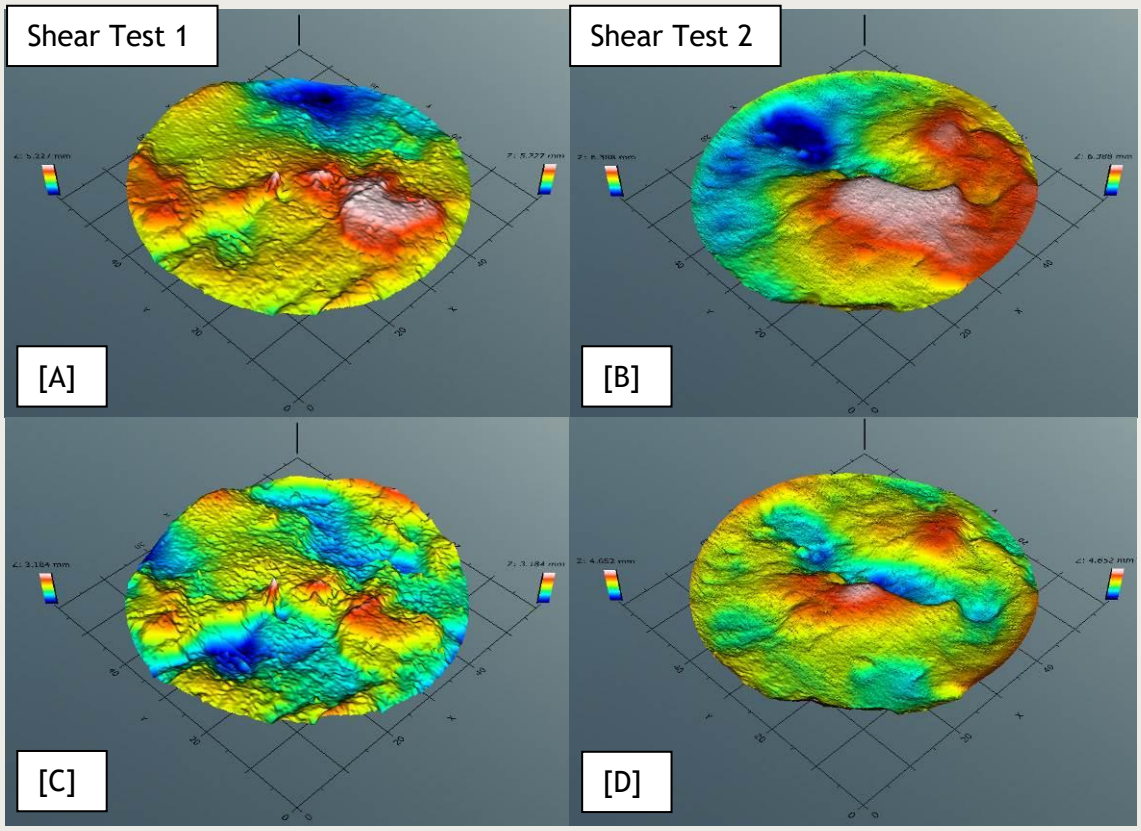

Figure 8-15: Surface topology of the top fracture surface following shear test 1 and 2 of test OPERA_Shear-1. [A] Shear test 1 top surface. [B] Shear test 2 top surface. [C] Shear test 1 top surface following removal of surface form. [D] Shear test 2 top surface following removal of surface form.

Parameter	Symbol	Units	Shear test 1				Shear test 2			
			Bottom		Top		Bottom		Top	
			Full	Corr	Full	Corr	Full	Corr	Full	Corr
Roughness average	S_a	mm	0.608	0.376	0.729	0.366	0.997	0.502	1.262	0.467
Root Mean Square (RMS) Roughness	S_q	mm	0.791	0.457	0.954	0.447	1.209	0.638	1.467	0.603
Peak Height	S_p	mm	2.239	1.436	2.329	1.757	3.371	1.642	2.932	2.258
Valley Depth	S_v	mm	2.326	1.38	2.898	1.427	2.324	2.147	3.456	2.394
Peak to Valley Height	S_t	mm	4.565	2.817	5.227	3.184	5.695	3.789	6.388	4.652
Kurtosis	S_{ku}		3.193	2.572	3.204	2.611	2.614	3.051	1.996	3.142
Skewness	S_{sk}		-0.27	0.066	-0.51	-0.05	0.518	-0.24	-0.08	0.138
Texture Direction	S_{td}	°	90		90		0.353		0.355	
Texture Direction Index	S_{tdi}		0.454		0.504		0.517		0.609	

Table 8-3: Surface parameters calculated for test OPERA_Shear-1.

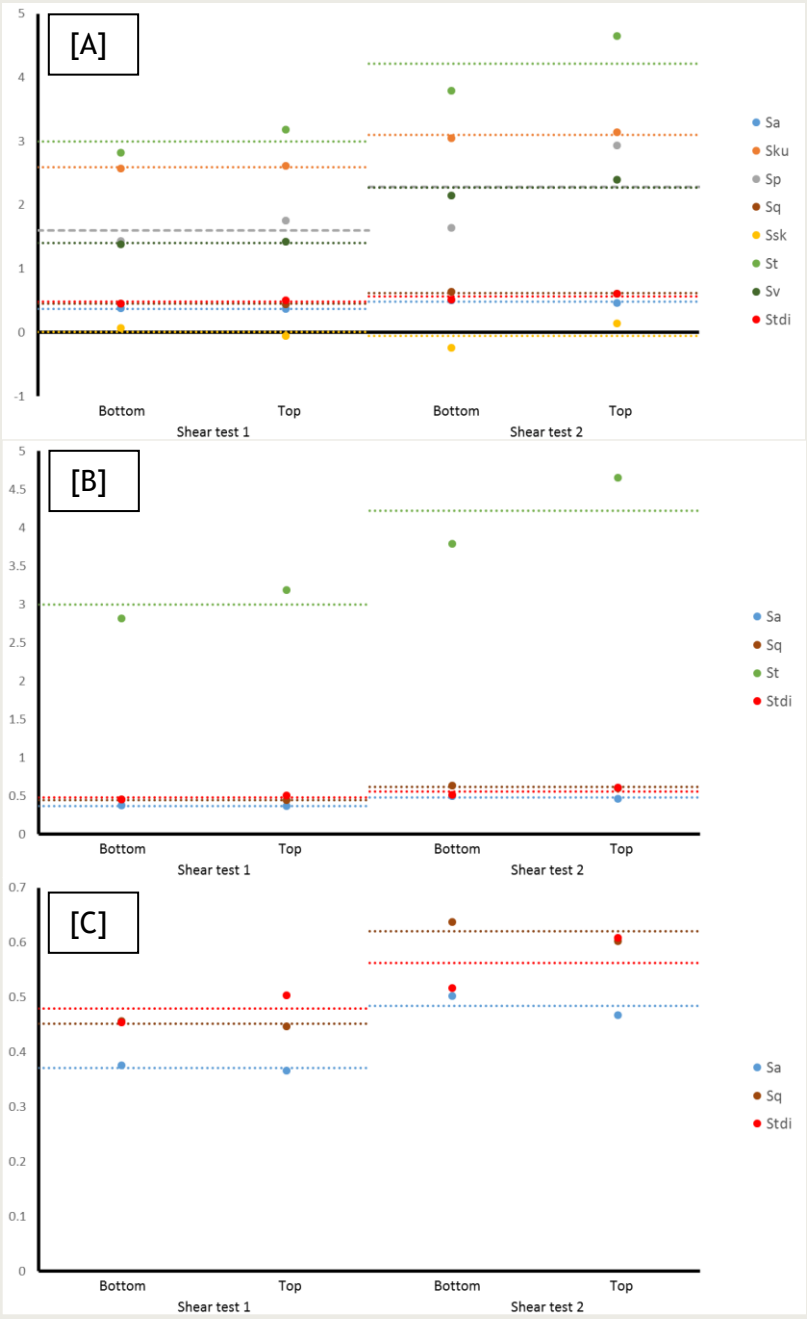

Figure 8-16: Surface texture data for test OPERA_Shear-1. [A] All surface parameters. [B] Key surface parameters. [C] Detail of S_a, S_q, and S_{tdi}. See Table 8-3: Surface parameters calculated for test OPERA_Shear-1.
for description of parameters and units of measure.

Key observations of fracture topology: a continuous fracture surface was formed sub-parallel with the shear direction; some polishing observed in shear test 1, generally a clean break; different fabric created in shear test 2 because of injection of water; change in colour, roughness and extrusion of clay; fracture surface 1 and 2 do not correspond; new fracture formed, self-healing of fracture occurred by the injection of water; clear agreement of fracture roughness comparing top and bottom sample surfaces; fracture roughness (0.371 – 0.485 mm), RMS roughness (0.452 – 0.621 mm), peak to valley height (3.001 – 4.221 mm) and textural direction index (0.479 – 0.563) all increased between shear test 1 and 2.

8.2.9 Key findings of test OPERA_Shear-1

Outcomes:

1. OPERA_Shear-1 was a six stage test that lasted 58.22 days (1397.34 hours). The sample underwent 0.5 % consolidation in response to applied normal stress, and the peak stress was 0.734 MPa at a strain of 0.022. The first indication of deformation occurred at 0.49 MPa, signifying formation of fractures. There was a residual stress of approximately 0.7 MPa.
2. The sample contracted during deformation. A series of stress drops showed the development of the shear zone. There was a total of 0.064 strain. Stress relaxation occurred and the shear stress decayed to 0.61 MPa.
3. The fracture initially would not sustain pore fluid pressure and experienced excessive flow rates. The fracture self-sealed due to swelling and could then sustain 0.5 MPa with a flow of 13 µl/h. The fracture initially started to dilate, but competing processes resulted in net contraction.
4. Repeat shearing gave a peak stress of 0.703 MPa at 0.028 strain and a residual stress of 0.623 MPa at 0.044 strain. The first indication of movement occurred at a shear stress of 0.4 MPa. Shear reduced flow from 14 to 2.7 µl/h, and the peak stress resulted in flow increasing by nearly one order of magnitude from 2.7 to 21.4 µl/h. Maximum flow at 0.083 strain was 35 µl/h at a shear stress of 0.88 MPa.
5. Both tests have similar shear modulus and peak stress, although differences were seen in the strain at which peak stress was achieved. Post-peak the two samples behaved differently.
6. The Boom Clay underwent self-healing.
7. A continuous fracture surface was formed sub-parallel with the shear direction.
8. Some polishing was observed in shear test 1. A different fabric was created in shear test 2 because of injection of water. There was a difference in colour, roughness and extrusion of clay and the fracture topology for tests 1 and 2 do not correspond.
9. New fracture formed, self-healing of fracture occurred by the injection of water.
10. Fracture roughness (0.371 – 0.485 mm), RMS roughness (0.452 – 0.621 mm), peak to valley height (3.001 – 4.221 mm) and textural direction index (0.479 – 0.563) all increased between shear test 1 and 2.

8.3 *Test OPERA_Shear-2*

Test OPERA_Shear-2 aimed to test Boom Clay at a stress condition representative of the disposal concept of the Netherlands, a state of stress higher than at which the material was cored at the Mol URL in Belgium. The core was consolidated to representative stress conditions prior to sample preparation (see Chapter 2). Therefore the test was conducted with a normal stress of 5.1 MPa.

Test OPERA_Shear-2 lasted a total of 27.04 days (649.05 hours), with **Figure 8-17** showing the test result data for the complete test history and **Table 8-4** summarising the individual test stages. The two main phases of the test can be seen (shear test 1, and shear test 2 – flow testing); this can further be divided into four stages (shear test 1, stress relaxation, rehydration of fracture, shear stress 2). Results for each stage are introduced in the following sections.

Stage	Time (h)		Event	Stage length
1	0	Shear test 1	Start of test: Normal stress = 5.1 MPa, shearing started	118.62
	81.97		Dilation sensor out of range	
	116.01		Drop in shear stress	
	118.62		End of shearing	
2	118.62		Start of stress relaxation	48.56
	167.18		End of stress relaxation	
3	170.00	Shear test 2: Flow experiment	Set-up of test for flow experiment	237.00
	171.83		Dilation sensor reset	
	192.10		Minimum in shear stress	
	212.43		Dilation sensor out of range	
	407.00		End of re-hydration	
4	407.00		Start of shear test	242.05
	413.07		Temperature event	
	496.79		Start of reduction of flow	
	576.90		Dilation sensor reset	
	602.12		Temperature event	
	612.27		Drop in shear stress	
	624.61		Temperature event	
	628.43		Temperature event	
	629.76		Drop in shear stress	
	649.05		End of shearing	
	649.05		End of test	

Table 8-4: Summary of experimental history of test OPERA_Shear-2 showing stage number, description of stage/event, and boundary conditions.

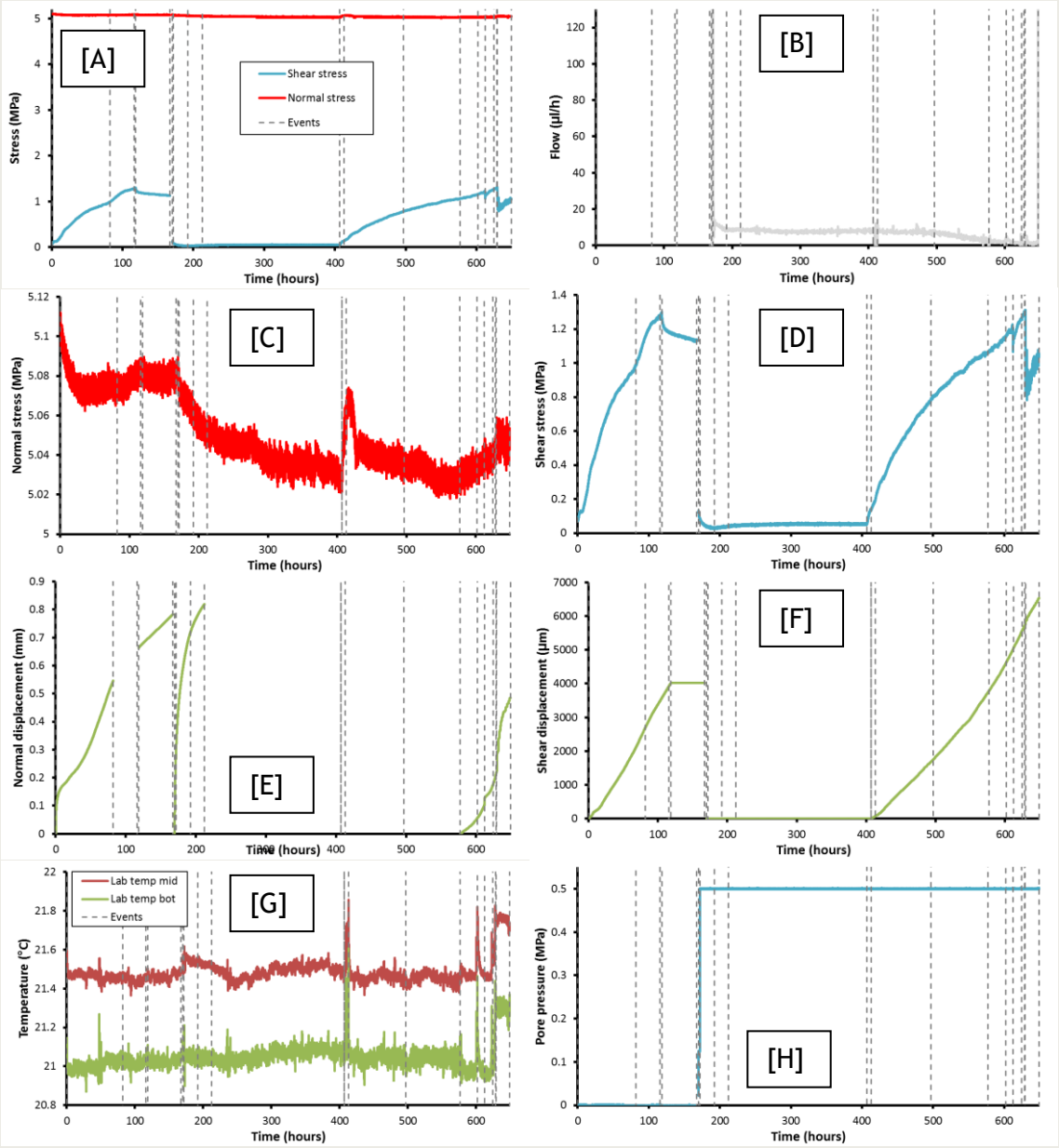

Figure 8-17: Data for the complete test history of test OPERA_Shear-2. [A] Stress history. [B] Flow into the sample. [C] Normal stress. [D] Resultant shear stress. [E] Normal displacement of the sample. [F] Shear displacement. [G] Temperature. [H] Pore pressure. Dashed lines represent events of note.

8.3.1 Stage 1: Shear test 1

The initial shearing phase of test OPERA_Shear-2 lasted a total of 118.62 hours and is summarised in **Figure 8-18**. As can be seen in **Figure 8-18 F**, a relatively linear shear rate was achieved with some non-linearity in the initial 20 hours of the test. This is likely to be movement of the shear mechanism of a result of the bearings in the drive mechanism. The shearing of the sample resulted in an initial, near-linear, stress-strain response (**Figure 8-18 D**). This quickly reached a plateau of 0.12 MPa and may be the result of non-perfect fitting of the sample within the collars, or between the collars and the shear-rig apparatus. Following this, an initial linear response is seen giving the shear modulus of the sample (26.93 MPa). During this initial period, the sample contracted in response to the applied load (**Figure 8-18 E**). The initial consolidation was considerable, and within 10 hours a

steady closure was noted. Normal load was seen to decrease during this period (**Figure 8-18 C**), due to the bending moment of the loading frame. The reduction is insignificant.

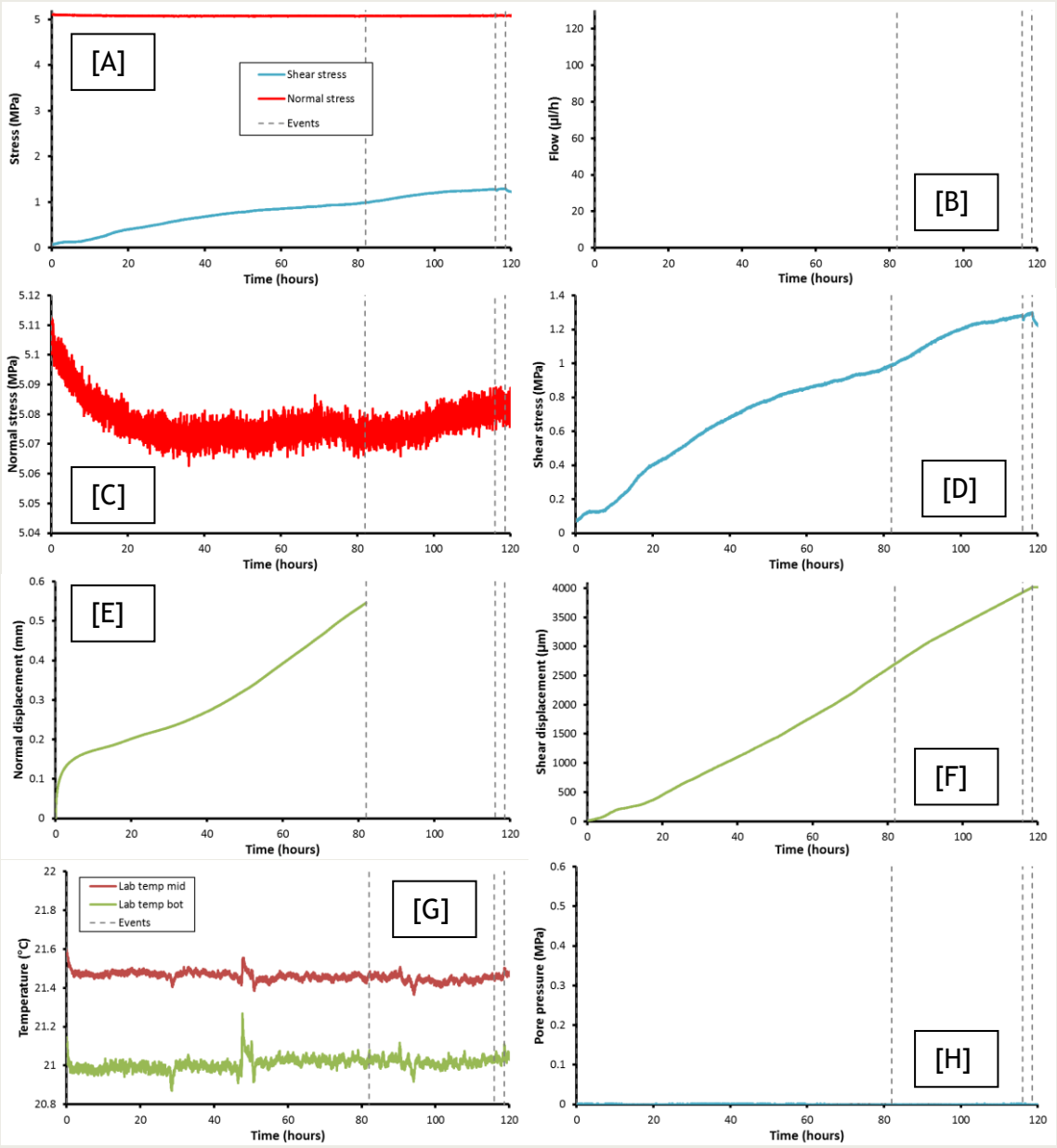

Figure 8-18: Data for shear test 1 (stage 1) of test OPERA_Shear-2. [A] Stress history. [B] Flow into the sample. [C] Normal stress. [D] Resultant shear stress. [E] Normal displacement of the sample. [F] Detail of normal displacement. [G] Temperature. [H] Pore pressure. Dashed lines represent events of note.

At around 0.02 strain (43 hours) the stress-strain response started to slowly deviate from linear showing a degree of strain softening (**Figure 8-18 D**). This is accompanied by increased consolidation of the sample (**Figure 8-18 E**). However, at around 80 hours the sample started to strain harden (**Figure 8-18 D**) and the slope of the stress-strain curve increased, until it once again strain softened at around 100 hours. Stress continued to increase until 116.01 hours when shear stress was at 1.28 MPa (0.065 strain) a small stress reduction of 0.03 MPa occurred. Unfortunately the dilation sensor was out-of-range at this time and it is not known if any dilatant behaviour occurred. However, this event is interpreted as the first evidence of sample failure.

Shearing was continued until 118.62 hours when active shear was halted with shear stress reaching 1.30 MPa at 0.067 strain. At this time there was concern that the shear mechanism had reached its limit of shear and that continued shearing would be influenced by steel-on-steel sliding of part of the mechanism. The decision was taken to perform a short stress-relaxation stage, then disassemble the apparatus to allow a greater shear distance to be achieved. However, when the apparatus was depressurised at 167.18 hours it was found that the sample had sheared into two.

Key observations of stage 1 (Shear test 1): Peak stress was 1.30 MPa at a strain of 0.067; stress drop when shear stress was 1.28 MPa signified the formation of the first fracture; shear modulus of 26.93 MPa; sample contracted throughout the test and accelerated contraction as the sample strain weakened; sample had sheared despite data suggesting peak stress had yet to be achieved.

8.3.2 Stage 2: Stress-relaxation; shear test 1

Shear displacement was halted and the time-dependent response of the shear stress transmitted through the fractured sample was investigated, as shown in **Figure 8-19**. During the 48.56 hours that the sample was held with constant boundary conditions, shear stress reduced by 0.16 MPa. This shows that the shear zone was creeping. The sample had not achieved an asymptote and the final stress would have been lower than the 1.128 MPa recorded. The sample was also continuing to contract, with 0.12 mm contraction occurring during the stage. However, it was decided to terminate the stress-relaxation stage and to re-configure the apparatus to allow greater shear. On extraction from the apparatus it was found that the sample had sheared into two halves and therefore shear test 1 was terminated. Both fracture surfaces were laser scanned to record the fracture topology.

Key observations of stage 2 (Stress relaxation; shear test 1): Shear stress reduced as the shear zone underwent creep; At least 0.16 MPa was relaxed, although shear stress had not achieved asymptote; prior to decommissioning, shear stress had decayed to 1.13 MPa; the sample continued to contract by 0.12 mm.

8.3.3 Stage 3: Rehydration of the fracture surface

A 4 mm diameter hole was drilled into the centre of the top sample to allow an injection bore to be added. The length of the injection pipe was adjusted so that it sat flush with the fracture surface. The interface between the Boom Clay sample and top block was sealed using Mastic, whilst Mastic was also added to the injection pipe prior to insertion into the sample. The apparatus was reassembled and the same boundary conditions were imposed with a normal stress of 5.1 MPa, as shown in **Figure 8-20**.

A pore pressure of 0.5 MPa was established in the fracture plane (**Figure 8-20 H**), which gave an initially high flowrate (**Figure 8-20 B**). This quickly decayed to sub-20 µl/h (sub-4.7×10^{-14} m^2/s), a level unlikely to result in excessive erosion of the fracture surface. Flow continued to decay linearly until around 192 hours, when shear stress (**Figure 8-20 D**) reached a minimum and flow stabilised at about 8 µl/h (1.9×10^{-14} m^2/s; **Figure 8-20 B**). During this period of time the sample continued to contract (**Figure 8-20 E**), although the dilation sensor was out of range following 212.43 hours. At around 242 hours the shear stress reached an asymptote (**Figure 8-20 D**) and flow started to slowly decay (**Figure 8-20 B**), reaching around 7 µl/h (1.7×10^{-14} m^2/s) by the end of the stage at 407 hours.

Key observations of stage 3 (rehydration of the fracture; shear test 2): Fracture maintained 0.5 MPa pore pressure; initial flow high, quickly stabilising at sub-20 µl/h (sub-4.7 × 10^{-14} m^2/s); flow decayed and stabilised at 8 µl/h (1.9 × 10^{-14} m^2/s) corresponding with minimal shear stress; sample contracted throughout the stage.

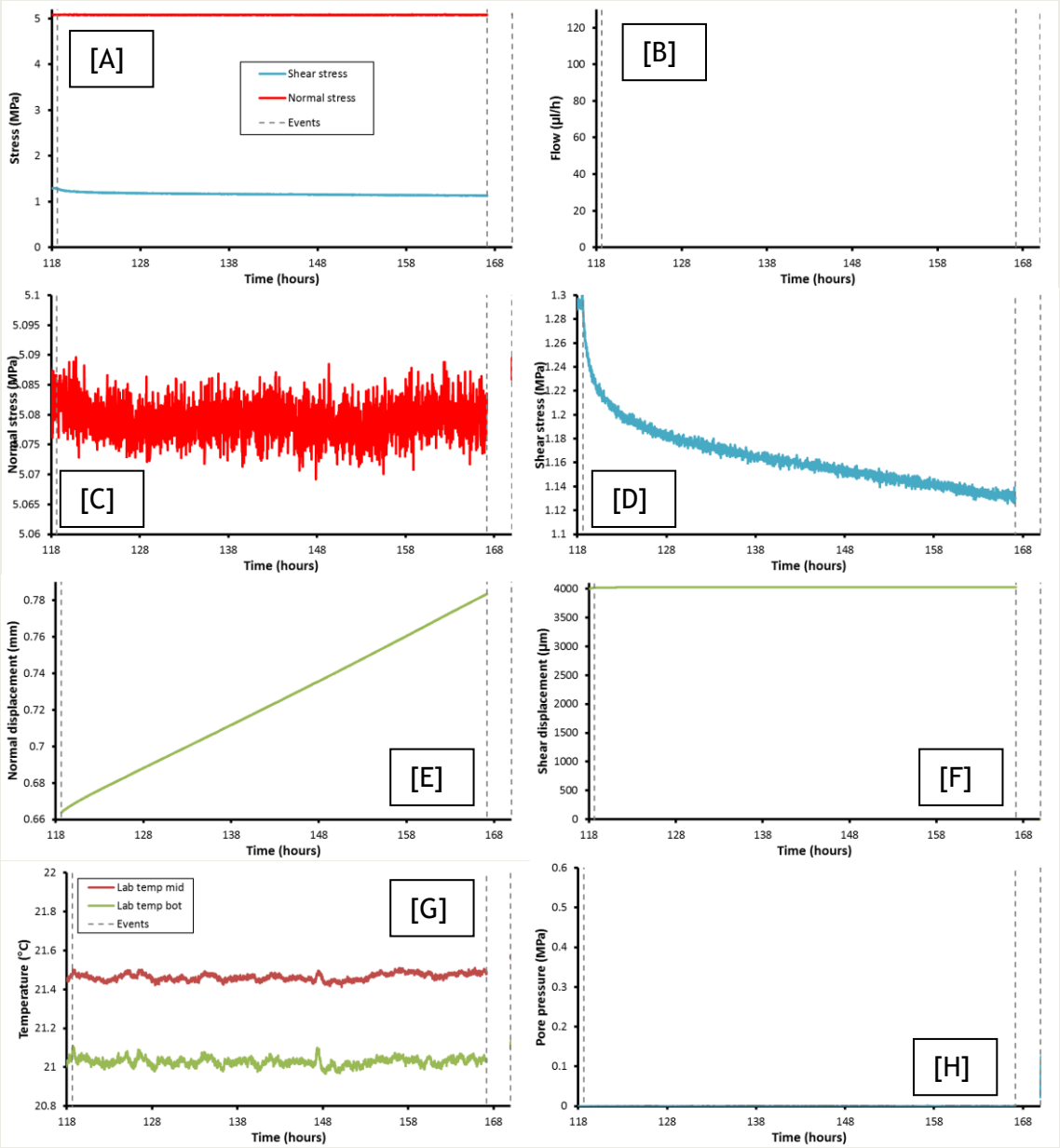

Figure 8-19: Data for the stress relaxation stage (2) of shear test 1 of OPERA_Shear-2. [A] Stress history. [B] Flow into the sample. [C] Normal stress. [D] Resultant shear stress. [E] Normal displacement of the sample. [F] Detail of normal displacement. [G] Temperature. [H] Pore pressure. Dashed lines represent events of note.

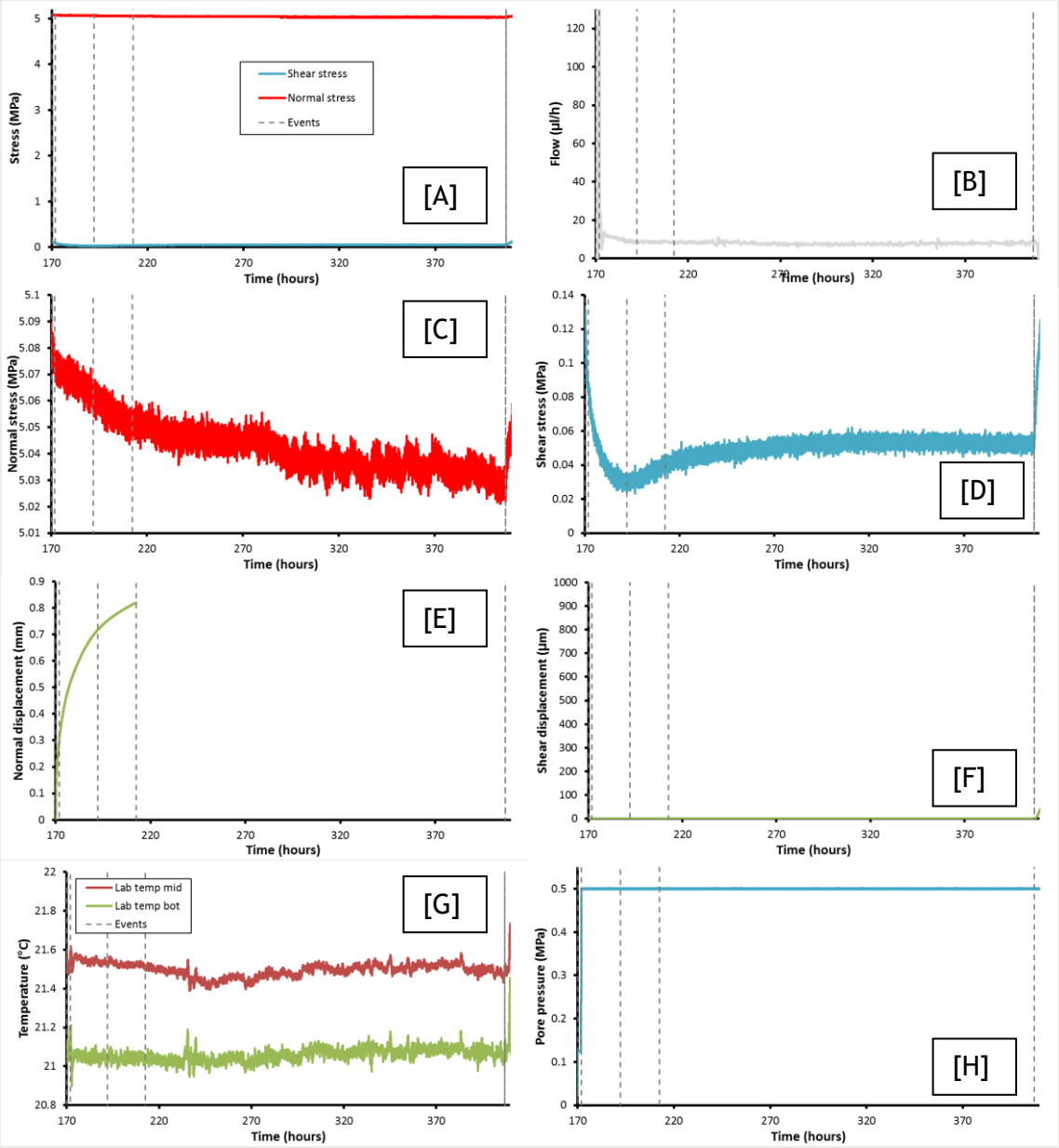

Figure 8-20: Data for the rehydration of the fracture stage (3) of test OPERA_Shear-2. [A] Stress history. [B] Flow into the sample. [C] Normal stress. [D] Resultant shear stress. [E] Normal displacement of the sample. [F] Detail of normal displacement. [G] Temperature. [H] Pore pressure. Dashed lines represent events of note.

8.3.4 Stage 4: Shear test 2

Figure 8-21 summarises the results achieved for the repeat shear test for OPERA_Shear-2. The aim of the repeat shear test was to observe how fracture transmissivity altered during shearing and to compare the mechanical results with those achieved during shear test 1 on intact Boom Clay. Constant shear was started at 407.00 hrs (**Figure 8-21 F**). The initial shear stress response was linear (**Figure 8-21 D**), which resulted in a maintained flowrate of around 8 µl/h (1.9×10^{-14} m^2/s; **Figure 8-21 B**).

From around 440 hr up until 500 hours the sample underwent strain softening (reducing stress-strain slope; **Figure 8-21 D**). During this period flow slowly reduced from around 8 to 7 µl/h (1.9 to 1.7×10^{-14} m^2/s; **Figure 8-21 B**).

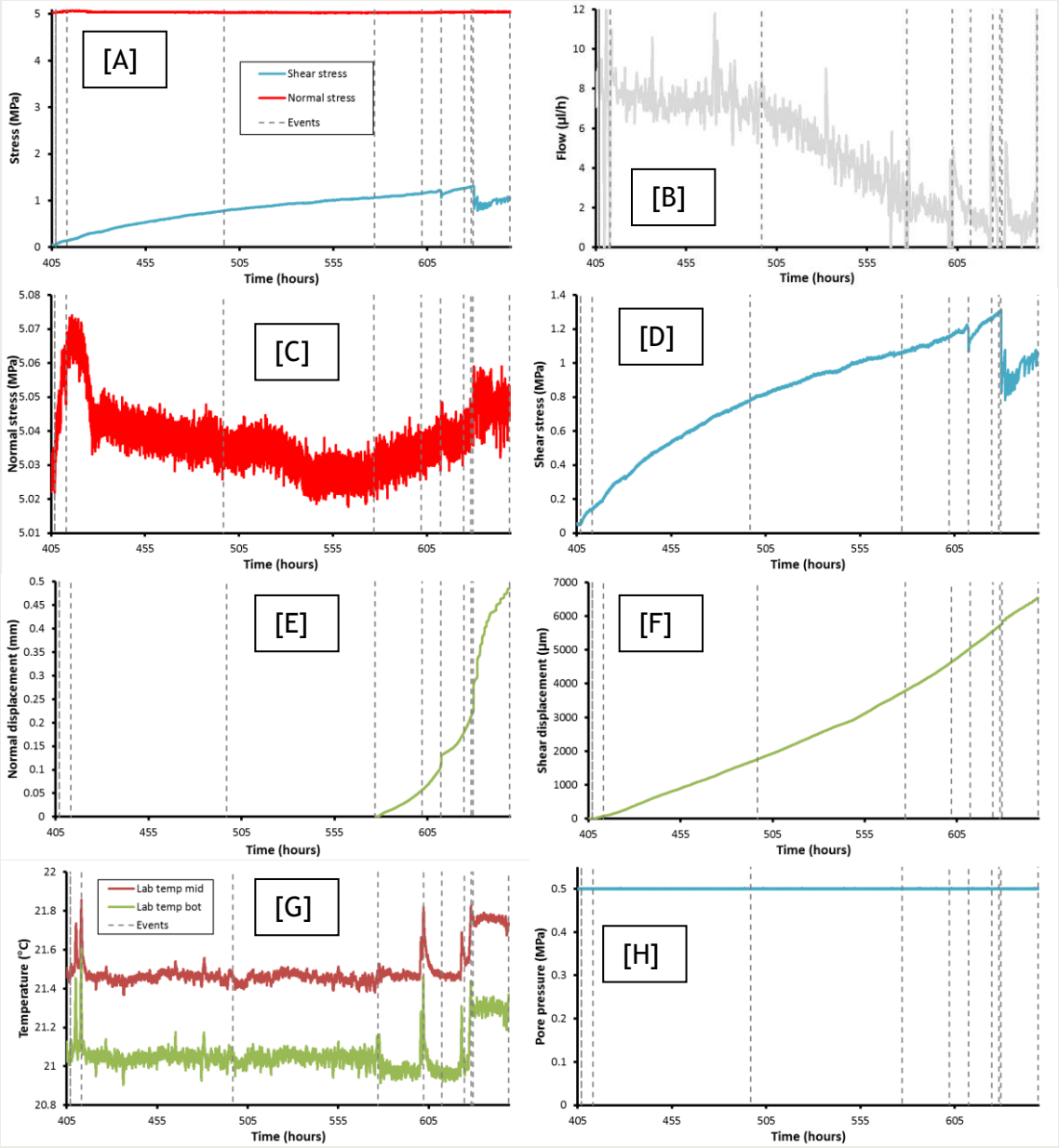

Figure 8-21: Data for shear test 2 (stage 4) of test OPERA_Shear-2. [A] Stress history. [B] Flow into the sample. [C] Normal stress. [D] Resultant shear stress. [E] Normal displacement of the sample. [F] Detail of normal displacement. [G] Temperature. [H] Pore pressure. Dashed lines represent events of note.

Following 500 hours shear stress increased in a near linear manner (**Figure 8-21 D**), whilst flow reduced at an increased rate (**Figure 8-21 B**). At a time of 612.27, flow had reduced to 1.5 µl/h (0.4×10^{-14} m^2/s) and shear stress had reached 1.23 MPa (0.084 strain). At this time a drop in shear stress of 0.2 MPa occurred (**Figure 8-21 D**) and the sample contracted (**Figure 8-21 E**). This event signified the movement along the pre-existing fracture, or the formation of a new fracture surface. No change in flowrate was noted during this event (**Figure 8-21 B**).

Shear stress (**Figure 8-21 D**) quickly recovered following the stress drop at 629.76 hours and reached a maximum of 1.31 MPa at 629.48 hours, a strain of 0.096. At this time the sample underwent movement, reducing shear stress by 0.5 MPa (**Figure 8-21 D**), contracting the sample (**Figure 8-21 E**), and a jump in shear movement was noted (**Figure 8-21 B** and **F**). This resulted in a short-term increase of flow (**Figure 8-21 B**), which

peaked at around 30 µl/h (7.1×10^{-14} m^2/s). This increase in flow only lasted for approximately 1 hour before returning to around 2 µl/h (0.5×10^{-14} m^2/s).

Shear stress recovered with a stick-slip behaviour for the remaining time of shear test 2 (**Figure 8-21 D**). Shear stress had recovered to 1.06 MPa by the end of shearing. During this period flow remained constant and low (**Figure 8-21 B**), while the sample continued to contract (**Figure 8-21 E**). At 649.05 hours the test was terminated as strain was approaching 0.11, 0.01 greater than the design of the Direct Shear Rig. The normal stress and pore fluid pressure were reduced carefully and the sample was extracted from the apparatus.

Key observations of stage 4 (Shear test 2): A peak stress of 1.31 MPa was achieved at 0.096 strain; A stress drop occurred resulting in a reduction of 0.5 MPa (to 0.82 MPa), contraction of the sample, and shear movement; the first indication of movement occurred at a shear stress of 1.23 MPa (0.084 strain); shear reduced flow from 8 to 1.5 µl/h (1.9 to 0.4×10^{-14} m^2/s); stress drop resulted in a short-term increase in flow of around 1 order of magnitude for less than 1 hour; shear stress recovered following movement with stick-slip behaviour; shear stress recovered to 1.06 MPa; test terminated following 0.11 strain.

8.3.5 Comparing shear tests 1 and 2

Figure 8-22 compares the mechanical results for shear tests 1 and 2 of test OPERA_Shear-2. Both tests have linear regions that can be defined, which give a slope of 26.93 MPa for shear test 1 (**Figure 8-22 A**) and 29.48 MPa for shear test 2 (**Figure 8-22 B**). These values correspond with the shear modulus of Boom Clay and show good agreement (**Figure 8-22 C**). Close agreement is also seen in peak stress, with shear test 1 giving 1.30 MPa and shear test 2 giving 1.31 MPa. These are remarkably similar, yet differences in the strain seen at peak stress were seen, with shear test 1 reaching peak stress at 0.067 and shear test 2 at 0.096. Agreement is also seen when comparing the stress at which the first indication of failure occurred, with 1.28 MPa in shear test 1 and 1.23 MPa in shear test 2. Agreement can also be seen in the slope of the stress-strain curves post yield, even considering the work-hardening seen in shear test 1 (**Figure 8-22 D**). In the current tests it appears that the fractured Boom Clay has similar mechanical properties to the intact rock. Therefore the reduction in flow properties prior to shearing (self-sealing) resulted in a degree of mechanical self-healing.

Differences are also noted. Shear test 1 underwent strain hardening at around 0.05 strain, the cause of this feature is unknown, but may be related to the locking of a shear surface forming at an unfavourable angle. Shear test 2 required considerably greater strain to achieve the stress magnitude seen in shear test 1. This test also underwent a considerable stress drop suggesting that the sample slipped along the shear surface. This is likely to occur if movement is along an existing fracture and suggests that the sample failed along the pre-existing fracture surface. However, it is usual for repeat testing to show a considerable reduction in strength and the results suggest that Boom Clay had self-healed and that a new fracture surface may have formed. The behaviour post-peak is also worth noting in shear test 2. Stick-slip behaviour suggests that the sample was sliding along a shear fracture. In shear test 1 it was thought that the sample had not reached failure, yet decommissioning of the sample showed that it had sheared into two halves. Stick-slip behaviour was not seen, neither was a significant stress drop. Therefore it is suggested that significant differences exist between the deformation in shear test 1 and 2.

Key observations comparing shear test 1 and 2: Both test have similar shear modulus, peak stress, and stress at which deformation is first inferred; differences seen in the strain at which peak stress was achieved; differences also noted, in test 1 the sample underwent work-hardening, test 2 saw a significant stress drop and stick-slip behaviour; significant differences exist between the deformation in shear test 1 and 2; Boom Clay underwent self-healing.

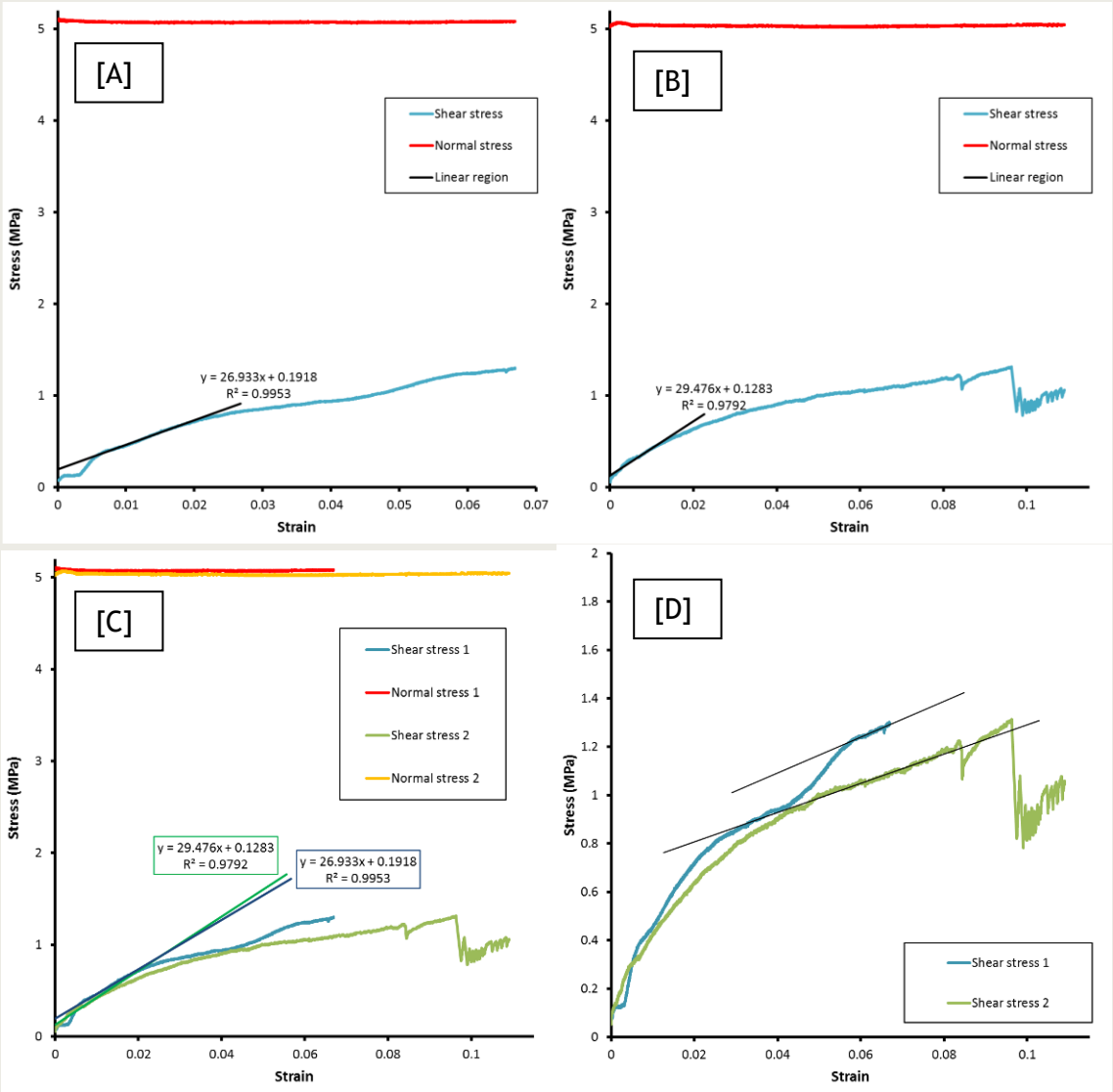

Figure 8-22: Stress-strain response of test OPERA_Shear-2. [A] Shear test 1. [B] Shear test 2. [C] Comparison of the shear tests. [D] Comparison of post-yield stress-strain slopes.

8.3.6 Fracture topology

Figure 8-23 shows a series of photographs of the fracture surface at the end of shear test 1 and 2 for comparison. As can be clearly seen, a continuous fracture surface was formed in the sample during the first shear test (**Figure 8-23 A** and **B**), exposing geological features within the sample, possibly of bioturbation. The fracture formed sub-parallel with the shear direction and resulted in some polishing. Generally the surface appeared a clean break in the Boom Clay.

Following shear test 2 (**Figure 8-23 C** and **D**), the fracture surface was still clearly seen. However, the addition of water during this shear test resulted in a change of the Boom

Clay fabric, as seen by a change in colour, roughness and extrusion of clay between the two collars of the sample holder. A clear indentation of the sample collars is also seen in **Figure 8-23 D**, this being the result of consolidation of the sample and the closure of the 3 mm gap between the collars. The extruded material (**Figure 8-23 C**) was seen to be very wet and was the result of sloughing. As with test OPERA_Shear-1, a small hard fossil-like object was exposed during shear test 2 (**Figure 8-23 C**). This was not apparent in shear test 1 (**Figure 8-23 A** and **C**) and suggests that a new fracture surface formed, or at least considerable re-profiling of the fracture plane occurred.

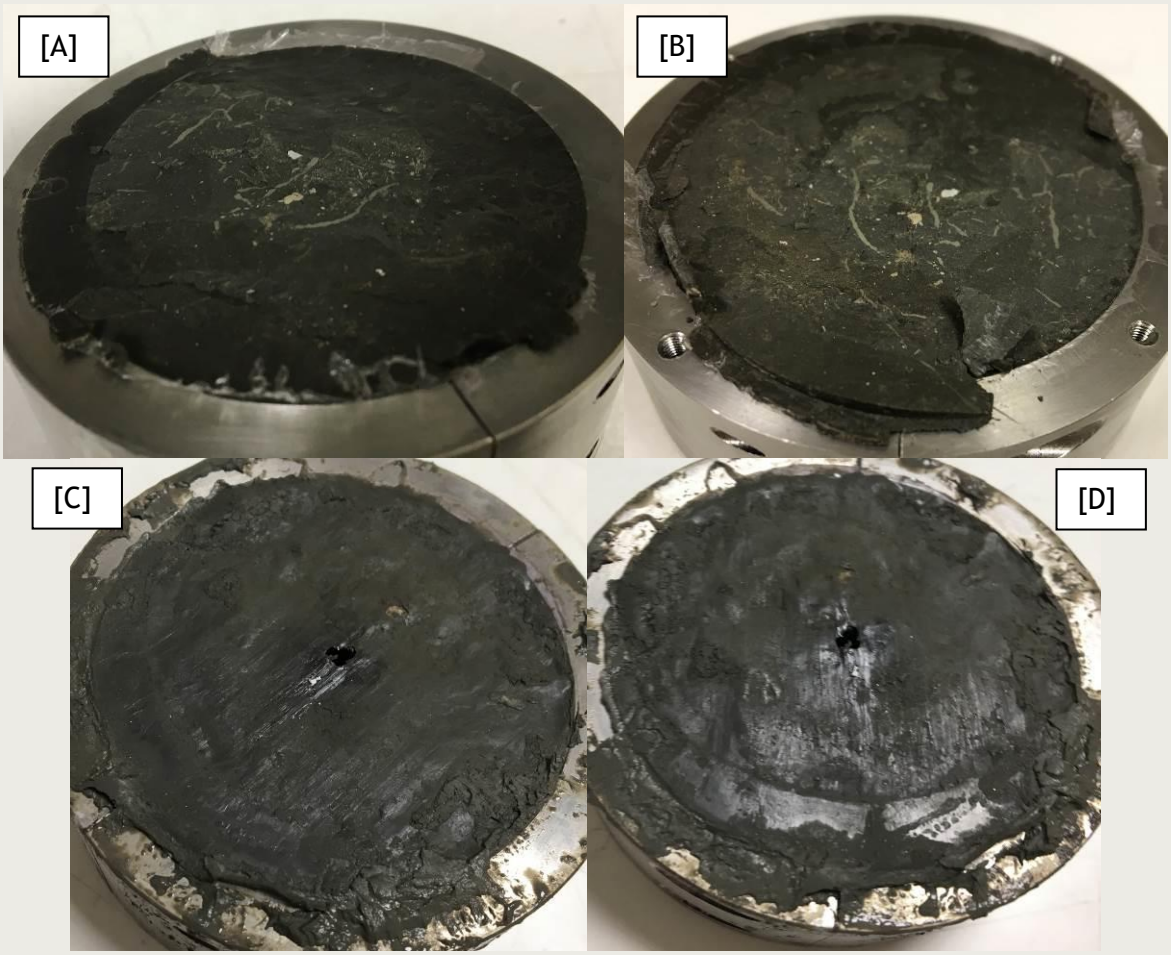

Figure 8-23: Observations of fracture surfaces in test OPERA_Shear-2. [A] Shear test 1 top surface. [B] Shear test 2 bottom surface. [C] Shear test 2 top surface. [D] Shear test 2 bottom surface.

The shear surfaces were scanned following shear test 1 and 2 using a NextEngine 3D Scanner HD, the results of which are shown in **Figure 8-24** and **Figure 8-25**. The upper images in each figure show the raw scanned surface height, whilst the lower images show this data following the removal of a 3rd order polynomial surface to remove the "form" of the fracture surface.

Comparing upper and lower fracture surfaces shows the same general features of the fractures surface (**Figure 8-24**, **Figure 8-25**). It should be noted that the scanned data has been trimmed to display a circle with a 58 mm diameter. No systematic matching selection of identical areas was undertaken and mismatch of fracture surfaces is likely. However, the data show that the two halves of the test sample fit together, although areas of mismatch can be inferred.

Carefully comparing the two shear surfaces after shear tests 1 and 2 does not show the same general features (e.g. **Figure 8-24 A** and **B**). Even accounting for differences in form based on the samples being at different orientations within the scanner (e.g. **Figure 8-24 C** and **D**), there is limited correlation between the results from shear test 1 and 2. Some correlation may exist between **Figure 8-24 C** and **D** if the image shown in **Figure 8-24 D** is rotated 90° anticlockwise. However, significant changes in the fracture are apparent comparing the raw surface data (**Figure 8-24 A** and **B**). Little correlation can be seen between the top fracture surfaces (**Figure 8-25**). These observations suggest that a new fracture surface formed between the two tests and that the prolonged injection of water at the start of shear test 2 resulted in the self-healing of the clay.

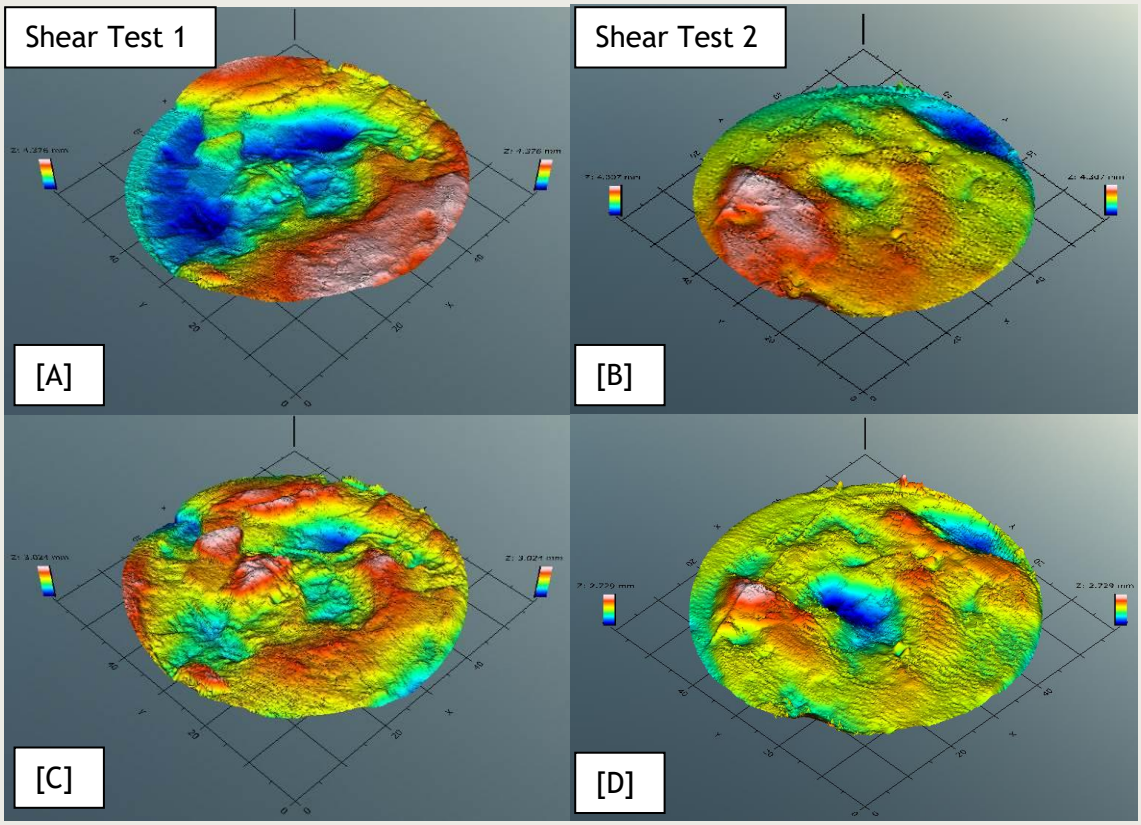

Figure 8-24: Surface topology of the bottom fracture surface following shear test 1 and 2 of test OPERA_Shear-2. [A] Shear test 1 bottom surface. [B] Shear test 2 bottom surface. [C] Shear test 1 bottom surface following removal of surface form. [D] Shear test 2 bottom surface following removal of surface form.

Surface topology data was processed using TrueMap 5.0 software. This can determine gross surface data or can be used to define parameters along profiles. For the current study only surface results are considered, as summarised in **Table 8-5** and **Figure 8-26**. As can be seen, most parameters compare well between the top and bottom fracture surfaces. However, peak height (S_p), kurtosis (S_{ku}) and skewness (S_{sk}) show marked differences between the top and bottom surfaces. The differences in peak height are not matched by differences in peak to valley height (S_t) and therefore may simply be the result of the polynomial surface removed that represented the fracture form.

Significant differences are seen between shear test 1 and 2. For instance, average roughness (S_a) decreased from 0.344 to 0.243 mm between test 1 and 2, whilst the route mean squared roughness (S_q), peak to valley height (S_t) and texture direction index (S_{tdi}) all decreased from 0.426 to 0.325 mm, 2.961 to 2.795 mm, and 0.595 to 0.566 respectively.

Therefore the fracture surface in shear test 2 had considerably less roughness and may be the result of wear on the existing fracture.

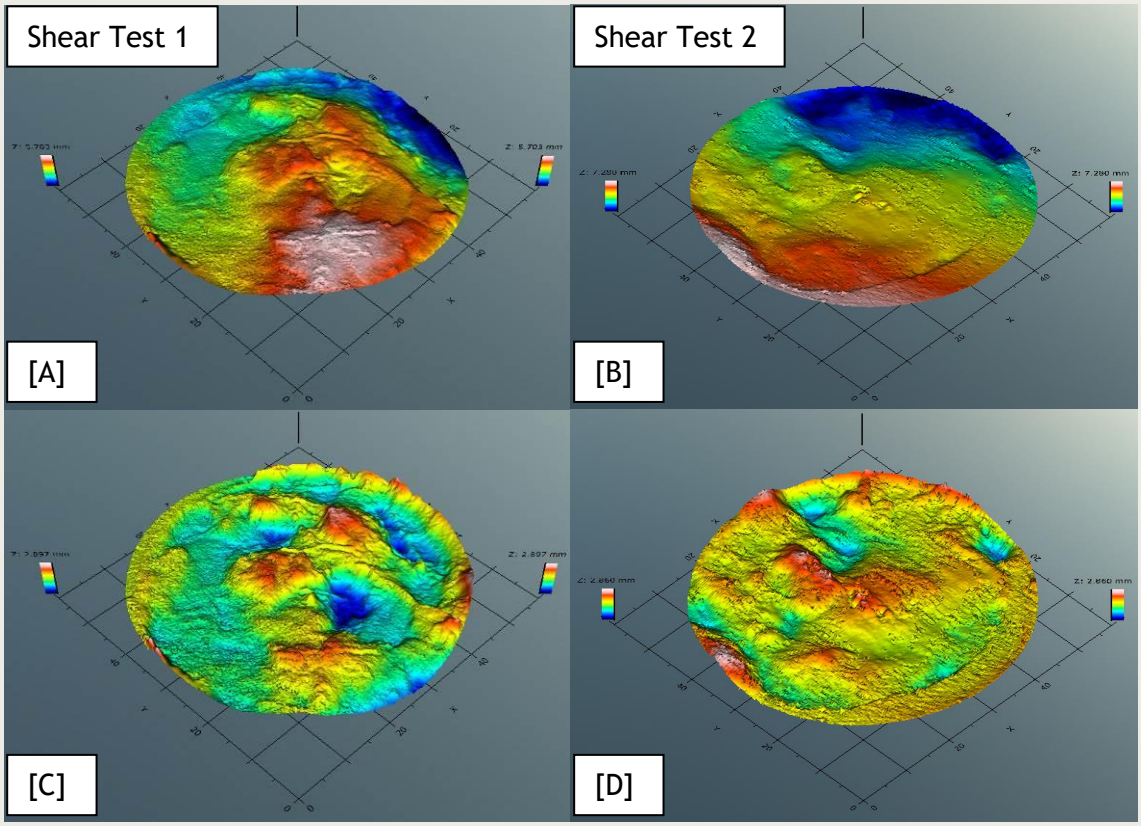

Figure 8-25: Surface topology of the top fracture surface following shear test 1 and 2 of test OPERA_Shear-2. [A] Shear test 1 top surface. [B] Shear test 2 top surface. [C] Shear test 1 top surface following removal of surface form. [D] Shear test 2 top surface following removal of surface form.

Parameter	Symbol	Units	Shear test 1				Shear test 2			
			Bottom		Top		Bottom		Top	
			Full	Corr	Full	Corr	Full	Corr	Full	Corr
Roughness average	S_a	mm	0.963	0.369	1.037	0.318	0.566	0.251	1.367	0.234
Root Mean Square (RMS) Roughness	S_q	mm	1.084	0.455	1.231	0.397	0.712	0.345	1.669	0.304
Peak Height	S_p	mm	2.15	1.26	2.643	1.562	1.737	1.288	3.584	1.219
Valley Depth	S_v	mm	2.226	1.764	3.06	1.335	2.570	1.441	3.696	1.641
Peak to Valley Height	S_t	mm	4.376	3.024	5.703	2.897	4.307	2.729	7.280	2.860
Kurtosis	S_{ku}		1.68	2.744	2.248	3.078	3.268	4.630	2.281	3.569
Skewness	S_{sk}		-0.02	-0.27	-0.17	0.194	-0.47	-0.54	-0.28	-0.10
Texture Direction	S_{td}	°	0.351		90		89.295		89.291	
Texture Direction Index	S_{tdi}		0.654		0.535		0.619		0.512	

Table 8-5: Surface parameters calculated for test OPERA_Shear-2.

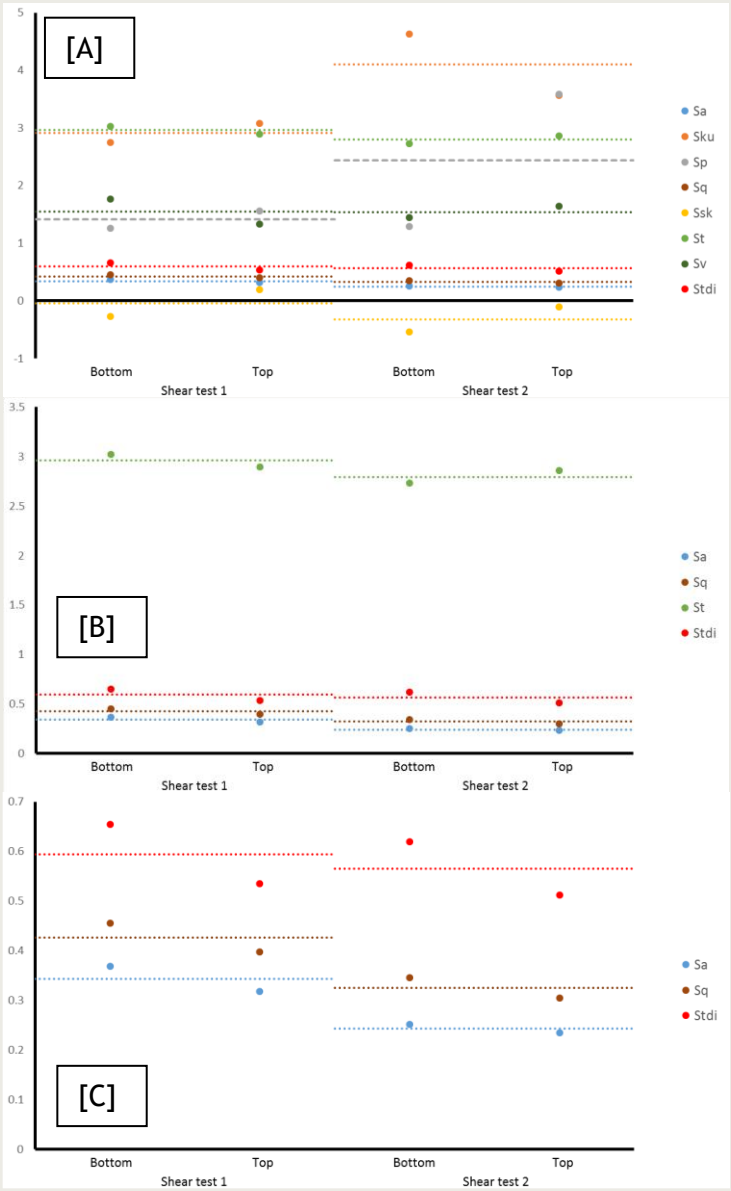

Figure 8-26: Surface texture data for test OPERA_Shear-2. [A] All surface parameters. [B] Key surface parameters. [C] Detail of S_a, S_q, and S_{tdi}. See Table 8-5 for description of parameters and units of measure.

Key observations of fracture topology: a continuous fracture surface was formed sub-parallel with the shear direction; some polishing observed in shear test 1, generally a clean break exposing geological features; different fabric created in shear test 2 because of injection of water; change in colour, roughness and extrusion of clay; indentation of collar apparent due to closure of 3 mm gap between collars; fracture surface 1 and 2 do not correspond; new fracture formed, self-healing of fracture occurred by the injection of water; general agreement of fracture roughness comparing top and bottom sample surfaces; fracture roughness (0.344 – 0.243 mm), RMS roughness (0.426 – 0.325 mm), peak to valley height (2.961 – 2.795 mm) and textural direction index (0.595 – 0.566) all decreased between shear test 1 and 2.

8.3.7 Key finding of OPERA_Shear-2

Outcomes:

1. OPERA_Shear-2 was a four stage test that lasted 27.04 days (649.05 hours). The stress drop at 1.28 MPa signified the onset of fracture formation. The shear modulus was 26.93 MPa, with a peak stress of 1.30 MPa at 0.067 strain. The sample contracted throughout the test and accelerated contraction occurred as the sample strain weakened. The shear stress reduced as the shear zone underwent creep, decaying to 1.13 MPa. The fracture maintained a 0.5 MPa pore pressure.
2. The initial flow was high, quickly stabilising at sub-20 µl/h (sub 4.7 × 10^{-14} m^2/s). During re-hydration (self-sealing), the flow decayed to 8 µl/h (1.9 × 10^{-14} m^2/s). The first indication of deformation occurred at a shear stress of 1.23 MPa (0.084 strain). Repeat shearing gave a peak stress of 1.31 MPa at 0.096 strain. Shear reduced flow from 8 to 1.5 µl/h (1.9 to 0.4 × 10^{-14} m^2/s);
3. A stress drop occurred (brittle behaviour), which resulted in a reduction of 0.5 MPa (to 0.82 MPa), contraction of the sample and shear movement. This stress drop resulted in a short-term increase in flow of around 1 order of magnitude for less than 1 hour. The shear stress recovered following movement with stick-slip behaviour. The shear stress recovered to 1.06 MPa, and the test was terminated following 0.11 strain.
4. Both shear tests have similar shear modulus, peak stress, and stress at which deformation is first inferred, but differences seen in the strain at which peak stress was achieved. Shear test 1 showed ductile behaviour, whilst shear test 2 showed brittle behaviour. The Boom Clay underwent self-healing. A continuous fracture was formed sub-parallel with the shear direction. Some polishing observed in shear test 1, giving a clean break exposing the geological features. A different fabric was created in shear test 2 because of the injection of water. A change in colour, roughness and extrusion of clay was observed. There was an indentation of collar apparent due to closure of 3 mm gap between collars;
5. Fracture surface 1 and 2 do not correspond, new fracture formed implying self-healing of fracture occurred by the injection of water;
6. Fracture roughness (0.344 – 0.243 mm), RMS roughness (0.426 – 0.325 mm), peak to valley height (2.961 – 2.795 mm) and textural direction index (0.595 – 0.566) all decreased between shear test 1 and 2.

8.4 *Test OPERA_Shear-3*

Test OPERA_Shear-3 aimed to test Boom Clay at a stress condition representative of the Mol URL in Belgium, the state at which the material was cored. This was a repeat of OPERA_Shear-1, which had been performed at a stress state too high to represent Mol. Test OPERA_Shear-3 lasted a total of 20.27 days (486.64 hours), with **Figure 8-27** showing the test result data for the complete test history and **Table 8-6** summarising the individual test stages. The four stages of the test can be seen (initial hydration and swelling stage at *in situ* conditions, shear test 1, fracture re-hydration, and shear test 2 – flow testing). Results for each stage are introduced in the following sections. Please note that temperature was not logged during the experiment. However, other tests running within the laboratory have confirmed that no temperature events occurred during the full duration of the test.

Stage	Time (h)		Event	Stage length
1	0.00	Hyd	Start of test: Normal stress = 2.1 MPa, Injection = 25 µl/h	234.57
	234.57		End of hydration stage	
2	234.57	Shear test 1	Start of shearing of intact sample	55.34
	238.09		Start of lowering of shear stress	
	238.37		Stabilisation of shear stress	
	239.01		Drop in shear stress and compaction event	
	243.58		Change in slope of shear stress (strain softening)	
	250.69		Change in slope of shear stress (work hardening) and start of enhanced compaction of sample	
	264.01		Change of slope, start of work hardening	
	267.36		Peak stress	
	289.91		End of shearing	
3	300.00	Shear test 2: Flow experiment	Set-up of test for flow experiment	152.33
	311.76		Dilation sensor out of range	
	356.55		Start of pore pressure at 500 kPa	
	360.11		Stopping of pore pressure	
	360.47		Re-setting of dilation sensor and start of pore pressure decay following re-pressurisation to 500 kPa	
	361.56		Re-introduction of pore pressure at 500 kPa	
	452.33		End of fracture re-hydration	
4	452.33		Start of shear	497.71
	455.63		Start of sample consolidation	
	456.18		Start of reduction of flow	
	461.37		Peak stress	
	477.17		Secondary peak stress following work hardening	
	486.64		End of shearing	
	486.64		End of test	

Table 8-6: Summary of experimental history of test OPERA_Shear-3 showing stage number, description of stage/event, and boundary conditions

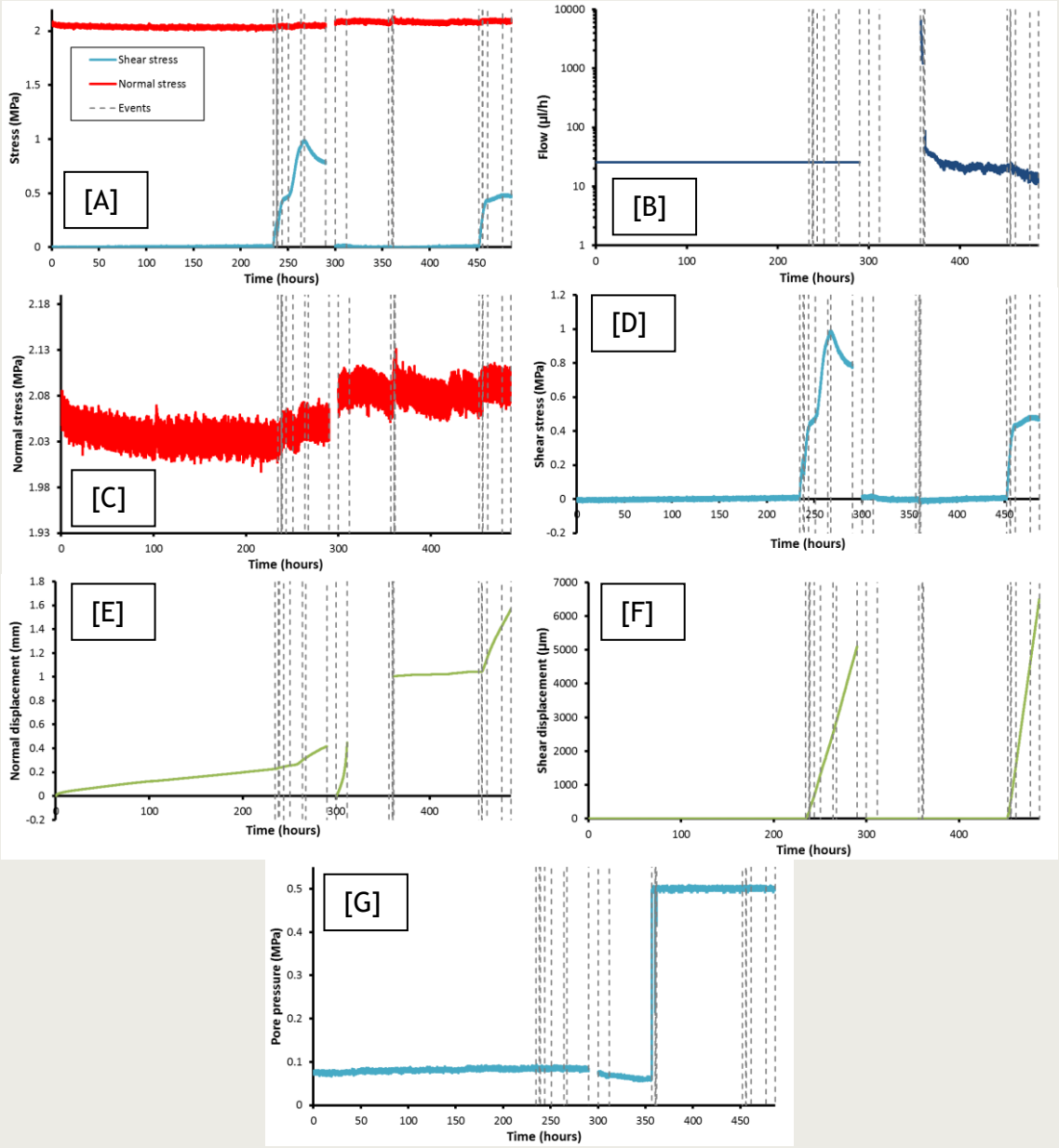

Figure 8-27: Data for the complete test history of test OPERA_Shear-3. [A] Stress history. [B] Flow into the sample. [C] Normal stress. [D] Resultant shear stress. [E] Normal displacement of the sample. [F] Shear displacement. [G] Pore pressure. Dashed lines represent events of note.

8.4.1 Stage 1: Sample hydration

The sample was loaded into the Direct Shear Rig and the boundary conditions were setup on the apparatus with a normal stress of 2.1 MPa (**Figure 8-28 A**). The pore pressure system was set to constant flow of 25 µl/h in order to saturate the sample (**Figure 8-28 B**). During this stage of testing little of note occurred. The low flow rate resulted in a small pore pressure less than 0.1 MPa (**Figure 8-28 G**). Of note was the contraction of the sample (**Figure 8-28 E**). Throughout the stage the sample consolidated by a total of 0.227 mm. This stage of the test lasted nearly 10 days (234.57 hours) and is summarised in **Figure 8-28**.

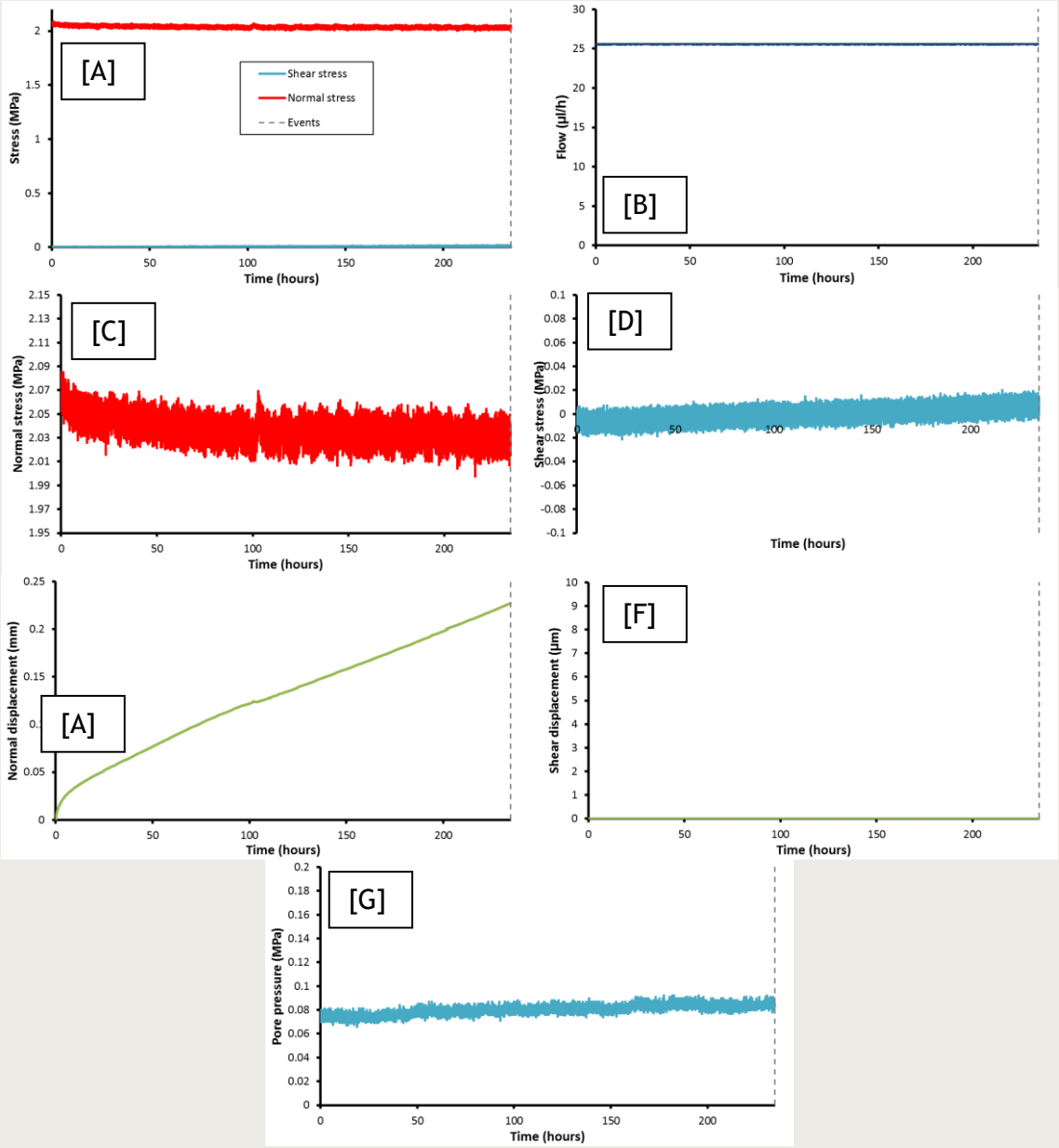

Figure 8-28: Data for the stage 1 (rehydration) of test OPERA_Shear-3. [A] Stress history. [B] Flow into the sample. [C] Normal stress. [D] Resultant shear stress. [E] Normal displacement of the sample. [F] Shear displacement. [G] Pore pressure. Dashed lines represent events of note.

Key observations of stage 1 (sample hydration): sample consolidated by 0.227 mm during the 10 day stage; consolidation reached a linear rate.

8.4.2 Stage 2: Shear test 1

The initial shearing phase of test OPERA_Shear-3 lasted a total of 55.34 hours and is summarised in **Figure 8-29**. As can be seen in **Figure 8-29 F**, a relatively linear shear rate was achieved. The shearing of the sample resulted in an initial, near-linear, stress-strain response (**Figure 8-29 D**); this corresponds to the shear modulus of the sample. At a relatively low shear stress of 0.242 MPa (0.003 strain, 238.09 hours) the shear stress started to reduce, suggesting failure of the sample. At this time the consolidation rate of the sample increased (**Figure 8-29 E**). Shear stress stabilised at 238.37 hours at about 0.2 MPa and dropped by 0.05 MPa at 239.01 hours giving a minimum shear stress of 0.146 MPa

(**Figure 8-29 D**). However, shear stress recovered and increased in a near linear manner. Strain softening initiated at 243.58 hours at a shear stress of 0.41 MPa (0.011 strain). The rate of consolidation of the sample reduced at this time, suggesting that a fracture had formed that was dilating, opposing the overall sample consolidation.

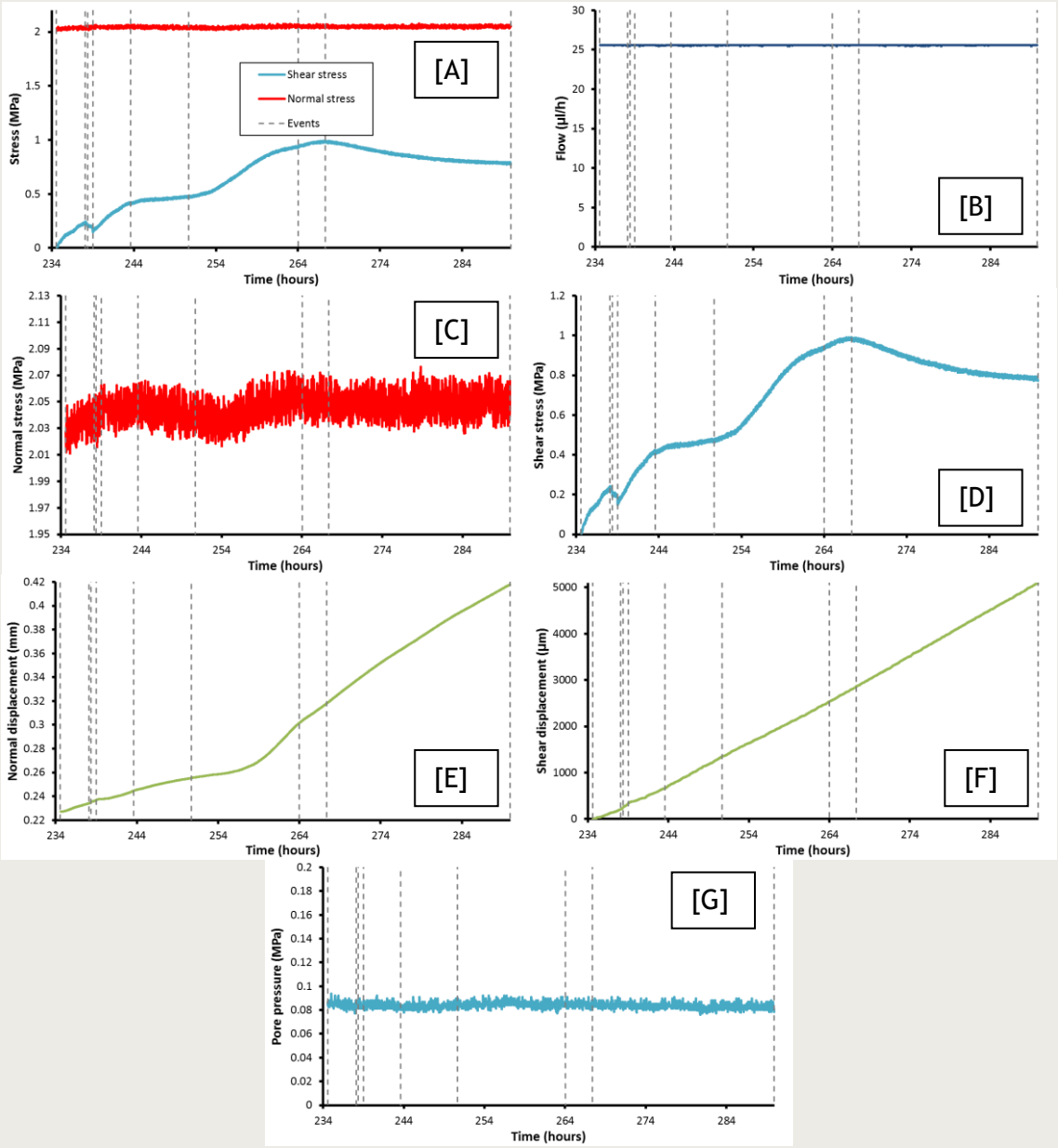

Figure 8-29: Data for the initial shearing of test OPERA_Shear-3. [A] Stress history. [B] Flow into the sample. [C] Normal stress. [D] Resultant shear stress. [E] Normal displacement of the sample. [F] Shear displacement. [G] Pore pressure. Dashed lines represent events of note.

At around 250 hours (0.475 MPa shear stress, 0.021 strain) the sample started to work harden (**Figure 8-29 D**) and the rate of consolidation further reduced (**Figure 8-29 E**), suggesting fracture dilation. This may suggest that the shear strength of the material was represented at this point and that the subsequent deformation was the result of a fracture sliding at unfavourable orientations. The sample continued to maintain increasing shear stress (**Figure 8-29 D**), with strain weakening and strain work hardening events occurring until a peak in shear stress was achieved at 267.36 hours. In the period of 250.69 to 267.36 hours the sample stopped dilating and consolidation accelerated (**Figure 8-29 E**), reaching

a linear consolidation rate at peak stress. The strain required to reach a peak stress of 0.992 MPa was 0.048. For the remainder of the stage, the sample underwent strain softening (**Figure 8-29 D**), with a near asymptote in shear stress achieved at 289.91 hours with a stress of 0.77 MPa at 0.085 strain. During this period the sample consolidated at a near-linear rate (**Figure 8-29 E**). Over the entire stage pore pressure remained low (**Figure 8-29 G**) and showed no variation as the sample underwent failure. This is not surprising as the failure plane was situated around 25 mm away from the pore fluid injection filter.

Key observations of stage 2 (Shear test 1): Three features may represent the shear strength of the sample: 1) 0.242 MPa (0.003 strain), 2) 0.475 MPa shear stress (0.021 strain), and 3) 0.992 MPa (0.048 strain); initial stress event (0.242 MPa) resulted in a clear reduction of shear stress; multiple strain-softening and work hardening events observed suggesting the fracture plane developed and did not slide easily; residual shear stress of about 0.75 MPa inferred at 0.048 strain; pore pressure remained low throughout the test and did not change as the fracture formed.

8.4.3 Stage 3: Rehydration of the fracture surface

A 4 mm diameter hole was drilled into the centre of the top sample to allow an injection bore to be added. The length of the injection pipe was adjusted so that it sat flush with the fracture surface. The interface between the Boom Clay sample and top block was sealed using Mastic, whilst Mastic was also added to the injection pipe prior to insertion into the sample. The apparatus was reassembled and the same boundary conditions were imposed with a normal stress of 2.1 MPa, as shown in **Figure 8-30**. The rehydration of the fracture surface lasted 6.35 days (152.33 hours).

At the start of stage 3 a pore pressure of 500 kPa was placed upon the pore injection circuit (**Figure 8-30 G**). This created a high flow rate (**Figure 8-30 B**), which flooded the fracture surface. Water injection was stopped and the fracture was allowed time to self-seal without excessive erosion of the fracture surfaces. During this period the consolidation of the sample was considerable (**Figure 8-30 E**), with 0.45 mm reduction in the first 11.8 hours. Unfortunately the dilation sensor went out of range at 311.76 hours and the full extent of the closure is unknown. However, the addition of water at the fracture plane and water within the bath of the shear apparatus promoted considerable consolidation compared with stage 1 of the test.

At 356.55 hours a pore pressure of 500 kPa was created by the pore injection pump (**Figure 8-30 G**). This created an initially high flow rate of 5,500 µl/h (1.3×10^{-11} m^2/s; **Figure 8-30 B**). This quickly reduced to sub-100 µl/h (2.4×10^{-13} m^2/s) within 6 hours. Flow continued to reduce and by the end of the stage had reduced to around 20 µl/h (4.7×10^{-14} m^2/s). At this time the dilation sensor was reset and for the remaining time of the stage showed little variation (**Figure 8-30 E**). This suggests that consolidation had ceased, or possibly indicates that the two collars were in contact with one another, or the gap was filled with sloughed clay that made further consolidation difficult.

At 360.11 hours the pore injection was stopped to investigate the apparatus for pore fluid leakage (**Figure 8-30 G**). This was identified and fixed, with pore fluid pressure re-established at 361.56 hours. The test stage was terminated at 452.33 hours when pore fluid flow had stabilised (**Figure 8-30 B**).

Key observations of stage 3 (Stress relaxation; shear test 1): It was initially difficult to sustain pore pressure within the fracture without excessive flow rates; considerable sample consolidation occurred, promoted by the addition of fluid at the fracture and the sloughing of clay; a 500 kPa pore fluid pressure created a high flow rate (5,500 µl/h (1.3×10^{-11} m^2/s)); flow reduced to sub-100 µl/h (sub-2.4×10^{-13} m^2/s) within six hours; fracture flow reduced to ~20 µl/h (4.7×10^{-14} m^2/s) demonstrating fracture self-sealing.

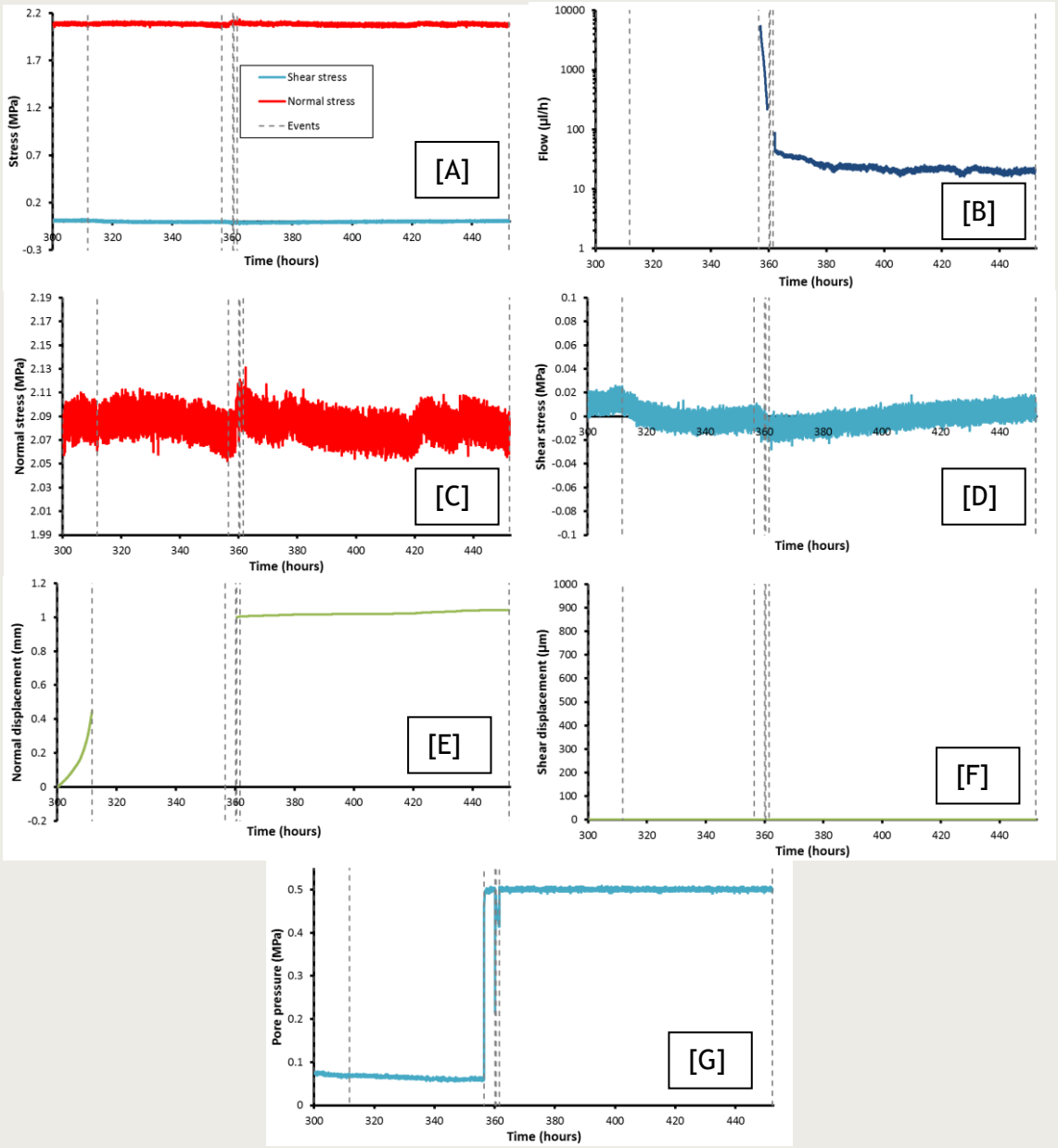

Figure 8-30: Data for the rehydration of the fracture stage (3) of test OPERA_Shear-3. [A] Stress history. [B] Flow into the sample. [C] Normal stress. [D] Resultant shear stress. [E] Normal displacement of the sample. [F] Shear displacement. [G] Pore pressure. Dashed lines represent events of note.

8.4.4 Stage 4: Shear test 2

A repeat shear test for OPERA_Shear-2 was conducted with the aim to observe how fracture transmissivity altered during shearing, comparing the mechanical results with those achieved during shear test 1 on intact Boom Clay (**Figure 8-31**). Constant shear was

started at 452.33 hrs (**Figure 8-31 F**). The initial shear stress response was near-linear (**Figure 8-31 D**). Initially flow remained constant and no sample dilation/contraction was noted. At 445.63 hours the sample started to contract and soon after the flow started to slowly reduce. This occurred at around the yield stress of the sample (0.3 MPa). At approximately 461 hours the sample achieved peak stress conditions (**Figure 8-31 B**) with a stress of 0.44 MPa (0.026 strain). This was followed by a small reduction in shear stress, before work hardening of the fracture began. This resulted in a secondary peak stress of 0.49 MPa at 0.078 strain. Stress was maintained at this magnitude for the remaining time of the period, with a final shear stress of 0.48 MPa at 0.108 strain. Following yield of the fracture, flow slowly reduced and stabilised at 13.5 µl/h (3.2×10^{-14} m^2/s; **Figure 8-31 B**). The test was terminated at 486.64 hours as the strain limit of the apparatus was reached (**Figure 8-31 F**). The sample was carefully depressurised and removed from the apparatus. Both fracture surfaces were scanned to determine the topology of the fracture faces.

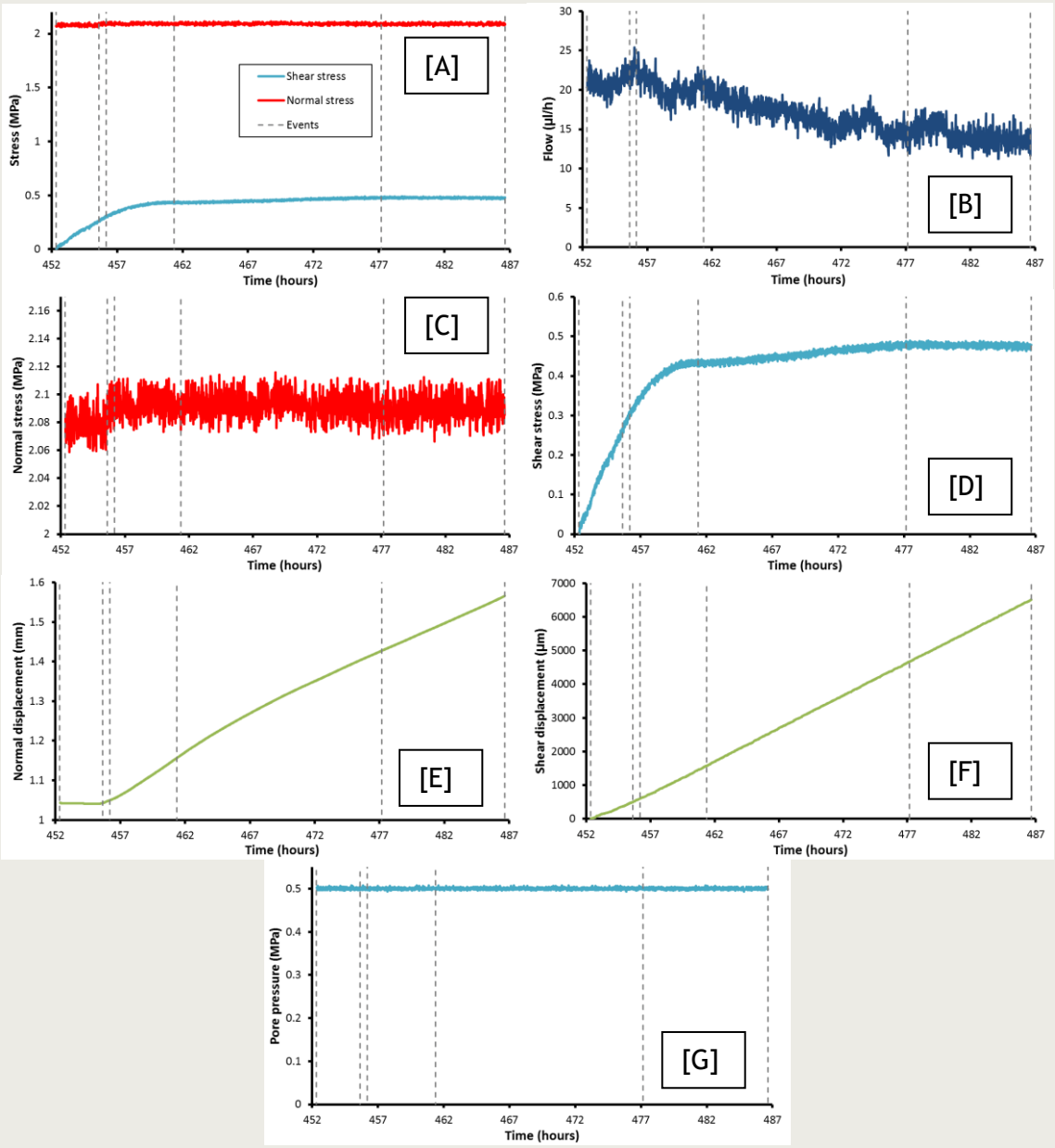

Figure 8-31: Data for shear test 2 of test OPERA_Shear-3. [A] Stress history. [B] Flow into the sample. [C] Normal stress. [D] Resultant shear stress. [E] Normal displacement of the sample. [F] Shear displacement. [G] Pore pressure. Dashed lines represent events of note.

Key observations of stage 5 (Shear test 2): A peak stress of 0.44 MPa at 0.026 strain; work hardening resulted in a secondary peak stress of 0.49 MPa at 0.078 strain; residual stress of 0.48 MPa at 0.108 strain – same as secondary peak stress; flow started to reduce at the yield stress (0.3 MPa); flow reduced from near 20 µl/h (4.7×10^{-14} m^2/s) to a stabilised 13.5 µl/h (3.2×10^{-14} m^2/s).

8.4.5 Comparing shear tests 1 and 2

Figure 8-32 compares the mechanical results for shear tests 1 and 2 of test OPERA_Shear-3. Unlike in previous tests, the comparison of the data is not straightforward as shear test 1 was complicated. As can be seen in **Figure 8-32 A**, three possible linear regions can be identified. It was suggested that the first represents the shear modulus of the sample. This, however, results in a much higher shear modulus (50.65) when compared with shear test 2 (29.84 MPa), or compared with the results achieved in tests OPERA_Shear-1 (30.08, 30.41 MPa) and OPERA_Shear-2 (26.93, 29.48 MPa). This is further exacerbated in the second linear region, which has a higher slope of 76.16 MPa. However, the third linear region gives a shear modulus of 35.5 MPa, which is comparable with other results.

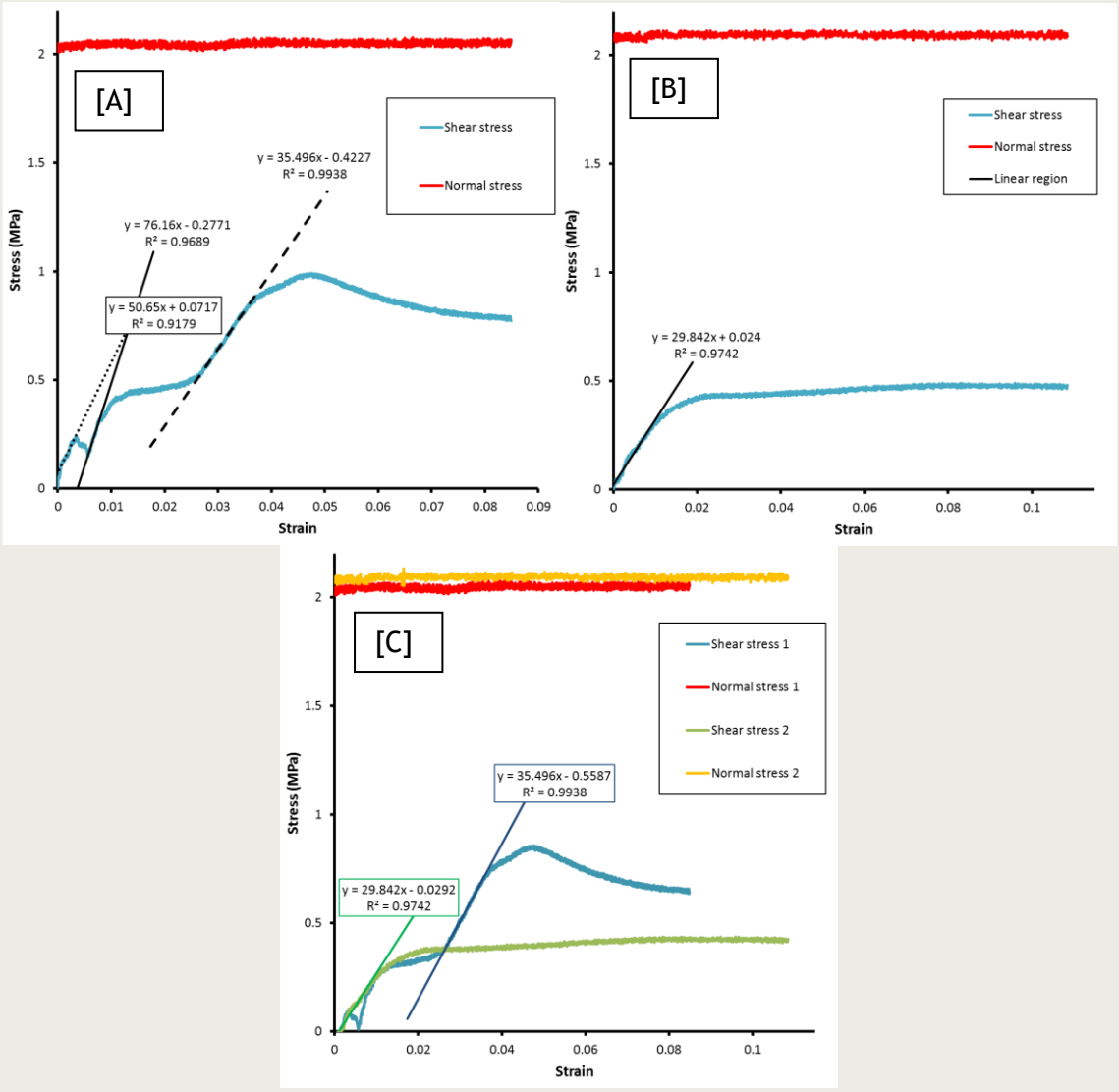

Figure 8-32: Stress-strain response of test OPERA_Shear-3. [A] Shear test 1. [B] Shear test 2. [C] Comparison of the shear tests.

In tests OPERA_Shear-1 and OPERA_Shear-2, good agreement was achieved for peak stress. **Figure 8-32 A** shows that three possible peak stresses can be defined for the current test. **Figure 8-32 C** suggests that the second of these corresponds well with shear test 2, giving peak stresses of 0.475 and 0.48 MPa. This suggests that the third peak stress seen in shear test 1 is the result of locking of the fracture at an unfavourable orientation and may be the result of the small 60 mm diameter samples used in the study.

Key observations comparing shear test 1 and 2: Shear modulus reduced on repeat testing; shear test 1 complicated and secondary peak may represent the strength of the sample, giving peak stresses of 0.475 and 0.48 MPa for shear tests 1 and 2 respectively.

8.4.6 Fracture topology

Figure 8-33 shows a series of photographs of the fracture surface at the end of shear test 1 and shear test 2 for comparison. As can be clearly seen, a continuous fracture surface was formed in the sample during the first shear test (**Figure 8-33 A** and **B**). This formed sub-parallel with the shear direction. This test showed a lot of polishing of the fracture surface, although in generally the surface appeared a clean break in the Boom Clay.

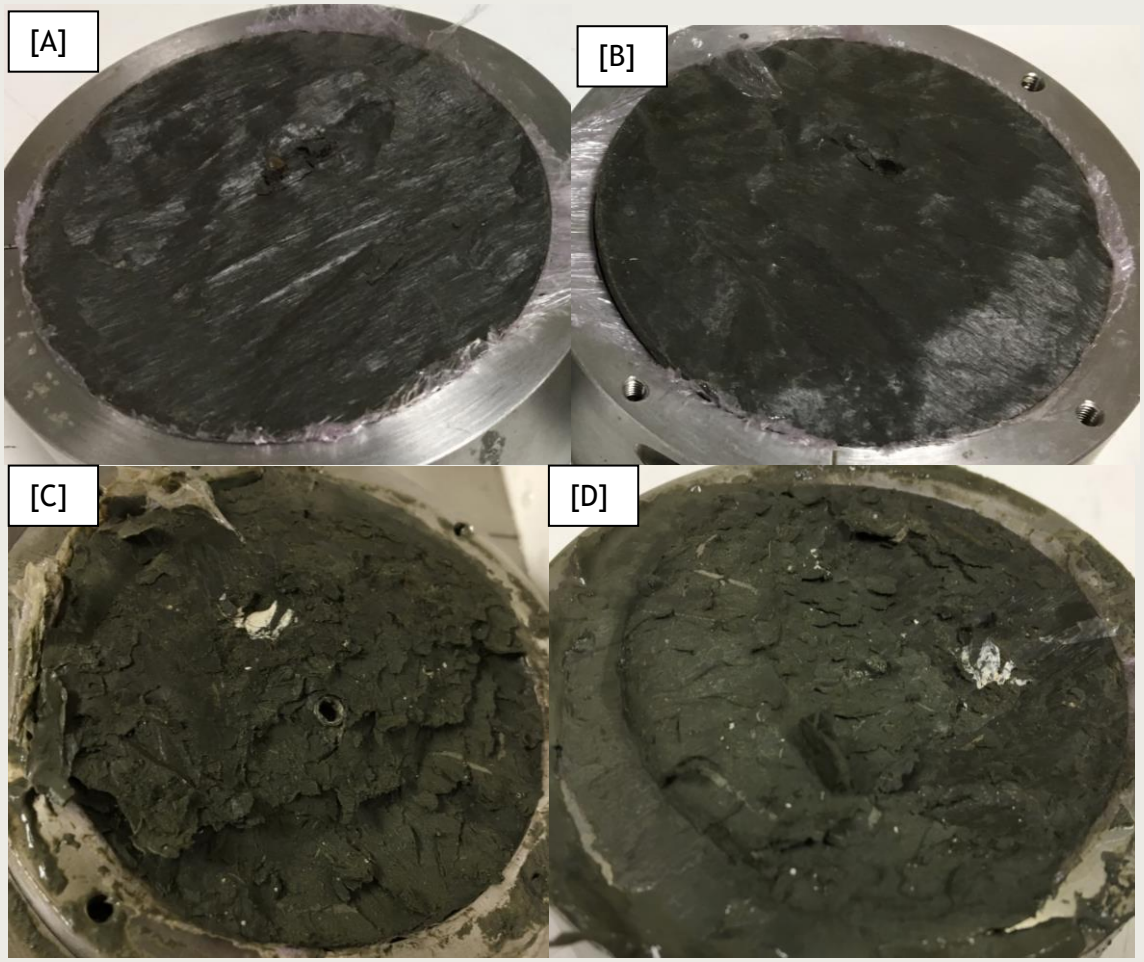

Figure 8-33: Observations of fracture surfaces in test OPERA_Shear-3. [A] Shear test 1 top surface. [B] Shear test 2 bottom surface. [C] Shear test 2 top surface. [D] Shear test 2 bottom surface.

Following shear test 2 (**Figure 8-33 C** and **D**), the fracture surface was still clearly seen. However, the addition of water during this shear test resulted in a distinct change of the Boom Clay fabric, as seen by a change in colour, roughness and extrusion of clay between

the two collars of the sample holder. The fracture surfaces had a number of platy sections, suggesting that multiple sub-parallel fractures formed. The lower block (**Figure 8-33 D**) clearly shows the indentation of the upper sample collar, suggesting that the sample had consolidated sufficiently that the original 3 mm gap between the collars was such that the collars were fouling the fracture. It should be noted that polishing appears significantly less in shear test 2. A nodule (white area, **Figure 8-33 C** and **D**) and other bioturbation features are apparent after shear test 2, whereas these were not seen after shear test 1 suggesting that a new fracture surface had formed.

The shear surfaces were scanned following shear test 1 and 2 using a NextEngine 3D Scanner HD, the results of which are shown in **Figure 8-34** and **Figure 8-35**. The upper images in each figure show the raw scanned surface height, whilst the lower images show this data following the removal of a 3rd order polynomial surface to remove the "form" of the result. Both **Figure 8-34** and **Figure 8-35** show the same general features of the fracture surfaces and show that the two halves of the test sample fit together, although areas of mismatch can be inferred.

Carefully comparing the two shear surfaces after tests 1 and 2 does not show the same general features (e.g. **Figure 8-34 A** and **B**). Even accounting for differences in form based on the samples being at different orientations within the scanner, there is little correlation between the results from shear test 1 and 2. This suggests that a new fracture surface formed between the two tests and that the prolonged injection of water at the start of shear test 2 resulted in the self-healing of the clay.

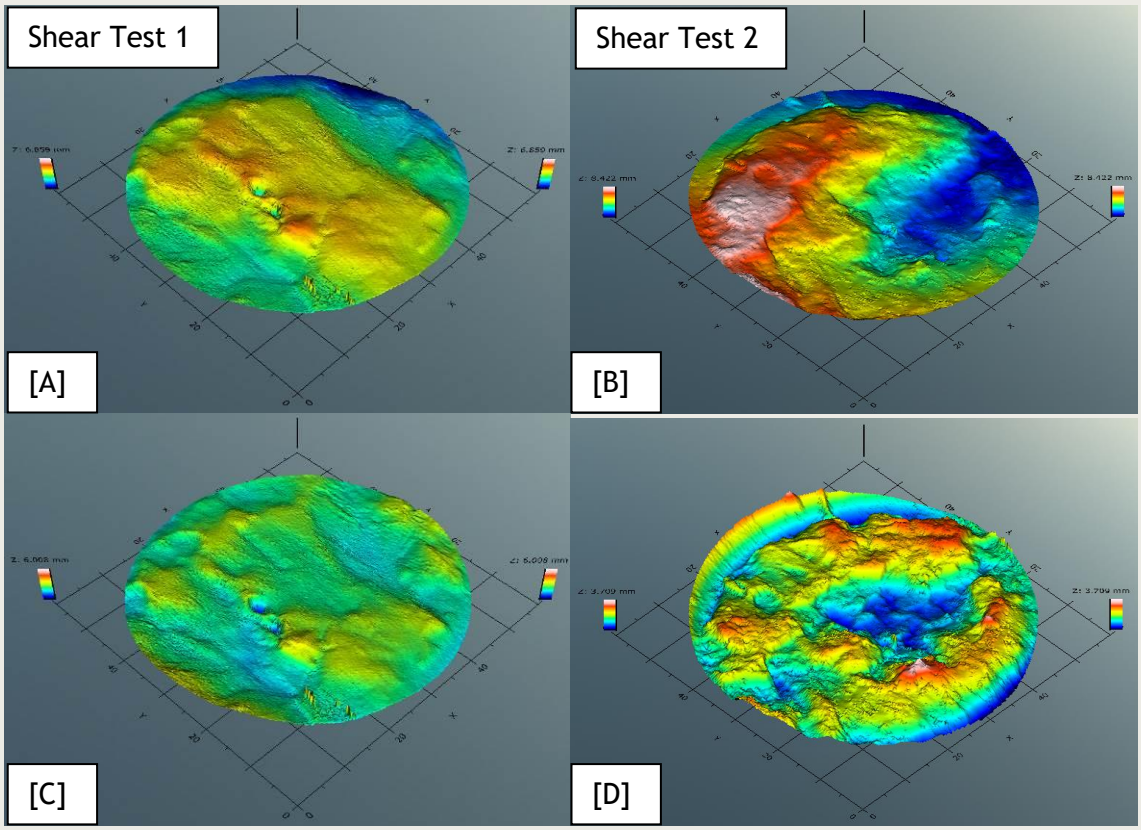

Figure 8-34: Surface topology of the bottom fracture surface following shear test 1 and 2 of test OPERA_Shear-3. [A] Shear test 1 bottom surface. [B] Shear test 2 bottom surface. [C] Shear test 1 bottom surface following removal of surface form. [D] Shear test 2 bottom surface following removal of surface form.

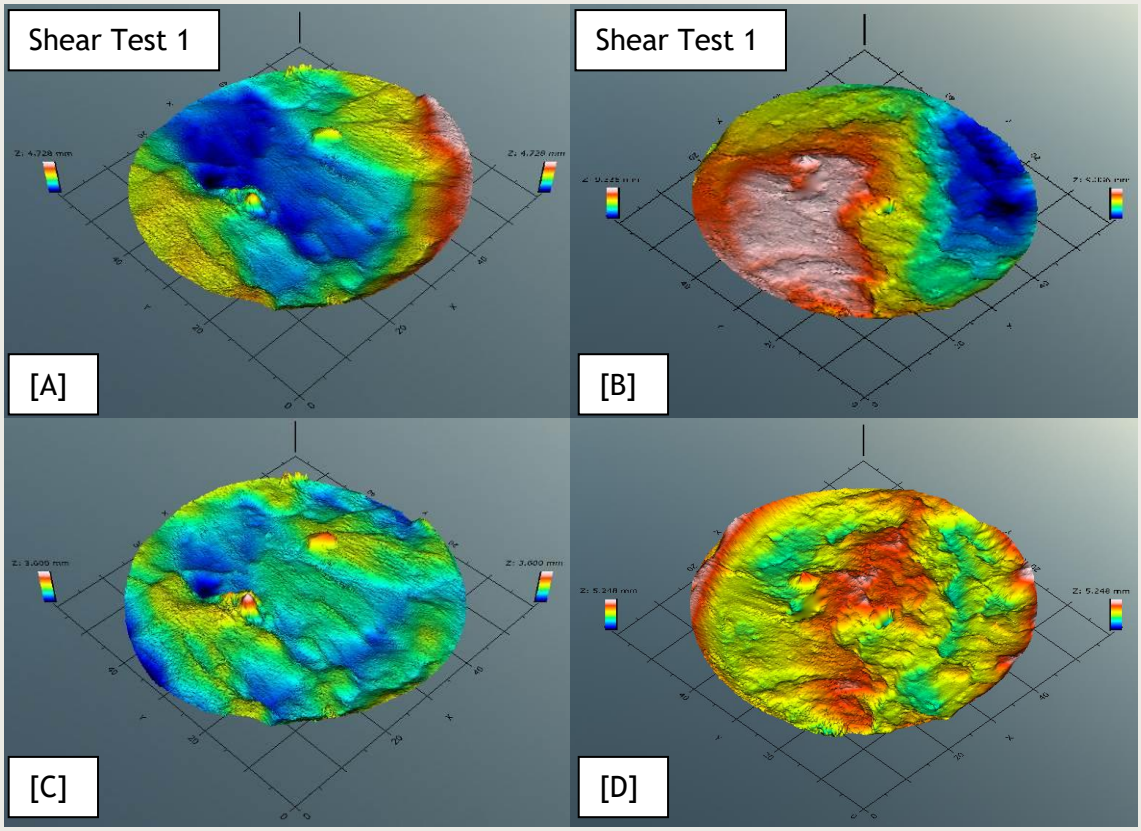

Figure 8-35: Surface topology of the top fracture surface following shear test 1 and 2 of test OPERA_Shear-3. [A] Shear test 1 top surface. [B] Shear test 2 top surface. [C] Shear test 1 top surface following removal of surface form. [D] Shear test 2 top surface following removal of surface form.

Surface topology data was processed using TrueMap 5.0 software. This can determine gross surface data or can be used to define parameters along profiles. For the current study, only surface results are considered, as summarised in **Table 8-7** and **Figure 8-36**. As can be seen, most parameters compare well between the top and bottom fracture surfaces, with some exceptions such as peak to valley height (S_t).

Parameter	Symbol	Units	Shear test 1				Shear test 2			
			Bottom		Top		Bottom		Top	
			Full	Corr	Full	Corr	Full	Corr	Full	Corr
Roughness average	S_a	mm	0.79	0.3	0.808	0.297	1.704	0.492	2.098	0.518
Root Mean Square (RMS) Roughness	S_q	mm	0.937	0.372	0.958	0.371	2.001	0.596	2.45	0.622
Peak Height	S_p	mm	3.656	3.592	2.912	2.318	4.317	2.030	3.893	2.114
Valley Depth	S_v	mm	3.204	2.416	1.816	1.282	4.105	1.678	5.443	3.135
Peak to Valley Height	S_t	mm	6.859	6.008	4.728	3.6	8.422	3.709	9.336	5.248
Kurtosis	S_{ku}		2.706	3.757	2.483	3.696	1.94	2.414	1.997	2.359
Skewness	S_{sk}		-0.55	-0.07	0.446	0.219	0.008	-0.06	-0.42	0.228
Texture Direction	S_{td}	°	0.352		89.295		89.296		89.293	
Texture Direction Index	S_{tdi}		0.518		0.658		0.481		0.588	

Table 8-7: Surface parameters calculated for test OPERA_Shear-3.

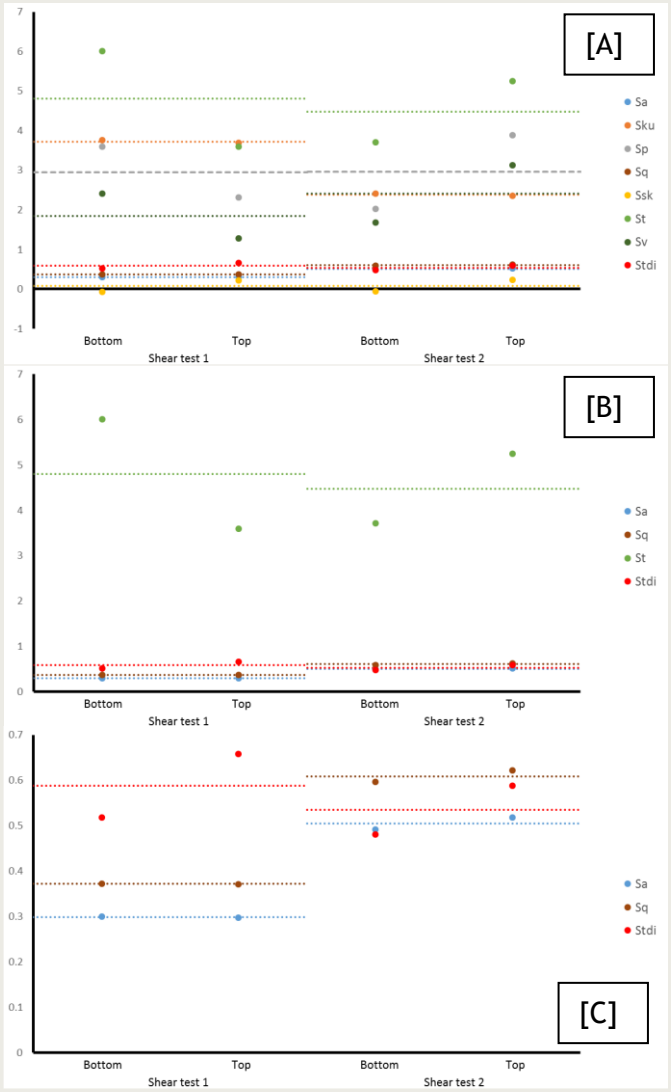

Figure 8-36: Surface texture data for test OPERA_Shear-3. [A] All surface parameters. [B] Key surface parameters. [C] Detail of S_a, S_q, and S_{tdi}. Parameters and units described in Table 8-3: Surface parameters calculated for test OPERA_Shear-1.

.

Significant differences are seen between shear test 1 and 2. Average roughness (S_a) increased from 0.299 to 0.505 mm between test 1 and 2, as is apparent in the photographs of the shear surfaces (**Figure 8-33**). Route mean squared roughness (S_q) also increased from 0.372 to 0.609 mm, whilst both peak to valley height (S_t) and texture direction index (S_{tdi}) decreased from 4.804 to 4.479 mm and 0.588 to 0.535 respectively. The variation in surface parameters and visually distinctive surface topologies seen between shear test 1 and 2 suggest that a new fracture surface formed in shear test 2.

Key observations of fracture topology: a continuous fracture surface was formed sub-parallel with the shear direction; significant polishing occurred during shear test 1; distinctly different fabric seen in shear test 2 with platy fragments, a change in colour, roughness, extrusion of clay, the imprint of a sample collar, and less polishing; fracture surface 1 and 2 do not correspond; geological features (nodule, bioturbation) apparent after shear test 2 that was not seen in shear test 1; a new fracture had formed showing the fracture had self-healed; fracture roughness (0.299 to 0.505 mm) and RMS roughness (0.372 to 0.609 mm) both increased between shear tests, while peak to valley height (4.804 to 4.479 mm) and texture direction index (0.588 to 0.535) both decreased between shear test 1 and 2.

8.4.7 Key findings of OPERA_Shear-3

Outcomes:

1. OPERA_Shear-3 was a four stage test that lasted 20.28 days (486.64 hours). Three features may represent the shear strength of the sample: 1) 0.242 MPa (0.003 strain), 2) 0.475 MPa shear stress (0.021 strain), and 3) 0.992 MPa (0.048 strain). Multiple strain-softening and work hardening events were observed suggesting the fracture plane developed and did not slide easily. The residual shear stress was about 0.75 MPa at 0.048 strain. Considerable consolidation of the sample occurred, promoted by the addition of fluid at the fracture and the sloughing of clay.
2. A pore fluid pressure of 500 kPa created a high flow rate of 5,500 µl/h (1.3×10^{-11} m^2/s), flow reduced to sub-100 µl/h (sub-2.4×10^{-13} m^2/s) within six hours. Flow then reduced to ~20 µl/h (4.7×10^{-14} m^2/s) demonstrating self-sealing;
3. A repeat peak stress of 0.44 MPa at 0.026 strain;
4. Work hardening resulted in a secondary peak stress of 0.49 MPa at 0.078 strain;
5. Residual stress of 0.48 MPa at 0.108 strain;
6. Flow started to reduce at the yield stress (0.3 MPa);
7. Flow reduced from near 20 µl/h (4.7×10^{-14} m^2/s) to a stabilised 13.5 µl/h (3.2×10^{-14} m^2/s);
8. Shear modulus reduced on repeat testing;
9. Shear test 1 complicated and secondary peak may represent the strength of the sample, giving peak stresses of 0.475 and 0.48 MPa for shear tests 1 and 2 respectively;
10. A continuous fracture formed sub-parallel with the shear direction;
11. Significant polishing occurred during shear test 1;
12. Distinctly different fabric seen in shear test 2 with platy fragments, a change in colour, roughness, extrusion of clay, the imprint of a sample collar, and less polishing;
13. Geological features (nodule, bioturbation) apparent after shear test 2 that was not seen in shear test 1;
14. Fracture surface 1 and 2 do not correspond, a new fracture had formed suggesting the fracture had self-healed;
15. Fracture roughness (0.299 to 0.505 mm) and RMS roughness (0.372 to 0.609 mm) both increased between shear tests, while peak to valley height (4.804 to 4.479 mm) and texture direction index (0.588 to 0.535) both decreased between shear test 1 and 2.

8.5 *Direct shear in Boom Clay*

The current study performed three direct shear tests on Boom Clay using the Direct Shear Rig. The three tests were performed at stresses representative of effective stress ranging from the URL at Mol to a stress condition representative of the Netherlands. All three tests gave good results that explain the likely behaviour of fractures in Boom Clay. Many similarities exist in the achieved results with some variation, which will be discussed in this section.

It should be noted that whilst experimental protocols were similar, variations exist that may have influenced experimental results. For instance, tests OPERA_Shear-1 and OPERA_Shear-3 both had initial periods of hydration, whereas test OPERA_Shear-2 started with the initial shearing phase. Only small quantities of water were injected at the upper face of the samples during the hydration stages and it is unlikely that this additional water significantly changed the properties of the sample. However, these prolonged periods prior to shear test 1 did mean that the samples had time to consolidate in response to the applied normal stress and this could play a role on subsequent deformation. Differences were also apparent during stress-relaxation stages, with test OPERA_Shear-3 not having any relaxation and test OPERA_Shear-1 having the longest relaxation times. This could potentially alter the surface characteristics of the fracture surfaces.

Figure 8-37 shows the stress-strain results for all six direct shear tests conducted. On first inspection it would appear that the stress-strain response was quite different for the three tests (shear test 1; **Figure 8-37 B**). However, close inspection shows common features. In all three tests an initial stress feature is seen during the first 0.05 strain. This is most clear in tests OPERA_Shear-2 and OPERA_Shear-3, although a small feature is seen in test OPERA_Shear-2. This is followed by a linear stress-strain response that then goes through yield and changes slope. It can be seen that as normal stress increased, the shear stress at which this occurs increases. In all three tests, between a shear stress of 0.3 and 0.7 a linear region was seen with similar slope for all three tests. However, as described above, the work-hardening feature in test OPERA_Shear-3 is interpreted as being post-peak. After the next change in slope of this region the behaviour of the three tests is dissimilar. In OPERA_Shear-1 (the lowest normal stress), the sample reached peak and brittle behaviour was seen with a reduction in stress to a condition of residual stress. In test OPERA_Shear-1 (intermediate normal stress) the sample showed near-perfect plastic behaviour, with little difference between the peak and residual stresses. In test OPERA_Shear-2 (highest normal stress and consolidated sample) the response was one of strain hardening and displays ductile behaviour. Therefore the three tests conducted span the range of deformation from brittle to ductile with a brittle-ductile transition at about 3 MPa normal stress.

The repeat shear tests (shear test 2) is compared in **Figure 8-37 C**. All three tests show a much more clean stress-strain response. At the lowest normal stress (OPERA_Shear-3), the sample displayed perfect plastic behaviour. An initial linear response transitioned into stable sliding at a constant shear stress. At intermediate normal stress (OPERA_Shear-1) the sample reached a peak and was followed by a stress reduction to a residual stress, which was followed by work hardening. At the highest normal stress (OPERA_Shear-2) the sample displayed work hardening behaviour up to a stress when perfect brittle behaviours was seen. This is unexpected and suggests a transition from ductile to brittle. This suggests that the pre-existing fracture plays a prominent role on shear test 2. At the lowest normal stress (OPERA_Shear-3) the sample behaviour suggests that the sample simply sheared along the pre-existing fracture. However, the results of the surface scan and photographs of the fracture would suggest that a new fracture was formed. At the intermediate stress a series of stick-slip events were noted. This suggests that the sample deformed by sliding along the pre-existing fracture, although a degree of stick-slip was seen during shear test 1.

However, as shear test 1 showed almost perfect plastic behaviour and shear tests 2 showed brittle deformation followed by work hardening it is suggested that the sample deformed through the combination of fracture reactivation and new fracture formation. At the highest normal stress the sample showed purely ductile behaviour during shear test 1 and brittle behaviour during shear test 2. This suggests that the sample started to deform through the formation of new micro-fractures until a point where the new features resulted in the slippage of the pre-existing fracture. Subsequent deformation resulted in stick-slip behaviour. As all three tests show a change in fracture topology it is interpreted that deformation during shear test 2 is the combination of new fractures forming that interact with the pre-existing fracture.

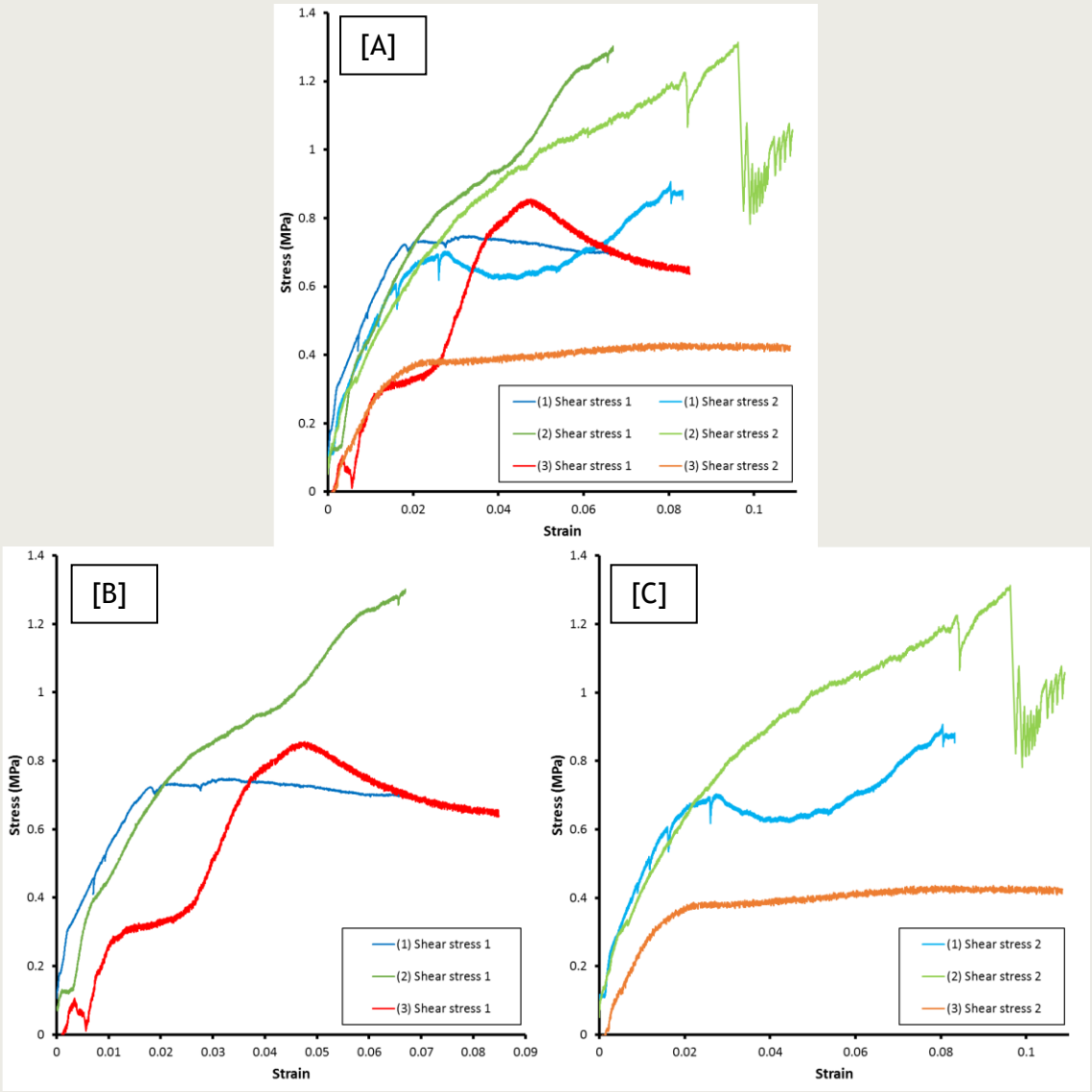

Figure 8-37: Comparison of stress-strain data for shear tests conducted at three normal stresses in Boom Clay.

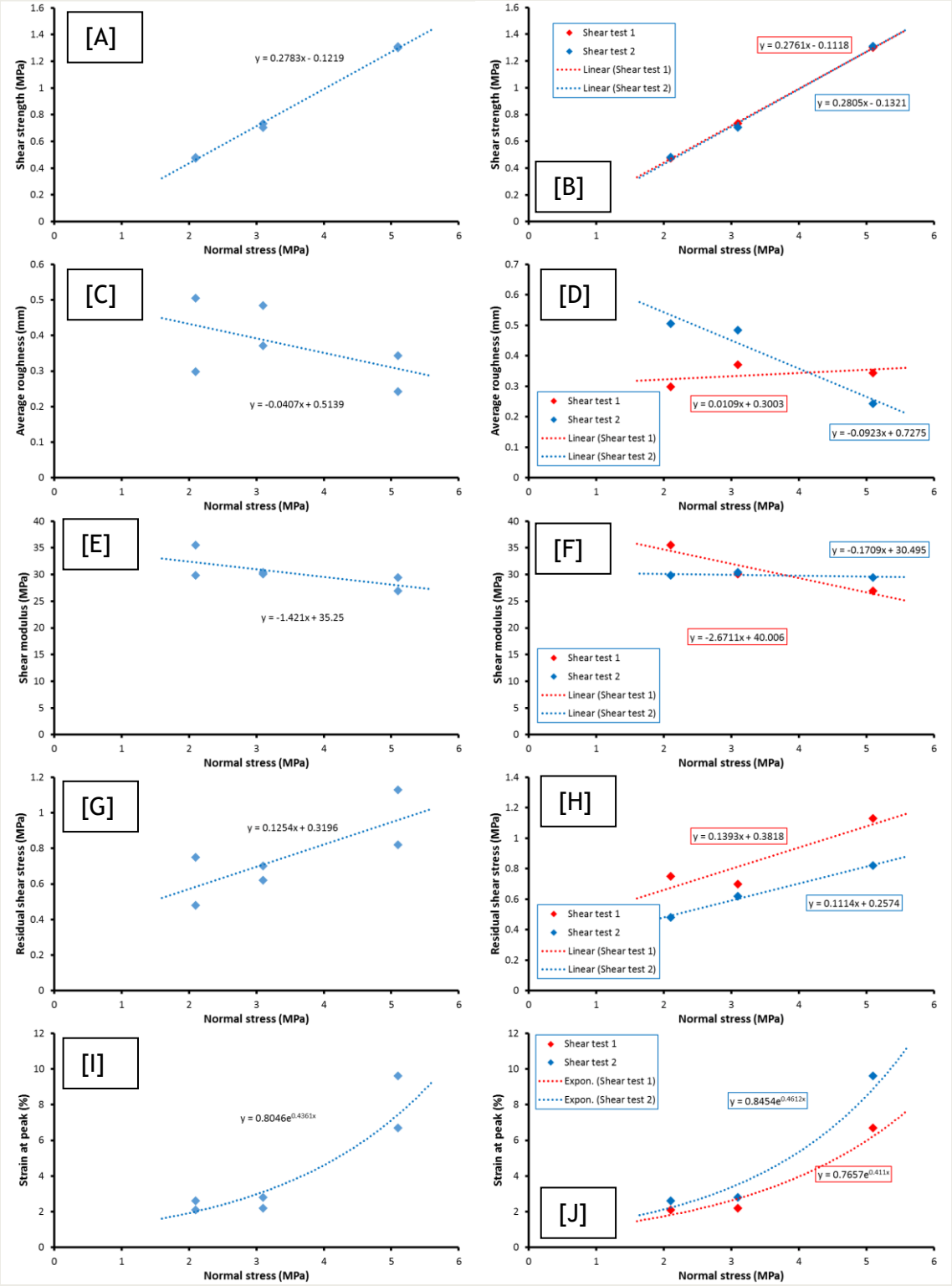

Figure 8-38: Comparison of parameters for shear tests conducted at three normal stresses in Boom Clay. [A] and [B] Shear strength. [C] and [D] Average roughness. [E] and [F] Shear modulus. [G] and [H] Residual stress. [I] and [J] Strain at peak stress. Note left graphs show all data, graphs on right compare shear test 1 and 2.

Figure 8-38, **Figure 8-38**, and **Table 8-8** compare the numerical results from the three shear tests. As seen in **Figure 8-38 A** and **B**, the shear strength of Boom Clay increases linearly with normal load by a factor of 0.278. The trend is matched when comparing results from shear test 1 and 2 (**Figure 8-38 B**). However, the trend gives a negative

intercept, which suggests that Boom Clay at atmospheric conditions (i.e. zero normal load) would have a negative shear stress. This is unlikely and requires further investigation at low normal stresses. Wiseall et al., (2015) summarise previous investigations of shear properties. From experimental studies a fault angle of 2 – 4° has been quoted for undrained tests, compared with 13 - 25° for drained tests. In the current tests the shear surface formed is of the order of 2 - 4° but the sample was tested in drained conditions. For shear strength 0.5 – 1.3 MPa is quoted for material from Mol depth. The current tests results (0.48 MPa) represent the low end of the undrained test results, but is much higher than the data quoted for drained tests (0.01 – 0.3 MPa). This would suggest the sample has behaved as if it was undrained, even though it was free to drain and suggests that the apparatus seals well. It should be noted that pore fluid injection during the hydration stages of test OPERA_Shear-3 did not result in pore fluid pressure generation, suggesting the sample was drained.

The shear modulus of Boom Clay is considered in **Figure 8-38 E** and **F**. On first inspection the data suggest a decrease in shear modulus with increasing normal stress (**Figure 8-38 E**). Considering data from shear test 1 and 2 separately (**Figure 8-38 F**) shows an interesting result. Shear modulus reduces at increased normal load for shear test 1 data by a factor of 2.67. However, for shear test 2 data the shear modulus can be seen to be constant. This suggests that deformation is occurring along the pre-existing fracture and that the sample had not fully self-healed.

As expected, the residual stress relationship mirrors that seen for peak stress (**Figure 8-38 G** and **H**). Generally, residual stress increases with normal stress by a factor 0.125 (**Figure 8-38 G**). Similar relationships are seen when considering data from shear test 1 and 2 (**Figure 8-38 H**), although the intercept of the relationship varies. These results show positive intercepts, unlike in peak stress, showing that Boom Clay will have strength at zero normal load.

A non-linear, or complex, relationship is seen when comparing the strain at peak stress for Boom Clay (**Figure 8-38 I** and **J**). These data are plotted with an exponential relationship. However, the data can be interpreted in an alternative way. Little variation is seen in strain for the tests conducted at normal stresses of 2.1 and 3.1 MPa, with a significant difference seen at 5 MPa normal stress. This may imply that conditioning of the samples to a depth representative of the Netherlands has caused the physical properties of the Boom Clay to change. It may also be described by the over consolidation ratio (OCR) of Boom Clay. Wiseall et al., (2015) quote an OCR for Boom Clay of 2.4 at Mol. If the material has been cored at a depth of 220 m the OCR would suggest a maximum burial depth of 528 m. This is similar to the 500 m depth that the samples have been conditioned. As OCR has been reported to be between 2 and 3 this means it is likely that the samples have been consolidated as far as virgin consolidation, i.e. the conditioned samples are normally consolidated with an OCR of 1. This could considerably impact the strain seen at peak stress. Further tests between 3 and 5 MPa and above 5 MPa are required to confirm this.

The average roughness of the fracture surfaces is considered in **Figure 8-38 C** and **D**. This suggests that roughness decreases with normal stress (**Figure 8-38 C**). Considering data for shear test 1 and 2 (**Figure 8-38 D**) shows that the relationship is more complex. For shear test 1 very similar roughnesses are seen and therefore roughness of virgin fractures in Boom Clay can be considered constant. On repeat testing (Shear test 2) the relationship shows that roughness decreases with increased normal stress by a factor of 0.09. At low normal stresses this means that higher roughness is resultant on repeat shearing, but at higher normal stresses (> 4 MPa) the repeat shearing results in less roughness. This relationship requires more data to confirm the relationship.

The flow of fluid in fractures in Boom Clay showed interesting results. In all tests, the transport of water reduced the flow of the fracture. In all tests the shearing of the sample further reduced flow. In test OPERA_Shear-1 the flow increased with continued shear, although this was not seen in the other two tests. This is likely to mean that fracture mismatch can result in the opening of conductive pathways that can enhance flow. Fracture topology data do not offer an explanation and no significant difference is noted for the shear surfaces. The stress-strain response could explain the behaviour (**Figure 8-37**). OPERA_Shear-1 was the only test to show brittle behaviour on repeat shearing and this would result in dilatant opening along the fracture, creating enhanced flow paths. Therefore it is interpreted that shear can open up fluid pathways and whether enhanced flow is resultant depends on the connectivity of the pathway with an egress site from the fracture or whether the re-shearing of a fracture results in brittle or dilatant deformation. Therefore it is likely that regions of a fracture will be conductive but on a larger scale the fracture is non-conductive unless a sink is found.

Figure 8-39 considers the final (lowest) flow experienced by the fractures tested. As seen very low flow is observed with a trend displayed suggesting that final flow reduces with increased normal stress. It should be noted that the final flow results in a fracture transmissivity of the order of 10^{-14} – 10^{-15} m^2/s.

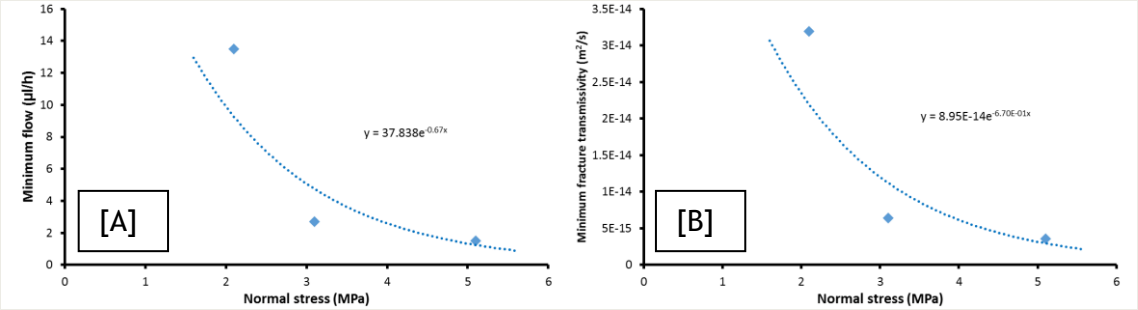

Figure 8-39: Variation of flow [A] and fracture transmissivity [B] for Boom Clay at three normal loads.

Parameter	Unit	OPERA_Shear-1		OPERA_Shear-2		OPERA_Shear-3	
		Test 1	Test 2	Test 1	Test 2	Test 1	Test 2
Normal stress	MPa	3.1	3.1	5.1	5.1	2.1	2.1
Shear strength	MPa	0.734	0.703	1.3	1.31	0.475	0.48
Roughness	mm	0.371	0.485	0.344	0.243	0.299	0.505
Shear modulus	MPa	30.08	30.41	26.93	29.48	35.50	29.84
Residual stress	MPa	0.7	0.62	1.13	0.82	0.75	0.48
First indication of deformation	MPa	0.49	0.4	1.28	1.23	0.24	/
Strain at peak		0.022	0.028	0.067	0.096	0.021	0.026
Minimum flow	µl/h	/	2.7	/	1.5	/	13.5
Min fracture transmissivity	$\times 10^{-15}$ m^2/s	/	6.39	/	3.55	/	31.9

Table 8-8: Comparison of parameters for shear tests conducted at three normal stresses in Boom Clay.

8.6 *Key observations of fractures in Boom Clay:*

Outcomes:

1. In all three tests an initial stress feature is seen during the first 0.005 strain;
2. This is followed by a linear stress-strain response, yield and a change of slope;
3. Yield stress increases with normal stress;
4. Shear deformation seen spans the brittle to ductile regimes, with a brittle-ductile transition of 3 MPa effective normal stress;
5. Repeat shearing suggests that the pre-existing fracture plays a prominent role on shear test 2;
6. All three tests showed a change in fracture topology, interpreted as deformation during repeat shearing is the combination of new fractures forming and the reactivation of the pre-existing fracture;
7. Shear strength of Boom Clay increases linearly with normal load by a factor of 0.278;
8. Shear stress at 2.1 MPa normal stress (0.48 MPa) represent the low end of the published undrained test results and is significantly higher than the data quoted for drained tests;
9. Shear modulus reduces at increased normal load for initial shearing by a factor of 2.67;
10. Repeat shearing gave constant shear modulus, suggesting that deformation occurred along the pre-existing fracture and that the sample had not fully self-healed;
11. Residual stress increases with normal stress by a factor 0.125;
12. Complex strain at peak stress for Boom Clay may be explained by the over-consolidation ratio (OCR) and conditioned samples having undergone virgin consolidation, i.e. normal consolidated with an OCR of 1;
13. Initial shearing results in a constant fracture roughness;
14. Repeat shearing shows that roughness decreases with increased normal stress by a factor of 0.09. At low normal stresses roughness is greater on repeat shearing, but at higher normal stresses (> 4 MPa) repeat shearing results in less roughness;
15. The transport of water reduced the flow of the fracture;
16. Shearing further reduced flow;
17. One test showed brittle deformation and enhanced fluid flow, therefore shear can open up fluid pathways and whether enhanced flow is resultant depends on the connectivity of the pathway with an egress site from the fracture or whether the re-shearing of a fracture results in brittle or dilatant deformation;
18. Low flow rates were seen with flow reducing with normal stress;
19. Fracture transmissivity of the order of 10^{-14} – 10^{-15} m^2/s;
20. Fracture/shear properties of Boom Clay are shown in **Table 8-9**.

Parameter	Unit	Value
shear strength	MPa	1.29
shear modulus	MPa	28
residual shear strength	MPa	0.96
Strain at peak stress		0.08
fracture roughness	mm	0.31
initial fracture transmissivity	m^2/s	5×10^{-14}
fracture transmissivity following self-sealing	m^2/s	2×10^{-14}
Fracture transmissivity following shearing	m^2/s	4×10^{-15}

Table 8-9: Fracture/shear properties of Boom Clay at depths relevant to the Netherlands

Recommendations:

1. Boom Clay has a tendency to consolidate within the 3 mm gap between collars. The apparatus should be modified to ensure this is lessened and to investigate the repeatability of shear testing.
2. Flow needs to be determined in non-sheared Boom Clay to determine the enhancement of flow along fractures.
3. Fractures within the engineered damaged zone will be subject to a range of normal stresses. Further tests over a greater range of normal stresses are required to investigate the effect of normal stress on the flow of fractures and mechanical behaviour of Boom Clay in shear.
4. Detailed gas injection experiments are required to investigate the gas flow properties of fractures.
5. All current experiments were sheared parallel with bedding. Shearing at distinct angles to bedding is required to determine the influence this has on fracture transmissivity.
6. Repeat experiments are needed to explore natural variability with the Boom Clay and variability of fractures, which are complex in nature.

9 Mechanical Deformation of Boom Clay

The mechanical properties of a host rock play an important role for the safe disposal of radioactive waste. Therefore, numerous studies have been conducted quantifying and describing the strength of host rocks and the resultant deformation. If deformation is likely it is important to predict the conditions that promote fractures, changes in volume, and changes in transport properties.

Numerous studies have been conducted on the Boom Clay with respect to the Belgian disposal concept, where the Boom Clay is at a depth of approximately 220 m below the surface. In this study we present the properties of the Boom Clay at a depth of 500 m, appropriate for radioactive waste disposal in the Netherlands. Increased depth results in different stress conditions as described in Chapter 1. These higher stress conditions have the potential to alter the mechanical behaviour of the Boom Clay.

Wiseall et al., (2015) comprehensively reviewed previous mechanical research on the Boom Clay. **Table 9-1** summarises the mechanical data from studies on the Boom Clay; these studies were predominantly carried out with regards to the Boom Clay in Belgium. As can be seen in **Table 9-1** the Young's Modulus is quoted as drained and undrained values. In this study we have conducted three drained tests on material from a depth of 223 m at Mol. In the literature the drained Young's Modulus, E_d, is quoted as being in the range of 150-300 MPa. These are predominantly for the expected *in situ* conditions at HADES (σ_{eff} ~ 2.2MPa). No literature could be found on the expected E_d at a depth of 500 m, with a σ_{eff} ~ 5.1 MPa.

Mechanical parameters	Symbol	Units	Drained	Undrained
Young's modulus	E	MPa	150 – 500	152 – 197
Poisson's ratio	ν		0.125	
Internal friction angle	ϕ	°	13 - 25	2 – 4
Fault angle	θ	°	38.5 – 32.5	43 - 44
Cohesion	C	MPa	0.08 – 0.3	0.5 – 1.3
Uniaxial compressive strength	qu	MPa	2 – 2.5	
Preconsolidation stress	P_c'	MPa	1.7 – 7.5	

Table 9-1: Summary of the mechanical properties of the Boom Clay. Please refer to Wiseall et al., (2015) for full list and source of data. All samples were derived from Mol, Belgium, at an approximate depth of 223m, unless otherwise denoted.

Drained UCS values for samples taken from HADES are widely reported, though often without provision of the original data source. Most of these values lie in the 2-3 MPa range, with a value of 2 being most commonly given (Bernier et al., 2007; Tsang et al., 2012). Bésuelle et al., (2013) report measuring a UCS of 2.5 MPa during compression testing of the Boom Clay from HADES. Whilst not a direct measure of the clay's response under *in situ* conditions, this quantity does provide a first estimate of the likely mechanical strength of the material. In the Netherlands, any differences in the compaction state of the clay are likely to result in changes to its UCS.

In the current study a combination of drained triaxial and Uniaxial Compressive Strength (UCS) tests has been used to describe the mechanical properties of the Boom Clay. Two sets of tests have been conducted; one set on material collected from Mol and another on material which has been consolidated in the laboratory to a stress representative of a depth of 500 m. In each set of experiments three drained triaxial experiments and one UCS

test was run, eight tests in total. This allows a comparison of current results with previously published values and allows a description of the effect that consolidation to 500 m has had on the mechanical properties of the Boom Clay.

9.1 *Experimental methodology*

9.1.1 Triaxial testing

Six drained triaxial tests were carried out to quantify the mechanical properties of the Boom Clay using the bespoke Triaxial Apparatus. This comprised 5 main components (**Figure 9-1**):

1) The specimen, surrounded by a flexible Hoek sleeve and main pressure vessel body.
2) An axial load system comprising of an Enerpac single acting hydraulic ram pressurised by an ISCO-500 series D syringe pump. This was connected via an axial strain jig to a Global Digital Systems optical encoder for measuring linear displacement accurate to 0.003 mm.
3) A confining pressure system using an ISCO-100 series D syringe pump allowing radial strain measurements to be calculated through volume change.
4) A backpressure system using a second ISCO-100 series D syringe pump allowing the measurement of porewater displacement from the specimen.
5) A state-of-the-art custom designed data acquisition system facilitating the remote monitoring and control of all experimental parameters.

It must be noted that for the purpose of this test programme a pore pressure was not applied to the system, therefore the backpressure pump described in (4) was not used. Prepared samples of 37 mm diameter and 64 mm length were placed in the Hoek sleeve, which in turn was placed in the main pressure vessel body. The pressure vessel contained an o-ring at each end, which when combined with the flexible Hoek sleeve ensured that the sample cannot come into contact with the confining fluid. The pressure vessel was placed in the triaxial rig and each face of the sample came into contact with a stainless steel platen. These transmit axial force generated by the Enerpac ram directly to the specimen. Retaining collars and axial tie-rods locked the system components together to provide a rigid test rig. Each of these steps is shown visually in **Figure 9-1**.

In total six samples were prepared to study the mechanical behaviour of the Boom Clay. The set of samples prepared from Mol were cut from core collected from the HADES research laboratory. The samples were cut by diamond blade to slightly above the 65 mm length used. The diameter of the samples were then trimmed to 37 mm and the faces of the sample were squared off using a lathe. The second set of samples were cut from the second large core which was consolidated to a depth of 500 m in the laboratory. These samples were made using a 37 mm diameter diamond tipped corer, the ends were then cut and squared off using the same process as described above. All samples were prepared perpendicular to bedding.

Axial load and confining pressure were stepped up gradually towards the target pressures (**Table 9-1**). Care was taken to avoid the confining pressure exceeding the axial, a condition that could result in the sample being strained extensionally. Once the target axial load and confining pressures were reached a period of time was left in order to ensure the pumps were not leaking and that the sample was not deforming. After this short period, of less than an hour, the pump controlling the axial load was set to a constant flow, resulting in constant displacement of the axial ram. Table 1 lists the axial strain rates used in each test. Test 1 included a study of strain-rate sensitivity to determine a target strain-

rate not affected by the low drainage of the Boom Clay (see Section 9.2.1). Data was logged constantly throughout the period of the test every 60 seconds, each test was designed to run for approximately 24 hours, or until the test had conclusively reached peak stress or the strain limit of the apparatus.

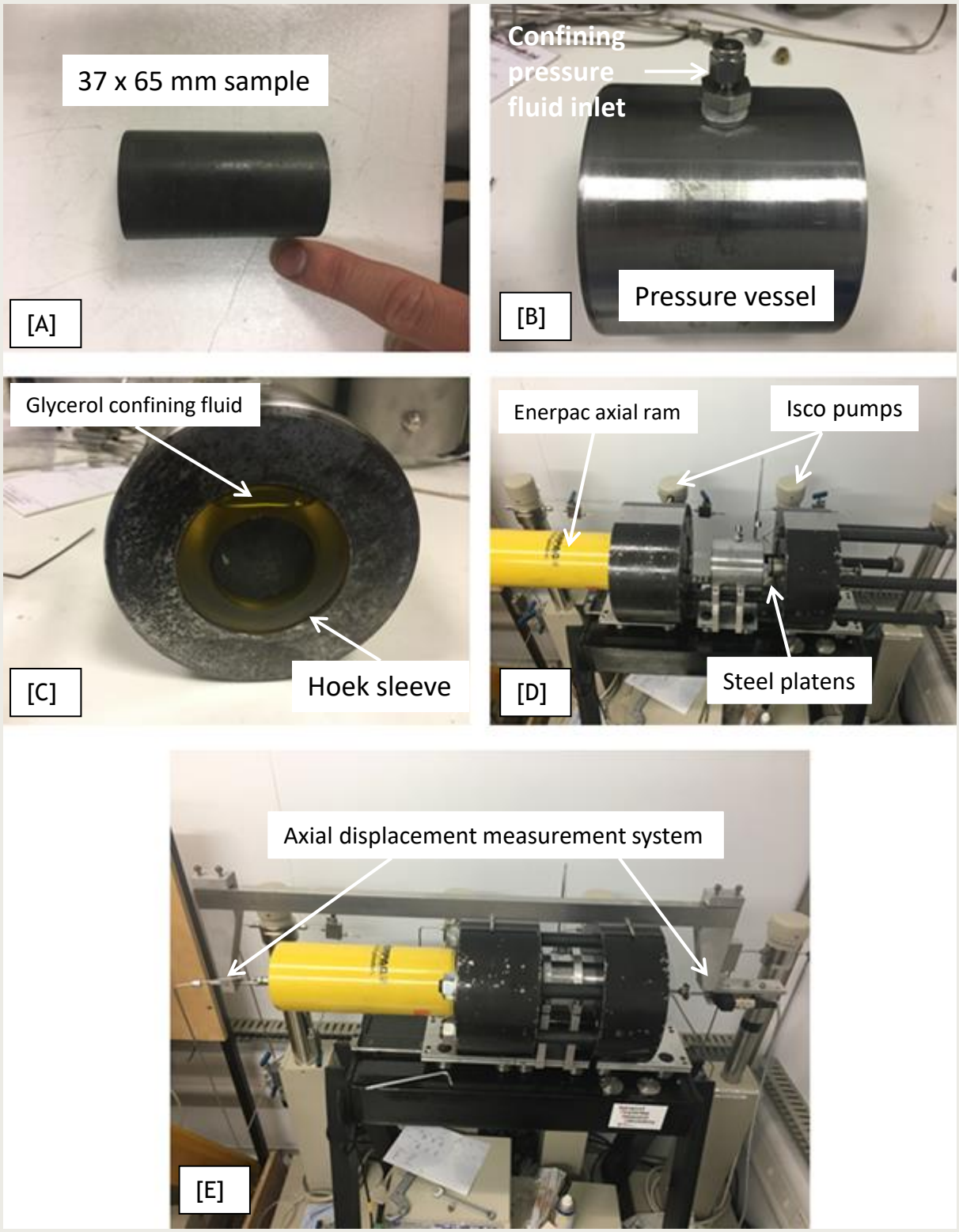

Figure 9-1: The Triaxial Apparatus and set-up. A) Boom Clay sample, b) pressure vessel, c) Hoek sleeve arrangement in the pressure vessel, d) pressure vessel within the full apparatus, and e) complete apparatus with axial measurement device attached.

Limited quantities of conditioned Boom Clay were available, limiting the study to four tests on this material. Although more unconditioned Boom Clay was available four tests were also conducted. One sample was used for uniaxial testing, one at maximum depth, and the remaining two sample at $^{1}/_{3}^{rd}$ and $^{2}/_{3}^{rd}$ of the maximum pressure. This range of stresses would allow a failure envelope to be defined.

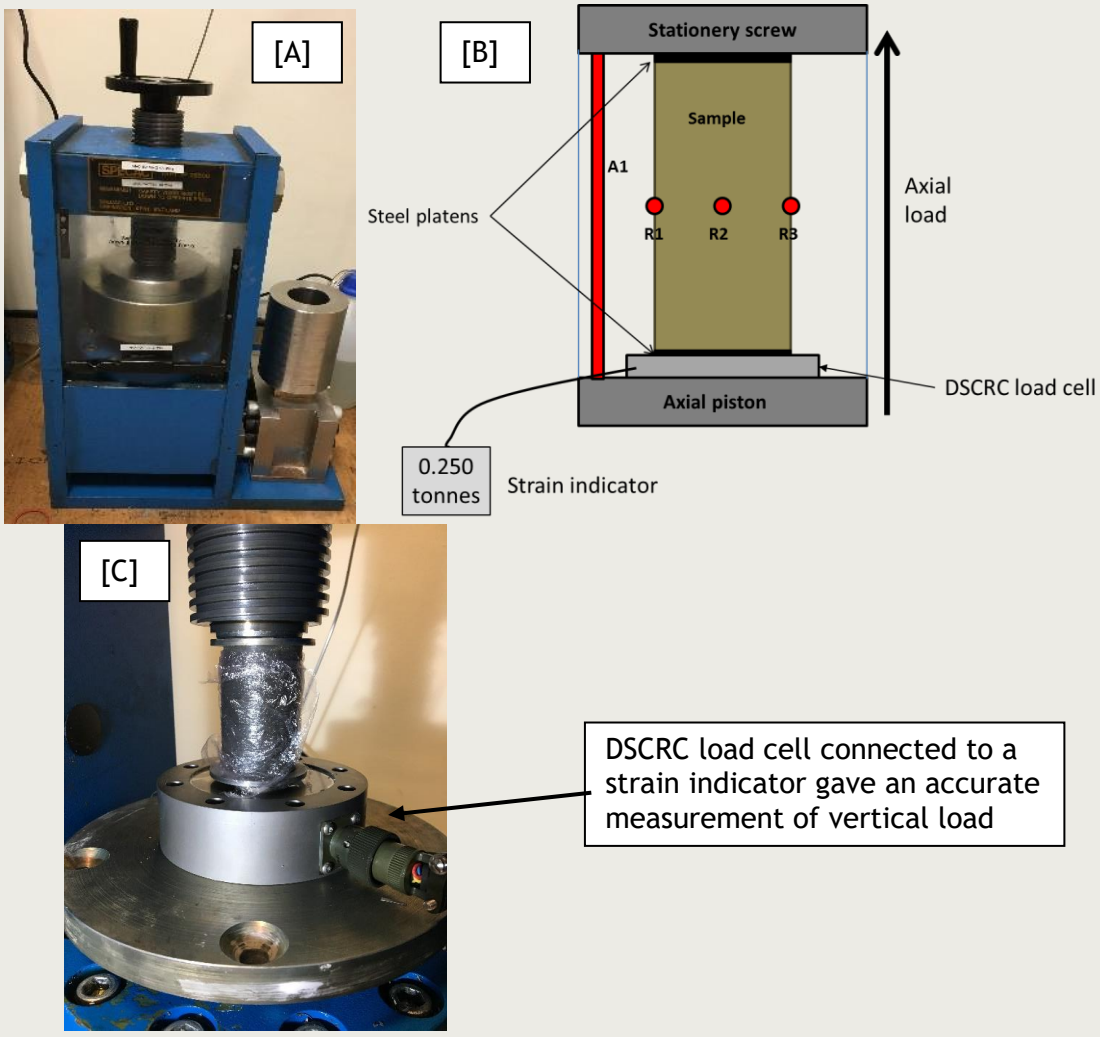

Figure 9-2: Uniaxial compressive strength test apparatus. [A] Photograph of the sample press. [B] Schematic of the sample assembly. [C] Sample following UCS test.

9.1.2 Uniaxial Compressive Strength testing

Two Uniaxial Compressive Strength (UCS) tests were performed; one on material from HADES URL in Mol (depth 223 m) and another on the material which was consolidated in the laboratory to 500 m depth. Samples were prepared identically to that described for triaxial deformation (Section 9.1.1). The UCS tests were performed on the sample press which is shown in **Figure 9-2 A**. The 100 tonne press had a two way piston which was controlled by a single Teledyne/Isco 260D pump. The sample press provides the axial force required to carry out the UCS test. The sample assembly is shown in **Figure 9-2 B**. The apparatus consists of four main components:

1) Axial piston providing the force to the sample as shown in **Figure 9-2 A**, this was controlled by a Teledyne/ISCO 260D pump.

2) A low profile DSCRC pancake load cell, connected to a pre-calibrated strain gauge indicator. This measured the vertical load in tonnes, which was converted into an axial stress.

3) Four Mitutoyo digital Linear Variable Differential Transformers (LVDT's). Three were arranged around the same radial plane to measure the radial displacement, these were labelled R1, R2 and R3 in **Figure 9-2 B**. A fourth was placed in contact with the press and measures the axial displacement, this was labelled A1.

4) Two small metal platens which ensure the axial load was spread evenly over the face of the material.

Figure 9-2 C shows a photo from the end of testing. It can be seen that the sample was wrapped in cling film, this was to ensure the sample did not dry out during testing; a change in moisture content could affect the UCS measurement. The DSCRC load cell can clearly be seen below the sample.

During testing the Teledyne/Isco pump controlling the vertical load was set to constant flow at 100 ml/h, this provided a constant axial displacement. All data were logged manually; initially every 0.005 tonnes of axial load, however when this slowed every 0.05 mm of axial displacement.

1.1.Results of Triaxial testing

The six triaxial tests completed are described in **Table 9-2**. Test Mech_500_1 was performed at a confining pressure of 5.1 MPa, this was set at a constant pressure for the duration of the test. **Figure 9-3 A** shows the stress strain response for the conditioned Boom Clay. As can be seen in **Figure 9-3** the stress strain response was complex. There was a long transition from the initial linear phase of elastic deformation to ductile deformation, this was due to the plastic nature of the Boom Clay. This made it difficult to interpret the exact point of yield (
Figure 9-4), the transition from purely elastic to permanent plastic deformation. In this study we use the point at which the pump supplying the confining fluid began to pull back, i.e. the dilation of the sample. **Figure 9-5** shows two correlated graphs of the confining pump volume and the stress strain curve. Yield is therefore defined as the stress at which the confining pump volume began to decrease.

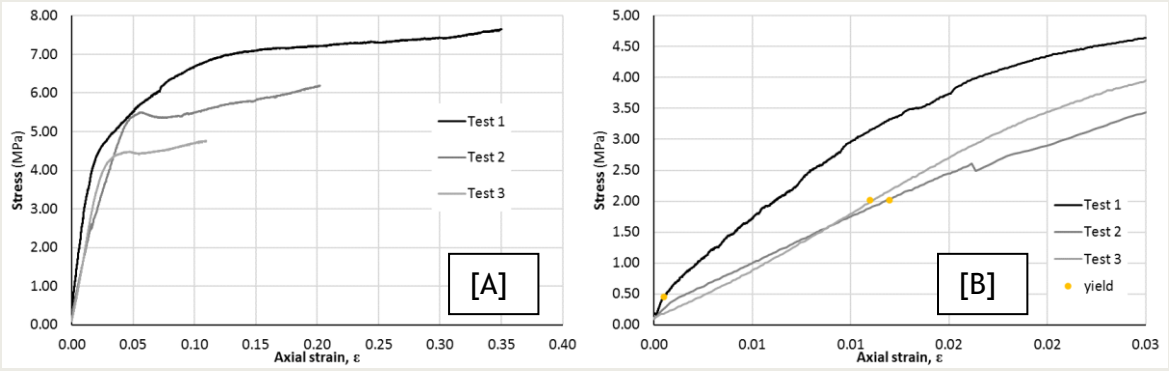

Figure 9-3: Triaxial test results for tests conducted on conditioned Boom Clay. [A] Full stress-strain result. [B] Detailed early response.

Tests Mech-500_2 and Mech_500_3 were carried out at one third and two thirds of the confining pressure of Test Mech-1. The stress-strain curves for both tests were of similar form and showed brittle behaviour with elastic-strain softening-plastic behaviour (**Figure 9-3 A**).

Test Mech_500_1 had a yield of 0.45 MPa, yield occurred at just 1.9 % strain. Test Mech_500_1 was performed at 5.1 MPa confining pressure, this was the expected effective stress at a depth of 500 m in the Netherlands. The gradient of the linear portion of the graph corresponds to the Young's Modulus (see **Figure 9-5**). In the case of Test Mech_500_1 this was 214 MPa. The peak strength and residual strength cannot be defined due to the nature of the curve with prolonged strain hardening.

Test Mech_500_2 was performed at a confining pressure of 3.4 MPa, the stress-strain curve has a clear linear portion until a yield point of 2.02 MPa. The linear section of the graph gave a Young's Modulus of 145 MPa. At the point of yield the strain was recorded as being 1.7 %. The non-linear portion of the curve then began and the curve reached a peak strength of 5.48 MPa, a small drop then occurred to 5.35 MPa. This small drop was a sign of brittle deformation and strain softening. After the residual strength the sample began to strain harden.

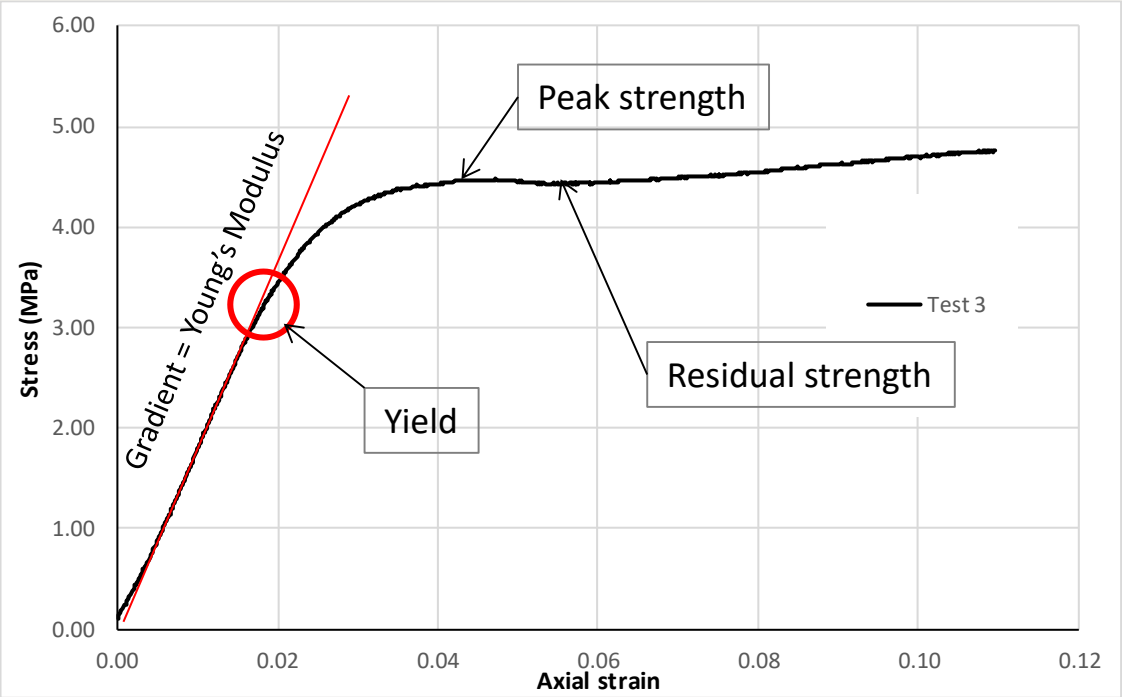

Figure 9-4: Example triaxial test result showing parameters of interest.

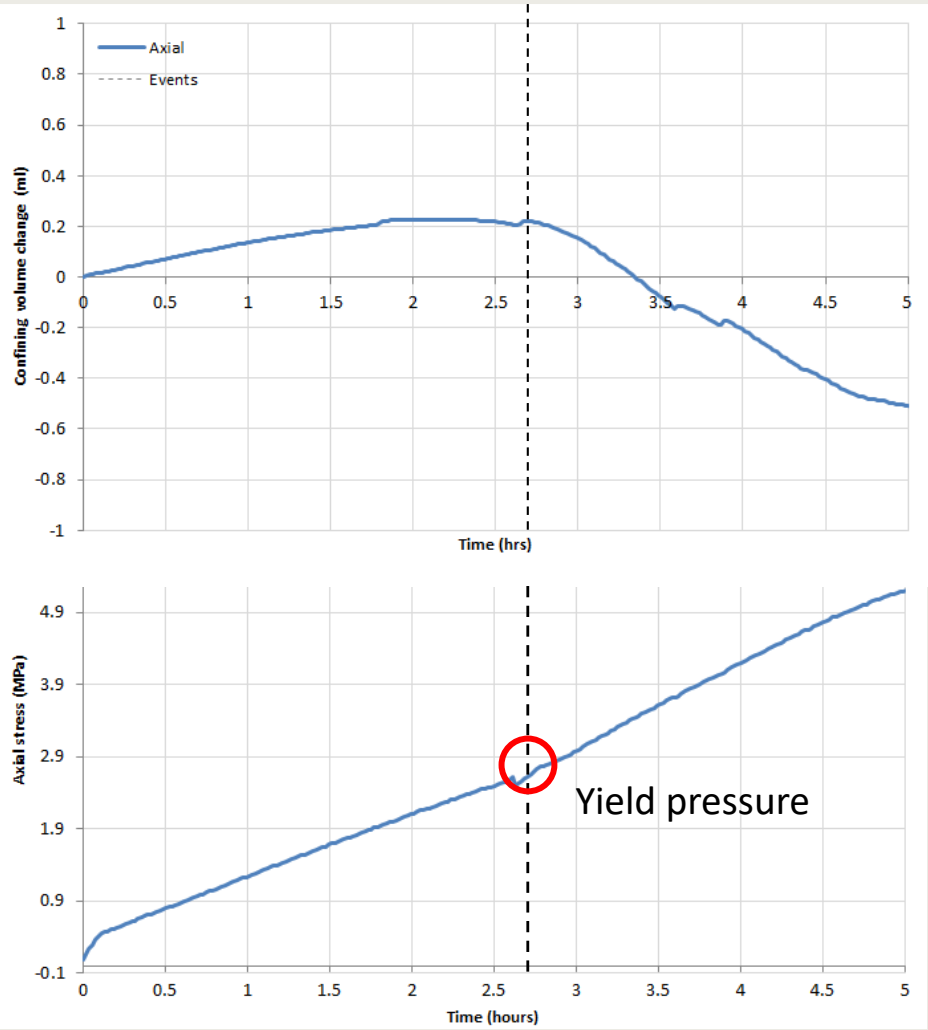

Figure 9-5: Definition of yield using the volume of the confining system and the slope of axial stress.

Test Mech_500_3 shows a similar form to Test Mech_500_2. The yield strength was 2.02 MPa, the Young's Modulus was 171 MPa. This is slightly higher than that of Test Mech_500_2. At the point of yield the sample had undergone 1.1 % strain. The non-linear portion of the graph then began and the curve reached a peak strength of 4.48 MPa. A small drop then occurred (strains softening) to a residual strength of 4.42 MPa. As the axial stress continued to increase the sample strain hardened.

Tests Mech_500_1, Mech_500_2 and Mech_500_3 were performed on conditioned Boom Clay to a depth of 500 m. The remaining triaxial tests were carried out on material from the HADES underground research laboratory at a depth of 223 m.

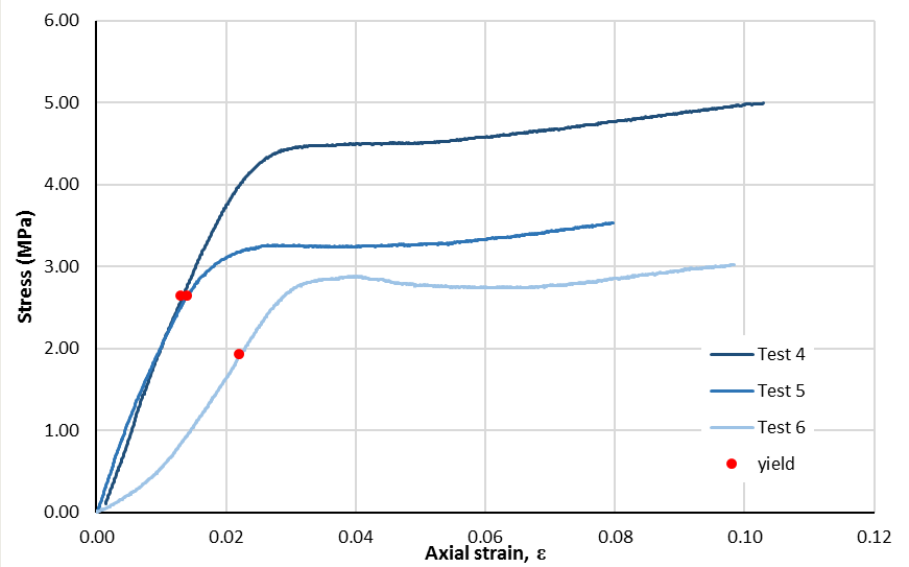

Figure 9-6: Triaxial test results for tests conducted on Boom Clay for HADES.

Figure 9-6 shows the stress-strain response of Tests Mech_223_4 to Mech_223_6. Test Mech_223_4 was performed at a constant confining pressure of 2.2 MPa, this corresponded to the effective stress conditions at a depth of 223 m. Yield was defined as 2.65 MPa, with a Young's Modulus of 215 MPa. This is similar to the result achieved in Test Mech-1. At the point of yield the sample had strained by 1.3 %. After yield the non-linear portion of the graph reached a peak strength of 4.5 MPa. The shape of the graph shows that there is almost no reduction in stress to a residual strength, the drop was only 0.01 MPa to 4.49 MPa. Following this strain hardening was seen.

Test Mech_223_5 (**Figure 9-6**) was performed at a constant confining pressure of 1.56 MPa. The yield strength was 2.65 MPa and Young's Modulus was 189 MPa. The non-linear portion of the graph evolved to a peak strength of 3.26 MPa. As with Test Mech-4, only a small reduction in stress occurred to a residual strength of 3.24 MPa.

Test Mech_223_6 (**Figure 9-6**) had an initial non-linear phase of deformation, it is suspected this may be associated with the test set up; this has been corrected from the data. A phase of linear elastic deformation occurred, giving a Young's Modulus of 112 MPa. This is lower than the other tests in this study. A yield of 1.94 MPa occurred, followed by a peak of 3.32 MPa and a residual of 3.21 MPa. In all three of the tests strain hardening was observed following residual stress conditions. The results of the six triaxial tests are summarised in **Table 9-2**.

9.1.3 Strain-rate sensitivity

A strain-rate sensitivity investigation was undertaken as part of Test Mech_500_1. Strain-rate was achieved by pumping oil at a constant flow-rate into the axial ram of the apparatus. During the first 48 hours of the experiment (2.6 % strain) the strain rate was doubled in a series of steps by setting the axial syringe pump to constant flow rates of 120, 240, 480, 960, and 1920 µl/h. No visual change in stress-strain slope was noted at the first change of strain-rate. During each change the data was scrutinised to ensure the change in shear-rate had no adverse effects on the data. It should be noted that immediately following increased strain-rate the sample showed stress variation, although this tended to quickly recover.

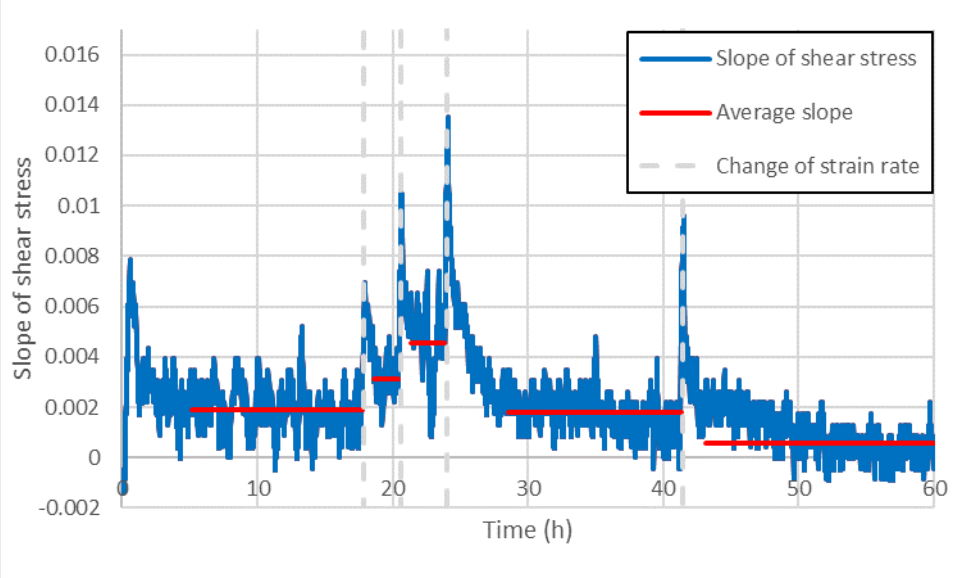

Figure 9-7: Investigation of strain-rate sensitivity in Boom Clay. Slope of stress-strain with the time of strain-rate changes highlighted. The red lines show the averaged slope results when steady drainage had been achieved.

Figure 9-7 shows the detailed analysis of the data following the end of the test. The figure shows the slope of stress-strain result and highlights the time of the changes of strain rate. This data has to be considered against a naturally evolving stress-strain response of the Boom Clay. As can be seen, immediately following the change in strain-rate a short-term transient increase in slope is observed. Within a few hours this response decayed to reach a constant level, the results from which have been averaged (red lines). This shows that for step 2 and 3 (constant flow rates of 240 and 480 µl/h) the average slope increased. However, step 4 (960 µl/h) shows that the transient tended to last longer than the length of steps 2 and 3 and suggests that these stages were not run for sufficient time. Good comparison is seen between steps 1 and 4 (average of 0.0019 and 0.0018 respectively), suggesting that once the transient had decayed, the Boom Clay was not strain-rate sensitive within the limits of the strain-rates imposed. Step 5 showed a decreasing average slope, although this may be natural variation of the Boom Clay as the sample approached peak stress conditions.

The short-term transient created by the change in strain-rate is caused by the drainage of the sample. Instantaneous changes in strain rate result in the pore fluid initially increasing until the sample achieves stable drainage. This hydrodynamic effect took an hour or two to result in steady-state flow.

Whilst short-term transient changes were observed as strain-rate was changed, the Boom Clay did not show strain-rate sensitivity over the range of strain-rates investigated. Therefore, all subsequent tests were conducted towards the upper end of the range investigated.

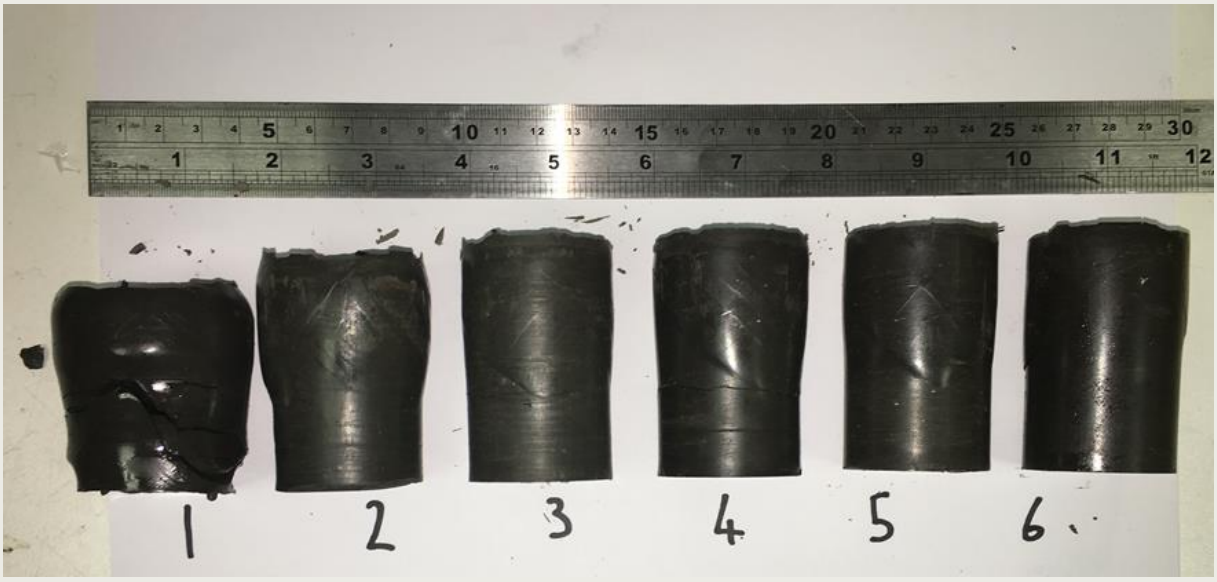

Figure 9-8: Photograph of the final samples following triaxial deformation.

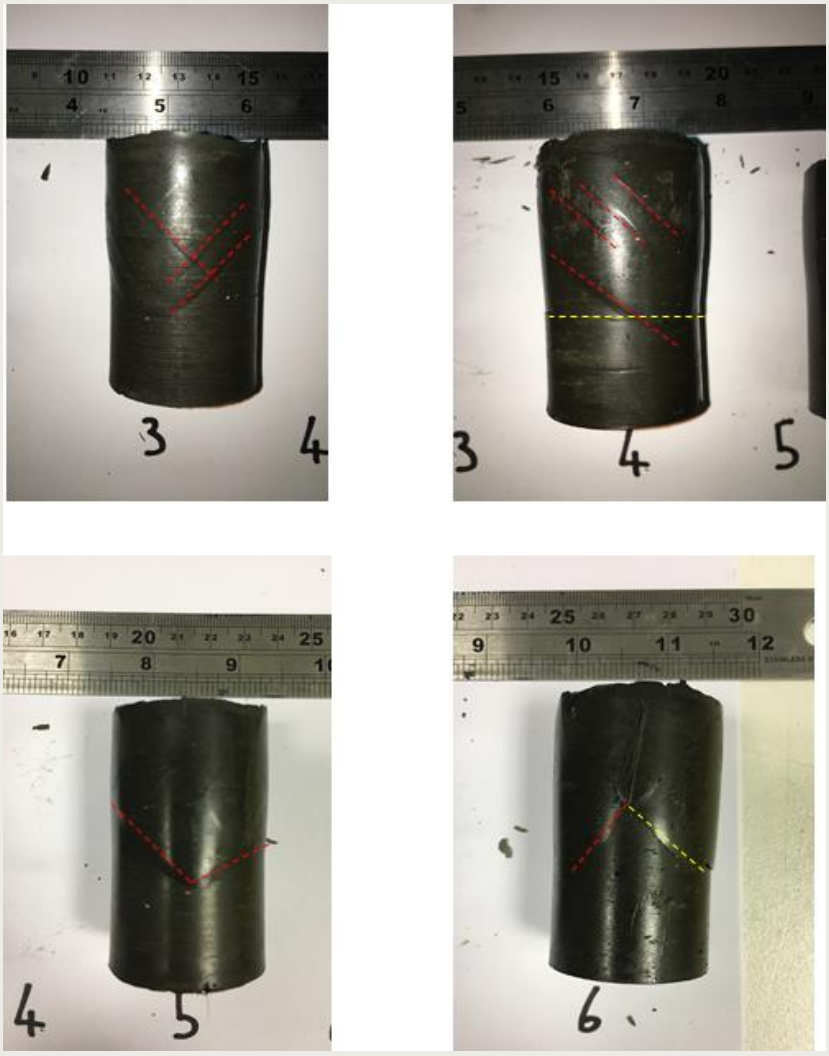

Figure 9-9: Detail of deformation in tests Mech-3 to Mech-6.

9.1.4 Post test sample observations

In order to gain a more complete understanding of each test the final samples were examined. **Figure 9-8** shows each sample used in all six of the tests. As can be seen the axial loading has had a significant effect on a number of the samples. Test Mech_500_1, which was carried out at the highest confining pressure of 5.1 MPa and was subject to the highest axial strain, shows significant bulging and widening at one end.

Tests Mech_500_1 and Mech_500_2 show the most amount of deformation, they have significantly shortened in length, this correlates to the high amount of strain (**Figure 9-8**). From **Figure 9-8** it appears that tests Mech_500_3 to Mech_223_6 did not experience as much deformation as tests Mech_500_1 and Mech_500_2, however closer inspections shows considerable deformation. **Figure 9-9** shows photographs of samples from tests Mech_500_3 Mech_223_6. The red dashed lines highlight planes of shear deformation, whereas the yellow dashed lines highlight fracture planes. It can be seen that many of the shear planes have formed at approximately 40° to bedding. Tests Mech_500_1 and Mech_500_2 (**Figure 9-8**) do not clearly show shear planes. **Figure 9-9 A** and **D** clearly show that both plastic and brittle deformation has occurred in this series of tests. Test Mech_500_1 in **Figure 9-8** shows brittle deformation with fracturing and plastic deformation with bulging. It is clear that the stress conditions in the tests have had a significant effect on the amount of deformation and show a transition from brittle to ductile deformation. Thin section analysis has not been performed and is an area where further work could be performed.

9.2 *Results of Uniaxial tests*

Two uniaxial compressive strength tests were performed; one using material from Mol depth of 223 m and another from the material consolidated to 500 m in the laboratory. Table 1-2 shows the results of the two tests, labelled Mech_223UCS_7 and Mech_500UCS_8 respectively.

Mech_223UCS_7 was carried out using material from a depth of 223 m, as shown in **Figure 9-10**. Axial stress initially increased in a linear manner, showing elastic deformation, until a yield of 1.11 MPa. This equates to a Young's Modulus (E) of 297 MPa (**Figure 9-10 D**). As the axial stress increased the volumetric strain remained constant. However, once the axial stress exceeded 1 MPa the diametrical strain began to increase. The ratio of the axial to diametrical strain gives the Poisson's Ratio (ν). **Figure 9-10 B** shows that Poisson's Ratio varies with stress throughout the entire test, suggesting that linear-elastic behaviour was not experienced. As the axial stress increased the amount of strain transferred orthogonally increased. The average value for the linear section of this graph gives a Poisson's Ratio of 0.09. It should be noted that rocks with high anisotropy, for instance created by alignment of minerals with the bedding plane, often show a non-steady Poisson's ratio.

Figure 9-10 C shows the volumetric strain relationship with axial stress. At an axial stress of 1 MPa the volumetric strain began to reduce, this is a result of the strain being translated into the diametrical plane and often signifies the onset of fracture growth in the sample. The linear portion of this graph is highlighted and the gradient produces a Bulk Modulus (K) of 407 MPa.

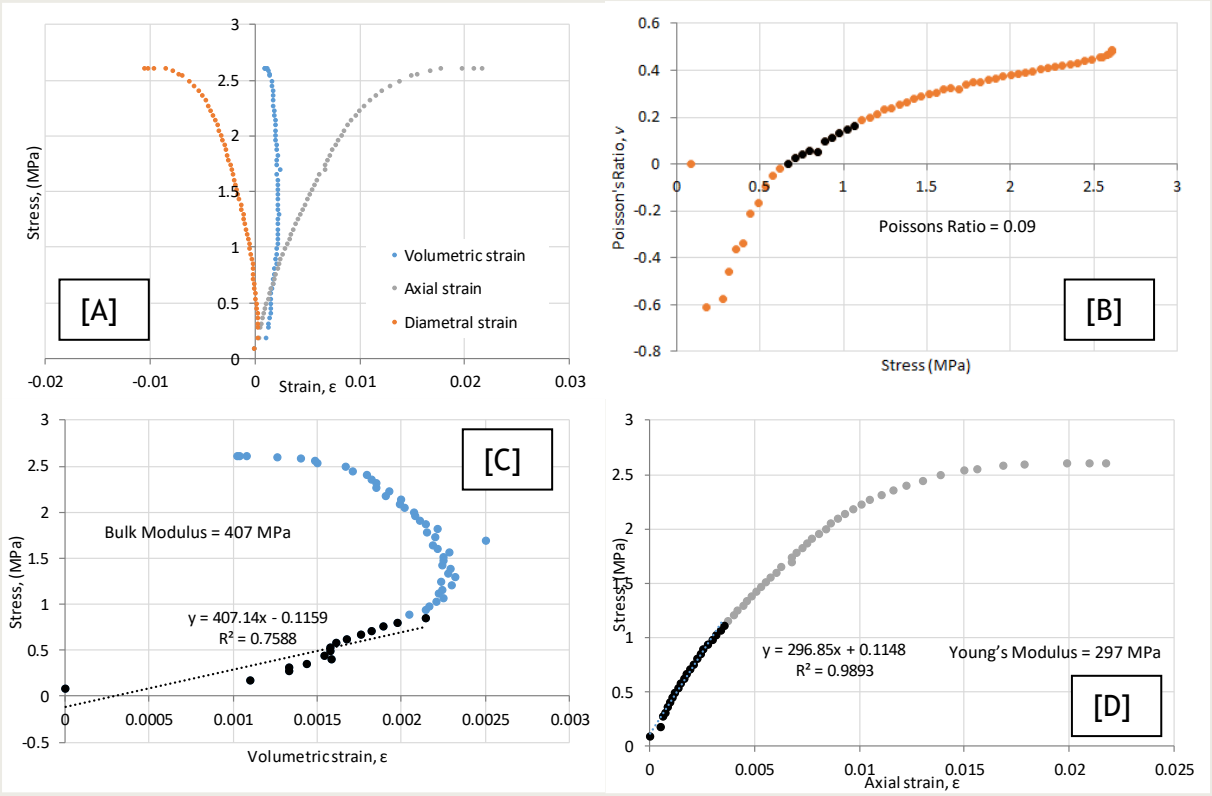

Figure 9-10: Uniaxial deformation test Mech_UCS223_7. [A] Stress-strain response. [B] Poisson's ratio. [C] Bulk Modulus. [D] Young's modulus.

Figure 9-11 shows the stress-strain response of test Mech_500UCS_8, which was performed on Boom Clay consolidated to 500 m. **Figure 9-11 A** compares the volumetric, axial and diametrical strain. Initially the axial strain increased at a linear rate with the axial stress, indicating a linear-elastic response. A Young's Modulus (*E*) of 210 MPa is observed (**Figure 9-11 D**). Deviation from the linear signifies the onset of permanent, plastic, deformation and occurred at a yield stress of 1.11 MPa (**Figure 9-11 D**). Volumetric strain initially increased at the same linear rate as the axial strain, up to a stress slightly below 1 MPa axial stress. The linear section of the volumetric strain curve is highlighted in **Figure 9-11 C** and equates to a Bulk Modulus (*K*) of 260 MPa. The volumetric curve began to change shape at an axial stress of 1 MPa. The Poisson's Ratio for test Mech_500UCS_8 did not show a constant value (**Figure 9-11 B**), as would be expected in an elastic medium, and varies between 0 and 0.2 during the elastic region, giving an average value of 0.10.

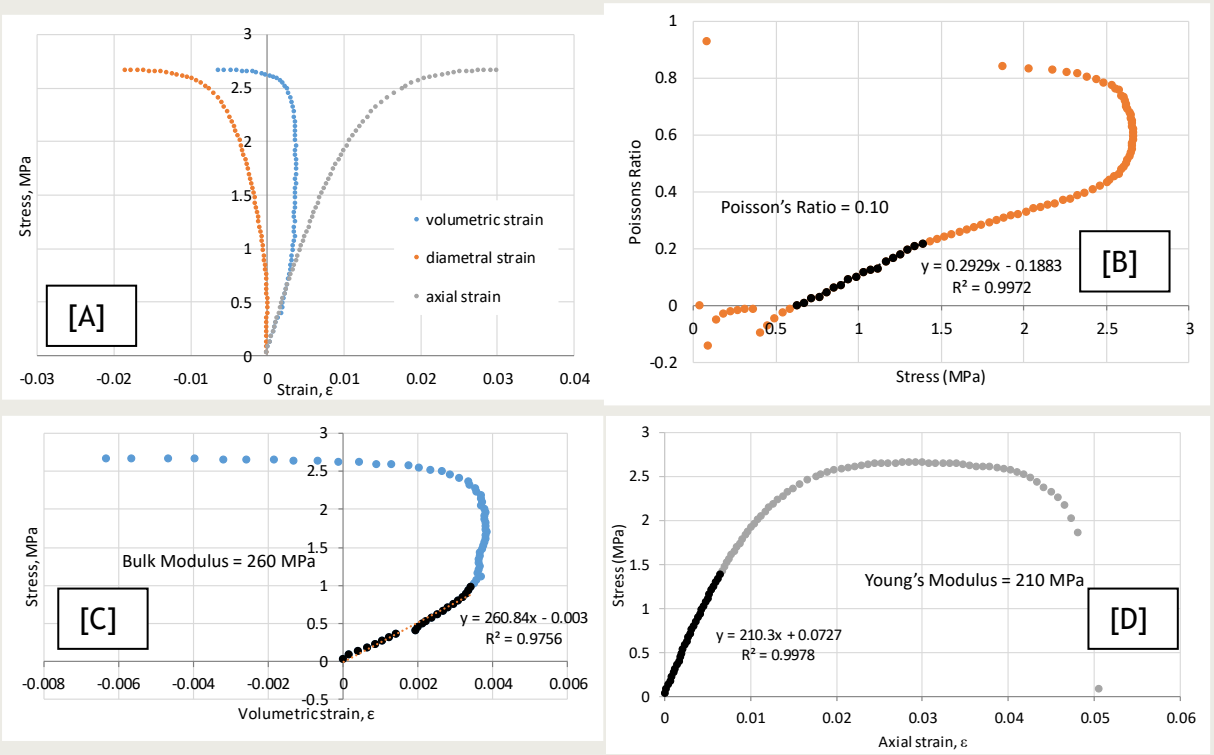

Figure 9-11: Uniaxial deformation test Mech_UCS500_8. [A] Stress-strain response. [B] Poisson's ratio. [C] Bulk Modulus. [D] Young's modulus.

The strain that both tests were subjected to resulted in failure of the samples. **Figure 9-12** shows the two samples used in Mech_UCS223m_7 and Mech_UCS500_8. The dashed red lines on Mech_UCS223m_7 highlight the planes of deformation. It should be noted that the test sample was still intact. This is in contrast to Mech_UCS500_8, which had a singular fracture plane (yellow dashed line). This suggests that test Mech_500UCS_7 experienced deformation close to the brittle-ductile transition, whereas Mech_500UCS_8 showed purely brittle response. This shows that the consolidation state of the Boom Clay influences the resultant deformation.

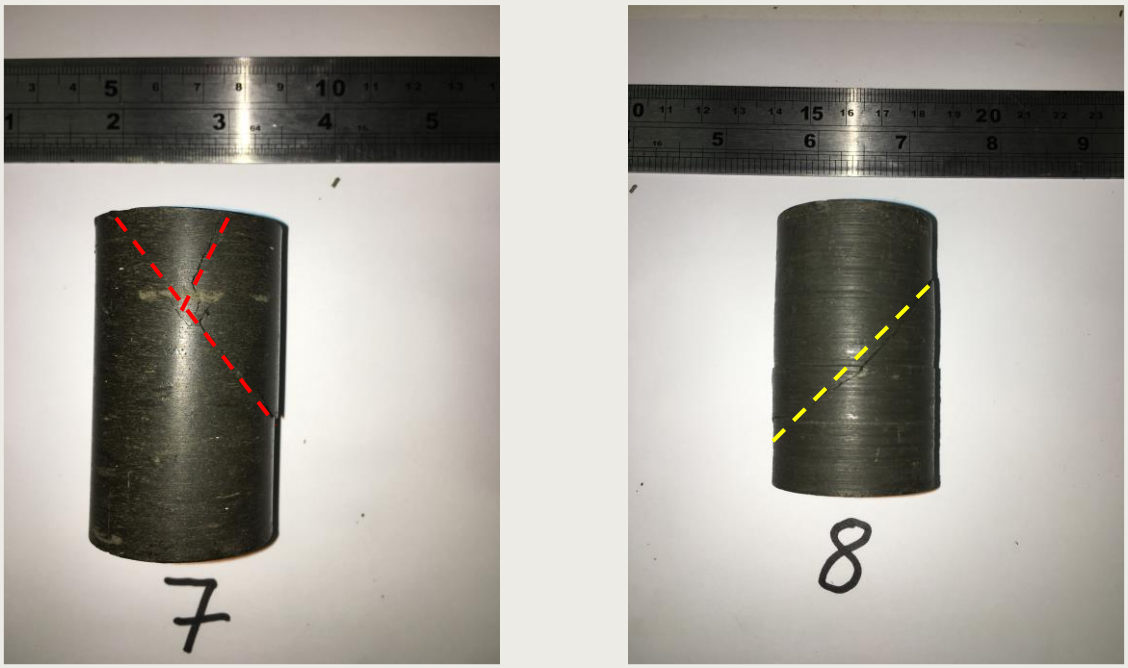

Figure 9-12: Photograph of the final samples following uniaxial deformation

9.3 *Discussion of results*

Table 9-2 summarises the main results from the study of the mechanical properties of Boom Clay. This section will compare the results for the two differently consolidated materials and will draw conclusions about the effect that consolidation has had on the mechanical properties. Comparisons will also be made from the available literature, as discussed in Wiseall et al., (2015).

Test		Consolid^{n} depth (m)	Confining pressure (MPa)	Axial stress at yield (MPa)	Peak strength (MPa)	Residual strength (MPa)	Axial strain at yield (%)	Young's Modulus (MPa)
Mech_500_1	**Tri**	**500**	5.1	4.43			1.9	214
Mech_500_2	**Tri**	**500**	3.4	2.70	5.48	5.35	1.7	145
Mech_500_3	**Tri**	**500**	1.7	2.02	4.48	4.42	1.1	171
Mech_223_4	**Tri**	**223**	2.2	2.65	4.5	4.49	2.22	215
Mech_223_5	**Tri**	**223**	1.57	2.65	3.26	3.24	1.6	189
Mech_223_6	**Tri**	**223**	0.75	1.94	3.32	3.21	2.55	112
Mech_UCS223_7	**Uni**	**223**	0	1.11	2.6	-	0.35	297
Mech_UCS500_8	**Uni**	**500**	0	1.38	2.66	-	0.61	210

Table 9-2: Results from the mechanical tests conducted on Boom Clay. Tri = triaxial compression test, Uni = uniaxial compression test.

Figure 9-13 shows the variation of peak strength with confining pressure. As confining pressure increased, so did the peak strength of the material. This is the case for the sample sets from 223 m and 500 m. The trend for each material is similar, with the material consolidated to 500 m depth having a slightly higher strength, although the scatter about the linear trend is considerable and more data are required to fully define

the relationship. It must be noted that due to the plastic nature of Mech_500_1 a peak stress could not be defined.

The line of peak strength corresponds to the line of ultimate strength. In the case of the Boom Clay both sets of tests have shown a linear relationship with confining pressure, as predicted by the Mohr-Coulomb relationship. However, some studies have shown that a non-linear relationship is possible. More test data are required to fully describe the form of the relationship.

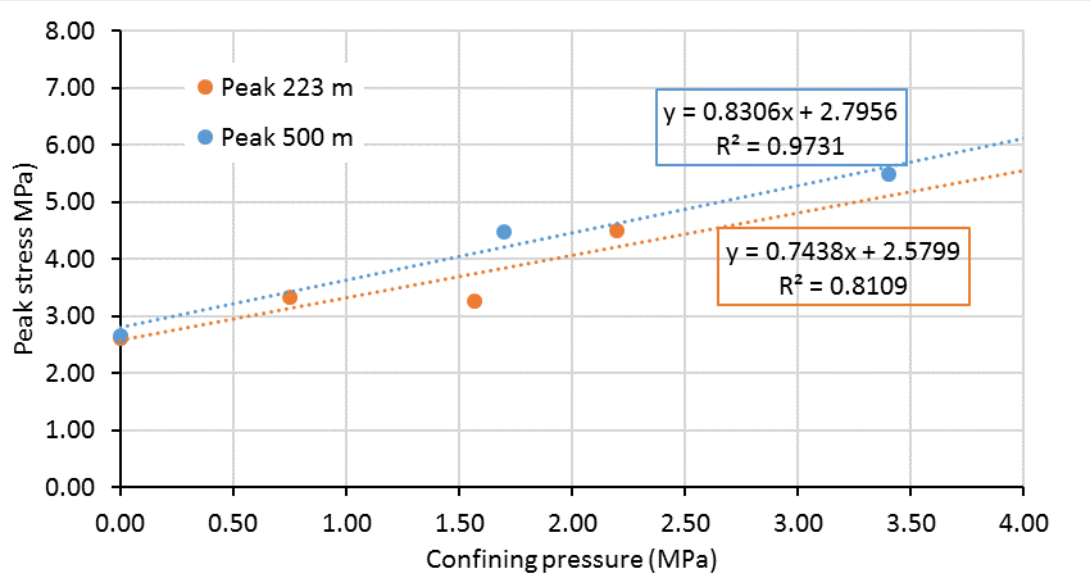

Figure 9-13: The relationship of peak strength with confining pressure for Boom Clay.

The results presented in **Table 9-2** show there is a clear variation in the strain at yield. For both UCS tests the axial strain is low at the point of yield when compared against the triaxial tests. This large variation in axial yield is associated with a lack of confining pressure.

The Young's Modulus for the material consolidated to 500 m varies from 214-145 MPa, whereas the material from 223m varies from 215-112 MPa. However, the low value of 112 MPa may be an anomaly as there may have been experimental issues early on in the test (**Figure 9-6**). The Young's Modulus measured in these tests have a large spread, which could be associated with the difficulty in finding a linear section of the stress-strain curve. The plastic nature of the clay meant that the yield point was difficult to define. This in turn meant that there is difficulty in recording the gradient of the line below yield. Despite this, the technique used to define yield is consistent and therefore the Young's Modulus values are reliable. There is no clear relationship to show that the consolidation of the material to 500 m has produced a change in Young's Modulus.

Wiseall et al., (2015) show that the Young's Modulus has consistently been measured at 300 MPa under drained conditions. This is significantly higher than those measured in this study. The reasons for this are unclear, however they may be associated with factors such as experimental method and sample preparation. **Table 9-1** shows that Horseman et al., (1993) measured an undrained value for the Boom Clay's Young's Modulus of 152-197 MPa, this data corresponds well with the current test. This could mean that the tests ran by Horseman et al., (1993) were not fully undrained, or that the current tests are behaving as if undrained. However, the stress variations seen after changes in strain-rate (Section 9.1.3) show that the sample behaves in a drained manner.

Wiseall et al., (2015) also predict that the undrained Young's Modulus would rise to 525 MPa in the Netherlands, this was assuming a preconsolidation stress of 7.45 MPa and an effective stress of 5.2 MPa. This is in large contrast to the values recorded in the current test programme. This variation may be due to experimental method or mineralogical differences in the Boom Clay. This discrepancy in recorded and predicted values highlights the need for further testing. It is important at this point to highlight that the material used in the current test programme was not preconsolidated to a stress of 7.45 MPa, but was subjected to a stress representative of 500 m depth. This would have resulted in samples that were close to virgin consolidation with an over-consolidation ratio (OCR) of 1. Future testing should examine the role of OCR on the mechanical properties of Boom Clay.

The UCS tests have resulted in two values for the Bulk Modulus of the Boom Clay. The Bulk Modulus is defined as the resistance to dimensional alteration. Wiseall et al., (2015) used values of Young's Modulus and Poisson's ratio from the literature to predict a value of 133 MPa at Mol. However, the current study has measured a value of 407 MPa for Mol depth (223 m) and 247 MPa for a depth of 500 m. This data comes from the linear gradient of the stress versus volumetric strain data from the UCS tests. There is a large discrepancy between the values predicted in Wiseall et al., (2015) and those measured in the current tests. However, there is also a large difference in the two measured values of 247 MPa and 407 MPa. This variation could be because of a number of reasons, for example sample preparation, experimental method or variations in the Boom Clay itself. The discrepancy could also result from the difficulty in defining the elastic region (linear deformation) in plastic clay.

The stress strain curves for all the triaxial tests show that at elevated strains the Boom Clay will begin to strain harden. These stress strain curves also show that the Boom Clay can have a very low yield stress, meaning the clay easily deforms in a plastic manner. Plastic deformation was clearly seen in the samples which were subject to higher axial stress (**Figure 9-3 A** and **Figure 9-5**). Significant barrelling was seen, especially in Tests Mech_500_1 and Mech_500_2 (**Figure 9-8**).

Table 9-1 shows that the most commonly quoted value for the Poisson's Ratio is 0.125 (Barnichon and Volckaert 2003, Bésuelle et al., 2013). This value is quoted as being measured under drain conditions. In this study Test Mech_UCS223_7 recorded a value of 0.09 for the Poisson's Ratio. The further consolidated material measured a similar value of 0.10. These values are in good agreement with the values from the literature as they are only 0.025 below. This small variation could be a result of where the yield point is defined. Interestingly this study showed no significant change in the Poisson's Ratio in the consolidated material, despite it having been artificially consolidated to a depth of 500 m.

Figure 9-10 **C** and **Figure 9-11 C** show the volumetric strain response for the two UCS tests. The gradient of the linear section of this graph equates to the Bulk Modulus, which were measured as 260 and 407 MPa for the material from 223 m and 500 m respectively. Wiseall et al.,, (2015) does not quote values from the literature. However, they use values of the Young's Modulus and Poisson's Ratio from Table 1-1 to calculate a predicted value of 133 MPa for 223 m depth. This value does not agree with the measured value of 260 MPa from the current study.

Wiseall et al., (2015) report a number of values for the UCS of the Boom Clay, the most commonly used being 2 MPa (Bernier et al., 2007; Tsang et al., 2012). However, Bésuelle et al., (2013) measured a value of 2.5 MPa. This is in close agreement with the values measured in the current study of 2.6 (223 m) and 2.66 (500 m). Uniaxial tests can be conducted at varying strain-rates, which for some rocks can result in different strength and

elasticity properties. Tests can also differ in sample dimension, the size of samples used in the current study were generally on the small size due to restrictions in sample preparation of the consolidated material and also did not have an ideal diameter to length ratio, which should be between 2 and 2.5. The current tests had a length ratio of 1.75 and this may have influenced results.

The main finding for the UCS tests in the current study was a small increase in strength as a result of material consolidation to 500 m. Considerable variations were noted on material tested in triaxial configurations and similar variation in uniaxial testing would be expected. However, within experimental uncertainty the UCS of the two tests were identical. This required further investigation as only two tests were conducted. The UCS test is a commonly used test due to its simplicity and ease compared with detailed triaxial testing. The current results would suggest little variation in the Boom Clay if just uniaxial test data were used, whilst the triaxial data suggest a more pronounced variation. A greater number of identical tests would provide a more precise value for the UCS at both 223 m and 500 m.

Despite the limited number of tests performed for the current study it is still possible to combine the triaxial and UCS tests to form a critical state envelope for both sets of tests. The critical state theory was initially proposed by Roscoe et al., (1958) as a unified model to describe the relationship between volume change and stress state. Initially the theory was related to soil mechanics, although this was later adapted so it could be applied to rock mechanics (Gerogiannopoulos and Brown, 1978; Shah, 1997). The state of a rock/clay subjected to a simple stress field is defined by its position in the mean effective stress (p') – deviatoric stress (q) space. This can be converted into a 3D envelope with the inclusion of volume change, voids ratio, or other material properties such as grain size (**Figure 9-14**).

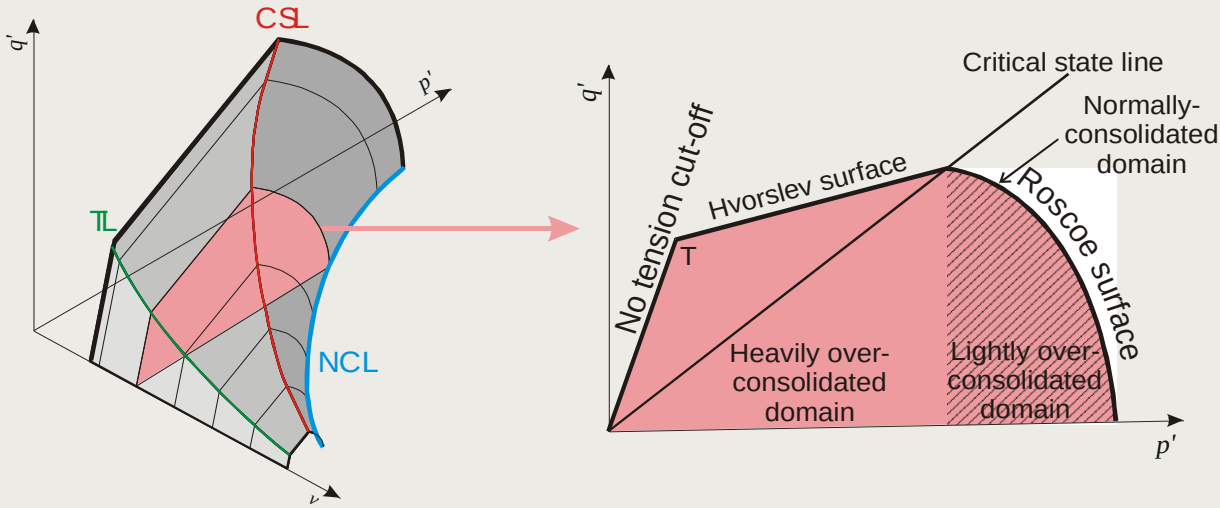

Figure 9-14: The critical state model of soil mechanics, showing the relationship of the tension line (TL), normal consolidation line (NCL) and critical state line (CSL). These lines bound the Hvorslev and Roscoe surfaces in the p' - q' space.

Figure 9-14 shows the critical state line (CSL) in relation to a yield surface. The yield surface can be split into three separate areas; the tension, Hvorslev and Roscoe surfaces. The tension line, the CSL and the Normal Consolidation Line (NCL), define these areas. The model predicts brittle deformation to the left of the critical state line (dry side) and ductile deformation to the right (wet side) with yield at the Roscoe surface. The critical state line represents the transition between brittle and ductile deformation, at this condition deformation is isovolumetric.

Critical state envelopes have been fitted to yield data from the current study. **Figure 9-15** clearly shows the zero tension line, Hvorslev and Roscoe surfaces for both the consolidated material (solid lines) and the material from 223 m (dashed lines). The two separate sets of tests have clearly formed two slightly different critical state envelopes.

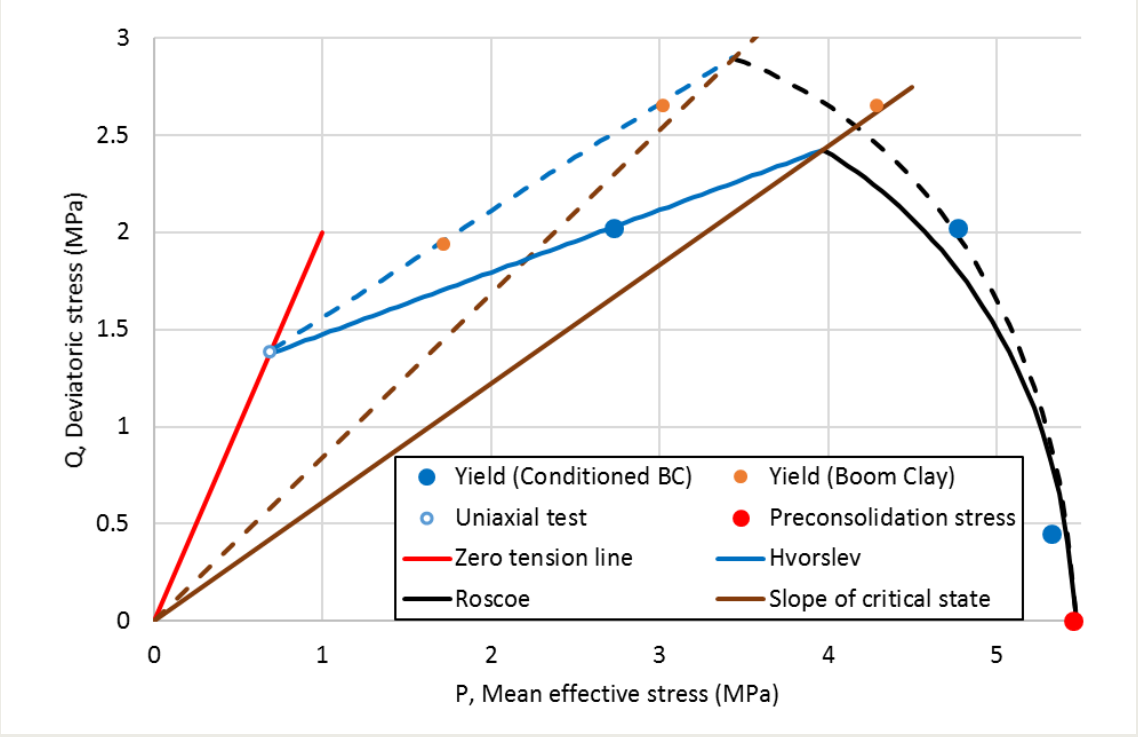

Figure 9-15: Critical state envelopes fitted to the current data. Solid lines represent data consolidated to 500 m. Dashed lines represent material from Mol.

Test Mech_500_1 was performed at a confining pressure of 5.1 MPa and yielded at just 0.45 MPa, this plots close to the pre-consolidation stress of 5.45 MPa. Thus, meaning that this material has acted as a very lightly consolidated material. This would be the expected behaviour as the material at Mol has been shown to have an OCR of 2.4 (Wiseall et al., 2015), however once this material is buried to 500 m then the OCR becomes almost 1. It must be noted that the OCR will likely change if the material is from the Netherlands as it is already at 500 m and has been to deeper depth in geological history. Predictions by Wildenborg et al., (2003) predicted that the material in the Netherlands would likely have a pre-consolidation pressure of 7.45 MPa, i.e. an OCR of nearly 1.5. This would likely alter the shape of the critical state envelope. There is a lack of data to further populate the critical state envelope with further points. Critical state parameters are not quoted here due to the limited number of experiments conducted and a more complete suite of tests would be required to establish the critical state parameters.

An alternative method to categorise the failure behaviour of a rock is to plot peak data in the Mohr space. This is a simplified failure criterion that is commonly used in rock mechanics and geotechnics. The Mohr-Coulomb equation relates material strength to the normal and shear stress at the point of failure. It assumes that strength increases with confining pressure in a linear manner, as was shown in **Figure 9-16**.

Figure 9-16 A shows the Mohr circles for each test carried out on the material from 223 m depth, **Figure 9-16 B** shows the failure envelope for the tests carried out on the material consolidated to 500 m. From this, a number of parameters can be calculated that describe the mechanical behaviour of the Boom Clay, as summarised in **Table 9-3**.

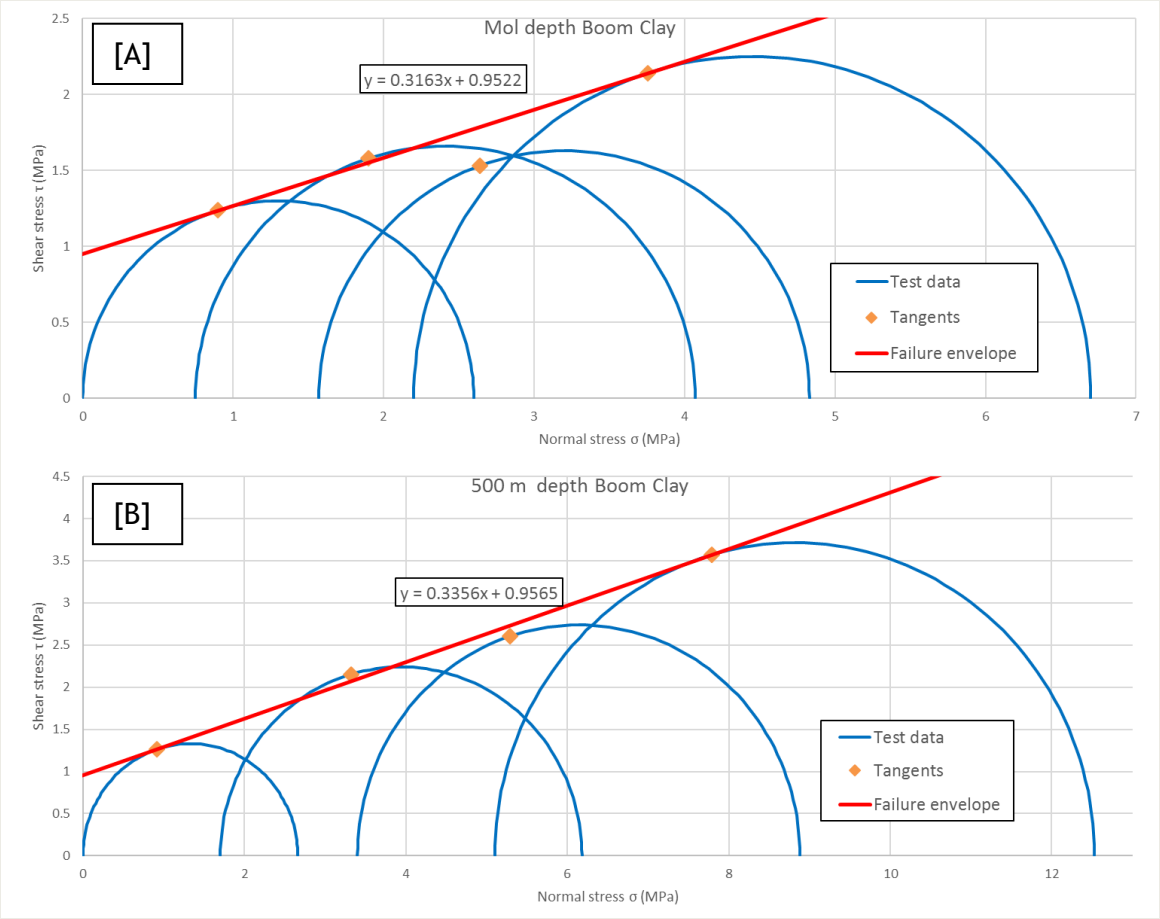

Figure 9-16: Mohr analysis of deformation in Boom Clay. [A] Data from 223 m depth. [B] Data from conditioned samples to 500 m depth.

Material	Co-efficient of internal friction	shear strength	Friction angle	Fault angle
	tan φ	C	Φ	ϴ
223 m	0.316	0.952	17.55	36.22
500 m	0.336	0.957	18.55	35.73

Table 9-3: Mechanical properties of Boom Clay determined from the Mohr approach.

When comparing this data against that gathered in the literature it can be seen that the friction angle measured for the material from Mol is in good agreement with that already studied. A value of 18° is commonly quoted (Bouzza et al., 1996; Barnichon and Volckaert, 2003; Bernier et al., 2007). The values measured in the literature were also carried out under drained conditions. This good agreement with previous studies also means that the value from 500 m depth is more reliable. The study shows that the friction angle drops slightly due to the consolidation to 500 m depth.

It must be highlighted that there are many assumptions made during the Mohr-Coulomb analysis, the main of these being the approximation of linearity. This has shown to be inappropriate for many materials, from incohesive soil to granite (Schofield, 1998; Ohnaka, 1973; Byerlee, 1975). Whilst representing an appropriate failure criterion for specific materials over a restricted interval of stress conditions, the Mohr–Coulomb criterion is not generally considered appropriate for use in repository assessment, where more detailed data should be available.

In Chapter 8 a number of direct shear measurements were made, these also measured the shear strength and fault angle of the Boom Clay. The shear strength was found to be 0.475 MPa and 1.31 MPa for the 223 m depth material and 500 m depth material respectively. The direct shear experiments showed a clear change in shear strength with consolidation, whereas this study using the triaxial and UCS apparatus found almost no change.

Figure 9-17 shows the calculated angles of deformation for tests Mech_500_3,4,7,8. These were the samples with the most clear deformation structures, which could easily be measured without further detailed microscopic analysis. The fault angles shown in Figure 1-15 range from 37-50°, the lower range of these are in good agreement with the predicted fault angle in **Table 9-1**. This data contrasts that in Section 9 of this report which when under direct shear the Boom Clay sheared at angles sub parallel to shear direction.

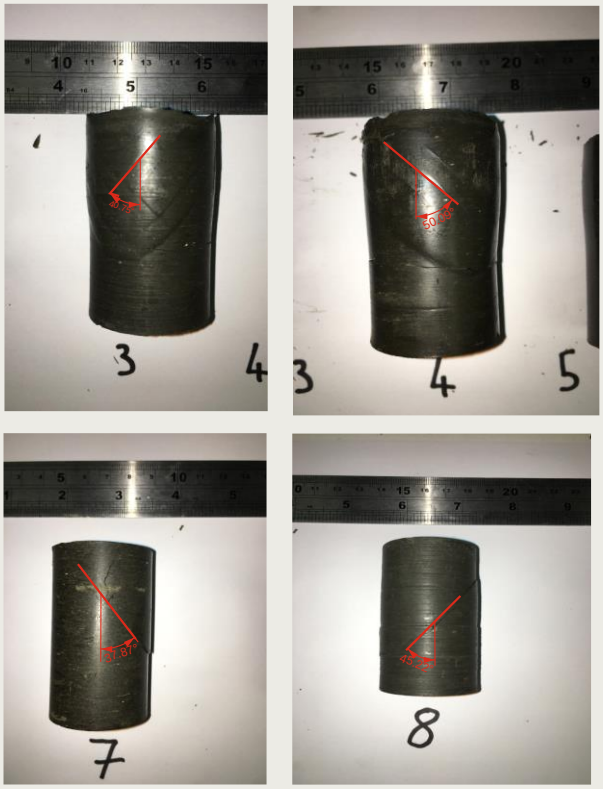

Figure 9-17: Angle of fracture for tests shown.

A series of triaxial and UCS tests have been presented in this study. Tests were carried out on material from the HADES URL, with half of the tests conducted on material that had been consolidated in the laboratory to a stress representative of 500 m depth. These tests have defined the mechanical properties of Boom Clay, which may impact many aspects of a potential repository. The Boom Clay was shown to have an increased strength with depth. As stress increased the material showed a transition from brittle to ductile deformation. The yield data allowed construction of critical state models for the two materials tested.

However, the limited number of tests conducted mean that full definition of the critical state parameters was not possible and further tests are required to give a full definition.

Outcomes:

1. The Boom Clay is observed to have a slight increase in strength when consolidated to 500 m depth.
2. As stress levels are elevated the Boom Clay transitions from brittle to ductile deformation.
3. A critical state envelope has been defined for the stress conditions at 223 and 500 m depths.
4. Variations in the mechanical properties, such as Young's Modulus, were observed between this test programme and those quoted in the literature.

Recommendations:

1. A greater number of tests under triaxial conditions will enable better, more accurate, descriptions of the yield behaviour of Boom Clay.
2. Detailed testing of the change in permeability during deformation.
3. Repeat testing to investigate sample variability.
4. Experiments to investigate the anisotropy of Boom Clay and the role this may play on a repository.

10 Summary

In defining the long-term fate of radionuclides in a repository for radioactive waste, it is necessary to understand the hydrogeological context of the site and how this may evolve temporally and spatially. In the Netherlands, the search for a site to host a national repository has focussed on the Boom Clay Formation (here after referred to as the 'Boom Clay'). Whilst there has been a considerable amount of work undertaken examining the behaviour of Boom Clay, this has tended to be at Belgium reference depths (approx. 220m), so the current study aimed to extend this knowledge to repository depths of interest in the Netherlands (circa 500m). In this study 20 experiments are reported examining a range of material properties including, consolidation, swelling, hydraulic, gas and mechanical deformation. These provide an estimate of the properties at 500m depth previously unavailable. However, it should be acknowledged that this is a scoping study only and not an exhaustive examination of the problem. Further detailed studies are required as highlighted by the current study.

The current study examines Boom Clay cored from the Hades URL at a depth of around 220 m. In a number of tests this unconditioned material has been investigated at a stress representative of the conditions from which it was cored. Clay has also been conditioned to a stress state representative of the Netherlands, circa 500 m depth of burial. This was achieved through 1D compression, isotropic consolidation or triaxial compression. An important consideration is the over-consolidation ratio (OCR) of the material as it directly impacts the physical properties of the material. In Section 3, the OCR of Boom Clay from Mol was shown to be 2.3, or a maximum burial depth of 506 m. So the condition of core to a depth representative of the Netherlands has resulted in an OCR close to unity. Wildenborg et al., (2003) suggest a preconsolidation stress of 7.45 MPa, giving an OCR close to 1.5. This suggests that Boom Clay has a variable OCR across its depositional basin and given the importance of this parameter in defining the hydromechanical properties of the Boom Clay, understanding this variation and its impact on material properties, remains a research priority. Given the uncertainty in OCR value within the Netherland reference concept, it was decided to adopt a value of unity for this study. Ideally, experiments should have been conducted at both values of OCR to assess its impact on material behaviour.

The sensitivity of permeability to changes in consolidation state, thermal loading and salinity have been examined. Permeability is shown to be sensitive to the state of stress applied to the clay. At a depth of 220 m permeability was found to be 1.5×10^{-19} m^2 $\pm 0.15 \times 10^{-19}$ m^2. At an OCR of unity equivalent to a depth of burial of 500 m, permeability reduced to 1.1×10^{-19} m^2, representing only a minor reduction in value. However, increasing preconsolidation stress to 7.95 MPa and then unloading to give an OCR = 1.5, yields a permeability value of 0.8×10^{-19} m^2. While the change in magnitude is relatively small it highlights the sensitivity of permeability to both preconsolidation stress and OCR. Permeability is also shown to be sensitive to thermal load. Temperatures within this study ranged from 30 to 185 C at depths representative of the Netherlands reference concept. Permeabilities were found to reduce from 1.1×10^{-19} m^2 at 30 °C to 0.7×10^{-19} m^2 at 185 °C. This suggests Boom Clay thermally contracts (i.e. consolidates) on heating. On cooling from 124 °C, the vast majority of the permeability change induced by thermal consolidation is non-recoverable, suggesting the material had exceeded the thermal maturity of the basin. Standard geothermal gradients suggest an in situ temperature of around 30-35 °C at a maximum burial depth of 750 m (equivalent to OCR = 1.5). In a repository for heat emitting waste, where temperatures are typically limited to 100 °C, such changes would appear to have minimal impact on the hydraulic behaviour of the Boom Clay. However, it should be acknowledged that in this scoping study a simple isotropic thermal load was applied to the sample, rather than a thermal gradient representative of an actual repository. The impact

of thermal gradient requires more detailed study to establish its importance in relation to potential drying, thermally induced damage and subsequent rehydration/self-sealing behaviour.

To assess the sensitivity of Boom Clay to changes in salinity, sodium chloride (NaCl) solution with salt fractions ranging from 0.001 to 0.08, was injected through the clay. While it was originally intended to measure the osmotic membrane properties of the Boom Clay, the ease at which fluids (solvent) were able to migrate through the clay at a very low pressure differential, made such measurement impractical in the current apparatus. Nevertheless, it indicates membrane efficiencies for natural material are likely to be low. As such, natural features, bedding planes and heterogeneity may render membrane potential ineffective through the backflow of solutes through the clay.

While testing was undertaken at two different effective stresses, changes in permeability, for the range in salt fractions examined, were minimal. Acknowledging the limited duration of these tests, simple changes in NaCl concentration appear to have negligible impact on the hydraulic properties of the clay. However, in a repository for radioactive waste, the evolution of near-field fluid chemistry will create complex changes in fluid composition. These may have a much stronger impact on both membrane efficiency and hydraulic properties of the Boom Clay.

The free swell behaviour of Boom Clay was not found to be significantly different between 220 m and 500 m. This is not surprising as the material will reside on the same rebound-reconsolidation line. At 500 m depth, primary swelling strains of >50% were observed, illustrating the free-swell capacity of the Boom Clay. This has important implications for the closure of engineering voids.

Swelling behaviour measured in a constant volume cell, for unconditioned material, yields swelling pressure in the range 0.5 to 0.75 MPa. Increases in porewater pressure to, e.g. symptomatic of glacial loading, resulted in a systematic reduction in swelling pressure. This observation is in line with previous measurements performed on compact bentonite (ref) and has important implications for the hydromechanical behaviour of Boom Clay. However, to assess its importance to repository depths of interest to Covra, additional tests are required on conditioned core material.

Gas migration behaviour was investigated in a number of experimental geometries. In all tests, gas was not mobile (i.e. gas entry) until a pressure close to, or exceeding, local stress. In the case of triaxial conditions, the minimum principal stress had to be exceeded for gas entry to occur. Following entry, flow is strongly coupled to total stress and porewater pressure. The migration of gas through the clay was accompanied by dilation of the sample (0.2 % volumetric strain) exceeding the poroelastic response of the Boom Clay, suggesting dilatant pathway formation. During this phase of pathway development, anisotropy in the distribution of stress and porewater pressure increases, both of which vary temporally and spatially within the sample. Depending on the test geometry, this can lead to large differential stresses internally within the clay, resulting in the expulsion of water and therefore desaturation of the Boom Clay, which is thought to be through gas induced consolidation of porous horizons within the sample, or, direct displacement of water from grain-supported sections of the clay. This is supported by post-test measurements of sample volume and mass, which appear to contradict previously published results (e.g. Horseman & Harrington, 1994). The well-documented variability of Boom Clay provides a possible explanation, though post-mortem analysis of samples would be required to confirm the observation and further work is required to adequately explain the reason for this important discrepancy.

A peak gas pressure of 10.7 MPa (excess pressure of 5.8 MPa) at stress conditions representative of the Netherlands, when major break-through occurred. Gas pressure evolved to a steady-state permeability of 2.3×10^{-20} m^2, and compares well with previous studies. The permeability of the network of pathways evolve temporally and spatially and during this period Boom Clay contracted. On the length scale of the tests performed, a minimal drop in gas pressure along the conductive pathways occurs, suggesting high gas pressure gradients exist around points of drainage. Capillary threshold pressure associated with the cessation of flow was not determined during the current study because of the non-linear nature of the shut-in transient and requires further investigation. The sensitivity of flow to gas pressure gradient and hysteresis of the clay caused by apparent desaturation is unclear, as is the role of gas induced consolidation in the self-sealing capacity of Boom Clay. Understanding these complex issues requires targeted detailed experimentation.

The mechanical behaviour of Boom Clay may impact and influence many aspects of a repository. The Boom Clay at depths representative of the Netherlands showed a transition from brittle to ductile deformation with increasing stress in both compression (triaxial) and shear. Deformation within the brittle regime resulted in single fracture formation, whereas ductile deformation resulted in considerable sample barrelling and the formation of multiple cross-cutting fractures. These were observed to form at an angle approximately 40°, which compares well with the calculated fault angle of 36.2°. Peak strength increases with stress and was used to define the ultimate strength, shear strength, friction angle and fault angle. The onset of deformation (yield) is of greater importance in radioactive waste disposal and defines the stress state at which the physical properties of the host rock alters. Yield is not straightforward to define in plastic clay as no linear elastic region is evident, but a robust methodology can define this parameter. Yield can be described using critical state mechanics, with the Hvorslev surface defining deformation within the brittle regime and the Roscoe surface defining deformation in the ductile regime. The brittle-ductile transition is defined as the critical state line and under these conditions deformation is isovolumetric. The yield data therefore plot as a near circle in the differential-mean effective stress space. The current study only used four samples to define the surface and as such the fit is non-ideal. Therefore further triaxial deformation experiments are required to fully define the critical state description of Boom Clay within the Netherlands. However, the limited data show that differences exist between the mechanical responses of Boom Clay at 220 and 500 m depths.

Fractures in Mode II (in-plane shear) form sub-parallel to the direction of shear, with repeat deformation creating distinctly different fracture surfaces. This indicates a capacity for Boom Clay to self-heal leading to the formation of new fractures, demonstrated by similar peak strengths during each cycle of testing. However, the shear modulus of these features suggests that the original fracture plays a role on reactivation. Therefore full self-healing was not evidenced. The shear, yield, peak and residual strength of Boom Clay all increase with increased normal load. Flow of water directly into fractures reduces the fracture transmissivity, mimicking hydraulic behaviour observed on intact Boom Clay, showing swelling of clay minerals reduces permeability. Fracture shearing leads to a reduction in flow, demonstrating self-sealing. If brittle behaviour or fracture misalignment is seen local flow is promoted.

Mechanical data has been measured directly and indirectly using a number of methods. For instance, shear modulus was directly measured as 28 MPa using direct shear and determined as 38 MPa during isotropic consolidation. Shear strength was also measured directly as 1.29 MPa and was calculated to be 0.95 MPa from triaxial and uniaxial test data. Therefore, good agreement has been achieved using different approaches.

Sample anisotropy was observed throughout the experimental programme. The Boom Clay is a complex rock that has not only anisotropy but spatial variability. These phenomena will play a significant role on hydromechanical behaviour and require careful consideration in the definition of future research. The values attained for material consolidated to 500 m depth are summarised in **Table 10-1**, **Table 10-2, Table 10-3** and **Figure 10-1.**

		Mechanical Properties											
Stress depth	Methodology	Shear strength	Shear modulus	Residual shear strength	Fracture transmissivity	Fracture roughness	Young's Modulus	Poisson's Ratio	UCS	Bulk Modulus	Co-efficient of internal friction	Friction angle	Fault angle
		MPa	MPa	MPa	m^2/s	mm	MPa		MPa	MPa	tan φ	Φ	ϴ
500 m	Drained triaxial						214				0.336	18.55	35.73
	Uniaxial test						210	0.1	2.66	407			
	Direct shear	1.29	28	0.96	5×10^{-14}	0.31							
	Permeameter												

Table 10-1: Mechanical properties of Boom Clay at 500 m depth.

		Hydraulic			
Stress depth	Methodology	Permeability	Hydraulic conductivity	Gas breakthrough pressure	Gas permeability
		m^2 (x 10^{-19})	m/s (x 10^{-12})	MPa	m^2 (x 10^{-19})
500 m	Drained triaxial	1.65			
	Uniaxial test			9.99	
	Direct shear	1.43 1.28	1.40 1.09		
	Permeameter	1.05 0.86	0.79 0.84		0.23

Table 10-2: Hydraulic properties of Boom Clay at 500 m depth.

Thermal properties	
Temperature (°C)	**Permeability** (m^2)
30	-
30	1.3×10^{-19}
30	1×10^{-19}
62	$1x\ 10^{-19}$
92	-
62	9.9×10^{-20}
93	9.1×10^{-20}
124	7.8×10^{-20}
93	8×10^{-20}
124	8×10^{-20}
155	7.8×10^{-20}
185	7.3×10^{-20}

Table 10-3: Variation of permeability with temperature.

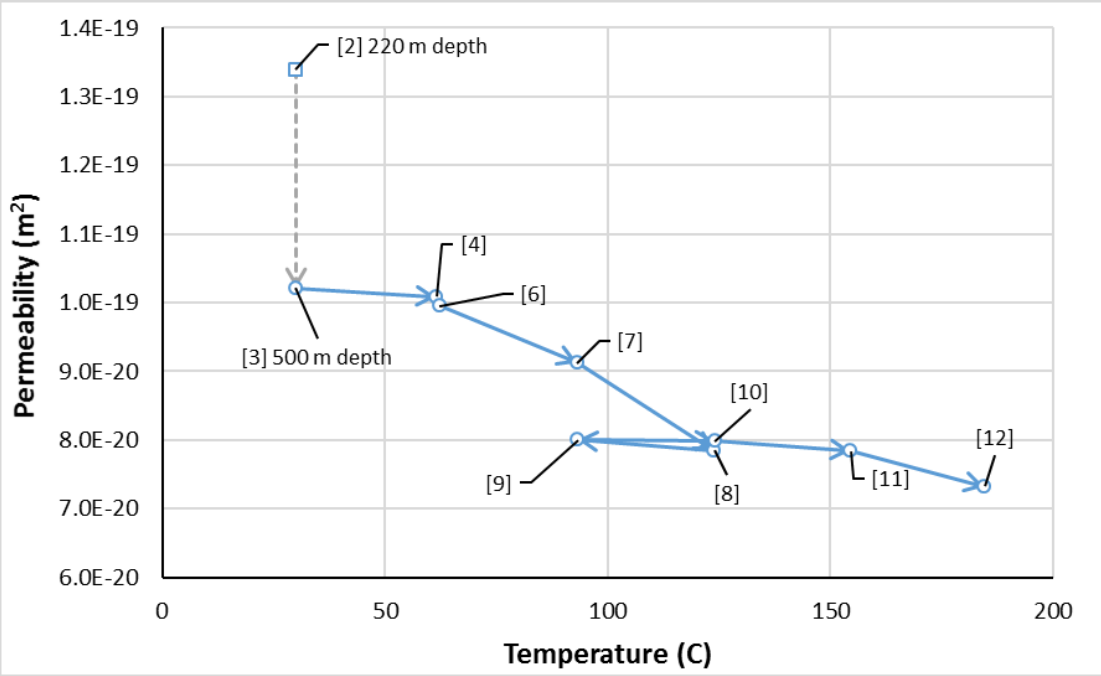

Figure 10-1: Variation of permeability with temperature.

References

Abuel-Naga, Hossam, M., Dennes, T, Bergado, and A, Bouazza, A, *Thermally induced volume change and excess pore water pressure of soft Bangkok clay, Engineering Geology* 89.1 (2007), 144-154.

ASTM Standard. Standard guide for assessment of surface texture of non-porous biomaterials in two dimensions. F2791-09. (2009).

Barnichon, J, Volckaert, G, *Observations and predictions of hydromechanical coupling effects in the Boom Clay, Mol Underground Research Laboratory, Belgium*, Hydrogeology Journal 11 (2003) 193-202.

Beerten, K, Leterme, B, *Physical geography of north-eastern Belgium – the Boom Clay outcrop and sub-crop zone SCK-CEN report* ER-202 12/Kbe/P-2 60p.

Bernier, F, Neerdel, B, *Overview of in-situ thermomechanical experiments in clay: Concepts, results and interpretation*, Engineering Geology 41 (1996) 51-64.

Bernier, F, Li, XL, Bastiaens, W, *Twenty-five years' geotechnical observation and testing in the Tertiary Boom Clay formation,* Géotechnique 57(2) (2007) 229–237.

Bésuelle, P, Viggiani, G, Desrues, J, Coll, C, Charrier, P, *A Laboratory Experimental Study of the Hydromechanical Behaviour of Boom Clay,* Rock Mechanics and Rock Engineering 47 (2013)143-155.

Biot, M, *General theory of three-dimensional consolidation*, Journal of Applied Physics 2 (1941) 155-164.

Bjerrum, L, *Progressive failure in slopes of overconsolidated plastic clay and clay shales,* Journal of Soil Mechanics and Foundation Divisions 93 (1967).

Bouazza, A, Impe, W, Haegeman, W, *Some mechanical properties of reconstituted Boom clay,* Geotechnical and Geological Engineering 14 (1996) 341-352.

Byerlee, JD, *The fracture strength and frictional strength of Weber sandstone*, In International Journal of Rock Mechanics and Mining Sciences and Geomechanics Abstracts 12 (1975) 1-4.

Chen, GJ, Sillen, X, Verstricht, J, Li, XL, *ATLAS III in situ heating test in boom clay: Field data, observation and interpretation,* Computers and Geotechnics, 38(5) (2011) 683-696.

Cui, Y, Tang, AM, *On the chemo-thermo-hydro-mechanical behaviour of geological and engineered barriers,* Journal of Rock Mechanics and Geotechnical Engineering 5(3) (2013) 169–178.

Cui, YJ, Delage, P, Le, TT, Li, XL, Tang, AM, *Investigating the time-dependent behaviour of Boom clay under thermomechanical loading,* Géotechnique, 59(4) (2009) 319-329.

Cuss, RJ, Harrington, JF, Giot, R, Auvray, C, *Experimental observations of mechanical dilation at the onset of gas flow in Callovo-Oxfordian claystone* (2014), Geological Society of London, Special Publications, 400 (1), 507-519.

Cuss, RJ, Harrington, JF, Milodowski, AE, Wiseall, AC. Experimental study of gas flow along an induced fracture in Opalinus Clay. *British Geological Survey Commissioned Report*, CR/14/051. (2014) 79pp.

Cuss, RJ, Harrington, JF, Noy, DJ, *Final report of FORGE WP4 1.1: the stress-path permeameter experiment conducted on Callovo-Oxfordian Claystone* (2012) FORGE WP4, EJP project.

Cuss, RJ, Harrington, JF. Experimental Observations of the Flow of Water and Gas along Fractures in Opalinus Clay. Extended abstract. Fourth EAGE Shale Workshop, Porto, Portugal, 6th April 2014. (2014) DOI: 10.3997/2214-4609.20140041

Cuss, RJ, Harrington, JF. Final Report of FORGE WP4.1.1: The stress path permeameter experiment conducted on Callovo-Oxfordian Claystone. *British Geological Survey Commissioned Report*, CR/12/140. (2012) 116pp.

Cuss, RJ, Milodowski, A, Harrington, JF Fracture transmissivity as a function of normal and shear stress: first results in Opalinus clay. *Physics and Chemistry of the Earth*. 36, (2011) pp.1960-1971. DOI: 10.1016/j.pce.2011.07.080

Daniels, KA, Harrington, JF, Zihms, SG, Wiseall, AC, *Bentonite Permeability at Elevated Temperature,* (2017) Geosciences, 7 (1).

De Craen, M, Wang, L, Van Geet, M, Moors, H, *Geochemistry of Boom Clay pore water at the Mol site,* SCK-CEN scientific report BLG-990. Waste and Disposal Department SCK-CEN (Mol, Belgium) (2004).

De Craen, M, Wang, L, Van Geet, M, Moors, H, *Geochemistry of Boom Clay pore water at the Mol site,* SCK-CEN-BL-990 04/MDC/P-48, SCK-CEN (2004b).

Dehandschutter, B, Vandycke, S, Sintubin, M, Vandenberghe, N, Wouters, L, *Brittle fractures and ductile shear bands in argillaceous sediments: inferences from Oligocene Boom Clay (Belgium),* Journal of Structural Geology 27(6) (2005) 1095–1112.

François, B, Laloui, L, Laurent, C, *Thermo-hydro-mechanical simulation of ATLAS in situ large-scale test in Boom Clay,* Computers and Geotechnics 36(4) (2009) 626-640.

Fritz, JJ, *Ideality of clay membralles in osmotic processes: A review,* Clays and Clay Minerals 34 (1986) 214-223.

Gerogiannopoulos, GN, Brown, ET, *The Critical State Concept Applied to Rock,* International Journal of Rock Mechanics and Mining Science and Geomechanics 15 (1978) 1–10.

Graham, C.C, Harrington, JF, Cuss, RJ, and Sellin, P, *Gas migration experiments in bentonite: implications for numerical modelling (2012),* Mineralogical Magazine, 76(8), pp.3279-3292. DOI: 10.1180/minmag.2012.076.8.41.

Graham, CC, Harrington, JF, Cuss RJ, Sellin, P, *Pore-pressure cycling experiments on Mx80 bentonite*, In: Clays in Natural and Engineered Barriers for Radioactive Waste Confinement, Geological Society, London, Special Publications, 400 (2015).

Hanor, JS, *On the non-importance of membrane filtration as a mechanism for producing subsurface brines in the Louisiana Gulf Coast,* In: Proceedings 21st Clay Min. Soc. Annual Meeting, Baton Rouge, USA (1984).

Hansbo, S, *Consolidation of clay, with special reference to influence of vertical sand drains,* Proceedings of Swedish Geotechnical Institute, 18 (1960).

Hansbo, S, *Influence of mobile particles in soft clay on permeability,* Proceedings International Symposium on Soil structure (1973).

Hanshaw, BB, *Membrane properties of compacted clays*, Ph.D Thesis, Harvard University (1962).

Harrington, JF, Graham, CC, Cuss, RJ, Norris, S, *Gas network development in a precompacted bentonite experiment: Evidence of generation and evolution,* Applied Clay Science (2017), 147, 80-89.

Harrington, JF, Horseman, ST, *Gas migration in KBS-3 buffer bentonite: Sensitivity of test parameters to experimental boundary conditions* (2003), Report TR-03-02. Svensk Kärbränslehantering AB (SKB), Stockholm, Sweden.

Harrington, JF, Horseman, ST, *Gas transport properties of clays and mudrocks*. In: Aplin, A.C., Fleet, A.J., Macquaker, J.H.S. (Eds.), Muds and Mudstones: Physical and Fluid Flow Properties. Geological Society, London, (1999) pp. 107-124.

Harrington, JF, Milodowski, AE, Graham, CC, Rushton, JC, Cuss, RJ, *Evidence for gas-induced pathways in clay using a nanoparticle injection technique,* Mineralogical Magazine, 76(8) (2012) 3327-3336.

Heister, K, Kleingeld, PJ, Gustav Loch, JP, *Induced membrane potentials in chemical osmosis across clay membranes*, Geoderma 136(1–2) (2006) 1-10.

Horseman, S, Harrington, J, *Migration of repository gases in an overconsolidated clay*, British Geological Survey, Keyworth (United Kingdom), Fluid Processes Research Group (1993).

Horseman, S, Harrington, J, *Migration of repository gases in an overconsolidated clay*, British Geological Survey, Keyworth (United Kingdom), Fluid Processes Research Group (1994).

Horseman, ST, Harrington, JF, *Gas migration under isotropic and K0 stress conditions,* In: Research into Gas Generation and Migration in Radioactive Waste Repository Systems (PROGRESS Project), Editor Rodwell, W.R., European Commission (2000).

Horseman, S, Winter, M, Entwistle, D, *Geotechnical characterisation of Boom Clay in relation to disposal of radioactive waste*, Report EUR 10987, Luxembourg: Commission of the European Communities (1987).

Horseman, S.T, Harrington, JF, Birchall, DJ, Noy, DJ, Cuss, RJ, *Consolidation and rebound properties of Opalinus Clay: a long-term, fully drained test*, (2005). BGS report, CR/05/128N.

Horseman, ST, Harrington, JF, Noy, DJ, *Swelling and osmotic flow in a potential host rock,* Physics and Chemistry of the Earth, Parts A/B/C 32 (2007) 408-420.

Horseman, ST, McEwen, TJ, *Thermal constraints on disposal of heat-emitting waste in argillaceous rocks,* Engineering Geology 41(1–4) (1996) 5-16.

Kell, GS, *Density, thermal expansivity, and compressibility of liquid water from 0. deg. to 150. deg.. correlations and tables for atmospheric pressure and saturation reviewed and expressed on 1968 temperature scale,* Journal of Chemical and Engineering Data 20.1 (1975), 97-105.

Kemper, WD, Evans, NA, *Movement of water as effected by free energy and pressure gradients: III. Restriction of solutes by membranes,* Soil Science Society of America Proceedings 27 (1963) 485-490.

Kemper, WD, Rollins, JB, *Osmotic efficiency coefficients across compacted clays*, Soil Science Society of America 30 (1966) 529-534.

Kutelek, M, *Non-Darcian flow of water in soils (Laminar Region),* 1st IAHR Symposium on Fundamentals of Transport Phenomena in Porous Meida, Haifa, Israel (1969).

Li, X, *TIMODAZ: A successful international cooperation project to investigate the thermal impact on the EDZ around a radioactive waste disposal in clay host rocks*, Journal of Rock Mechanics and Geotechnical Engineering, 5(3) (2013) 231-242.

Miller, RJ, Low, PF, *Threshold gradient for water flow in clay systems*, Soil Science society of America, (1963), 27 (6), 605-609.

Mitchell, JK, *Fundamentals of Soil Behaviour,* John Wiley and Sons, New York (1976).

Monfared, M, Sulem, J, Delage, P, Mohajerani, M, *On the THM behaviour of a sheared Boom clay sample: Application to the behaviour and sealing properties of the EDZ,* Engineering Geology 124 (2012) 47-58.

Neuzil, C, *How permeable are clays and shales?* Water Resources Research 39 (2) (1994) 145-150.

Nickel, E, *Oligozäne Beckendynamik und Sequenzstratigraphie am Südrand des Nordwesteuropäischen Tertiärbeckens,* (2003), Dissertation Universität Bonn, pp 151.

Oakes, DT, *Solids concentration on effects in bentonite drilling fluids,* Clays and clay minerals 8 (1960) 252-273.

Ohnaka, M, *The quantitative effect of hydrostatic confining pressure on the compressive strength of crystalline rocks,* Journal of Physical Earth 21 (1973) 125-140.

Roscoe, K. H_, Schofield, AN, Wroth, CP, *On the yielding of soils.* Geotechnique 8.1 (1958), 22-53.

Schofield, AN, *The 'mohr-coulomb' error,* Cambridge University Press (1998).

Shah, KR, *An elasto-plastic constitutive model for brittle-ductile transition in porous rocks,* International Journal of Rock Mechanics and Mining Sciences 34 (1997) 283.

Sultan, N., Cui, Y.J. and Delage, P., 2010. Yielding and plastic behaviour of Boom clay. Geotechnique, 60 (9), 657-666.

Tamayo-Mas, E, Harrington, JF, Graham, CC. *Numerical modelling of consolidation processes: an iterative algorithm to calibrate the time-dependent parameters*, International Journal of Engineering Sciences, (In Press).

Tsang, C. F., Barnichon, J. D., Birkholzer, J., Li, X. L., Liu, H. H. and Sillen, X., 2012. Coupled thermo-hydro-mechanical processes in the near field of a high-level radioactive waste repository in clay formations. International Journal of Rock Mechanics and Mining Sciences, 49: 31-44.

Van Oort, E, *A novel technique for the investigation of drilling fluid induced borehole instability in shales,* Proceedings of Conference on Rock Mechanics in Petroleum Engineering, Delft, SPE (1994).

Verhoef, E, Neeft, E, Grupa, J, Poley, A, Outline of a disposal concept in clay, OPERA, Netherlands (2011).

Vis, GJ, Verweij, JM, *Geological and geohydrological characterization of the Boom Clay and its overburden,* OPERA-TNO 411 Technical Report (2014).

Volckaert, G, Canniere, PD, Hooker, P, Fioravante, V, Grindrod, P, Impey, M, *MEGAS Modelling and experiments on gas migration in repository host rocks,* EUR 16235 EN, European Commission, Brussels, Belgium (1995).

Wildenborg, AFB, Orlic, B, Thimus, JF, Lange, G, De Cock, S, De Leeuw, CS, De Veling, EJ, M, *Radionuclide transport in clay during climate change,* Netherlands Journal of Geosciences/Geologie En Mijnbouw 82(1) (2003) 19–30.

Wiseall, AC, Graham, CC, Zihms, S, Harrington, J, Cuss, R, Gregory, S, Shaw, R, *Properties and Behaviour of the Boom Clay formation within a Dutch Repository Concept*, (2015) OPERA-BGS-615.

Wong, SW, Heidug, WK, *Borehole stability in shales: A constitutive model for the mechanical and chemical effects of drilling fluid invasion,* Rock Mechanics in Petroleum Engineering Society of Petroleum Engineers (1994).

Wong, T, Batjes, DAJ, de Jager, J, (Eds.) *Geology of the Netherlands*. Herent: Royal Netherlands Academy of Arts and Sciences (2007).

Young, A, Low, PF, *Osmosis in argillaceous rocks,* AAPG 47 (1965) 1004-1008.

OPERA
Meer informatie:

Postadres
Postbus 202
4380 AE Vlissingen

T 0113-616 666
F 0113-616 650
E info@covra.nl

www.covra.nl